Advanced materials for plasma facing components in fusion devices

Gareth Thomas

The Queen's College

Submitted for the Degree of Doctor of Philosophy, Hilary Term 2009

Abstract

Advanced materials for plasma facing components in fusion devices

Gareth Thomas

The Queen's College

Submitted for the Degree of Doctor of Philosophy, Hilary Term 2009

This thesis describes the design, manufacture and characterisation of thick vacuum plasma sprayed tungsten (W) coatings on steel substrates. Fusion is a potentially clean, sustainable, energy source in which nuclear energy is generated via the release of internal energy from nuclei. In order to fuse nuclei the Coulomb barrier must be breached - requiring extreme temperatures or pressures - akin to creating a 'star in a box'. Tungsten is a promising candidate material for future fusion reactors due to a high sputtering threshold and melting temperature. However, the large coefficient of thermal expansion mismatch with reactor structural steels such as the low activation steel Eurofer'97 is a major manufacturing and in-service problem. A vacuum plasma spraying approach for the manufacture of tungsten and tungsten/steel graded coatings has been developed successfully. The use of graded coatings and highly textured 3D interface surfi-sculpt substrates has been investigated to allow the deposition of thick plasma sprayed tungsten coatings on steel substrates. Finite element models have been developed to understand the residual stresses that develop in W/steel systems and made use of experimental measurements of coating thermal history during manufacture and elastic moduli measured by nano-indentation. For both the graded and surfi-sculpt coating, the models have been used to understand the mechanism of residual stress redistribution and relief in comparison with simple W on steel coatings, particularly by consideration of stored strain energy. In the case of surfi-sculpt W coatings, the patterned substrate gave rise to regular stress concentrating features, and allowed 2mm thick W coatings to be produced reproducibly without delamination. Preliminary through thickness residual stress measurements were compared to model predictions and provided tentative evidence of significant W coating stress relief by regulated coating segmentation.

Preface

The work which makes up this thesis was carried out by the author in the Department of Materials, University of Oxford, between October 2003 and October 2007 under the supervision of Prof. P.S. Grant. The work is original and no part of it has been submitted or accepted for any degree or other qualification in this university or elsewhere. Results and concepts are freely taken from the literature and are acknowledged in full.

Parts of this work have already been published or presented elsewhere:

- A paper presented at the International Thermal Spray Conference, Seattle USA, May 15-18 2006, entitled Vacuum Plasma Spraying of Thick W Coatings onto Surface Sculptures for Fusion Armour Applications, and presented in the Proceedings (on CD). Authors: G. Thomas, P.S. Grant, P. Coad, G. Matthews, R. Castro.

- A paper presented at the 3^{rd} International Conference on Spray Deposition and Melt Atomiization (SDMA), Bremen, Germany, September 4-6 2006, entitled Interface Topography and Residual Stress Distributions in W Coatings for Fusion Armour Applications and presented in the Proceedings (on CD). Authors: G. Thomas, R. Vincent, G. Matthews, B. Dance and P.S. Grant. This paper was subsequently published in a revised form in Vol. 477 of Materials Science and Engineering A (2008), pages 35-42.

Acknowledgements

I would like to express my gratitude to the many persons who helped me directly or indirectly throughout the course of this D.Phil. In particular, I would like to thank my supervisor, Prof. Patrick Grant for many years of encouragement and support through the wilderness that research can be at times. I am grateful to the UKAEA for financial support and to my sponsors Dr Guy Matthews and Prof. Paul Coad for encouragement and advice over the past several years. I would like to acknowledge the EPSRC for financial support of this project and the Queen's College for both financial support for attendance at conferences and brilliant personnel backup whenever I needed advice.

I am indebted to numerous colleagues and friends in the Department of Materials and would like to take this opportunity to thank Mr Robin Vincent for excellent advice, help and backup with the VPS machine, Dr Chris Salter and Mrs Gabriella Chapman for aid with microscopy, Mrs Lesley Jenkins and Mrs Lyn Richmond for providing friendly points of contact and all members of the PSG group for backup and advice over the course of this project. Additionally I would like to thank Dr Richard Castro for practical advice, aid and encouragement.

I would also like to express my thanks to my parents Michael and Anna, my brothers Ben and Alun and my wife Caroline for providing unwavering support and advice over the course of this project and for always being there whenever I asked. In addition, I would like to acknowledge the encouragement (in the form of smiles and grins) from my beautiful daughter Mary-Ann during the final stages of producing this Thesis.

In memory of Marie Davies and Phyllis May Skeat.

Gareth Thomas

The Queen's College

Hilary 2009

Contents

Chapter 1

Introduction

Fusion is a potentially clean and sustainable energy source in which nuclear energy is generated via the release of internal energy from nuclei. In order to fuse nuclei the Coulomb barrier must be breached - requiring extreme temperatures or pressures. In practice fusion is akin to creating a 'star in a box'. The extreme environment in which fusion on Earth can occur poses difficult materials challenges. Few materials are suited to the high temperatures and aggressive neutron flux which will be encountered. The difficulties in achieving fusion mean that the current generation of reactor plasma facing components (PFCs - essentially tiles) which are C-C composites are being reconsidered due to the tendency of C to quench the plasma once eroded. This is likely to occur with C-C composites because C is susceptible to chemical erosion from the PFC surface during inevitable plasma-wall interactions. A further disadvantage is the tendency of C to trap Tritium (T) in T-based hydrocarbons. As the refractory metal with the highest melting temperature, and a high sputtering threshold, W is a primary candidate for PFC applications. The melting point and toughness of W make processing and machining difficult and therefore vacuum plasma spraying (VPS) in which molten W droplets are rapidly solidified in quick succession to build up a thick W layer is a promising route for the manufacture of W based PFCs. W PFCs will have to be attached to the structural elements of the reactor which will most likely comprise low activation steels such as Eurofer'97. Unfortunately, W has a significantly lower coefficient of thermal expansion (CTE) than steel. This CTE mismatch will lead to significant thermal residual stresses both post-manufacture and during in-service life of the W

based PFC.

This project aims to investigate practical methods for managing this CTE mismatch stress in W/steel systems. Two different approaches are considered: (a) the use of graded interlayers to re-distribute stresses away from a planar W/steel interface, and (b) W deposition on modified surfi-sculpt substrates. These are substrates where regular millimetre scale structural features have been introduced to the substrate surface by a rastered e-beam - a process developed by TWI UK.

1.1 Research objectives and scope

This work was principally a proof-of-concept study to determine a suitable experimental approach for the manufacture of thick VPS W coatings on steel and had three main strands:

1. **Manufacture**. A strategy for the VPS deposition of W is developed and optimised (itself a non-trivial task). This was then used to co-spray different architectures of W/steel graded layers with various W fraction distributions as well as thick VPS W coatings on surfi-sculpt substrates.

2. **Characterisation**. Different microscopy techniques were applied to learn about the microstructure of the as-sprayed W, to confirm graded compositions and to locate and identify gross internal defects. Nano-indentation was used to extract elastic material properties for VPS W for use in subsequent FE calculations.

3. **FE modelling**. Thermal histories of the as-sprayed coatings were recorded and used in subsequent FE modelling to investigate how the two approaches managed significant thermal residual stresses. Due to the intractable complexity of surfi-sculpt topographies and the symmetric nature of graded coatings only 2D FE models were employed. Elastic and elastic-plastic material models were considered and calculated stress distributions compared to preliminary X-ray diffraction residual stress measurements.

Thermal testing of the manufactured coatings was not considered due to time constraints and lack of a suitable high energy neutron source to simulate in-service conditions. This and other areas not covered are suggested for future work at the end of this thesis.

Chapter 2

Literature review

2.1 Introduction

Fusion is a potentially clean, sustainable, energy source in which nuclear energy is generated via the release of internal energy from nuclei. The binding energy (BE) per nuclei for the known elements is illustrated in Figure 2.1 [1]:

Fusion involves the combination of light nuclei to create more stable heavier nuclei, with energy released by climbing the BE curve towards Fe. For two elements to undergo fusion the Coulomb energy barrier V_C between them must be overcome, as shown in Equation 2.1, for nuclei Z_1 and Z_2 of radii R_1 and R_2 respectively and where $e = 1.60 \times 10^{-19}\text{C}$ and $\varepsilon_0 = 8.85{\times}10^{-12}\text{C}^2\text{N}^{-1}\text{m}^{-2}$ [2]:

Figure 2.1: Binding energy per nucleon [1].

Figure 2.2: Cross sections for various fusion reactions [2].

$$V_C = \frac{e^2}{4\pi\varepsilon_0}\frac{Z_1 Z_2}{R_1 + R_2} \tag{2.1}$$

As indicated by Equation 2.1, the Coulomb barrier is largely dependent on the product $Z_1 Z_2$ and is therefore lowest for smaller nuclei - indicating why the fusion of isotopes of H to form He is energetically favourable. Of such fusion reactions, the deuterium-tritium (D-T) reaction is favoured, as shown in Equation 2.2 [3]:

$$D + T \longrightarrow 4He + n(14MeV) + 17.6MeV \tag{2.2}$$

The desirability of this reaction arises principally because of its larger interaction cross-section $\sigma(b)$ at elevated reactor temperatures, as shown in Figure 2.2 [2]. Additionally, the D-T reaction is found to have the lowest effective temperature threshold to net yield power, the lowest requirements for plasma confinement and the largest power output for a given plasma pressure.

Two methods have been proposed for the implementation of controlled fusion [3]. The first of these involves physically compressing nuclei until the Coulomb barrier is overcome, while the second involves heating an ionised gas or 'plasma' of nuclei sufficiently to induce highly energetic collisions. In terms

of a deployable reactor, these two methods for inducing fusion take the following forms [2]:

1. Inertial confinement: a form of particle acceleration in which a pellet of fuel is compressed via laser implosion sufficiently to initiate fusion.

2. Magnetic fusion: a form of thermonuclear fusion. A magnetically confined plasma composed of the ionised fuel nuclei is heated sufficiently to cause the probability of adjacent nuclei overcoming the Coulomb barrier to become statistically significant.

Practical difficulties with inertial confinement, such as repeating the fusion events fast enough to create a continuous power source, mean that magnetic fusion is favoured for a future reactor, in particular the currently favoured tokamak concept. Tokamak is Russian for 'toroidal magnetic chamber' and they are based on confinement of plasma particles in a 'doughnut' shaped ring via the interaction of a toroidal and induced poloidal field that prevents plasma-surface interactions (except via diffusion across magnetic field lines) [2, 4]. There are three main areas within a tokamak - the 1^{st} wall, the limiters and the diverter.

The 1^{st} wall comprises the main interior of the body of the vessel - different regions must withstand different environmental conditions, but under normal operational circumstances, conditions at the 1^{st} wall are relatively benign.

Limiters are regions within the vessel designed to physically 'limit' the extent of the plasma, to aid the control of impurities (by minimising wall/plasma edge contact areas). The limiter physically cuts-off the outer layer of plasma diffusing across the tokamak - defining both the 'last closed flux surface' and the 'scrape-off layer' (SOL) - see Figure 2.3 [5]. The SOL is the region within which the energy from the outer layer of the plasma diffuses into the limiter. It is the outer cooler/denser layer of the confined plasma that interfaces with the tokamak walls [6].

Unfortunately, the proximity of limiters to the main plasma inevitably resulted in some contamination via sputtered atoms, etc. Therefore, a new confinement method designed to isolate the main body of the plasma from inevitable plasma-surface interactions was developed - taking the form of a separate region known as the diverter. A poloidal diverter configuration is illustrated in Figure 2.4 [7].

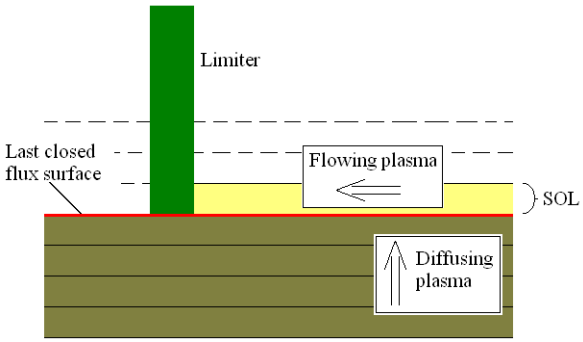

Figure 2.3: Scrape off layer (SOL).

The figure originally presented here cannot be made available via ORA for copyright reasons.

Figure 2.4: Poloidal diverter schematic [7].

Property:	JET	ITER
Main wall power density (MWm^{-2})	0.05	0.2
Stored energy (MJ)	max. 7, typically 3	320
Plasma current (MA)	3	15

Table 2.1: Key properties of JET and ITER [6].

The 'separatrix' defined by the x-point in Figure 2.4 is required for tokamaks to operate under the optimal High-mode ('H-mode') [5, 6, 8]. This separated region of plasma confines surface interactions to the diverter targets, minimising plasma contamination from any sputtered particles. The large flux densities of $\sim$50MWm^{-2} in the Joint European Torus (JET), resulting from the presence of the narrow SOL region at the diverter feet, are ameliorated by arranging an expansion of the flux tube at the diverter feet and by the transient nature of the flux at any particular point [5].

2.2 Plasma facing components (PFCs)

PFCs comprise 1^{st} wall, limiter and diverter elements and must be able to absorb high heat loads while maintaining their structural integrity and not releasing significant levels of impurities into the plasma, as subsequent ionisation of impurities will radiate away power. Usefully, $\sim$4/5 of the power created in a D-T fusion reaction is emitted in the form of high energy neutrons, which pass straight through the tokamak walls to an underlying Li thermal blanket, where heat-exchange takes place. The flux of the 14 MeV neutrons may, however, lead to embrittlement of the PFCs. The final 1/5 of fusion power is contained in the emitted alpha particles shown in Equation (2.2). While in a reactor this energy helps maintain fusion by heating the plasma, this heat will eventually escape via the reactor walls [5]. Key loads experienced in JET and the future ITER project (formally known as 'International Thermonuclear Experimental Reactor'), are shown in Table 2.1 [6].

As Table 2.1 illustrates, the transition from JET to ITER will result in a massive increase in stored energy. While the increased surface area in ITER results in only a fourfold increase in the main wall power density, the increased energy stored means that off-normal events such as disruptions will result in more damage to the tokamak wall in ITER.

Magnetic confinement of plasmas is not perfect and plasma-surface interactions are worsened by insta-

Property	ITER	DEMO	Power-plant
Total power (GW)	0.5	2-4	3-4
Neutron load (MWm^{-2})	0.56	2-3	2-3
Integrated neutron load ($MW_{YEARS}m^{-2}$)	~ 0.3	~ 10	~ 15
Expected degree of neutron damage (dpa)	3	30-80	150
Mode of operation	Pulsed $\sim$ 1000 s	Semi-continuous	Continuous
Expected lifetime (years)	....	....	~ 30

Table 2.2: Comparison of expected requirements for ITER, DEMO and a future power plant [12].

bilities of varying magnitudes which arise throughout confined plasmas. The main instabilities affecting the plasma edge are, in order of increasing severity, ELMs, VDEs and disruptions [5, 6, 7, 9, 10, 11].

- Edge localised modes (ELMs) are sudden and transient losses of particle confinement at the plasma edge - analogous to the turbulent effects in the boundary layers of ordinary fluids.
- Vertical displacement events (VDEs) are vertical instabilities of $\sim$60MJm^{-2} over relatively long timescales ($\sim$0.1-1s).
- Current disruptions involve complete collapse of plasma confinement in $\sim 100\mu$s - giving likely 1^{st} wall power densities of $\sim$GWm^{-2} in ITER.

Environmental conditions that PFCs will face in the successor to JET (ITER) plus future fusion devices are outlined in Table 2.2 [12]. The greatest challenges are the increased operational lifetime and total contained power expected of successive generations of reactors - combined with the resultant increases in neutron loading.

Both surface and bulk damage may result from plasma instabilities [9, 13]. Surface damage takes the form of surface erosion and re-deposition. Erosion may arise due to: surface vaporisation, spallation, particle emission and/or the formation of melt-layers. This eroded material must be immediately removed to prevent subsequent plasma contamination and build-up of potentially dangerous detritus e.g. Be that is easily activated. Bulk damage arises from the effects of more significant instabilities such as disruptions that deposit large amounts of energy in both the structural materials and at the PFC/structural interfaces. The resultant large increases in temperature inevitably increase thermal

stresses and over the longer term lead to fatigue based failure at the PFC/structural boundaries. Additionally, other bulk damage such as crack propagation, re-crystallisation and grain growth are likely to occur both within the PFCs and underlying structural materials.

2.3 PFC materials

PFC materials will face extreme environmental conditions and must fulfil numerous requirements including:

- Plasma compatibility. Migration of material into the plasma must not interfere unduly with plasma performance.
- Lifetime. A compromise between material thickness and PFC lifetime is required. Heat extraction is most efficient when the distance between the cooling channel and surface is minimised, giving an advantage to thinner coatings. Conversely, thicker coatings will be able to resist erosion over longer periods, but will also suffer from increased internal stresses - potentially leading to spallation.
- Reliability. Commercial viability dictates that the PFC must be reliable enough not to require servicing between scheduled re-fit times ($\sim$ once every 5 years [14]).
- Neutron irradiation resistance. PFC activation and transmutation must be minimised.
- Availability. This will become an issue when commercial considerations emerge.
- Machinability. A convenient method must exist for producing PFCs on an industrial scale.

Because of these extreme requirements, PFC material choice is limited to a few materials: C, Be and high-Z materials like W. Although Be has many attractions, it has largely been discounted for high temperature areas such as the diverter because of its low melting point, susceptibility to neutron induced embrittlement and extreme toxicity. C has a high thermal conductivity, undergoes sublimation rather than melting and can be readily manufactured into PFCs. The 1^{st} wall in JET is currently

Material	Advantages	Disadvantages
Be	Low T retention Strong O_2 gettering Low core plasma radiation	Low T_M $\sim$1290^{o}C Brittleness on neutron irradiation Toxicity of BeO
C	High temperature resistance Sublimation Low core plasma radiation	Susceptibility to chemical sputtering T retention Degradation of thermo-mechanical properties on neutron irradiation
W	Erosion resistance High T_M $\sim$3410^{o}C High Z (Z_W=74) Little T retention	CTE mismatch with likely base materials Unknown behaviour of melt loads under off-normal events High core plasma radiation

Table 2.3: Advantages and disadvantages of the three main PFC candidate materials; Be, C and W - *based on the overview gained during research for this literature review.*

covered with carbon-fibre composite (CFC) tiles. The key advantages and disadvantages of Be, C and W in terms of PFC applications are outlined in Table 2.3.

With CFC based PFCs the main erosion process is normally a combination of physical and chemical sputtering. However, at the higher power densities encountered during short duration off-normal events such as disruptions first sublimation and then particle emission begin to dominate. Linke *et al.* [9] described the use of an electron beam facility named JUDITH to investigate material damage in PFC mock-ups, including Be and doped/un-doped CFCs [9, 15, 16]. JUDITH accelerates electrons with currents up to 400mA at 120kV to produce power densities up to $\sim$ 15GWm^2 rastered over sample areas of 100mm^2. Pulse duration can range from 1ms to continuous [15]. Figure 2.5 shows particle emission from a CFC indicating that the erosion of C-based PFCs involved particle emission as well as sublimation. Figure 2.6 shows the corresponding absorbed current as a function of time for a number of electron beam pulses. Once the surface of the specimen was roughened by erosion (n=5), the absorbed current tended to a steady value and surface erosion via particle emission was approximately constant.

These results illustrated that CFC PFC erosion is dominated by thermionic particle emission. This is a major disadvantage of the current generation of CFC PFCs because emitted particles migrate into the plasma, radiating away energy and quenching the plasma. C-based PFCs also suffer from a high propensity to trap hydrogen isotopes due to their chemistry, particularly tritium (T) - a highly radioactive strategic material whose inventory in a future reactor will be the subject of strong licensing

Figure 2.5: Particle emission resulting from 5ms loading at 4.8MJm^{-2} of a CFC PFC [9].

Figure 2.6: Decay of absorbed current for 5 ms 4.8MJm^{-2} pulses, n = 1, 3 and 5 [9].

Property	Value
Physical sputtering threshold (eV)	200 (for D)
Melting temperature (^oC)	3410
Density at RT (gcm^{-3})	19.3
Young's modulus (GPa)	390-410
Poisson's ratio	0.28-0.30
Anisotropy at 24^oC	1.010
DBBT range (^oC)	100-400
Thermal expansion coefficient at RT (K^{-1})	4.5 x 10^{-6}
Vapour pressure at T_{MELT} (Pa)	1.3 x 10^{-7}
Thermal conductivity ($Wm^{-1}K^{-1}$)	RT: 145, 1000^oC: 113
Specific heat at RT ($Jg^{-1}K^{-1}$)	0.14
Re-crystallisation temperature range(^oC)	1150 - 1350
Ultimate strength at RT (MPa)	1000

Table 2.4: Key properties of W [17, 18].

restrictions.

2.3.1 Tungsten

W is under consideration for all PFC areas and is the primary candidate for the ITER diverter. Extensive use of W in fission applications, including shielding, has provided a substantial body of W expertise within the nuclear community. Some of the important physical properties of W are shown in Table 2.4 [17, 18]. Of particular note is the high melting temperature (3410^{o}C) and thermal conductivity (113Wm^{-1}K^{-1}). The W vapour pressure is the lowest of any metal or metallic alloy, so plasma contamination by any melted PFC material will be reduced. The high toughness and Z make W resistant to erosion and any sputtered W atoms are likely to be re-deposited via the gyro motion of the local magnetic field before migration to the main plasma occurs. Significantly, T retention in W is much lower then for C-based PFCs [17, 19].

Unfortunately, as Table 2.4 shows, W has a high ductile to brittle transition temperature (DBTT) that causes significant difficulties under thermal cycling and the coefficient of thermal expansion (CTE) of $\sim$4.5$\times$10^{-6} K^{-1} is substantially below that of steels such as Eurofer-97 ($\sim$11-12$\times$10^6 K^{-1} [20]), a likely structural material for a future reactor. DBTT and CTE behaviour increase residual stresses during both thermal cycling and manufacture. The high density of W will also be significant in terms of mechanical handling of PFC structures - the heavy weight of bulk W means that coatings on less dense materials would be preferable even if the thermal properties of bulk W were ideal for structural

materials [21]. Another potential disadvantage is that due to the high Z, any eroded W atoms that reach the plasma will not be fully ionised, resulting in these atoms radiating away significant plasma energy. W also has a high self-sputtering rate [22], meaning it is generally considered most relevant for low temperature, high density diverter conditions. W undergoes transmutation in a high neutron flux environment, in particular to Re, however in the short term, such transmutations may prove beneficial as W-Re alloys have lower DBTTs than pure W [17]. Different thicknesses of W will be required in different areas of a tokamak. For example, in the ITER diverter [19]:

1. Thicknesses of ∼10mm are required at the dome and vertical target in order to withstand the physical erosion which will result from disruptions at these exposed areas; and
2. Thicknesses of ∼30mm are required at colder regions such as the liner surface ($< \sim 1\text{MWm}^{-2}$) in order to maintain a suitable temperature profile throughout the coating to prevent C co-deposition.

Different forms of W have being considered for use in ITER, including [19]: (i) pressed, sintered and hot-worked pure W; (ii) mechanically alloyed, pressed, sintered and hot-worked dispersion-strengthened W, and; (iii) cast W alloys.

Thermal testing of W

Linke *et al.* demonstrated that by keeping the working temperature of pure W above the DBTT during irradiation, surface damage decreased, and even when relatively high energy loads were applied, surface cracks in the resultant re-crystallised melt layers were minimised [9].

Tokunaga *et al.* also looked at heat loading and thermal fatigue of W-based PFC mock-ups [21]. Here, 0.5mm thick VPS W coatings were deposited on 20mm × 20mm × 10mm carbon/carbon-fibre composite (CFC) CX-2002U isotropically fine-grained graphite, IG-430U and TZM (Mo-0.5Ti-0.07Zr) substrates. These were subsequently Ti-brazed (using a 0.05mm thick Ti foil) to 20mm × 20mm × 20mm oxygen free high purity Cu (OFHC) blocks with integral cooling tubes. Thermal loading was carried out using a 30keV electron beam collimated to a 20mm × 20mm area. Heat fluxes of 10MWm^2

Figure 2.7: Actively cooled VPS W PFC mock-ups, a) experimental setup and, b) results of themal fatigue test over 100 cycles on W/TZM/OFHC mock-up [21].

(20s ramp-up, 16s plateau, 16s ramp-down) were applied over 100 cycles and potential delamination was monitored via thermocouples and electrical conductivity. The experimental setup and resultant thermal/electrical distributions after thermal fatigue testing are illustrated in Figure 2.7 [21]. While the temperature at the surface (point T1) in Figure 2.7 did decrease by $\sim 100^{o}$C with cycle number, the temperature at the brazed interface did not change. In addition, as the current across the sample was reasonably constant, these results indicated that no significant failure (either delamination or cracking) occurred either at the brazed interface or within the VPS W during thermal cycling - implying that such W-based PFCs can successfully withstand a rector-relevant thermal load.

A slightly different approach was taken by Lehto *et al.*, who studied the effects of heat loading on pure W via neutral beams and additionally placed six CFC marker tiles coated with 2cm wide, $\sim 3.4 \mu$m thick poloidal W stripes in the inner and outer diverter regions of JET [23]. Over the 1^{st} five months of subsequent JET operation, these tiles were examined *in-situ* by remote imaging. The coatings on the tiles on the inner diverter were noted to be hidden beneath a layer of impurities, while coatings on the outer diverter remained visible. The coatings were removed from JET for full analysis in 2004. This study shows the difficulty in testing any PFC in a realistic environment, and the long timescales involved for subsequent analysis. Lehto *et al.* [23] also used Rutherford backscattering (RBS) on a number of smaller CFC samples coated with identical thicknesses of W to show that there was no measurable change in W coating thickness after several D beam exposures as shown in Table 2.5, concluding that W had not undergone any sputtering due to impinging D atoms (the high sputtering threshold of W being of the upmost importance for PFC applications). Figure 2.8 shows the results

3 s: $T_{MAX} \sim$ **900^{o}C**	**1 s:** $T_{MAX} \sim$ **1280^{o}C**
95 Pulses @ $5.8 MWm^{-2}$	4 Pulses @ 8.0 MWm^{-2}
	6 Pulses @ $10.0 MWm^{-2}$
	3 Pulses @ $12.4 MWm^{-2}$
	5 Pulses @ $15.7 MWm^{-2}$

Table 2.5: Deuterium neutral beam exposures for W coated CFC marker tiles [23].

Figure 2.8: RBS spectra for W before/after exposure to D neutral beam [23].

of these studies, backing-up those from [9] and [21], indicating the resistance of pure W to thermal loading/cycling.

Bolt *et al.* [24] studied the thermal loading and D retention of plasma sprayed W, using several e-beam and ion facilities [9, 15, 16]. Three different W/steel combinations were investigated, in each case a 2mm W coating was deposited on-top of a 50:50 W/steel interlayer by VPS. The steels were 316L, Eurofer-97 and F82H (a low-activation steel developed in Japan - see later). Tests were conducted with power densities of up to 3.5MWm^{-2}, while cyclic testing involved up to 1000 20s pulses at 2MWm^{-2}. All the tests achieved broadly similar results and Figure 2.9 shows the results of heat flux testing on a W/Eurofer-97 sample. For different heat flux loadings, temperatures at various points on/within the actively cooled arrangement were measured using a combination of pyrometers and thermocouples. Predicted temperatures from a numerical simulation of through-thickness heat flow for each section are also included. Even at 2.5MWm^{-2}, over double the predicted 1^{st} wall power density for ITER during standard operation [12, 24] (see Table 2.1), W temperatures did not exceed 1200^{o}C - well below T_M. They further showed that after an initial period, the temperature of the W upper-surface stabilised at a pseudo steady state for a given thermal load.

Figure 2.9: W coating temperature versus heat flux for a variety of positions within the W/Eurofer-97 arrangement [24].

Figure 2.10: Cross-sectional scanning electron micrographs of plasma sprayed W coatings before/after thermal cycling [24]. Left - before thermal cycling; Right - after thermal cycling.

Figure 2.10 shows the cross-sectional microstructure of the W coatings before and after the thermal cycling tests [24]. The relatively rough surface and initial porosity (∼20%) of the as plasma sprayed coating was retained after thermal cycling and there was no evidence of cracks or other induced damage in the loaded samples.

Bolt *et al.* [24] also conducted tests similar to those of Lehto *et al.* [23] into the degree of D retention by W, where D acts an an analogue for T that is too regulated/radioactive for these types of experiments. 600eV D_3^+ (200 eV/D) ions with a fluence of $1.0 \times 10^{24} Dm^{-2}$ were accelerated towards both plasma sprayed W coatings with ∼30% porosity and polycrystalline W samples to produce surface temperatures in the range 323-793 K. Deuterium retention was measured by a resonance technique integrated over a depth of 7mm throughout this temperature range, and the results are shown in Figure 2.11.

The pores in the plasma sprayed W gave greater D retention at all irradiation temperatures. Both plots in Figure 2.11 decreased in two stages. At $T_{IRAD} = 550$K, corresponding to 1.4eV - the dissociation energy of D_2 - the molecular D_2 fraction escapes. The second decrease in absorbed D occurred at $T_{IRAD} = 750$K, corresponding to the BE of 2.1eV. Overall, deuterium/tritium retention will be

Figure 2.11: Retained D as a function of irradiation temperature for both plasma sprayed W and polycrystaline W [24].

minimised if W operating temperatures $> \sim$ 800K are maintained, in agreement with previous work [23].

Taking these preceding studies together [9, 23, 24] it is reasonable to conclude that under 'standard' fusion reactor operating conditions, W is a strong PFC candidate. Further evidence of W's durability has been demonstrated in other small-scale tests e.g. [25, 26, 27]. However, none of the above investigations have been able to take into account the effects of off-normal events such as disruptions, or the issue of transmutation and embrittlement in a 14MeV neutron environment.

W PFC applications

W has been utilised in real PFCs in a number of operational tokamaks, such as ASDEX [22, 28]. Additionally, limited areas of W and Mo have been introduced to the limiter in TEXTOR [29]. In the ASDEX 1^{st} wall, W has been deposited by: arc deposition $\sim 1\mu$m, plasma vapour deposition (PVD) $\sim$0.5-1.5μm and vacuum plasma spraying (VPS) $\sim$100-500μm. While a few W atoms migrated beyond the SOL into the main plasma - presumably due to the relatively short ionisation length of the eroded W atoms - subsequent analysis of the W test tiles showed that the majority of sputtered W atoms redeposited on the PFC close to their original site [22, 28].

The diverter in ASDEX was formed from a C-substrate with a 0.5mm thick VPS layer of W deposited on top, in turn covered by a 20μm thick VPS W-Re multilayer to prevent the formation of carbides (from C eroded elsewhere in the tokamak before migrating to the diverter) within the W layer [28]. Although this arrangement showed both micro and macro cracks in the W layer after 400 cycles in an electron/ion beam irradiation test, after $\sim$500 cycles in the tokamak with normal power densities of around 6.5MWm^{-2} and power densities of up to 15MWm^{-2} during ELM's, no damage was noted. Furthermore, spectroscopic investigation showed few W impurities in the ASDEX plasma, although some C contamination was noted due to the chemical erosion of the base layer [22]. Similar results were found using Mo in TEXTOR [29].

Neutron irradiation of W was largely beyond the scope of this study, however the transmutation products of W are found to have little long-term activity [30, 31].

Property	**W**	**W-1La$_2$O$_3$**
Density at RT (gcm^{-3})	19.3	18.9
Coefficient of thermal expansion at RT (K^{-1})	4.5×10^{-6}	4.7×10^{-6}
Thermal conductivity at RT/1000^{o}C ($Wm^{-1}K^{-1}$)	145/113	120/98
Ultimate strength at RT (MPa)	1000	900
Thermal neutron capture cross-section (b)	18.5	18.0
DBBT range (^oC)	100-400	100-400
Re-crystallisation temperature range (^oC)	1150-1350	1250-1700
Melting point (^oC)	3410	3410
	W-5Re	**W-30Cu**
Density at RT (gcm^{-3})	19.4	14.0
Coefficient of thermal expansion at RT (K^{-1})	4.5×10^{-6}	11.5×10^{-6}
Thermal conductivity at RT/1000^{o}C ($Wm^{-1}K^{-1}$)	70/83	300/$\sim$220
Ultimate strength at RT (MPa)	1100	520
Thermal neutron capture cross-section (b)	21.8	10.4
DBBT range (^oC)	50-200	<RT
Re-crystallisation temperature range (^oC)	>1500	<RT
Melting point (^oC)	3300	1080 (Cu)

Table 2.6: Properties of W and various W alloys [30].

2.3.2 W alloys

W alloys tend to have lower DBTTs than pure W - as illustrated in Table 2.6 [30], presumably because of W lattice distortion, an increase in dislocation 'width' and a reduction in the Pierls-Nabarro stress required for dislocation motion. The two main W alloy classes that have been investigated are W-5Re and W-La_2O_3.

W-5Re

A relatively large body of data exists on alloying W with Re, due to Soviet and Western space research in the 1970's and 1980's. W-5Re has been used in thermocouples because of its increased chemical stability, while the ability of W-10Re to resist extreme thermal shocks has led to its use in areas such as the upper regions of X-ray targets [17]. As shown in Table 2.6, the addition of Re to W serves to reduce the DBTT while also increasing ultimate strength. The reduction in T_{MELT} and change in coefficient of thermal expansion (CTE) is slight since Z_W (74) $\sim$ Z_{Re} (75). Re additions to W also increase the re-crystallisation temperature following cold work as well as reducing the swelling encountered by pure W at high neutron dose rates [19].

Dispersion strengthened W (W-La_2O_3)

The addition of a fine dispersion, typically ∼1%, of La_2O_3 particles results in an increase in re-crystallisation temperature. The dispersoids interact with the matrix during re-crystallisation, impeding secondary grain growth. The corresponding reduction in thermal conductivity is minimal and there is no change in either DBTT or melting point and only a slight increase in CTE.

W-La_2O_3 is surprisingly easy/inexpensive to machine at room temperature because no micro-cracks form in the vicinity of the dispersed La_2O_3 particles - they deform evenly with the W matrix. The microstructure and homogeneity of the dispersoids can be refined via a combination of thermo-mechanical treatments - further increasing the re-crystallisation temperature. The greater the amount of hot work, the greater the resultant degree of refinement of the dispersoids during subsequent annealing [19].

W-La_2O_3 was originally developed to replace thoriated W for high temperature applications where high erosion resistance and a low electron work function are needed [30]. Because of the relatively well balanced combination of physical properties and machining cost as well as the likely high neutron fluence in the 1^{st} generation ITER diverter, W-La_2O_3 has been chosen as a reference high Z armour for the ITER diverter.

Thermal testing of W alloys

Unlike C based PFCs, erosion of W alloys under off-normal loads is not dominated by particle emission, rather it is dominated by thermal shock related events [9, 16]. The effects of a 5ms 11.8MJm^{-2} pulse on W-30Cu, W-5Re and W-La_2O_3 are shown in Figure 2.12 [9]. W-La_2O_3 and W-5Re showed large scale cracks running vertically from the horizontal surface and parallel to platelet-shaped grains orientated perpendicular to the material surface. In contrast, voids within the Cu phase formed in the W-30Cu alloy [9, 12]. W-La_2O_3 shows arguably less severe failure to thermal shock than the other two alloys, presumably because of the dispersoid strengthening as well as slightly improved crack growth resistance.

Figure 2.12: Effects of a 5ms 11.8MJm^{-2} pulse on various W based alloys [9].

RAFM steel	Composition by wt.%					
	C	**Cr**	**Ni**	**Mo**	**V**	**Nb**
MANET II	0.10	10.30	0.65	0.57	0.19	0.14
F82H Modified	0.089	8.16	0.019	0.0018	0.16	0.0001
OPTIFER IV	0.12	9.35	0.007	< 0.002	0.26	< 0.0006
EUROFER-97	0.12	8.93	0.022	0.0015	0.2	0.0022
	Si	**Mn**	**Ta**	**B**	**W**	**N**
MANET II	0.14	0.75	N/A	0.08	N/A	0.03
F82H Modified	0.11	0.161	0.02	< 0.0002	2.17	0.0065
OPTIFER IV	0.022	0.54	0.07	< 0.004	1.03	0.05
EUROFER-97	0.06	0.47	0.14	< 0.001	1.07	0.018

Table 2.7: Compositions by weight of various RAFM steels [32, 33, 34, 35].

2.3.3 Reduced activation ferritic/martensitic (RAFM) steels

ITER will be operated in a strongly pulsed mode (Table 2.2) with a relatively low neutron flux compared to both DEMO and future power plants making austenitic steels such as 316 LN-IG likely candidates for major structural components, in part due to their fission heritage [31]. However, in the longer term the high neutron fluxes and the necessity of continuous plasma operation mean that structural members (and heat extraction conduits) are more likely to be replaced by the lower activation class of RAFM steels. In ITER PFC's are likely to be be bonded to these RAFM steels, with the final components secured to a 316 LN-IG superstructure. [31].

Activation of structural elements involves the formation of radioactive products from neutron irradiation, inducing transmutation into other elements. This has two main disadvantages: (i) the precise type and fraction of transmutated elements is hard to predict and may represent a safety hazard if they undergo decay themselves, and; (ii) transmutation changes the composition of the structural elements - potentially affecting their ability to perform their function effectively. Therefore reduction in structural material neutron activation will be beneficial for long-term structural stability.

Compositions of a selection of current reduced activation Cr-WVTa containing steels (with Eurofer-97 the European version) are summarised in Table 2.7 [32, 33, 34, 35]. The core characteristic of these steels are their relatively high Cr contents, typically $\sim$9%, which increase thermal conductivity by $\sim$1.5 times compared to austenitic (Cr-Ni) steels for T$<$700^{o}C [20]. Since Cr is a ferrite stabilizer and there is no Ni present, and as their name implies, these steels tend to be ferritic or martensitic in nature.

Figure 2.13: Dose rate in milli-Gray's/hour ($JKg^{-1}h^{-1}$) for various steels measured at 100mm 9 months after neutron irradiation to 0.8-1 dpa in the Osiris reactor, modified from [36].

In all cases, Mo and Nb were replaced by similar proportions of the lower-activation elements W and Ta (plus V in newer steels) and concentrations of Ni and minor alloying elements that contributed significantly to long-term activation were limited. Figure 2.13 illustrates the lower activation of reduced activation steels, which exhibited lower count rates following identical activation compared to their austenitic counterparts.

The microstructure of Eurofer-97 has been studied extensively [34, 35, 37, 38, 39, 40]. The key characteristics of Eurofer-97, compared with F-82H as appropriate are [35, 40]: (a) a finer prior austenite grain size due to the increased concentration of the grain refining Ta, (b) a higher number of Ta and V rich secondary precipitate phases because of the increased concentration of carbide formers, (c) Eurofer-97 is fully martensitic and free of δ-ferrite, (d) two types of carbide are present, the Cr-rich $M_{23}C_6$ type and the Ta/V-rich (Ta,V)C type, (e) Eurofer-97 and F-82H have broadly similar ultimate tensile, yield strengths and elongations of $\sim$ 500MPa, 450MPa and 15% respectively at 400^{o}C, and (f) Eurofer-97 has a DBTT of -51^{o}C compared with -25^{o}C for F-82H and provides improved toughness at a given temperature. Both ageing and increasing W concentration increased DBTT [41]. This ageing behaviour was attributed to coarsening of inter-granular precipitates such as $M_{26}C_6$ and Laves phases and similar results were found for thermally and/or chronologically aged samples [35, 37]. Further, replacing Mo with W increased creep rupture strength [41], while excess W led to the formation of δ-ferrite and Laves phases, known to degrade toughness (the optimum W content in Eurofer-97 is

consequently ∼1% [35, 37]).

Neutron irradiation is outside the scope of this study, however, broadly speaking irradiation and associated atomic displacement in RAFM steels led to ∼2% swelling, which was reduced by lowering tempering temperatures [42, 43]. Precipitation formation along grain boundaries was observed to degrade RAFM steel toughness and Ti addition was seen to depress secondary M_6C precipitation [44].

2.4 Plasma spraying

Because the requirements of PFCs are so severe and various, it is unlikely that a single materials solution will be employed in evolving reactor designs. This review has already reflected the current trend towards using W for those components subject to the most severe environmental conditions - the diverter - and the use of RAFM steels for structural, load bearing elements. Current designs assume that thick W armor coatings will be applied to RAFM components, and the role of plasma spraying has been introduced.

The particular attributes of plasma spraying are now described more fully and previous work on plasma spraying of refractory metals is described. This is a relatively specialised and narrow area of research with restricted information in the public domain. Wherever possible, relevant studies outside this area are also described.

Figure 2.14 shows a schematic of the commonest variant of the plasma spraying process [45]. A DC arc is struck between a W anode and a water cooled cathode to ionise feed gases, normally Ar and H_2 in order to form a plasma. The particulate feedstock is then radially injected into this plasma 'flame' where it is entrained, accelerated and melted within the high velocity flow before deposition on a substrate.

Although the term flame is commonly used to describe the ionised gas flow, no combustion takes place, rather heat is imparted to the particulate by a combination of radiation, convection and bombardment by H^+ and Ar^+ ions [46]. The use of a secondary diatomic gas enhances melting by increasing the power of the plasma. A strong magnetic and thermal pinch effect operates close to the end of the

Figure 2.14: Schematic of plasma spraying [45].

plasma 'gun' due to complex magnetohydrodynamic effects - the effect of which is to produce a well collimated central plasma core. Plasma sprayed coatings build-up by successive impacts/splats on the substrate surface - and some residual porosity usually remains in the final coating. The very high temperatures involved allow refractory metals and high melting point ceramics to be processed [47]. Particle sizes are typically $<70\mu$m since although plasma temperatures are high, particle transit times in the plasma core are typically milli-seconds [48].

As previously mentioned, in order to ensure complete melting of the feedstock, the time that each particle from the feedstock powder remains in the plasma flame, t_{DWELL}, must be prolonged. Factors affecting t_{DWELL} will include angle of injection, particle size and morphology and the power of the plasma. In order to achieve consistent coatings and to minimise porosity, spray parameters must be optimised for each particular powder used. In particular, if t_{DWELL} is too short, coating efficiency will be reduced because partially melted particles will simply bounce off the substrate.

The key parameters and their typical ranges are plasma current (400-900A), plasma voltage (30-60V), Ar flow rate (20-50 standard litres per minute (slpm)), H_2 flow rate (0-10slpm), ambient pressure (0.1-1 atmospheres), ambient atmosphere (air or Ar), spray distance (50-300mm), powder mass flow rate (0-1gs^{-1}) and powder carrier gas flow rate (0-5slpm). The precise combination of parameters varies from powder to powder and have traditionally been arrived at by trial and error and on the basis of operator experience. More recently, statistical design methods have been shown to dramatically reduce trial and error experiments for Al, Ti and $MoSi_2$ based materials [49]. Computer models of the plasma spraying process have also been developed but have yet to reach the point where they can be used to predict close to optimum process parameters for a powder a *priori* [50].

2.4.1 Vacuum plasma spraying (VPS)

VPS is carried out in an evacuated chamber that is then back-filled to typically 50-150mbars of Ar. The lower pressure environment leads to a higher pressure differential between the anode/cathode where the plasma is formed and the nozzle, resulting in the following compared to atmospheric plasma spraying (APS) [17, 51]:

- increased particle velocities, leading to deposition densities of up to ∼97% of theoretical;
- much reduced O_2 contamination in the final coating;
- increased adhesion between coating and substrate because of the higher deposition velocities;
- the ability to employ a high tension bias between the anode and substrate to provide pre-spray and/or simultaneous sputter cleaning or electrostatic substrate heating; and
- a reduction in t_{DWELL} because of higher jet velocities, mandating reduced powder diameters $<45\mu$m.

2.4.2 Plasma spraying of refractory materials

W is the primary refractory PFC candidate and various efforts have been made to plasma spray W. Until recently, these have been conducted largely at atmospheric pressure, where densities in the range 50-95% of the theoretical maximum have been achieved. In comparison, VPS W layers have been deposited with densities of ∼97%. Density is directly related to thermal conductivity, so ambient environment is particularly important for W coatings for PFC applications. For example, typical percentage thermal conductivities - of the maximum theoretical value for pure W - achieved using different atmospheres have been reported as [17]: VPS (60%), APS with air (5%), APS with N_2 (15%) and APS with Ar (35%). Consequently, VPS is mandatory for W for PFC applications. Because of this, various companies have been contracted by researchers in the fusion community to develop strategies for the VPS processing of W e.g. Plansee AG [52] and Plasma Processes Incorporated [53].

VPS W has a number of uses outside of PFCs, for example, NASA have successfully utilised VPS to deposit refractory metals such as W on graphite bases to form containment cartridges for the growth of semi-conductors in microgravity environments [54]. Castro *et al.* [51] were among the first to spray W successfully in a low pressure environment, and formed a Cu/W multi-layered material. First, separate VPS parameters for both Cu and W were developed, before a single plasma torch with dual powder hoppers was utilised to form Cu/W multi-layered materials. The VPS parameters developed for W are included in Table 2.8.

Processing parameter	**Value**
I (A)	900
V (V)	42
Back-fill gas	Ar @ 27 kPa $\sim$ 270 mbars
Primary gas	Ar @ 3.7 $m^3 hour^{-1} \sim$ 61.7 slpm
Secondary gas	He @ 1.1 $m^3 hour^{-1} \sim$ 18.3 slpm
Carrier gas	Ar @ 0.3 $m^3 hour^{-1} \sim$ 5 slpm
Powder feed rate ($g min^{-1}$)	22
Spray distance (mm)	130
W powder size distribution (μm)	-10 +2
Substrate preparation	Grit blasting (60 mesh Al_2O_3) @ 551 kPa

Table 2.8: VPS spray parameters for the W powder used in [51].

Processing-parameter	Value
I (A)	740
Power (kW)	50
Back-fill gas	Ar @ 120 mbars
Primary gas	Ar @ 40 slpm
Secondary gas	H_2 @ 10 slpm
Carrier gas	Ar @ 0.7 slpm
Powder feed rate ($gmin^{-1}$)	10.84 (at 4rpm)
Spray distance (mm)	*not quoted*
W powder size (μm)	1-10, ave. = 5.5

Table 2.9: VPS spray parameters for the W powder used in [55].

Castro *et al.* [51] successfully produced these Cu/W microlaminate structures in both bar and concentric ring forms as a technological demonstrator, with up to 100 alternate Cu/W layers. The microstructure of the VPS deposited W was found to exhibit epitaxial, columnar growth with a grain width of $\sim$1μm across the deposited W layers. Even under their optimised conditions, un-melted particles remained in the coating. Despite the thermal cycling resulting from layer deposition/cooling and the large difference in CTE between Cu (α $\sim$18$\times10^{-6}$K^{-1}) and W (α $\sim$4$\times10^{-6}$K^{-1}) there was no evidence of significant cracking or delamination in the Cu/W layers.

Because coolant pipes within the walls of a future reactor vessel will be Cu based, a number of other investigations have concerned the VPS deposition of W onto Cu/Cu alloys. For example, Smid *et al.* [30] highlighted the idea of depositing W armour onto a W-30Cu pseudo alloy for low heat flux areas of a reactor, such as the 1^{st} wall since it was suggested that the CTE difference for W/W-30Cu is $\sim$ 2 times smaller than that between W/Cu. This work has recently been developed further by Pintsuk *et al.* in [55].

Pintsuk *et al.* [55] focused on the production of W/Cu-composites via VPS, but using VPS parameters optimised for 1-10μm (ave. 5.5μm) W powder provided by Plansee AG, Reutte, Austria (the Cu powder size was selected to suit these parameters) as outlined in Table 2.9. This decision reflects the difficultly in melting W and the narrow band of VPS parameters within which it is possible to successfully deposit VPS coatings.

The VPS W parameters outlined in Table 2.9 were developed using a Sulzer Metco VPS machine. However, no details of the particular plasma torch or spray distance used are given in [55]. By comparison, the lower plasma power ($\sim$38kW) for the VPS deposition of W outlined in Table 2.8 was

Figure 2.15: W and Cu plumes within a VPS flame under the settings outlined in Table 2.9 [55].

likely countered by the higher chamber pressure of ~270mbar. This would have led to a increased particle dwell time in the flame and correspondingly a higher degree of melting for a particular plasma power - although at the cost of decreased deposition velocity (and therefore resultant coating adhesion). In both cases a high secondary gas flow rate is notable, required to increase the enthalpy of the plasma and therefore ensure adequate W melting. [55] also illustrates one of the major problems with the VPS deposition of W - namely that of centering the W in the plasma flame in order to ensure adequate melting, as shown in Figure 2.15.

The tendency for W to form a highly collimated stream of particles within the plasma flame is visible in Figure 2.15 and comparison may be drawn with the much wider distribution of the less dense/lower melting temperature Cu also visible in this figure. The high degree of W collimation will inevitably lead to high degree of dependance on material carrier gas flow rate - too high a flow rate and material will penetrate through the hot core of the flame with no melting occurring and conversely, too low a flow rate and the material will not penetrate into the hot central region.

One of the most recent and comprehensive reports of VPS of W is due to Bolt *et al.* [24] and concerned:

- The development of bespoke VPS parameters for both W and steel in conjunction with Plansee AG [52], which remain proprietary (likely similar to those outlined in Table 2.9);
- Manufacture of trial W/steel composite inter-layers with up to a further 2mm of W armour on top;
- Initial metallurgical and mechanical characterisation of VPS deposited W; and

Figure 2.16: Cross-section of upper section of VPS W on Eurofer [24].

- Thermal loading studies using both neutral beam and D sources up to ∼2.5MW.

The main finding of [24] was that Bolt *et al.* successfully deposited reactor-relevant 2mm thick W using VPS onto candidate structural steels including Eurofer-97. A typical W cross-section micrograph from [24] demonstrating the residual porosity is shown in Figure 2.16.

It is worth noting that the porosity evident in Figure 2.16 will lead - in common with other plasma sprayed materials - to the VPS coating having a substantially lower Young's modulus than bulk W - for example, You *et al.* [56] calculated that a VPS W coating deposited under similar conditions had a Young's modulus ∼14% of that of bulk W (∼54-58GPa as opposed to ∼400GPa for bulk).

2.5 Functionally gradient materials (FGMs)

The concept of FGMs largely evolved out of Japanese aerospace research in the 1980s directed towards a proposed spaceplane [57, 58, 59]. FGMs were initially conceived to solve the problem of the large stresses which build up under thermal loading at dissimilar material interfaces in composites. The central idea is to substantially relieve thermally induced stresses by replacing the discreet material interface with a more 'diffuse' one, as illustrated in Figure 2.17 [57].

The gradient does not have to take the smooth form illustrated in Figure 2.17, but may also take the form of a single or series of inter-layers or alternately a matrix/inclusion form of structure [60]. Fun-

Figure 2.17: Schematic demonstration of the FGM concept [57].

damentally, FGMs exhibit variations in composition and/or microstructure over significant distances across material boundaries [61]. In its purest sense, any composite with graded material properties (chemical, electrical, optical or nuclear rather than mechanical) may be classified as an FGM [57, 58].

There are two routes via which this required grading can be obtained [58]:

1. **Constructive processes:** the gradient is established in a series of individual layers e.g. via the isostatic compression of ready-mixed powder pre-forms; or
2. **Transport based processes:** these processes rely upon naturally occurring transport mechanisms such as inter-diffusion to create a composition gradient across the material boundaries.

Plasma spraying is a 'constructive process' as direct control of the feed rate of feedstock material and deposition conditions can be maintained at virtually all times. A typical example of a plasma sprayed FGM comprises: (i) partially stabilised zirconia (ZrO_2-$8Y_2O_3$ or PSZ) used as a thermal barrier coating (TBC) in the aerospace industry, and; (ii) an alloy used as a bond coat on Co and Ni [46, 61]. A Ni/PSZ FGM has been produced successfully using two different methods, alternate deposition of layers of increasing thickness and simultaneous spraying of both feedstock materials to create a stepped through-thickness FGM profile [62]. A plasma sprayed five-layer CoNiCrAlY/yitria stabilised zirconia (YSZ) FGM and a conventional bi-layer CoNiCrAlY/YSZ are shown in Figure 2.18 [63]. The FGM comprised a 100% YSZ top coat; a 100% CoNiCrAlY base/bond coat, and three intermediate layers with varying proportions of YSZ/CoNiCrAlY of 25/75, 50/50 and 75/25 weight fractions. Both 600μm and 1000μm thick FGMs were produced.

The CTE and elastic modulus of individual FGM layers (obtained by a rule of mixtures) are shown in Figure 2.19 as a function of temperature [63]. The CTE increased and elastic modulus decreased with increasing temperature and CoNiCrAlY content, and show how 'bulk' properties may be graded.

Micro-hardnesses of a ZrO_2 and Ni alloy bi-layer coating and a five-layered FGM of the same materials are shown in Figure 2.20 [63], and show that in practice micro-hardness was effectively graded across the coating.

The same authors [63] developed an axially symmetric cylindrical finite element model to investigate

Figure 2.18: Cross-sectional micrographs for the CoNiCrAlY/YSZ system: Left: five-layer FGM, Right: bi-layer coating [63].

Figure 2.19: Physical properties of 5 FGM layers based on CoNiCrAlY/ZrO_2: Left: CTE versus temperature, Right: elastic modulus versus temperature [63].

Figure 2.20: Micro-hardness values for; Left: bi-layer material, Right: 5-layer FGM [63].

Figure 2.21: Effects of variation in FGM composition and layer thickness on residual stresses [64].

post-spraying residual stresses in the FGM. The model provided qualitative insights, rather than accurate predictions, but in common with other similar studies, showed that stresses were considerably relaxed at all interfaces in the FGM in comparison with the bi-layer equivalent. Figure 2.21 shows how variations in FGM constituent components affected axial residual stresses (the calculations were carried out using a similar numerical simulation approach [64]). The predicted axial stresses in Figure 2.21 have been normalised, and two FGM thicknesses of 4 and 8mm were considered. For both thicknesses, Figure 2.21 shows that lowest residual stresses were predicted for a profile exponent of P$\sim$0.6. A thicker FGM reduced residual stresses for all types of gradient variations.

Ahn *et al.* studied the production of graded TBCs, producing five FGMs combining YSZ and MSZ (magnesia-stabilised zirconia) with NiCrAlY, Inconel 625 and SUS 316 for aerospace applications via both VPS and APS [65]. A comparison of thermal shock performance for bi-layer and 5-layer YSZ/NiCrAlY coatings (both with reaction derived bond coats) was then conducted involving 80 cycles of raising the sample to 1000°C, dropping it into water at RT followed by drying. As Figure 2.22 illustrates, the FGM structure proved more resistant to thermal shock than the bi-layer coating, most likely because of a) the lack of stress build up at a discrete interface (the more diffuse structure of the FGM would have re-distributed stresses) and b) protective micro-cracking in the FGM upper layers allowing for built up residual stress to be relived before spallation occurred.

W/Cu FGMs hold great promise in many different areas subject to extreme thermal conditions, with

Figure 2.22: SEM cross-sections of PSZ/NiCrAlY a) bi-layer structure and b) 5-layer FGM after 80 1000°C to ∼RT thermal shock cycles [65].

Figure 2.23: SEM cross-sections of four different W (lighter phase)/Cu mixed coatings; a) 26 vol.% Cu, b) 43 vol.% Cu, c) 52 vol.% Cu and d) 78 vol.% Cu [55].

applications in a broad range of potential areas including electronics, (principally heat sinks), military technology (vehicle components, armour), nuclear fusion (PFCs) and space (control of residual stresses due to solar-induced thermal excursions) [55]. Pintsuk *et al.* manufactured two different morphologies of W/Cu FGMs on graphite substrates (to aid layer removal for further study) via VPS. As discussed previously, this was achieved by choosing the VPS recipe based on the optimum for W and adjusting the Cu particle size accordingly [55]. Both a fully graded 1.1mm thick pure W to pure Cu coating and a partially graded 2.5mm thick 95 to 75 vol.%. W coating with a 20 vol.% W bond-layer at the Cu rich end were successfully manufactured. Layer properties were investigated via the manufacture of 2-3mm thick individual 26, 43, 52 and 78 vol.% Cu (remainder W) layers, also on graphite substrates. Scanning electron images of these coatings are shown in Figure 2.23 [55]. There was no evidence of oxide formation at the constituent layer boundaries. In addition, it is worth noting that even using the VPS conditions outlined in Table 2.9, full W melting was not achieved as evidenced by the presence of circular un-melted particles.

Ultrasonic measurements were used to determine the elastic properties of the mixed layers, with elastic modulus varying approximately linearly with composition, as shown in Figure 2.24.

Figure 2.24: Variation of Young's modulus with Cu content in W/Cu composites [55].

Figure 2.25: Schematic representation of failure mechanisms in the SEM cross-sections of PSZ/NiCrAlY shown in Figure 2.22 after 80 1000°C to ∼RT thermal shock cycles; a) bi-layer structure and b) 5-layer FGM [65].

2.5.1 FGM failure

Figure 2.25 shows schematically how an PSZ/NiCrAlY FGM changed the failure mode and gave improved thermal cycling life over the bi-layer equivalent [65].

Cracking in the FGM involved formation of micro-cracks in the upper YSZ layer which on meeting pores or other sub-surface defects propagated horizontally forming micro-crack networks. It was surmised that these then became connected, forming the vertical cracks evident in Figures 2.22 and 2.25. These then acted to relieve the tensile and compressive residual stresses whereas in a bi-layer equivalent, thermal stress arising out of CTE mismatch was concentrated at the interface so that when micro-cracking appeared, micro-cracks rapidly propagated to macro-cracks leading to spallation as illustrated in Figure 2.22.

Xiong *et al.* [66] investigated failure mechanisms in four different thickness (0.75, 1.1, 1.6 and 2.1mm) 5-layer NiCrAlY through to PSZ FGMs that were thermally cycled using a H_2/O_2 flame to heat the front face while the back face was water cooled. Multiple thermocouples monitored back face temperature, the surface temperature was measured by pyrometry and an acoustic sensor monitored cracking. Thermal shock tests were carried out at 1400°C with successive 180s heating and cooling cycles. Four different modes of fracture behaviour were noted within the FGM coatings as shown in Figure 2.26. These failure modes were classed as: 1) transverse cracks within the coating; 2) surface cracks; 3) local spallation, and; 4) transverse cracking/spallation at the substrate/FGM interface.

Figure 2.26: Optical micrographs illustrating failure modes within FGMs: 1) 0.75mm after 1 cycle; 2) 0.75mm after 2 cycles; 3) 0.75mm after 5 cycles, and; 4) 1.6mm after 1 cycle, modified from [66].

Overall Xiong *et al.* [66] found that thicker FGM coatings exhibited greater surface temperatures at a given flux and therefore greater temperature differences across the specimens. The higher surface temperatures on thicker samples contributed to differences in fracture mode with the greater thermally induced stresses in the thicker coatings leading to complete spallation at the substrate/FGM interface while in the thinner (0.75 and 1.1 mm) coatings local spallation tended to occur. This local spallation was believed to arise from the linkage of numerous transverse cracks that developed at the interface with the FGM upper coat because of local tensile stresses exceeding the critical fracture stress along the uneven FGM upper coat interface.

2.5.2 FGMs as PFCs

High heat loads and neutron fluxes lead to a requirement for reliable and efficient bonding mechanisms between PFCs and structural materials. An FGM approach is suggested as an important strategy to manage the mismatch between PFCs and structural materials [67]. A good overview of the proposed use of W based FGMs in ITER, citing both 1^{st} wall and diverter applications, is given in [68].

Ge *et al.* [69] investigated potential FGM PFCs based on: W/Cu, B_4C/Cu and SiC/C. The W/Cu FGM was manufactured by pressing a compact of three W pre-forms, each containing different volume fractions of W and Cu, in a steel die, before sintering the resultant structure in a graphite crucible embedded with Al_2O_3 powder at 1300^oC for 1 hour. Molten Cu was then allowed to flow into the residual pores of the W frame for 30min at 1300^oC. Finally, a W plate was attached to the base by hot-pressing, giving the required W/Cu FGM. A similar infiltration method for the manufacture for W/Cu is described in [30]. Unfortunately, few test results or performance data was reported by Ge *et al.* [69]. Both SiC and B_4C protective coatings have been used on C based PFCs to reduce C sputtering. Both materials have excellent thermal properties and in the case of SiC, resistance to activation. B_4C/Cu FGMs were manufactured by plasma spraying with nominal compositional distribution exponents, $P = 0.2$, 1.0 and 2.0, according to [69]:

$$V_f = \left(\frac{x}{t}\right)^P \tag{2.3}$$

Figure 2.27: Thermal desorption data for a 160μm thick linearly graded ($P = 1.0$) B_4C/Cu FGM (bottom curve) plus 160μm thick bi-layer material (upper curve) [69].

where V_f is the volume fraction of one phase, x is the distance to the surface from the top of the FGM layer in question, t is the thickness of the FGM layer in question and P is a constant.

Thermal shock resistance of the three B_4C/Cu FGMs was tested by repeatedly baking for 5 minutes at 500^{o}C followed by quenching in water. The $P = 0.2$ and 2.0 specimens had begun to spall after 2-5 cycles, while the $P = 1.0$ FGM survived 20 cycles [69].

Figure 2.27 shows the superiority of a 160μm thick linearly graded ($P = 1.0$) B_4C/Cu FGM over its non-FGM counterpart in terms of the thermal desorption of CH_4 as a proxy for the tendency to form CT_4. The FGM coating (the bottom curve) had significantly lower desorption at all temperatures investigated - suggesting lower erosion rates in any future application. Thermal shock experiments were also carried out by subjecting the FGM and non-FGM 160 and 260μm B_4C/Cu specimens to 30$\times$ 2ms pulses from a 400mA, 5000eV laser. Only the FGM sample showed no cracks. Finally, the B_4C/Cu FGM was subjected to thermal tests involving heat loads of 6.4MWm^{-2} and pulse durations of 1000ms. Over 1000 cycles, only minimal surface damage was observed.

Five-layered 5mm thick SiC/C FGMs with good inter-layer bonding were fabricated [69] by sintering multi-layered green pre-forms at temperatures up to 1950^{o}C and pressures of 20MPa for 1hr. The SiC/C FGM showed a lower tendency to the sputtering of C from the surface under D beam loading, when compared to monolithic graphite - attributable to the SiC top layer. Ge *et al.* [69] demonstrated that various reactor-relevant properties of W/Cu, B_4C/Cu and SiC/C FGMs were largely superior to

Figure 2.28: A backscattered electron micrograph of the SiC/Cu FGM [70].

conventional bi-layer coatings.

In [70], a SiC/Cu FGM was proposed as a replacement for graphite in a reactor environment in order to reduce T retention. The idea was to create a composite material combining SiC's excellent thermal and corrosion resistance with Cu's high thermal conductivity and machinability. However, there is a ΔCTE$\sim 12\times10^{-6}\mathrm{K}^{-1}$ between SiC and Cu. Figure 2.28 shows a back-scattered electron micrograph of the resulting SiC/Cu FGM manufactured by a graded sintering technique in an attempt to manage the CTE difference.

The performance of the SiC/Cu FGM was assessed principally by comparing sputtered product intensity to that of nuclear graphite SMF800 under 3KeV, 4.6×10^{15} $\mathrm{D}^{+}\mathrm{s}^{-1}\mathrm{cm}^{2}$ loadings by mass spectrometry. Figure 2.29 shows a substantial reduction in CD_4 production from the FGM as intended [70].

Thermal desorption of the same material was investigated after implantation of a total flux of 1.2×10^{18} 2.7keV ions, around a base pressure of 1.0×10^{-6}Pa [70]. The resultant thermal release spectra again showed a significant drop-off in CD_4 production in the FGM compared with graphite, consistent with Figure 2.29. Further thermal shock tests were conducted using a 4ms, 0.4cm diameter pulsed laser with energy density of $398\mathrm{MWm}^{-2}$. Exposures of 100 and 300s increased FGM weight due to Cu oxidation. When tested against monolithic SiC, the SiC/Cu FGM survived without macro defects through the entire 300 pulses, while the monolithic SiC failed after 20 pulses.

Figure 2.29: Comparison of sputtered product intensity for a SiC/Cu FGM and nuclear graphite [70].

Figure 2.30: Schematic illustrating construction of a Be-Cu FGM [67].

Other investigators [67] sought to take the approach described in [69, 70] to investigate a Be-Cu FGM for a PFC application. In this case, the Be-Cu FGM was manufactured by sintering layers of mixed Be/Cu powder with differing relative fractions - as shown schematically in Figure 2.30 [67]. However, this method was not totally effective because the intermetallic compounds, $Be_2Cu(\delta)$ (as a $\sim 5\mu$m layer) and $BeCu(\gamma)$ solid solution formed in an uncontrolled manner in the region around Be/Cu interfaces [67].

As previously discussed (Section 2.4.2) Castro *et al.* [51] investigated W-based FGMs by producing Cu/W microlaminate structures in both bar and concentric ring forms utilising VPS. More than one hundred alternate Cu/W layers were deposited as concentric rings where thermal stresses were generally compressive. The grain size in the W layers increased from $\sim 2\mu$m to 20μm as deposition continued because of *in-situ* heating effects arising from the deposition of successive layers. Microscopy indicated that successful bonding of all layers had occurred - despite each layer being subjected to severe thermal shocks by the application of the next.

Mechanical analysis of the manufactured Cu/W FGMs via a 4-point bend test indicated that while the elastic modulus of the Cu/W was consistent with predictions from a simple rule-of-mixtures method, tensile strength was less than expected - limited by a lower than predicted density of the sprayed materials. An attempt to increase density via hot isostatic press (HIP) processing of the Cu/W FGM was un-successful because of the high creep resistance of W.

Finally, the 'proof-of-concept' work on VPS W layers by Bolt *et al.* which culminated in a 50:50

Figure 2.31: 50:50 W/Eurofer-97 interlayer, 250× [24].

W/steel interlayer shown in Figure 2.31 on a Eurofer substrate with a thick VPS W coating represents the current 'state-of-the-art' in terms of W/steel FGMs [24].

2.6 Residual stresses

If residual stress exceeds either the yield strength or fracture stress then an FGM will fail during manufacture. Residual stresses give rise to stored strain energy that will drive interfacial failure if it exceeds the interfacial fracture energy (related to interfacial strength and toughness [71]). This means that a knowledge of residual stress state is important for a PFC both to aid manufacture and also to ensure a satisfactory subsequent in-service life. Two approaches exist for the determination of a systems residual stress state; practical measurement - either during or after manufacture and theoretical determination/numerical simulation - most often via a modeling technique such as finite element analysis (FEA), an approach outlined briefly in Section 2.5 [63, 72, 73]. These two approaches are complementary - it is often impractical to measure residual stresses, particularly if a destructive technique such as hole-drilling is required [71, 74, 75, 76]. However, simulation alone is not sufficient without the confidence in results given by comparison to experimentally determined results. In this section these two approaches will be explored, with particular emphasis on experimental determination during manufacture and the finite element approach. Other experimental approaches, such as X-ray diffraction which have been employed in this project are outlined in more detail in the experimental section of this thesis.

2.6.1 Experimental determination of residual stresses

Various approaches to determining residual stress levels within coatings have been investigated, including shifts in X-ray diffraction peaks caused by stress concentrations within crystallographic planes and direct analysis techniques such as hole drilling where changes in surface strain are monitored as material is removed [71, 74, 75, 76]. However, such techniques have only have limited capabilities: X-ray analysis can only determine strain levels in very thin surface regions of coatings while hole drilling is an involved and semi-destructive analytical technique, with limited ability for the determination of precise stress distributions in coatings. [74] details a method for calculating composite CTE values for both bi-layer and FGM coatings by obtaining the derivative of measured thermal expansions, but cannot provide overall stress levels within coatings. Instead, a method of inferring stress distributions from in-situ measurements as coatings are deposited is often used. Such a technique involves monitoring sample curvature during manufacture [75, 77] and subsequently inferring the contribution of residual stress from a numerical model.

Most of these approaches consider the differential thermal contraction during cooling resulting from CTE mismatch between different FGM layers. However as Tsui *et al.* [77] explained, such models do not fully take into account the environmental conditions encountered in rapid solidification techniques such as VPS - namely the quenching stresses which build up within the rapidly solidifying droplets. The misfit strains if not relieved would result in the fracture stress quickly being exceeded, but relaxation mechanisms such as creep, yielding or microcracking act to relieve stresses. Tsui *et al.* [77] approached residual stress generation in VPS by constructing a model combining two sections: a) one based on Bernoulli-Euler beam theory, based around a succession of force and moment balances to describe the curvature of composite beams beams (those made of two or more different materials) under load [78, 79, 80], which are used to calculate changing stress distributions/sample curvature due to misfit stresses, and b) a conventional differential thermal contraction model.

Tsui *et al.* [77] showed how experimental data of curvature could then be used in these models (neglecting inelastic strain) to obtain stress distributions in APS NiCrAlY on steel, VPS B_4C on Ti-6Al-4V and VPS ZrO_2-8($wt.\%$)Y_2O_3 on PK33 coatings, an approach extended to cylindrical geometries in [71]. The approach employed by Tsui *et al.* [77, 81] has been successfully implemented by numerous

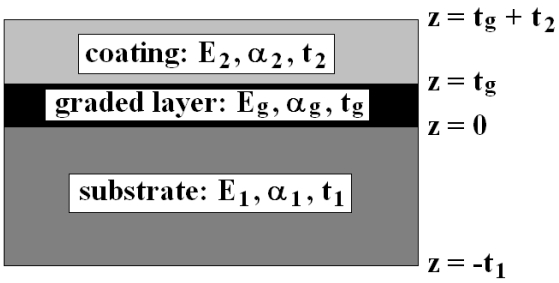

Figure 2.32: Schematic illustration of graded structure modeled in [82].

groups including You *et al* [56], where calculated residual stresses in VPS W on steel were calibrated against surface residual stress measurements estimated from X-ray diffraction.

Gill *et al.* [75] presented a practical technique for monitoring curvature changes during VPS deposition of Mo coatings on both stainless steel and Ti substrates using a video camera, similar to that used in [71]. They extended the method of Tsui *et al.* to quantify complicating factors such as heat extracted during spraying due to the method of sample retention and sample deflection due to the plasma flame.

2.6.2 Predicting residual stresses - numerical techniques

There are many different approaches to the estimation of residual stress distributions via numerical techniques. These range from the explicit/exact closed-form solutions [82, 83] to finite element analysis [60, 84].

A simplified/refined (compared to Tsui *et al.* [77] and excluding the effects of quenching stress) approach to the theoretical prediction of elastic thermally induced stresses is presented in [82]. In this paper, Hsueh *et al.*, building on previous work described in [83], described an exact solution for the distribution of elastic thermal stresses within FGM structures. Elastic thermal stress distributions were calculated for FGM interlayers between two dissimilar materials subject to both external bending and the effects of internal residual stresses. The geometry analysed is illustrated in Figure 2.32.

The free surfaces of the coating and substrate materials (materials 2 and 1 respectively) are defined to lie at $z = t_g + t_2$ and -t_1 respectively, where z is the vertical distance from the substrate/graded layer interface, t_1 the substrate thickness, t_g the graded layer thickness and t_2 the coating thickness. Material properties of Young's modulus E and coefficient of thermal expansion α are assigned to each

layer in Figure 2.32. The main assumption was that strain could be decomposed into two different components, a uniform component and a bending stress component arising from sample curvature. The bending axis was defined as the cross-sectional line at which the bending strain component was zero and was shown to be inversely proportional to the radius of curvature and directly proportional to the distance from the bending axis. Defining the position of the bending axis as $z = t_b$, this leads to an equation for the strain distribution in Figure 2.32:

$$\varepsilon = c + \frac{z - t_b}{r} \longrightarrow -t_1 \leq z \leq t_g + t_2 \tag{2.4}$$

where ε is the strain at any distance z from the substrate/graded layer interface, c is the uniform strain component, and r is the radius of sample curvature.

The three parameters, c, t_b and r were solved for by Hsueh *et al.* in a similar manner to that outlined by Tsui *et al.* in [71, 77, 81]. Two key assumptions were made which allowed these parameters to be determined. First, a force-balance was calculated with net force due to the uniform strain component c assumed to be zero. Secondly, the sum of the bending moments with respect to the bending axis ($z = t_b$) was taken, by definition, to be zero. These assumptions allowed the derivation of the following values for the three unknowns in Equation 2.4 [82, 83]:

$$c = \frac{(E_1 t_1 \alpha_1 + E_2 t_2 \alpha_2 + \int_0^{t_g} E_g \alpha_g dz)\Delta T}{E_1 t_1 + E_2 t_2 + \int_0^{t_g} E_g dz} \tag{2.5}$$

$$t_b = \frac{-E_1 t_1^2 + E_2 t_2 (2t_g + t_2) + 2\int_0^{t_g} E_g z dz}{2(E_1 t_1 + E_2 t_2 + \int_0^{t_g} E_g dz)} \tag{2.6}$$

$$\frac{1}{r} = \frac{3[E_1(c - \alpha_1 \Delta T)t_1^2 - E_2 t_2 (c - \alpha_2 \Delta T)(2t_g + t_2) - 2\int_0^{t_g} E_g (c - \alpha_g \Delta T) z dz]}{E_1 t_1^2 (2t_1 + 3t_b) + E_2 t_2 [6t_g^2 + 6t_g t_2 - 3t_b (2t_g + t_2] + 6\int_0^{t_g} E_g z (z - t_b) dz} \tag{2.7}$$

where ΔT is the temperature change experienced by the system.

Equations 2.5 to 2.7 may be substituted into Equation 2.4 to calculate the strain at any z position

within the 2D system shown in Figure 2.32. The FGM layer properties were determined using a 'rule-of-mixtures' approach, with the fraction at any particular z position within the FGM defined using a compositional exponent, n, in an analogous manner to Equation 2.3 [69]. For each of the three layers defined in Figure 2.32, within the constraints on z-position defined by this arrangement, the normal in-plane stresses σ_n in layer n after a temperature change ΔT were given by 2.8:

$$\sigma(n) = E_n(\epsilon - \alpha_n \Delta T) \tag{2.8}$$

By substituting the calculated strain distribution from Equation 2.4 into Equation 2.8, the stress distribution at any point within the FGM could then be calculated. Typical resultant stress distributions calculated by Hsueh *et al.* for a NiCrAlY/FGM/ZrO_2-Y_2O_3 system with the geometry outlined in Figure 2.32 are presented in Figure 2.33 [82].

These stress distributions show the effect of changing the exponent value, n. The variation in phase fractions was linear for n=1 and non-linear for $0<n<1$, or $n>1$. Figure 2.33(b) illustrates that σ_n stresses with the FGM coatings e.g. σ_g, for $0<z<200\mu$m, were both compressive and tensile in different regions. While compressive stresses increased with n, the peak tensile stress within the FGM layer occurred for $n\sim6$. This numerical approach is well established, with many similar studies in the literature e.g. [85].

2.7 Summary

Tokamaks, in which isotopes of hydrogen undergo fusion in a magnetically/electrically confined plasma, currently represent the most advanced potential avenue for commercially viable fusion power. However, as discussed in this chapter, plasma confinement is not perfect and the extreme conditions encountered within/at the edge of plasmas mean that PFC materials must comply with stringent requirements, principal amongst which are:

1. Plasma compatibility - PFCs must survive the extreme thermal conditions found both under normal operation at the plasma edge and also during off-normal events such as disruptions -

Figure 2.33: Calculated stress distributions in the NiCrAlY/FGM/Zr$O_2Y_2O_3$ composite outlined in Figure 2.32, (a) substrate, (b) FGM + coating [82].

additionally, they must not interfere unduly with the plasma itself if eroded; and

2. Neutron irradiation resistance - this is required in order to minimise both neutron induced embrittlement and possible transmutation/activation.

These requirements severely limit the choice of available materials. Low Z options are primarily based on either C or Be. However, both materials present potential issues, particularly during off-normal events when plasma confinement fails and PFCs have to deal with (a) high transient power loads, and (b) close interaction with the plasma. Unfortunately, C is subject to chemical sputtering; tends to trap radioactive T in the form of hydrocarbons, and in the typical PFC forms of CFCs, suffers from degraded mechanical properties on neutron irradiation. Be also suffers neutron induced embrittlement and additionally has a relatively low melting temperature. The main high Z PFC candidate materials are W/alloys such as W-5Re and W-La_2O_3. Tungsten has the highest melting temperature and sputtering threshold of any refractory metal. If eroded its high density makes rapid local re-deposition likely, however, the high atomic weight of W atoms means that if they do escape into the main plasma they will become highly ionized, radiating a large amount of power. The high toughness of W makes machining problematic making plasma spraying efficient as a near-net-shape manufacturing route.

VPS W coatings of up to 2mm thickness [24] have been manufactured for PFC applications: for thinner $<100\mu$m thick coatings VPS deposition has been directly onto substrates, whereas for thicker VPS coatings interlayers have been employed to ensure adhesion. Experiments with VPS W as a PFC have been successfully carried out for both ASEDX Upgrade [22, 28] and TEXTOR [29], albeit with a maximum thicknesses of 0.5mm. Testing has focused on the thermal properties and deuterium retention of VPS W which has been shown to be controllable by both Lehto *et al.* [23] and Bolt *et al.* [24]. These studies also illustrated the difficulty of developing suitable W VPS recipes. High plasma powers of 38-50kW were used along with feedstock powder sizes of $<10\mu$m, although even then full melting was not achieved. PFC substrate materials will have to provide both structural support and a suitable heat extraction path - choices include both Cu and low activation steels. Cu substrates will likely be used where rapid heat extraction is required (e.g. the diverter), with reduced activation ferritic/martensitic steels designed to minimise long term activation such as Eurofer 97 employed

elsewhere. Following on from the non-trivial task of manufacturing up to 2mm thick VPS W coatings with high as-sprayed densities, the difference in CTE between plasma sprayed W and these potential structural materials (steel and Cu) has been a major focal point of research.

Functionally graded interfaces which replace discrete interfaces with more diffuse versions have been actively considered for this task. In [65] and [66] it was shown that graded interfaces relieved residual stresses by changing the nature of coating failure. Compared with bi-layer systems where failure occurred at the substrate/coating interface, with graded coatings either the position of failure moved or the failure mode changed altogether, with micro-cracking leading to coating segmentation which relieved residual stresses, rather than propagating to failure. Techniques such as in-situ monitoring of the curvature of substrate/coating systems during VPS coating deposition [75, 77] have been combined with numerical modelling to predict through-thickness residual stress distributions. Similar numerical techniques have also been employed by a variety of researchers to try and understand management of residual stresses by FGMs [63, 71, 72, 73, 74, 76], although no precise mechanism has been identified. Such work has, however, further highlighted the importance of FGM architecture in the management of residual stresses which has also been observed experimentally [69]. Properties including CTE, elastic modulus and microhardness have been shown to vary with composition through the thickness of as-sprayed FGMs [55, 63], which have been successfully manufactured and tested as possible PFC candidates e.g. W/Cu, B_4C/Cu and SiC/Cu [51, 69, 70]. With regards to W/steel FGMs, Bolt *et al.* [24] deposited 2mm of VPS W onto a 50:50 W/Eurofer 97 mixed interlayer on a Eurofer 97 substrate. This successfully relieved the thermal residual stresses associated with substrate/coating CTE mismatch during both manufacture and subsequent thermal testing. Mixing between the W/steel phases was on the macro-scale, with no visible evidence of alloying.

This literature review has highlighted the emerging emphasis on VPS W as a potential PFC material. This thesis focuses on the problems associated with managing the CTE mismatch between W/steel components in PFCs. An optimal VPS deposition strategy for W powder was developed that allowed coatings of up to 2mm thickness to be sprayed successfully. Both graded coatings with a variety of architectures and a novel substrate modification technique known as 'surfi-sculpt' were employed to try and achieve an improved W/steel interface. The aim was to move beyond the current state-of-

the-art in this area, namely the 2mm VPS W coating/50:50 W/Eurofer 97 interlayer arrangement developed by Bolt *et al.* [24]. Commercial finite element software (Comsol Multiphysics^{TM}) was used to extend some of the previous numerical modelling. In particular, this software was employed to try and shed further light on the mechanism behind relief of residual stresses in both FGMs and systems involving surfi-sculpt interfaces. Manufactured coating microstructure and through-thickness post-manufacture residual stresses were investigated. The measured residual stress distributions were subsequently combined with the finite element models to help identify likely stress relief mechanisms in both FGM and surfi-sculpt vacuum plasma coated systems.

Chapter 3

Experimental

3.1 Introduction

Tungsten has the highest melting point of any refractory metal at 3,695K [18]. Because of this, the VPS plasma power required to melt a substantial fraction of the W was relatively high. The plasma power is determined by the plasma current and voltage, the plasma primary gas and its flow rate and the plasma secondary gas and its flow rate. Other key parameters that determine the extent of W melting at deposition are the spray distance, chamber/spray pressure and substrate preparation.

An initial literature search established that perhaps half a dozen groups had worked on VPS W, with only one report of 'thick' VPS W coatings on steel via the use of interlayers performed at Plansee AG (Austria) [24, 86]. Further, the overall mix of process parameters or 'recipe' chosen to deposit any particular powder is often highly dependent upon the equipment being used, for example, even with identical plasma guns, the erosion of one anode/cathode set can have a significant effect on output power. Therefore VPS parameters given in previous work could not be simply copied here and the first task was to establish suitable VPS conditions at Oxford to deposit good quality W coatings. This chapter details the experimental equipment employed, some theoretical background to help interpret results, the various methodologies for VPS recipe development, and the techniques used for coating examination.

3.2 Methodology and equipment

3.2.1 VPS

The in-house VPS equipment comprised a Plamsa-Technik (now Sulzer Metco of Switzerland) VPS machine equipped with a F4-VB (Sulzer Metco) plasma gun mounted on a 5-axis ASEA (now ABB) robot and an index-linked turntable providing the capability to plasma spray a variety of complex shapes, as illustrated in Figure 3.1(a).

The main vacuum chamber is shown in Figure 3.1(a) with a diameter of ∼1.5m. The machine was equipped with twin powder feedstock hoppers which allowed for two different materials to be sprayed simultaneously. The powder was transported from the hoppers by an Ar flow and delivered to the top or bottom 'injector' into plasma torch, as shown in Figure 3.1(b). The 5-axis robot/index-linked turntable system was capable of moving the plasma torch in a controlled manner around complex geometry substrates. However, only a simple raster pattern was used here, with start/finish points to one side of the sample, stepping downwards in 10mm vertical increments to ensure full coverage, as shown schematically in Figure 3.2.

Two powders were vacuum plasma sprayed in the course of this project: pure W and a commercially available powder called Diamalloy 1008, which was chosen as an approximate analogue to Eurofer'97, a low activation RAFM steel envisaged for fusion reactor rear wall applications. The composition of Diamalloy 1008 and Eurofer'97 are given in Table 3.1, showing Diamalloy 1008 was not a close match to Eurofer. However, Diamalloy 1008 was readily available in the correct size range for VPS, was relatively cheap, and given the large difference in steel versus W thermophysical behaviour, likely gave a good enough approximation to the behaviour of Eurofer'97. The W powder had a typical faceted morphology, while the Diamalloy 1008 had a spherical morphology, as shown in Figures 3.3(a) and (b) respectively. The W powder was 99.9% pure and was supplied by William Rowlands Ltd of Sheffield, UK with a mean particle size of 11.4μm, and a particle size distribution shown in Figure 3.4. The Diamalloy powder, supplied by Sulzer Metco, had a particle size of 5.5-45μm. Three types of steel substrate were sprayed (detailed later): mild steel, 316L stainless steel and surfi-sculpt 316L stainless steel.

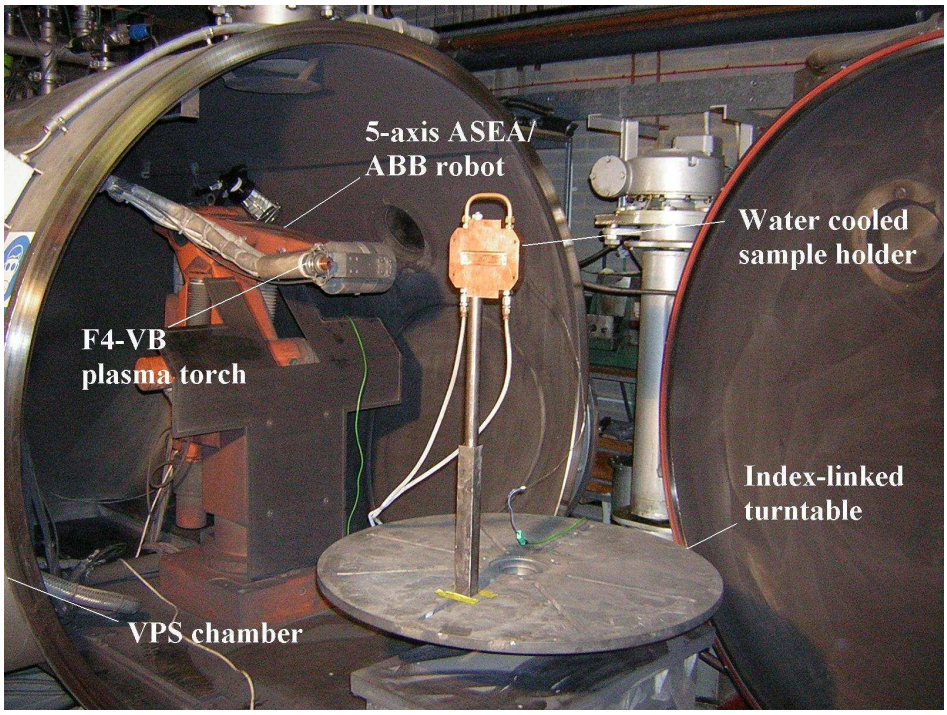

(a): Robot with plasma gun mounted and index-linked turntable in the VPS chamber

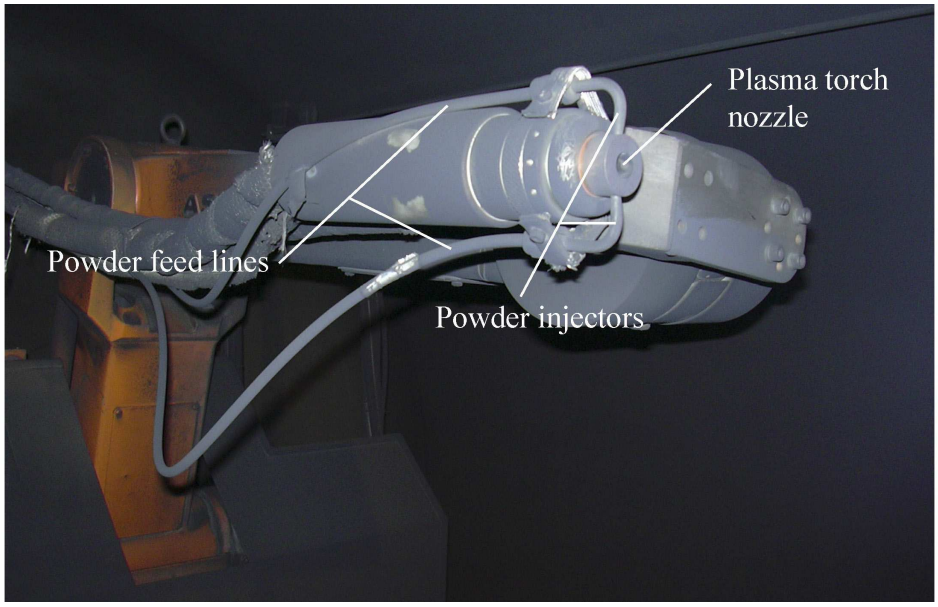

(b): Close-up of plasma gun/torch

Figure 3.1: VPS chamber/gun.

Material	Fe	Cr	Mo	Ni	Si	Cu	B	C
Diamalloy 1008	58.6	17	11	3	3	3	4	0.4
Eurofer'97	89	8.93	0.0015	0.018	0.06	0	<0.001	0.12

Table 3.1: Composition by wt.% for Diamalloy 1008 and Eurofer'97 [32, 33, 34, 35, 87].

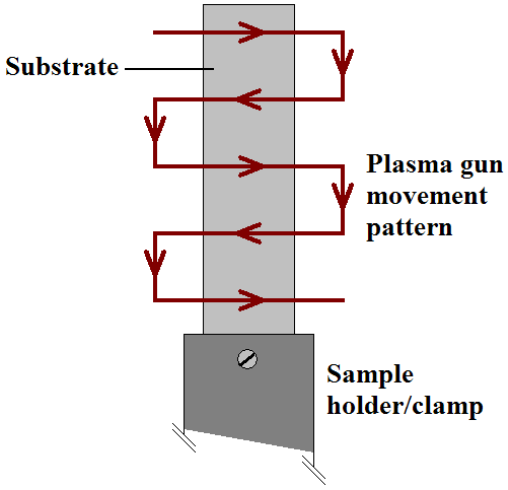

Figure 3.2: Schematic of VPS robot movement pattern or raster over the substrate holder.

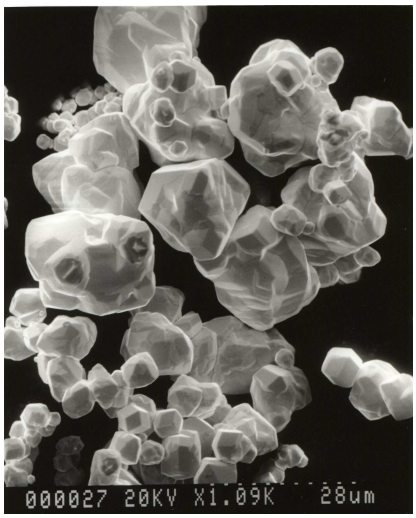

(a): Secondary electron image of the W feedstock powder

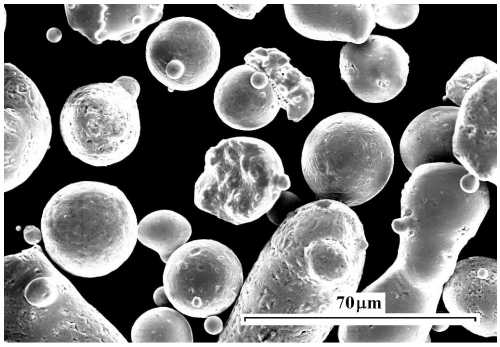

(b): Secondary electron image of the Diamalloy 1008 feedstock powder

Figure 3.3: Secondary electron images of the two powders used in VPS experiments.

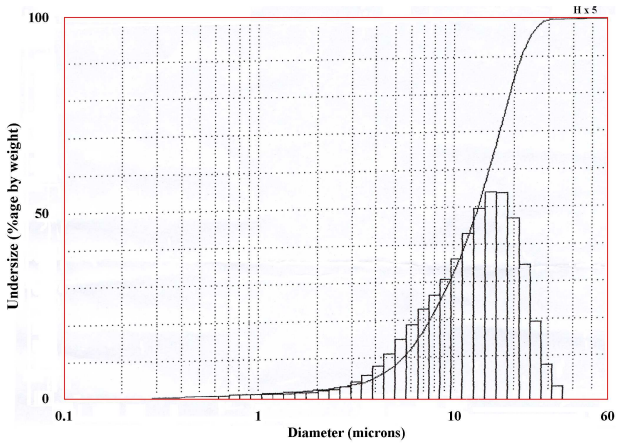

Figure 3.4: Size distribution of W feedstock powder.

A typical VPS experiment comprised:

1. The substrate was grit blasted using 175-250μm Guyson saftigrain 60/80 Al_2O_3 blast media (for non surfi-sculpt substrates only) and was placed in the holder and the robot programmed by hand (point and teach) to raster across the surface at a constant spray distance and velocity, for a set number of times.

2. The substrate water cooling was started and checked for leaks.

3. Any thermocouples for recording substrate thermal histories were inserted and secured.

4. The chamber door was closed and the chamber evacuated to <0.1mbar.

5. The chamber was back-filled with Ar to the spray pressure, typically 80mbar.

6. The datalogging was started.

7. The plasma was initiated at a current of 500A and a primary Ar flow rate of 40lmin^{-1}. The resulting plasma voltage was typically 38V giving a plasma power of 19kW.

8. The VPS parameters were adjusted to the chosen settings, with a plasma power of 52-53kW. Plasma gun recirculating water temperature started to rise from $\sim 10^o$C towards 60^oC.

9. Powder was introduced into the plasma gun from the feedstock hoppers using Ar transport (carrier) gas under the chosen conditions of mass flow rate, typically 8gmin^{-1}.

10. Robot movement according to the pre-programmed path plan was initiated and powder was melted and deposited across the substrate according to the pre-determined number of passes. Substrate temperatures began to increase.

11. Powder flow was halted at the end of the last pass; gun recirculating water temperatures were $\sim 55^o$C.

12. Plasma conditions were returned to the initial conditions and the robot returned to the start-up position away from the substrate; the substrate quickly cooled to room temperature because of the water flow; the plasma gun recirculating water temperature slowly decreased to $\sim 10^o$C.

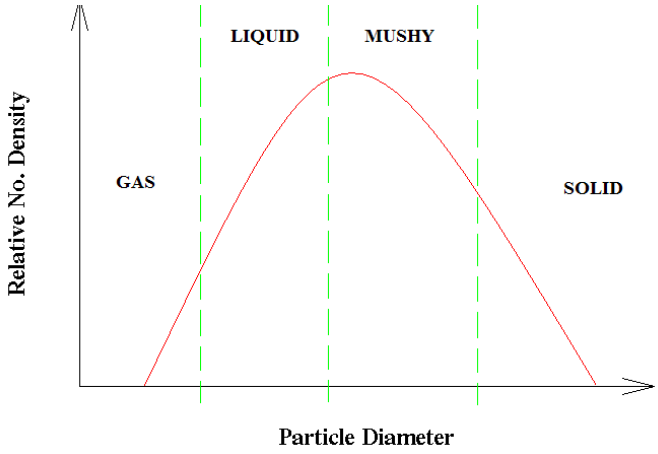

Figure 3.5: Schematic VPS feedstock powder particle distribution.

13. Steps 8 to 12 were repeated as necessary.

14. When the last pass was complete the plasma was extinguished and the chamber again evacuated to <0.1mbar.

15. Ar and then air was introduced into the chamber to reach atmospheric pressure.

16. A high flow rate of air was passed through the chamber for ∼5mins to remove any airborne powder fines.

Derivation of VPS parameters

While the spraying and deposition of Diamalloy 1008 was comparatively straightforward, significant effort was required to discover combinations of VPS parameters that would allow deposition of a significant fraction of the W powder at a sensible rate. Figure 3.5 shows schematically a feedstock powder distribution. At the point of deposition the smallest particles may be vaporised by the plasma, intermediate diameters may be mushy or liquid, and larger diameters remain solid. The specific positions of the boundaries between these behaviours is determined by the VPS parameters chosen for the given powder.

The objective in deriving a particular set of VPS parameters is to maximise the deposition yield ϵ:

Processing parameter	Value
Power	>52kW
Back-fill gas	Ar @ 80mbars
Primary gas	Ar @ 40lmin^{-1}
Secondary gas	H_2 @ 4lmin^{-1}
Carrier gas	Ar @ 2lmin^{-1}
Spray distance	255mm

Table 3.2: First iteration of VPS spray parameters for W.

$$\epsilon = \frac{A_{LIQUID} + A_{MUSHY}}{A_{TOTAL}} \tag{3.1}$$

where A_{LIQUID} is the area under the distribution curve in Figure 3.5 within the liquid region, A_{MUSHY} the area under the curve within the mushy region and A_{TOTAL} the entire area under the distribution curve.

In practice, the challenge in obtaining a suitable set of VPS parameters is to find a method that quantifies ϵ. Coating thickness for a constant spray pattern is directly related to ϵ and surface roughness reduces as ϵ increases [50], in both cases because the fraction of well-melted particles is increasing.

It was known from the literature [24, 30, 51, 55] that developing a combination of VPS parameters for W would be difficult because of its very high melting point, and that the VPS equipment would have to operate near its capacity in terms of plasma energy. This limit is determined by the limit in the safe flow rate of gases (Ar and H_2) to the plasma, the available current (voltage is dependent on the electrical conductivity of the plasma) and the ability of the recirculating water system to keep the plasma gun cool i.e. $<60^oC$. In practice, this last factor was the most important. It was quickly determined that very high currents of 700-800A would be required, together with an H_2 content of up to one third of the plasma gas. Chapter 2 described the strong effects of increasing H_2 fraction on increasing plasma thermal conductivity, enthalpy, voltage and overall power. Table 3.2 shows the preliminary VPS parameters for W based on initial experiments.

In initial experiments relative deposition efficiency was estimated by micrometer measurements of coating thickness on grit blasted planar 100mm×20mm, 5mm thick, mild steel substrates and/or coating weight. Throughout these initial experiments, it was observed that low relative deposition

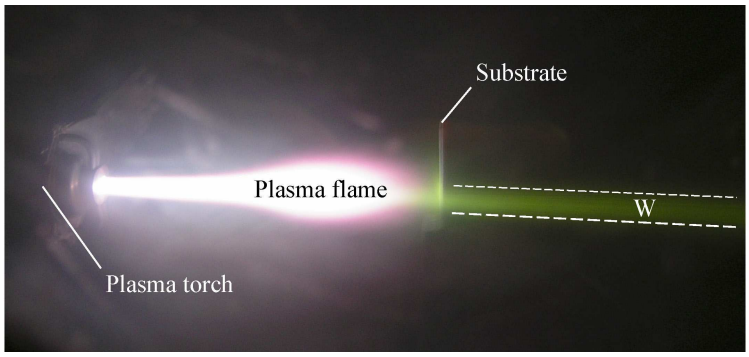

(a): Photograph showing the W particles in the plasma 'flame' during VPS

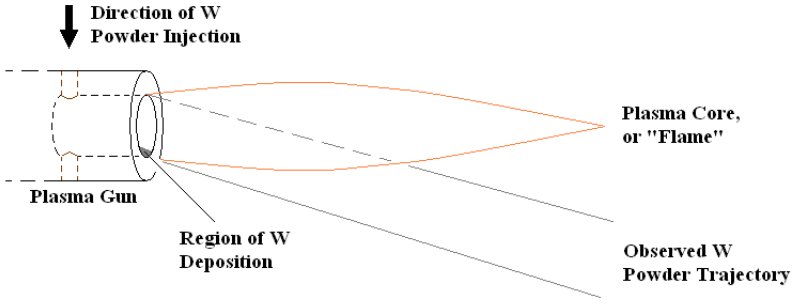

(b): Schematic illustrating the problem with centering W in the plasma flame

Figure 3.6: Illustration of behavior of W powder during vacuum plasma spraying.

efficiencies, or no coating at all, resulted when the W powder was not entrained into the core of the axial plasma jet. The W gave a distinctive green colour when heated and the approximate trajectories of the highly collimated W particles as they traversed the plasma could be seen by eye, as shown in Figure 3.6(a). In particular, the dense W would traverse the plasma core and 'drop out' of the flame when introduced from the upper injector under incorrect plasma/injection conditions, as shown schematically in Figure 3.6(b). This was normally accompanied by a corresponding build-up of W on the lower lip of the cathode.

Switching the W injection to below gave partial improvement as shown in Figure 3.6, with the W following a parabolic arc through the hot plasma core, with a noticeable increase in deposition efficiency in all cases. Correct selection of the W mass flow rate and the Ar carrier gas flow rate were also critical in ensuring the highest fraction of melted particles. If a too high W flow rate or too low Ar flow rate was selected, then the Ar was unable to carry the W powder out of the hopper and W would build up in the hopper exit and choke the flow. Too high W flow rate also required a high Ar flow rate, which

then quenched the plasma and exhausted its ability to melt the W. Further, deposition efficiency was maximised when the injected W was 'buffered' by a corresponding Ar flow from the opposite injector (see Figure 3.1(b)), since this was required to reduce erosion of the Cu cathode at the upper lip. A compromise between practical W flow rate and deposition efficiency was chosen based on trial and error experiment of up to 12gmin^{-1} and 2lmin^{-1} respectively.

Experiments were carried out at a variety of settings and W coatings could be ensured at plasma powers of >52kW and spray distances of ∼250mm. At shorter spray distances, no coatings were deposited and excessive substrate surface damage occurred while at greater spray distances deposition efficiency fell off, presumably due to W re-solidification. A chamber pressure of around 80mbar of Ar during spraying was settled upon as a good compromise between higher and lower pressures: lower spraying pressures gave rise to higher flame velocities leading to increased adhesion, but also led to reduced particle dwell times in the plasma hot zone and therefore lower melting.

Surface roughness and wipe tests

The variable chosen for the most detailed analysis of its effect on deposition efficiency was the secondary H_2 flow rate. Two different approaches were studied for the determination of the effects of H_2 flow rate on VPS W coatings: as-sprayed coating roughness and wipe tests. The plasma current was adjusted so that only the effects of the variation in plasma enthalpy due to the proportion of H_2 in the plasma flame had any effect on material melting. For the as-sprayed coating roughness tests, W was sprayed onto grit blasted mild steel substrates according to the conditions in Table 3.3.

As-sprayed coating roughness was investigated using a portable Taylor Hobson 13+ Tallysurf profilometer and associated software. This device consisted of a diamond stylus mounted on a lever-arm which was slowly drawn across the sample surface. Deflections of the stylus were recorded using a hand-held data logger and subsequently downloaded to a PC for post-processing. The measure of surface roughness R_a used is given by [88]:

$$R_a = \frac{1}{L}\int_0^L \mid z \mid dx \tag{3.2}$$

H_2 content ($lmin^{-1}$)	**Plasma power (kW)**	**W feed rate ($gmin^{-1}$)**	**Carrier gas flow rate (Ar - $lmin^{-1}$)**
5.15	52.3	6.2	1.9
6.90	52.3	6.2	1.9
9.00	51.5	6.2	1.9
10.20	52.9	6.2	1.9
11.10	52.2	6.2	1.9
Plasma gas flow rate (Ar - $lmin^{-1}$)	**Spray pressure (Ar - mbar)**	**Spray distance (mm)**	**Strike**
40	80	255	175a
40	80	255	176a
40	80	255	177a
40	80	255	195a
40	80	255	178a

Table 3.3: VPS settings for investigation of the effect of H_2 flow rate on VPS W coatings (as-sprayed coating surface roughness).

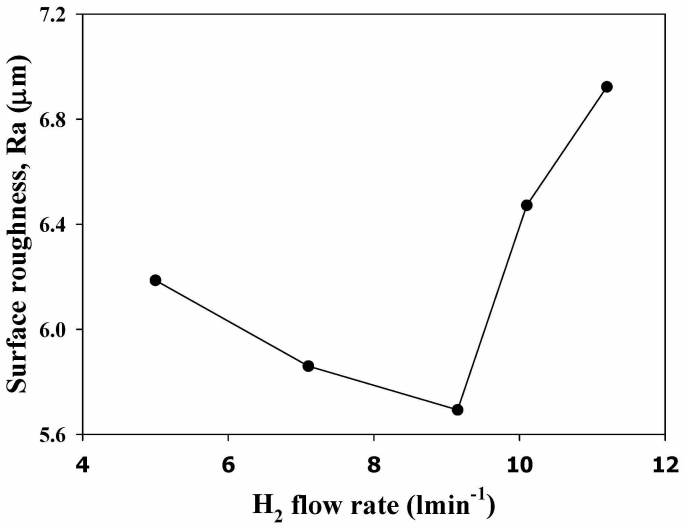

Figure 3.7: The effects of H_2 content on surface roughness at a constant plasma power.

where the length of the measured region in the x-plane is L and z is the vertical position of the stylus as it passed over the surface measured relative to its mean height above the surface.

Seven measurements of roughness were made of each coating and the average variation in VPS W surface roughness with H_2 flow rate is shown in Figure 3.7. There was an initial reduction with increasing H_2 flow rate with R_a $\sim$5.7μm at H_2=9lmin^{-1}. However, at increased H_2 flow rates, there was a sharp increase in surface roughness.

In a wipe test, a very high relative speed is established between the plasma gun and the substrate such that droplets do not overlay one another but remain distinct [89]. If the substrate is polished, the resulting droplet impacts can be viewed directly in plan view by microscopy and statistical information gained regarding number density of deposited droplets, or maximum splat diameter, both of which can be indicative of the extent of powder melting. Figure 3.8 shows the experimental arrangement.

Wipe tests were carried out using polished stainless steel discs mounted in a custom holder and rotated at high relative velocity through the plasma flame. The wipe tests were carried out under the conditions in Table 3.4, each of which had an equivalent to the surface roughness tests set out in Table 3.3.

Figures 3.9(a) to (e) show optical microscope images of the wipe test substrates as a function of H_2 flow rate. There were a mixture of approximately circular splats associated with the impact of well

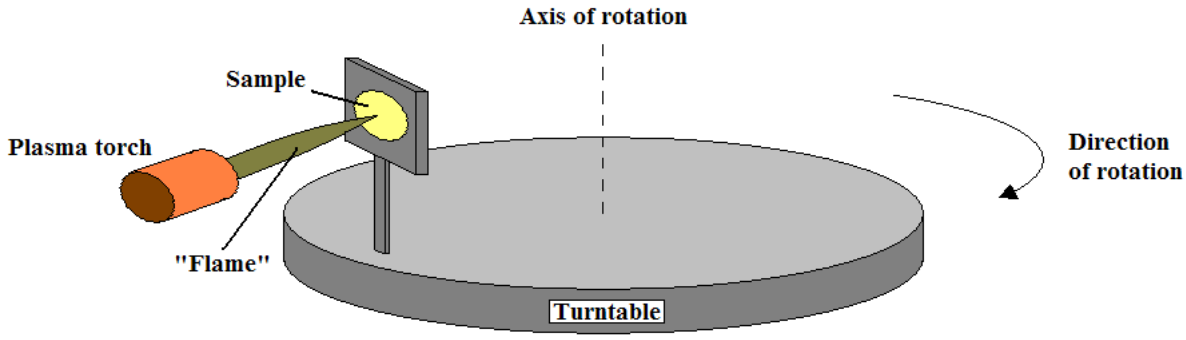

Figure 3.8: Schematic of the experimental arrangement for wipe tests.

H_2 content	Plasma power (kW)	W feed rate ($gmin^{-1}$)	Carrier gas flow rate (Ar - $lmin^{-1}$)
5.00	53.1	6.2	1.9
7.10	52.9	6.2	1.9
9.15	53.8	6.2	1.9
10.10	52.3	6.2	1.9
11.20	52.4	6.2	1.9
Plasma gas flow rate (Ar - $lmin^{-1}$)	**Spray pressure (Ar - mbar)**	**Spray distance (mm)**	**Strike**
40	80	255	190a
40	80	255	192a
40	80	255	191a
40	80	255	194a
40	80	255	193a

Table 3.4: VPS settings for investigation of the effect of H_2 flow rate on VPS W splat distribution/morphology (wipe tests).

melted particles as well as more angular blocky splats associated with less well melted particles. As the H_2 flow rate increased to 9lmin^{-1} there was an increase in the density of splats of all types, followed by a reduction at further increases in the H_2 flow rate.

The number density of droplet splats was determined by hand on printed images. While this approach was time intensive, it was felt to be more accurate than automated image analysis. Figure 3.10 shows the variation of splat density obtained from Figures 3.9(a) to (e). Similarly to the roughness measurements, melting was first enhanced by the H_2 additions up to 9lmin^{-1}, but this effect rapidly disappeared at higher flow rates.

The minimum in surface roughness and peak in deposition efficiency (no. of deposits/μm^2) occurred at a secondary gas flow rate of $\sim$9lmin^{-1}. Initially it was supposed that increasing H_2 content would simply increase the flame 'temperature' and increase particle melting and deposition efficiency. Despite many efforts to model the heat and mass flow inside the plasma during spraying e.g. [90], it remains difficult to state with certainty what the increasing H_2 flow rate may be doing to particle melting behaviour to produce the observed behaviour in the roughness and wipe tests. However, it is known that deposition efficiencies can reduce with excessive H_2 flow rate in plasma spraying because although energies increase slightly, so does plasma velocity, because of the increased energy and associated thermal and magnetic 'pinch', and reducing viscosity (the H_2 viscosity is an order of magnitude lower than Ar [91]).

Figure 3.11 shows schematically a possible interplay between the effects of increasing H_2 flow rate on plasma temperature and velocity and the resulting overall deposition efficiency [46]. As plasma velocity increases, particle dwell time reduces and eventually this becomes the dominant effect on net resulting behavior. Below this optimum, the greater plasma power and thermal conductivity of H_2 dominates, steadily increasing plasma power and particle melting, while above the optimum, the reduced particle dwell time overrides the greater flame temperature.

Based on this work, and considering the need to minimise thermal loads on the VPS equipment, a H_2 flow rate of 7lmin^{-1} was chosen for subsequent VPS W work. The slight reduction in deposition efficiency associated with this choice was accepted as cooling of the plasma torch as well as substrates proved much more difficult with higher H_2 flow rates. This choice gave plasma powers of 52-53kW.

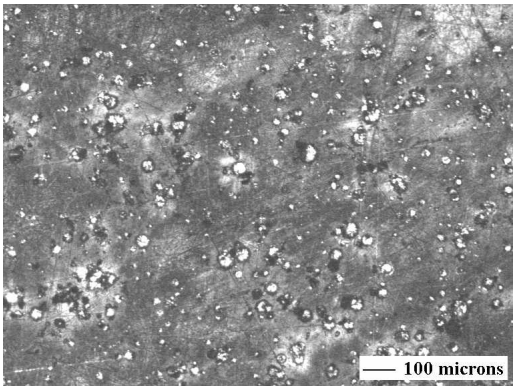

(a): H_2 flow rate of $5 l min^{-1}$

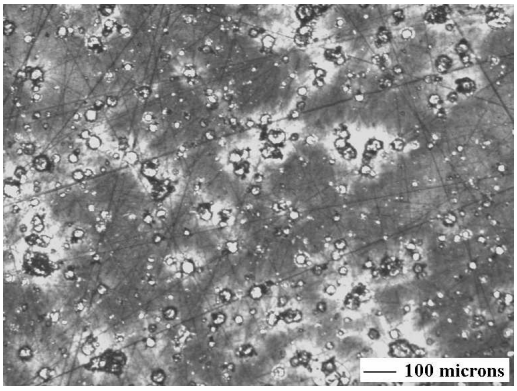

(b): H_2 flow rate of $7 l min^{-1}$

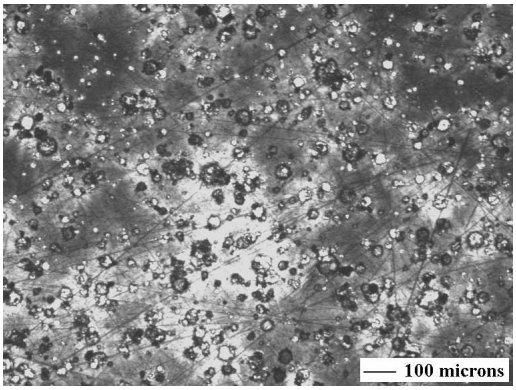

(c): H_2 flow rate of $9 l min^{-1}$

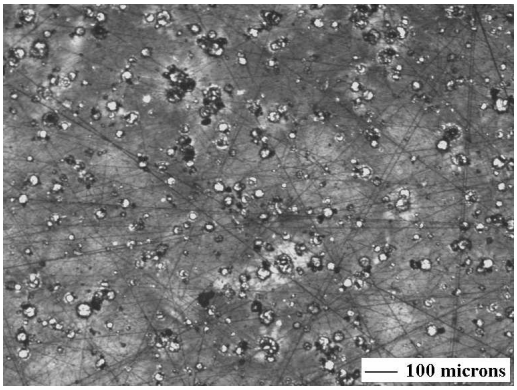

(d): H_2 flow rate of $10 l min^{-1}$

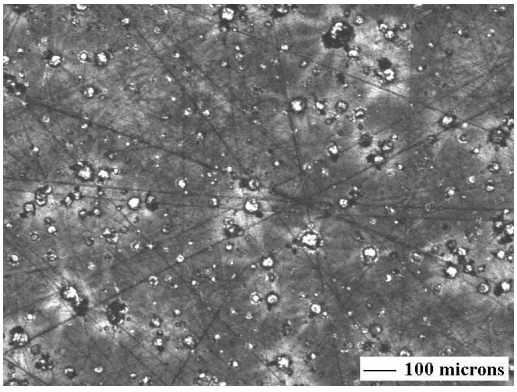

(e): H_2 flow rate of $11 l min^{-1}$

Figure 3.9: Optical microscope images of W wipe tests at various H_2 flow rates.

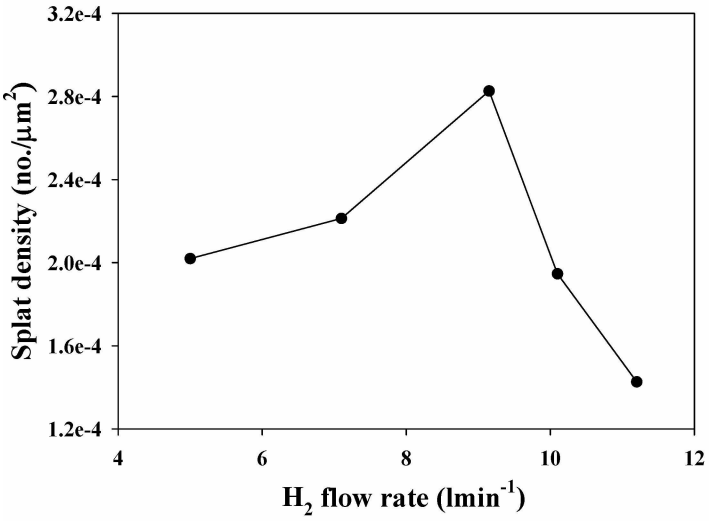

Figure 3.10: The W splat density from 2s wipe tests as a function of H_2 flow rate at constant plasma power.

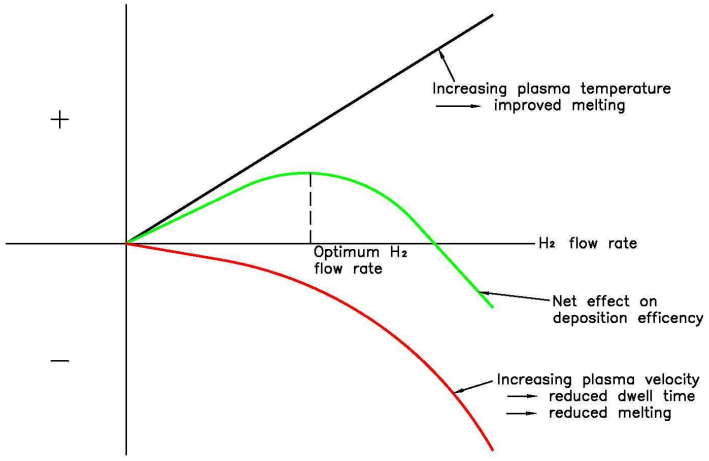

Figure 3.11: Schematic plot of the contribution to increase (+) or decrease (-) in melting of W powder as a function of increasing H_2 flow rate, for otherwise constant conditions.

Processing parameter	Value
Power	∼52.5kW (I∼760A, V∼70V)
Back-fill gas	Ar @ 80mbars
Primary gas	Ar @ 40lmin^{-1}
Secondary gas	H_2 @ 7lmin^{-1}
Carrier gas	Ar @ 2lmin^{-1}
Spray distance	255mm

Table 3.5: Optimum VPS spray parameters for W.

Table 3.5 summarises the optimum VPS parameters for W selected.

Graded coatings by VPS

There are several approaches to the manufacture of coatings with mixed W/steel compositions by VPS, including: (1) co-spraying of the separate graded coating constituents via one plasma gun; (2) the use of a pre-mixed powder; and (3) the co-spraying of the graded coating constituents via separate plasma torches. Option (2) is inflexible because different mixed powder fractions would be required for the different graded layers, and more suited for the manufacture of inter-layers. Option (3) is capital intensive and not possible on the Oxford equipment. Option (1) was used here and necessitates the use of a single set of plasma parameters even when spraying two different materials. In this case, a compromise between the optimum VPS parameters for the two powders may be chosen. However, because W melting and deposition efficiency was so difficult, the W VPS parameters were used even when co-spraying with Diamalloy 1008. This no doubt resulted in over-melting and vaporisation of some of the Diamalloy 1008.

In order to maintain control over the W and Diamalloy fraction when co-spraying from separate hoppers it was necessary to establish relative deposition efficiencies. This was achieved via many experiments involving the deposition of W, Diamalloy 1008 and mixed W/steel coatings with the resultant coating thicknesses measured either in cross-section in the the microscope or by using a micrometer. Figure 3.12 shows the variation in deposited W and Diamalloy thickness as a function of powder feed rate. In both cases the deposition efficiencies increased approximately linearly with feed rate, with the Diamalloy thickness increasing faster.

Typical feed rate settings for a steel/W 5-layer graded coating with 100% steel, 75% steel 25% W,

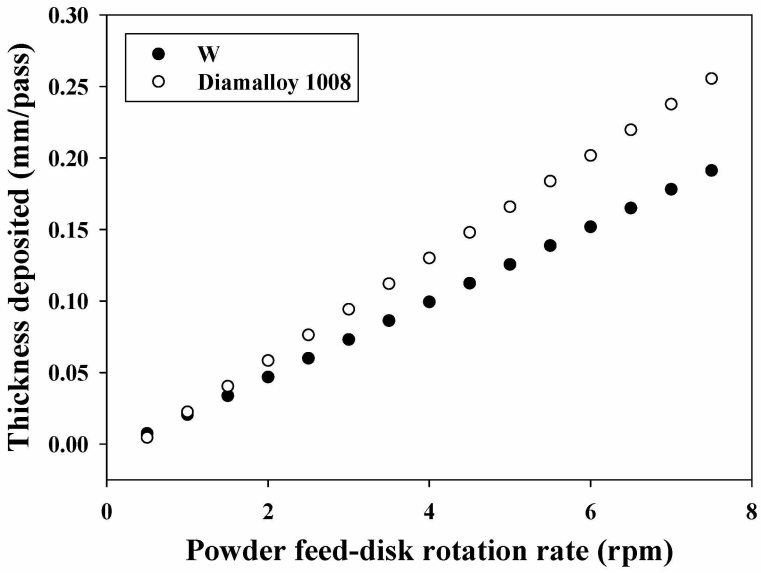

Figure 3.12: Relative deposition efficiencies for W and Diamalloy 1008 at the co-spray/graded coating VPS settings.

Layer no./ composition	Powder feed rate ($gmin^{-1}$)		No. of passes
	Tungsten	Diamalloy	
1: 0% W, 100% steel	0	12.0	1
2: 25% W, 75% steel	4.0	8.9	1
3: 50% W, 50% steel	8.2	5.9	1
4: 75% W, 35% steel	6.2	1.5	2
5: 100% W, 0% steel	8.2	0	2

Table 3.6: Feed rate settings for W/Diamalloy 5-layer linearly graded coatings.

50% steel 50% W, 25% steel 75% W and 100% W layers based on the data from Figure 3.12 are shown in Table 3.6.

In order to minimise and regulate approximately the thermal residual stresses from experiment to experiment the following steps were employed: (1) the use of RS Components Ltd (UK) Heat sink compound heat transfer paste, applied between the substrate back face and the substrate holder; (2) a water cooled substrate holder shown in Figure 3.1(a); and (3) substrate Cu masks spaced by 5mm from the substrate front face to ensure the same area of coating was deposited each time, to protect the substrate holder and to stop overspray adhering to the substrate sides and preventing the removal of substrates from the holder. This arrangement, with the Cu shield removed, is shown in Figure 3.13. K-type thermocouples were inserted through holes in the water cooled substrate holder into holes drilled ∼1mm from the substrate surface and they were then secured using heat proof aluminium tape and tie wraps to the back of the water cooled holder. Temperatures were recorded during all VPS experiments using K-type thermocouples, K-type extension leads (either with glass-fibre insulation or protected from the chamber environment via glass-fibre blankets) exiting through an air-tight flange in the VPS chamber to a T100 thermocouple interface block supplied by VInstrumentation, Glasgow (UK). This was connected to a data-logging PC running VIPS/VILS (Virtual Instrument Presentation/Logging Software, also provided by VInstrumentation) and provided up to six configurable thermocouple channels with the ability to log temperature up to 10Hz.

Surfi-sculpt substrates

Surface sculpture refers to a process in which regular millimetre scale features known as surfi-sculptures are introduced to the surfaces of substrates via a new technique for modifying the surface of mate-

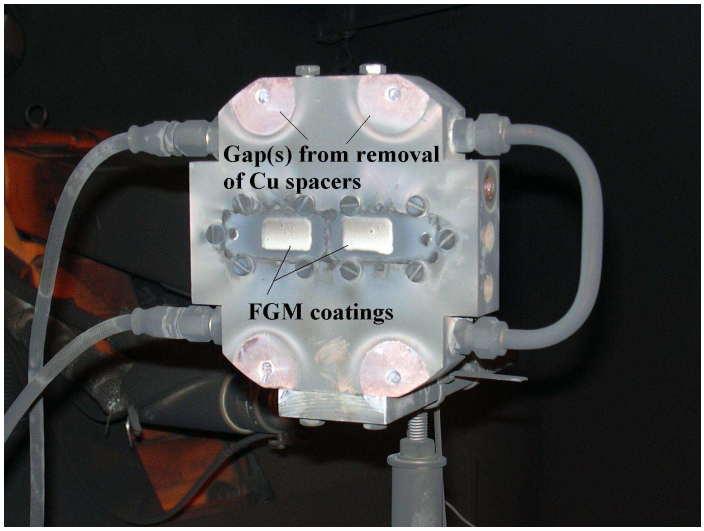

Figure 3.13: Two mild steel substrates with 5-layer graded coatings post-spray.

Test no.	Strike no.	Surfi-sculpt samples	Total passes	Thermocouple position
1	12b	4, 6 and 7 (6 central)	21 (9×2 + 1×3)	back face of sample 6
2	16b	1, 2 and 3 (2 central)	14 (12×1 + 1×2)	∼1mm from front of sample 2
3	18b	5, 8 and 9 (8 central)	15 (7×2 + 1)	∼1mm from front face of sample 8

Table 3.7: Experimental details for initial surfi-sculpt experiments.

rials using an electron beam known as 'surfi-sculpt' developed by TWI, UK [92, 93]. Two different experimental tests were carried out using surfi-sculpt samples provided by TWI. In the first, nine different surfi-sculpt topographies on 25mm^2, 5mm thick, 316L stainless steel substrates were coated three-at-a-time with ∼1mm of VPS W in order to investigate the effects of surfi-sculpt topography on coating adhesion and quality. In the second, numerous 37.5mm × 25mm, 5mm thick, surfi-sculpt substrates with the optimum surfi-sculpt topography determined in the first experiment were coated with different thicknesses of VPS W. These larger substrates only had surfi-sculpt features on the central 25mm^2, with 6.25mm × 25mm sections of unmodified steel either side. Conversely, in the first experiments, the entire surface of all nine 25mm^2 substrates was modified with surfi-sculpt structures.

All VPS W coatings were manufactured using the settings previously derived for graded coating production and outlined in Table 3.5. VPS gun movement programs were identical and designed to simply ensure full sample coverage. The substrates were mounted in a modified form of the water cooled holder. Table 3.7 outlines the different experimental parameters used in surfi-sculpt experiment 1. In all experiments, a W feed-disk rotation rate of 2.5rpm was used, approximately equivalent to 8gmin^{-1}.

In subsequent experiments, thicker >1mm VPS W coatings were deposited using the same experimental approach on optimum surfi-sculpt substrates as shown in Table 3.8.

3.3 Metallography

The majority of microscopy undertaken involved analysis of cross-sections of as-sprayed coatings. Coatings were typically sectioned using electro-discharge machining with Cu or bronze wire. Cross-

Strike	**Surfi-sculpt samples**	**Total passes**	**Notes**
151b	14 and 26	11	
158b	16 and 35	25	Sample 16 sent for XRD analysis
164b	15 and 23	35	VPS W coating thickness ∼2mm, residual stress analysed in sample 15

Table 3.8: Experimental details for subsequent surfi-sculpt experiments.

sections were then typically mounted using a Struers ProntoPress-10 hot press in Struers Polyfast hot mounting resin. This was a conductive thermosetting resin (a phenolic resin with carbon filler) that provided good edge retention. Cold mounting and vacuum impregnation was also used with Struers Epofix, a slow-curing fluid transparent epoxy resin that was designed for vacuum impregnation in order to retain structure in porous materials.

After mounting, polishing was a two stage process, with initial material removal carried out using progressively finer grades of SiC paper (400→800→1200→2500→4000) and final polishing using 1μm diamond paste on a Struers MD-Nap cloth. The 1μm polish gave a sufficient finish for all applications including SEM, EBSD, EPMA and hardness testing. At all times care was taken to minimise the chances of cross-contamination in case subsequent EPMA analysis was required.

3.3.1 Microscopy

Hitachi S520

Early scanning electron microscopy (SEM) images were captured using a Hitachi S520 SEM. This instrument was equipped with a W filament, had a large loading chamber and an energy dispersive detector (EDS) allowing it to take both secondary electron and back scattered electron images as well as energy dispersive X-ray (EDX) spectra via an Oxford Instruments ISIS system. Images were captured on Polaroid 35mm film and processed using in-house development facilities. This microscope was typically operated at 20kV with working distances of ∼20mm.

Jeol JSM-840A

This instrument was used for the majority of the microstructural characterisation work using both secondary electron and backscattered electron detectors as well as a ISIS EDX system. The JSM-840A was typically operated at 20kV with a working distance in the range 15-25mm, with lower working distances used for high resolution work.

Jeol 6500F - electron backscatter diffraction (EBSD)

Dr Simon Hogg, Department of Materials, Oxford University, undertook preliminary investigation of the VPS W microstructure using EBSD, and a small number of results are presented. However, since this was not a major activity by the author, the reader is directed elsewhere for details of EBSD [94]. Measurements were obtained in the Jeol 6500F operating at 20kV on several different VPS W regions.

Jeol JXA-8800R electron-probe microanalyser (EPMA)

The EPMA was equipped with four wave dispersive X-ray (WDX) detectors to allow compositional analysis of as-sprayed samples, particularly around the coating/substrate interface, with the aim of detecting evidence of any chemical bonding. It was typically operated at an accelerating voltage of 20kV, with probe currents of $\sim$0.03μA and step sizes as low as 0.25μm. Most experiments were carried out under the supervision of Dr Chris Salter, Department of Materials, Oxford University.

3.3.2 Residual stress measurements

In order to understand the evolution of residual stress within as-sprayed coatings several techniques were investigated to measure residual stress. All had some limitations. Following a brief theoretical background, details of X-ray diffraction measurements in a standard powder diffractometer are described here. Other X-ray techniques that were used at the very end of the study are introduced briefly in Chapter 6.

X-ray diffraction

X-ray diffraction is a useful technique for determination of crystalline material structure (material type, lattice parameter) and also for quantification of residual stresses [47, 95]. Residual stresses are obtained from measurement of residual strain in the crystal structure of the material.

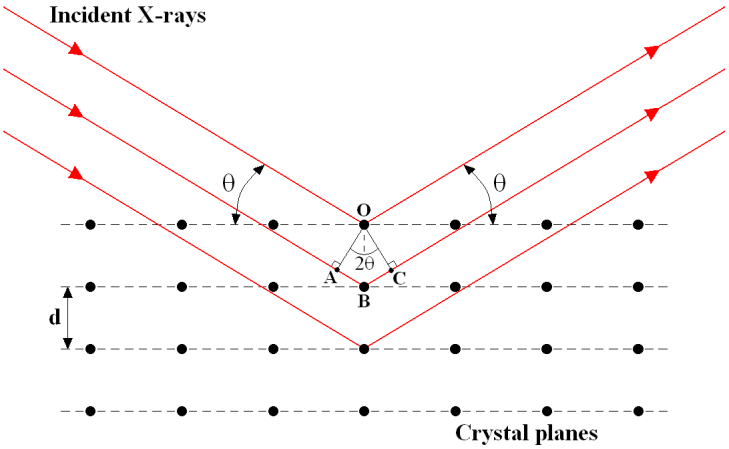

Figure 3.14: Incident x-ray reflection at crystal planes (d = lattice spacing) [47].

XRD theoretical background

X-ray diffraction employs the fact that the wavelength of X-ray radiation is close to the interatomic spacing in atoms (typically a few tenths of a nm). If radiation strikes a crystal plane at an angle θ, as illustrated in Figure 3.14, then reinforcement of the incident X-rays will only occur when the difference in path length between X-rays reflected from different atomic planes is equal to an integer multiple of the X-ray radiation wavelength, λ [47].

The condition of a difference in path lengths equal to an integer n multiple of λ can only be satisfied under certain conditions. From Figure 3.14:

$$OA = d \longrightarrow AB = OASin\theta = dSin\theta \longrightarrow ABC = 2AB = 2dSin\theta \tag{3.3}$$

Therefore, from Equation 3.3 and Figure 3.14, maximum reflection occurs when:

$$2dSin\theta = n\lambda \tag{3.4}$$

The condition in Equation 3.4 is known as Bragg's Law. Different crystal planes (hkl) will by their nature have different orientations and lattice spacings and will therefore produce these Bragg reflections at different angles of X-ray incidence. In XRD measurements, incident X-rays are focused at different

angles θ to the normal of the sample surface. The lattice constant a can than be determined from the Bragg angle at each lattice spacing using:

$$a = \lambda \frac{\sqrt{h^2 + k^2 + l^2}}{2Sin\theta} \tag{3.5}$$

The resultant pattern of Bragg angle (2θ) reflection peaks is indicative of the crystallographic structure in question. An ideal crystal would give a series of delta peaks representing the different atomic planes, but in reality there are always imperfections and in a polycrystalline system the resultant peaks always have a finite width. Both the peak position and width provide information on the residual stress present in the crystal. Uniform macrostrain, due to its effect on interplanar spacings, causes a shift of the diffraction lines to new 2θ positions. A broadening of diffraction lines arises from a combination of non-uniform microstrain (e.g. dislocations) and fine grain size; the latter effect becomes noticeable when grain sizes fall below 100nm [96]. In order to quantify this residual stress, the difference between the measured lattice parameter and the lattice parameter for the un-strained material (a_0) may be related to the angle at which the Bragg reflection is found to occur by [95, 97]:

$$\epsilon_{hkl} = \frac{a - a_0}{a_0} = \frac{a}{a_0} - 1 = \frac{1}{2} S_2(hkl) \sigma_\phi^I Sin^2\Psi + S_1(hkl)(\sigma_1^I + \sigma_2^I) \tag{3.6}$$

where

- ε_{hkl} is the strain in the (hkl) plane;
- $S_1(hkl)$ and $S_2(hkl)$ are the X-ray elastic constants;
- σ_1^I and σ_2^I are the principal stresses parallel to the surface at which XRD measurements are being taken;
- Ψ is the angle between the perpendicular to the specimen surface and the reflecting plane (hkl), and;
- ϕ is the angle between the direction of σ_1^I and the projection of the normal to the plane (hkl) on the sample surface $\rightarrow$ with σ_ϕ^I being the stress in this direction.

The two X-ray elastic constants are proportional to the elastic constants of the material under investigation and, for an isotropically elastic system, may be calculated from $S_1 = -\frac{\nu}{E}$ and $S_2 = \frac{2(1+\nu)}{E}$ [98] (where E and ν are the Young's modulus and Poisson's ratio of the material in question). For elastically anisotropic materials numerical approaches (such as Kröner's model) may be used to calculate these constants [95]. Equation 3.6 assumes that the strains in the z-direction e.g. normal to the measurement surface, are essentially zero within the measured volume. This is a valid assumption as incident X-rays will only penetrate a small distance into bulk materials. Equation 3.6 may be re-arranged:

$$a = \frac{1}{2}a_0 S_2(hkl)\sigma_\phi^I Sin^2\Psi + a_0(S_1(hkl)(\sigma_1^I + \sigma_2^I) + 1) \tag{3.7}$$

Equation 3.7 has the general form y = mx + c, where $y = a$, $m = \frac{1}{2}a_0 S_2(hkl)\sigma_\phi^I$, $x = Sin^2\Psi$, and $c = a_0(S_1(hkl)(\sigma_1^I + \sigma_2^I) + 1)$. Therefore, the gradient of a plot of a against $\sin^2\Psi$ (m) can be used to calculate the in-plane stress in the substrate surface (in the direction of measurement) using the known elastic properties of the material - known as the $\mathrm{Sin}^2\Psi$ technique:

$$\sigma_\phi^I = \frac{2m}{a_0 S_2(hkl)} \tag{3.8}$$

Siemens D500 powder diffractometer

Initial XRD measurements were carried out using a Siemens D500 powder diffractometer employing a Cu K-alpha X-ray tube (λ=0.15406nm) with a secondary monochromator. Samples were spun continually and scanned in 0.05° 2θ increments in the range 30° to 148° for a count time of 10s per step. Phase identification was automated and carried out against pre-loaded standards from the International Centre for Diffraction Data (ICDD). Sample preparation simply involved providing a relatively flat surface by grinding.

3.3.3 Image analysis

Image analysis of electron images of the majority of graded coatings was undertaken to allow an estimation of the variation in material composition. This involved sampling 40×40 pixel square boxes at varying positions across polarised binary versions of cross-sectional micrographs. With the lowest magnification micrographs considered, these boxes represented a minimum area of 1798μm^2 - sufficient to resolve pores as small as 1μm in size. This work was carried out using the commercially available package Scion Image. The contrast between W and steel regions in the micrographs resulted in black-and-white images, with the W regions white (a pixel intensity of zero) and the steel regions black (a pixel intensity of 255). By recording the average pixel intensity count within each 40×40 pixel square box the relative proportion of W could than be determined.

3.3.4 Indentation tests

Vickers micro-hardness

Micro-indentation was carried out on a variety of samples using a Leitz (Wetzlar, Germany) Vickers micro-indenter. A Vickers four-sided indenter was employed giving indents with two diagonals. Various indentation masses ranging between 0.1Kg and 2.0Kg were available and the associated microscope (the indenter stage and fixed-magnification microscope stage were setup to allow each to be swiveled into position in succession) was calibrated to ±0.25μm. Samples were prepared for micro-indentation by polishing with 1μm diamond paste. The indent diagonals were compared to standard Vickers hardness tables to calculate the hardness.

Nano-indentation

Nano-indentation is a derivation of standard hardness testing, but using a smaller indenter head that can enable the mechanical properties of features at the sub-micron scale to be investigated directly. The technique involves monitoring the depth of an indenter beneath the surface of a sample during loading and un-loading cycles. From the resultant loading/un-loading curves mechanical properties,

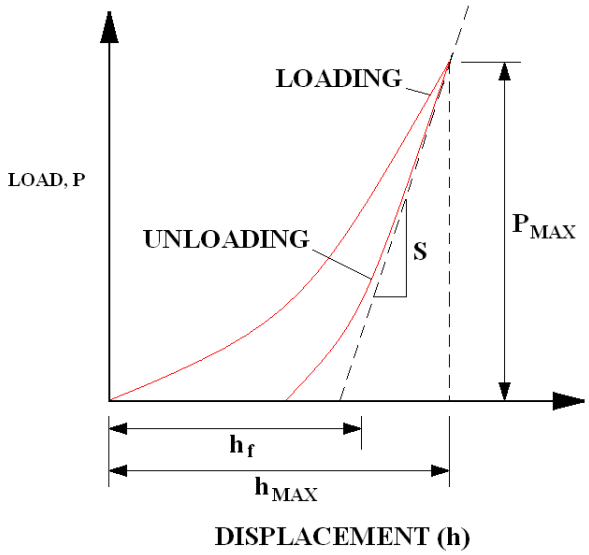

Figure 3.15: Illustration of typical nano-indentation cycle highlighting key features, modified from [99].

principally hardness and Young's modulus, may be derived [99, 100, 101]. In the course of this project, both Young's modulus and hardness of as-sprayed coatings were determined via nano-indentation.

Hardness values are determined directly from the depth of indent and the force used to drive the indenter (hardness values are quoted in units of force/unit area - pressure, Pa). The calculated value is the Meyer hardness H and is defined as the mean pressure that the material will withstand under load [99, 100]:

$$H = \frac{P_{MAX}}{A_{MAX}} \tag{3.9}$$

where P_{MAX} is the maximum load and A_{MAX} is the projected contact area at maximum load.

A Berkovich indenter, which is a three-sided/pyramidal indenter with a half angle of $\sim 65.3^{o}$ and an area-to-depth function equal to that of a Vickers indenter, was used in all experiments [101]. Young's modulus values are determined from the slope of the upper part of the unloading curve. Initially, an effective modulus that takes into account the properties of the indenter is calculated. A typical loading/un-loading curve is shown in Figure 3.15 [99].

As illustrated in Figure 3.15, un-loading is not linear even within the elastic regime. More commonly,

the unloading curve follows a power law of the form $P = A(h - h_f)m$ where $(h - h_f)$ is the elastic displacement and A and m are material specific constants [99]. The unloading gradient S is equal to dP/dh and is known as the 'contact compliance'. It represents the slope of the unloading curve at the point of maximum loading (P_{MAX}). Oliver and Pharr demonstrated that it is linked the reduced modulus according to [99, 100, 101, 102]:

$$E_r = \frac{\delta P}{\delta h} = \sqrt{\frac{\pi}{A_{proj}}}\frac{S}{2} \longrightarrow \frac{1}{E_r} = \frac{(1-\nu^2)}{E} + \frac{(1-\nu_i^2)}{E_i} \tag{3.10}$$

where E_i and ν_i are the Young's modulus and poisson's ratio of the indenter given as 1140GPa and 0.07 respectively for the equipment used [102].

It is possible to estimate yield stress from the measured hardness. In general, $\sigma_y \sim H/3$. However various refinements to this approach have been suggested such as $\sigma_{y(10\%)} \approx \frac{H}{2.8}$ when H/E is of the order of 0.1 [102].

Nano-indentation tests were undertaken using a Nano Test platform from Micro Materials Ltd, Wrexham, UK. The equipment comprised an electromagnetic pendulum that applied a constant calibrated force to an indenter, facilitating its loading/un-loading, a calibrated microscope so that once a particular indentation start point had been identified the first indent would occur at this point, and a temperature controlled cabinet held at $\sim 25^oC$. The motion of the pendulum on the Nano Test platform was carefully calibrated before each test to ensure consistent/repeatable results. Each week the system was calibrated against fused silica that has a known hardness and Young's modulus. In addition, calibration tests on 99.9% pure bulk W were carried out and the values found to be consistent with those in the literature.

During the indentation, the indenter was held at the maximum load P_{MAX} for a period of time before unloading was allowed to occur. This was done for two reasons: first to ensure that only elastic loading/unloading would dominate and that any time-dependent plastic effects such as creep would damp-out; and secondly, so that any effects due to thermal drift could be calibrated in subsequent post-processing. Thermal drift is the term used to describe the effects of fluctuations in the experimental equipment temperature. Increases/decreases in the experimental temperature would lead to

expansion/contraction. Therefore, by holding the sample at maximum load for a set period before unloading (typically ∼30s for W as it exhibits virtually no creep at room temperature) any of these effects can be recorded and taken into account by assuming an identical rate of thermal drift over the entire cycle.

Other post-processing corrections include a correction for the shape of the indenter as well as the compliance - the inverse of stiffness - of the loading system e.g. the contribution to recorded depth of the loading system itself. These effects are known as the diamond area function and load frame compliance respectively [99, 101]. Over time the indenter head will naturally become worn and no longer remain a perfect pyramid. This means that the area of contact represented by a particular depth of indentation will be over-estimated leading to inaccurate estimations of material hardness. Diamond area functions may be estimated in a variety of ways including various types of microscopy. However, Oliver and Pharr proposed a technique that did not require analysis of the indenter head [99]. This involved plotting ideal contact areas against load compliance ($C = 1/S$). It was found that the gradient of a plot of C against $A^{-0.5}$ gave the load frame compliance [99]. In turn, a standard of known Young's modulus and hardness could be used to generate a plot of A as a function of actual contact depth of the indenter for different loads. A model, normally a power law, could than be fitted to this curve with the resultant best-fit approximating the area function of the actual indenter used [99, 101].

Such standardisation was carried out regularly with the Nano Test machine used and a Berkovich function for the indenter used (regularly updated) was utilised to correct measured indentations for indenter damage. Once all these corrections had been taken into account, the Nano Test software automatically implemented the Oliver-Pharr technique, giving Young's modulus and hardness values in units of GPa [99].

Chapter 4

Results - experiments

Coatings manufactured during this project were investigated using the techniques described in Chapter 3. The coatings studies may be grouped into three broad categories: (1) graded coatings, with/without heat-treated bond-coats; (2) initial VPS W surfi-sculpt coatings; and (3) thick $\geq$1mm VPS W surfi-sculpt coatings. Coatings are denoted by a code that comprises the strike number of the plasma torch at manufacture and a letter (either a or b) corresponding to the anode/cathode set used.

4.1 Nano-indentation - W standard

Since nano-indentation was applied to various VPS W coatings hereafter, a bulk W sample was studied by nano-indentation for comparison. A 5×25 array of nano-indentations in a >99% dense W standard polished to a 1μm finish were indented using a load of 60mN. The measured Young's modulus and hardness varied from 340GPa to 420GPa and from 5.4GPa to 6.5GPa respectively. The average Young's modulus was 370GPa and the average hardness was 6GPa. According to [18], the room temperature Young's modulus of W is 410GPa, as measured by ultrasonic techniques. The lower modulus measured here may be due to a slightly lower density since W is notoriously difficult to fully densify. Overall, nano-indentation was concluded to give an acceptable measurement of modulus in W.

Coating feature	Details
Strike No.	227a
Architecture	100% Diamalloy 1008 bond coat, 50:50 interlayer, 100% W upper coat
Thermal paste	No
Heat treated bond-coat	No

Table 4.1: Coating details for 50:50 interlayer 227a.

4.2 Graded coatings with non heat-treated bond coats

In all coatings, a coating of the Eurofer analogue Diamalloy 1008 was first deposited to act as a bond coat for the subsequent Diamalloy/W graded coating. In early experiments these bond coats were used as-sprayed for convenience; in later experiments the substrates and bond coats were heat-treated to improve adhesion and to eliminate spalling.

4.2.1 50:50 interlayer

These experiments, detailed in Table 4.1, were an attempt to match the previous 'state-of-the-art' in W on steel coatings for PFC applications by Bolt *et al.* [14, 24] performed at Plansee AG, where Bolt *et al.* used pre-mixed powders, whereas different and varying powder mass feed rates from separate W and Diamalloy hoppers were used here. The target was a 50:50 (by volume) mixed interlayer by VPS, topped with $\sim$100μm of VPS W. Figure 4.1(a) is a backscatter electron image of the coating cross-section showing the substrate, a $\sim$700μm thick Diamalloy bond coat, an $\sim$250μm intermixed W/Diamalloy region, and a W top coat of thickness of $\sim$100μm. A binary version of Figure 4.1(a) is shown in Figure 4.1(b) where the W has a gray scale value of zero and the Diamalloy a gray scale value of 255, and was used to estimate an average W fraction of $\sim$67% in the intermixed region, compared with a target of 50%. The higher W fraction was due to an underestimate of W deposition efficiency. However, rather than re-optimisation of the two powders' relative flow rates, it was decided to focus on alternative graded coatings.

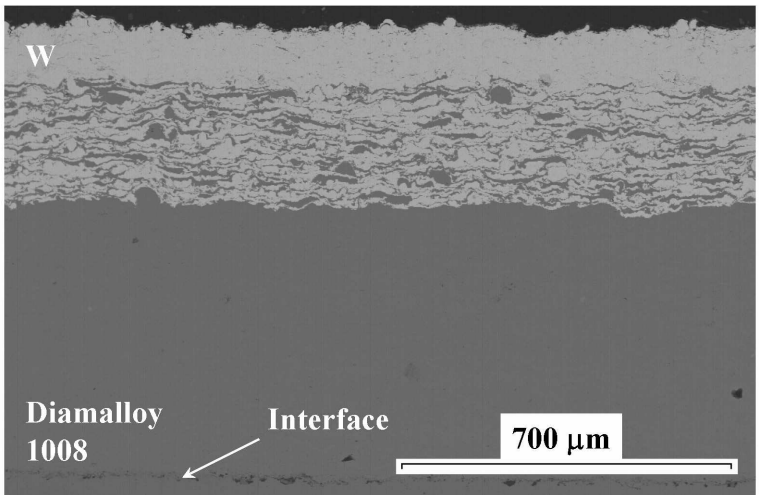

(a): Backscattered electron image of a cross-section of coating 227a

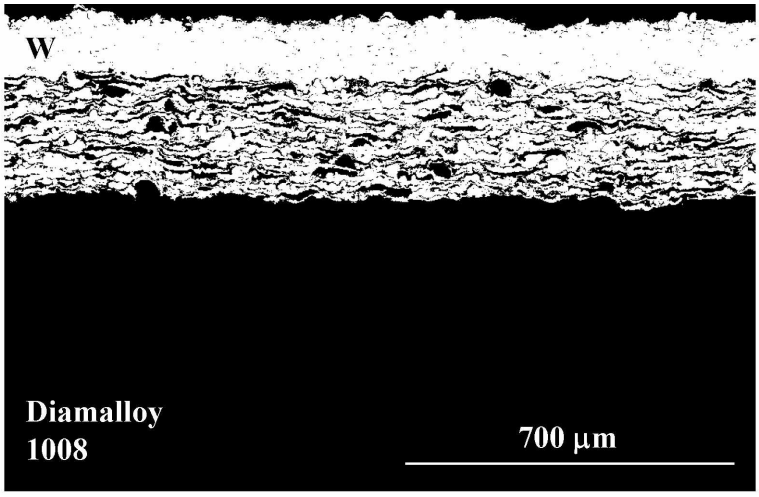

(b): Binary version of a backscattered electron image of a cross-section of coating 227a

Figure 4.1: Backscattered electron images of cross-sections of coating 227a.

Coating features	**Details**
Strike No.	63b and 65b
Architecture	5-layers, linear (0%, 25%, 50%, 75% and 100%)
Thermal paste	No
Heat treated bond-coat	No
Additional notes	Coating 63b - partially delamination

Table 4.2: Coating details for 5-layer graded coatings (63b and 65b).

4.2.2 5-layer graded coatings

Figure 4.2(a) shows a backscattered electron image typical of the graded VPS Diamalloy/W coatings in which W is the lighter phase. The graded nature of the coating was immediately apparent - with a progressively greater proportion of W with coating thickness. The progressively graded region total thickness was $\sim$400μm. However, within the five sub-layers comprising the graded region and the W/Fe-rich layers, W and Fe were also layered at the 'splat' length scale. This arose because there was little W/Diamalloy powder/droplet mixing in the plasma en-route to the substrate since they were injected from opposite sides of the gas stream, and the W and Diamalloy deposition regions were not co-incident due to the tendency of W to remain collimated in the plasma flow while the Diamalloy was more uniformly distributed [55].

The higher magnification view in Figure 4.2(b) shows better the typical plasma sprayed layered microstructure with micro-cracks between 'splats'. Despite using conditions for the best W behaviour melting capable from the apparatus, some un-melted particles remained, as commonly reported by others [55].

Figure 4.3(a) shows a version of Figure 4.2(a) for coating 63b with superimposed vertical lines indicating the centreline of 40×40 pixel sampling boxes (which given a pixel size of 1.06μm/pixel represented an area of 1798μm^2, sufficient to resolve pores $\sim$1μm in diameter) used to estimate the local W fraction as described in Section 3.3.3. As the sampling box moved from bottom to top, the fraction of W was estimated, and is shown in Figure 4.3(b) that plots the W fraction as a function of distance from the substrate/coating interface.

Because the sampling box size was greater than the average splat thickness, Figure 4.3(b) does not generally show the splat-scale layering effects, although this could be discerned occasionally for some of the lines, e.g. line 4, and smeared out local variations to show an approximately linear variation of W fraction with thickness in the graded region. Overall, the desired W fraction in the central three mixed layers of approximately 25%, 50% and 75% W was achieved. Finally, note that the porosity of the coating was relatively low by W plasma spraying standards, with porosity in the W region typically 3-10%. This level of porosity was based on a minimum sampling/pore size of $\sim$1μm. Even this level of

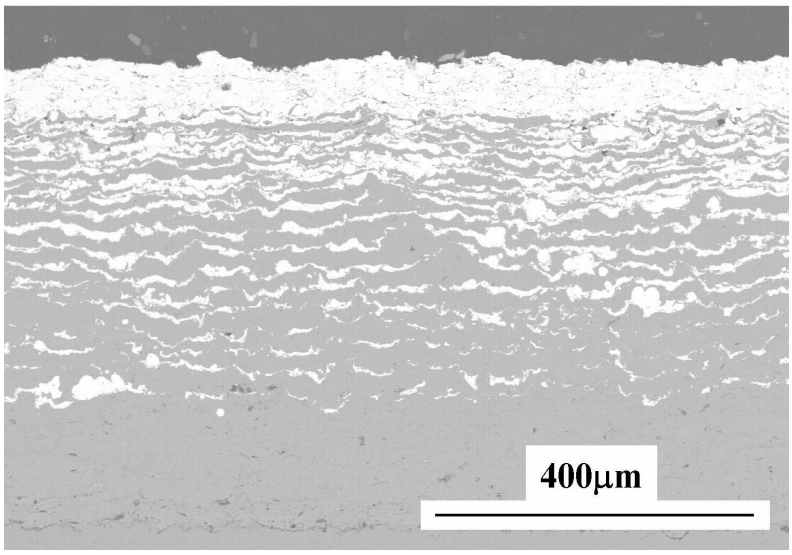

(a): Backscattered electron image of a cross-section of graded coating 65b

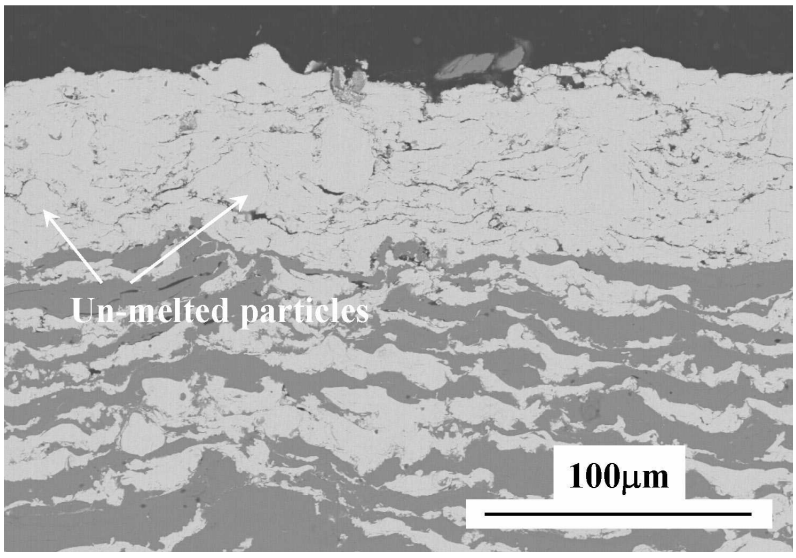

(b): Backscattered electron image of the W layer of graded coating 65b

Figure 4.2: Backscattered electron images of coating 65b.

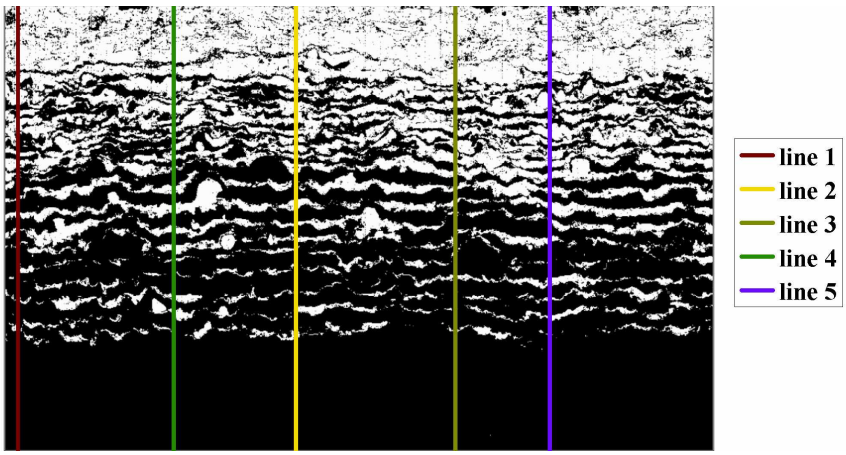

(a): Polarised backscattered electron image of coating 63b showing compositional sampling positions

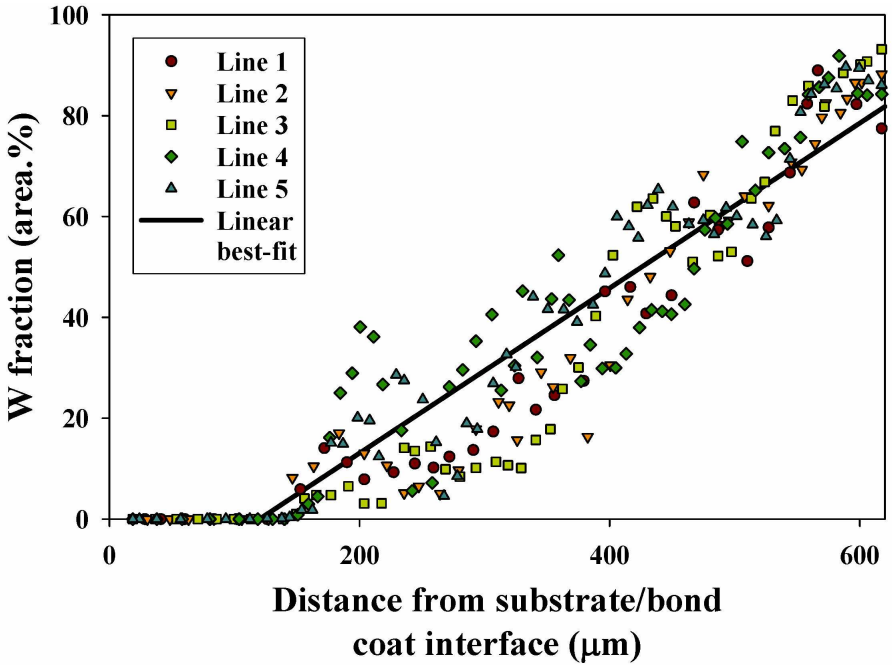

(b): W fraction through-thickness variation for coating 63b

Figure 4.3: Determination of W fraction through-thickness variation for coating 63b.

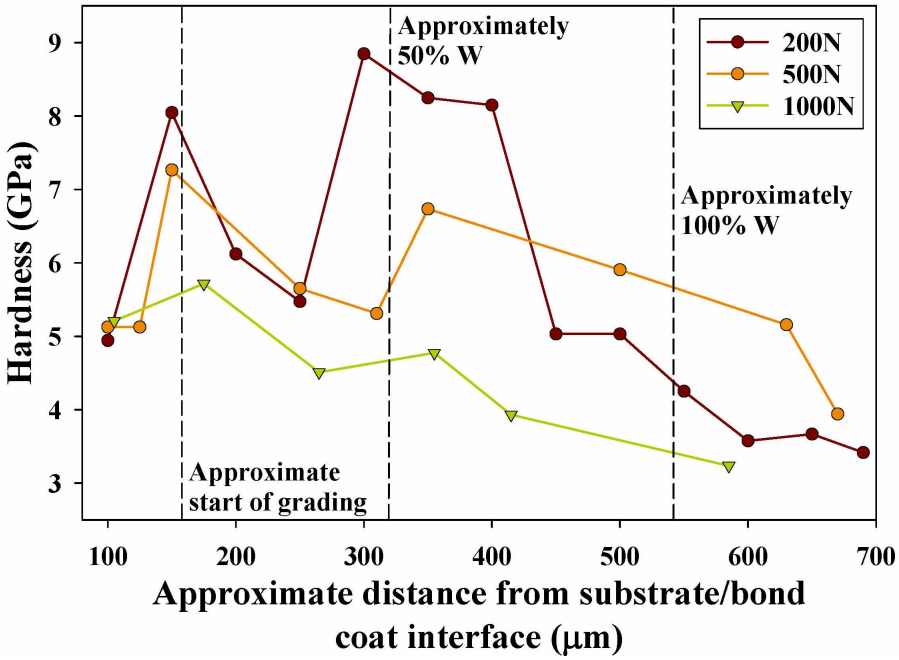

Figure 4.4: Vickers micro-indentation hardness for loads of 200N, 500N and 1000N as a function of distance from the substrate/bond coat interface through a cross-section of coating 63b.

porosity may have been somewhat exaggerated since metallographic preparation of sprayed coatings is well-known to promote 'pull-out' of material [103], and these were early coatings when preparation technique may not have been as informed as later coatings.

A series of Vickers micro-indentations were placed across a polished cross-section of coating 63b as described previously in Section 3.3.4 using loads of 200N, 500N and 1000N. Between two and four indents were taken at the same vertical height across the coating, and the averages are shown in Figure 4.4. At 1000N the bond coat had a hardness of 5-6GPa, and as W was progressively introduced the hardness reduced to ∼3.5GPa at the uppermost 100% (but porous) W layer. As lower loads were used and smaller indents and plastic zones resulted, hardness became progressively more variable since rather than local averages of hardness, as the indent size approached the splat dimensions, small numbers of splats only were indented that likely had varying fractions of W/Diamalloy, as well as pores, micro-cracks and unmelted particles. Consequently, as load reduced, average hardness varied more.

The variation of hardness across the graded coating thickness was also investigated using nano-indentation as described in Section 3.3.4. This involved two 15×6 (with a pitch between indents of

20μm in both directions) arrays of nano-indents spaced by approximately 45μm, as shown in Figures 4.5(a) and (b).

The corresponding contour maps of hardness and Young's modulus for the two arrays combined are shown in Figures 4.6(a) and (b) respectively. The region up to a thickness of y~80μm corresponded to the mild steel substrate. The mild steel average hardness and Young's modulus were 2.9GPa and 196GPa respectively and were in good agreement with the literature [104]. The upper row of indents of array 1 in Figure 4.5(a) lay just within the W coating and gave an average hardness and Young's modulus of 10.9GPa and 188.6GPa respectively, which were 33-50% lower than comparable nano-indentation results for bulk W [105]. Reduction of Young's modulus and hardness in the thermally sprayed coatings is well known and arises due to a combination of porosity and micro-cracks between layers, of the type previously shown in Figure 4.2(b).

Variations in hardness and Young's modulus in the graded region of the contour maps in Figures 4.6(a) and (b) were better illustrated by vertical slices through the data shown in Figures 4.7(a) and (b). Noting that each successively sprayed layer was ~100μm thick compared with a indent vertical spacing of just 20μm, Figure 4.7(a) shows that overall there was little change in average nano-hardness across the coating, apart from the softer mild steel substrate where hardness was ~2.9GPa. Figure 4.7(b) shows a stronger variation of Young's modulus with distance, increasing from ~120GPa for the Diamalloy adjacent to the mild steel substrate to ~190GPa for the W, with once again the comparatively low Young's modulus in both cases arising from inherent porosity of the as-sprayed coatings.

Figure 4.8 compares the Vickers micro-hardness profiles in Figure 4.4 to the nano-indentation hardness distribution in Figure 4.7. The two methods shows an increased variation in hardness with reducing indentation load when microstructural features were dominant; at higher loads, 'average' behaviour of the microstructure was measured, with an approximately linear decrease in hardness with increasing W fraction and increasing load [55, 63].

EPMA analysis was carried out on a section of graded coating 65b with the aim of identifying any inter-diffusion that might have occurred at the substrate/coating interface. The concentration of the major alloying Diamalloy elements and W were investigated. No inter-diffusion across the substrate/coating

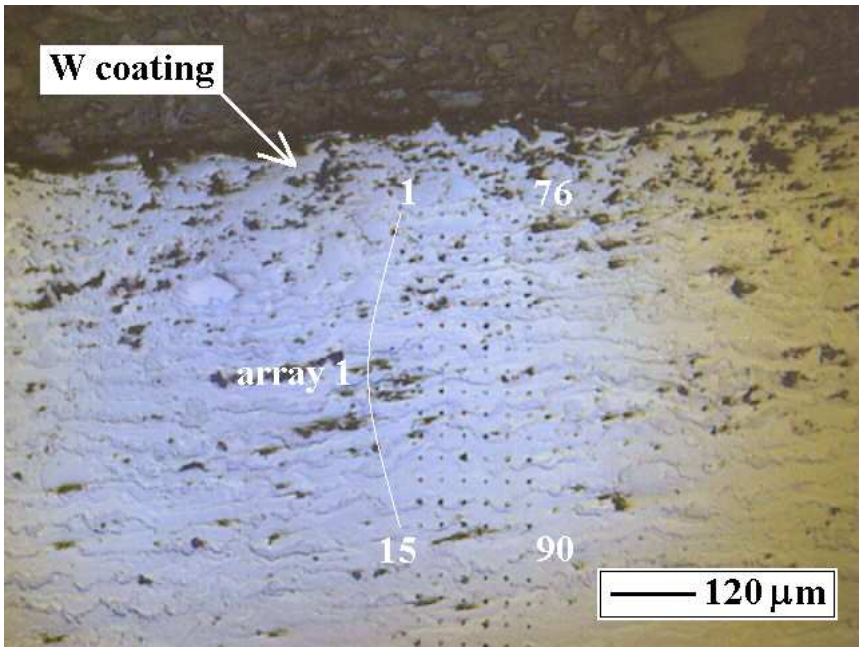

(a): Array 1

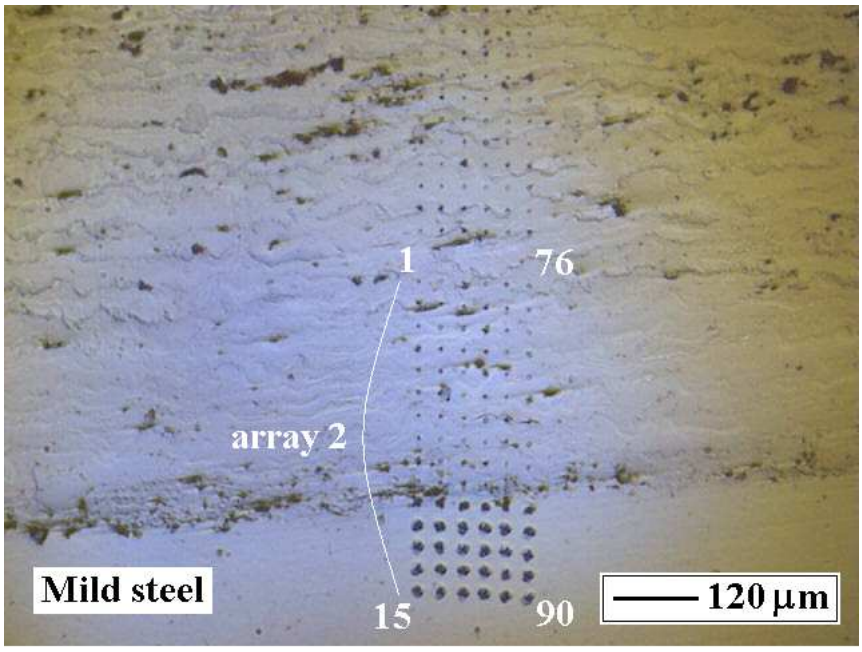

(b): Array 2

Figure 4.5: Optical micrographs showing the nano-indentation arrays across graded coating 65b.

.

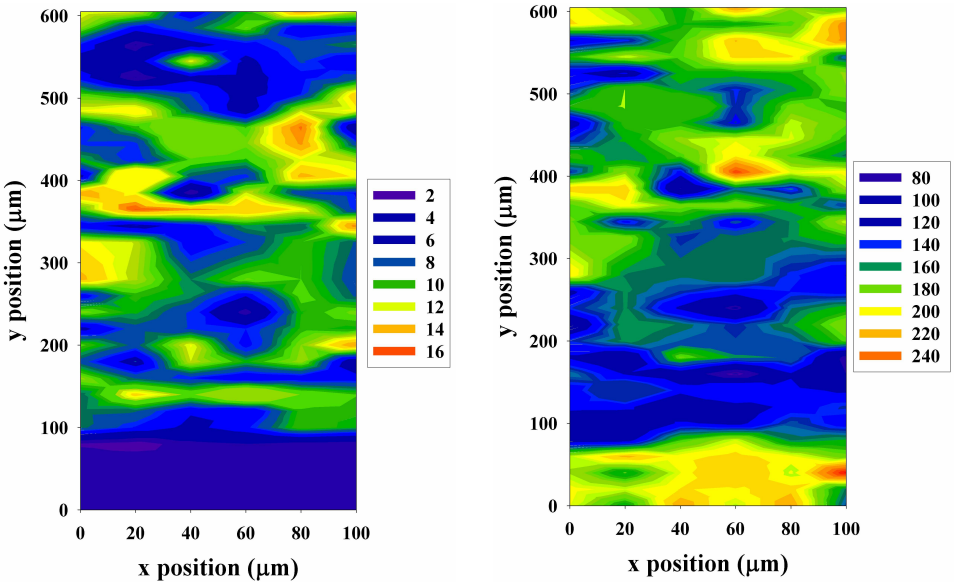

(a): Contour map of hardness for coating 65b (GPa)

(b): Contour map of Young's modulus for coating 65b (GPa)

Figure 4.6: Contour maps showing the variation of hardness and Young's modulus with position across graded coating 65b.

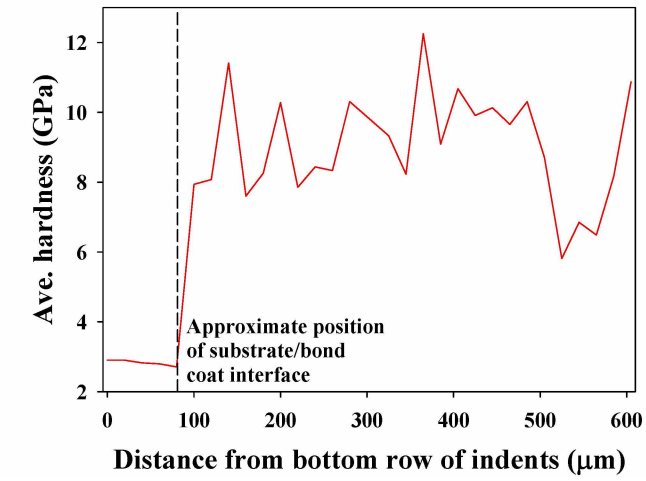

(a): Average hardness

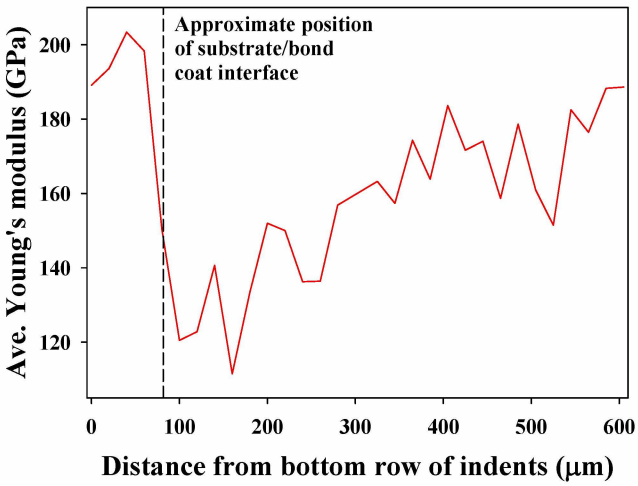

(b): Average Young's modulus

Figure 4.7: Variation of average hardness and Young's modulus with position across graded coating 65b.

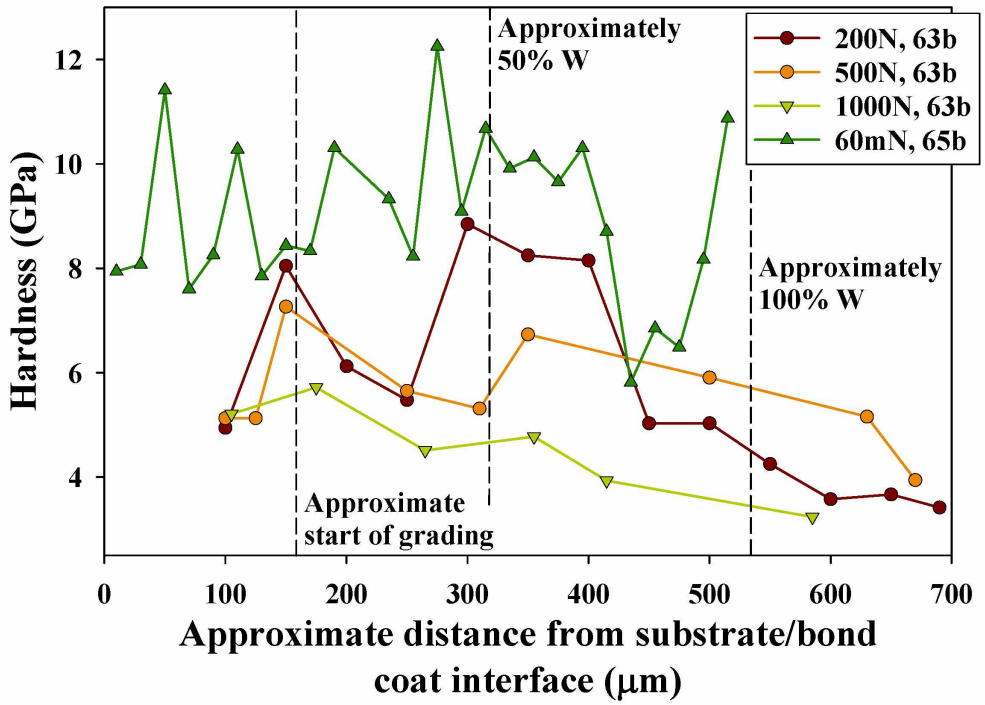

Figure 4.8: Comparison of Vickers micro-indentation hardness for loads of 200N, 500N and 1000N across graded coating 63b and nano-indentation hardness across graded coating 65b using a load of 60mN.

Coating feature	Details
Strike No.	119b
Architecture	5-layers, linear (0%, 25%, 50%, 75% and 100%)
Thermal paste	Yes
Heat treated bond-coat	No

Table 4.3: Coating details for 5-layer graded coating 119b.

interface was evident and there were no significant oxygen/oxide concentrations or secondary phases. This confirmed effective VPS operation as W oxidation readily occurs on any exposed surface at or above room temperature and accelerates significantly at temperatures >200^{o}C, producing $WO_{2.75}$, and consequently forming WO_3 at temperatures >600^{o}C [18]. As expected Cr, Ni, Mo, Si , Mn and S were found only coincidentally with a high Fe concentration in the Diamalloy 1008. The concentrations of W and Fe as a function of distance across the substrate/coating interface are presented in Figures 4.9(a) and (b) respectively. For the first $\sim$50μm in the mild steel substrate, the W concentration was effectively zero and there was a strong Fe intensity. Once the bond coat/graded layer interface was crossed, there was alternate and interleaved peaks and troughs in the W and Fe concentrations indicating the interleaved Fe-rich and W splats. There was no evidence of W-Fe interaction or dissolution, on account of the forced cooling applied to the substrate during manufacture restricting peak temperatures to $\sim$300^{o}C and times <200s. To complement the EPMA line-scans, Figures 4.10(b) to (d) show EPMA chemical composition maps for W, Fe and Cr respectively over the area in Figure 4.10(a). Again there was no large-scale Fe-W interaction.

Although initial graded coatings were successful and graded microstructures were reproducible, it was judged essential to ensure that thermal histories were known and reproducible from experiment to experiment, since thermal history as well as coating 'architecture' would control residual stresses. A thermal heat-transfer paste was therefore always used between the substrate and water cooled holder. Coating 119b was typical of coatings made under these conditions, and further details are given in Table 4.3.

In this case, two substrates - 'left' and 'right', were coated simultaneously during strike 119b, and their thermal histories during manufacture are presented in Figure 4.11. The thermal history comprises eight peaks, including a pre-heat pass to clean the substrate and encourage substrate/bond coat interdiffusion. Each of the spraying passes in Figure 4.11 comprised four passes/rasters of W/Diamalloy

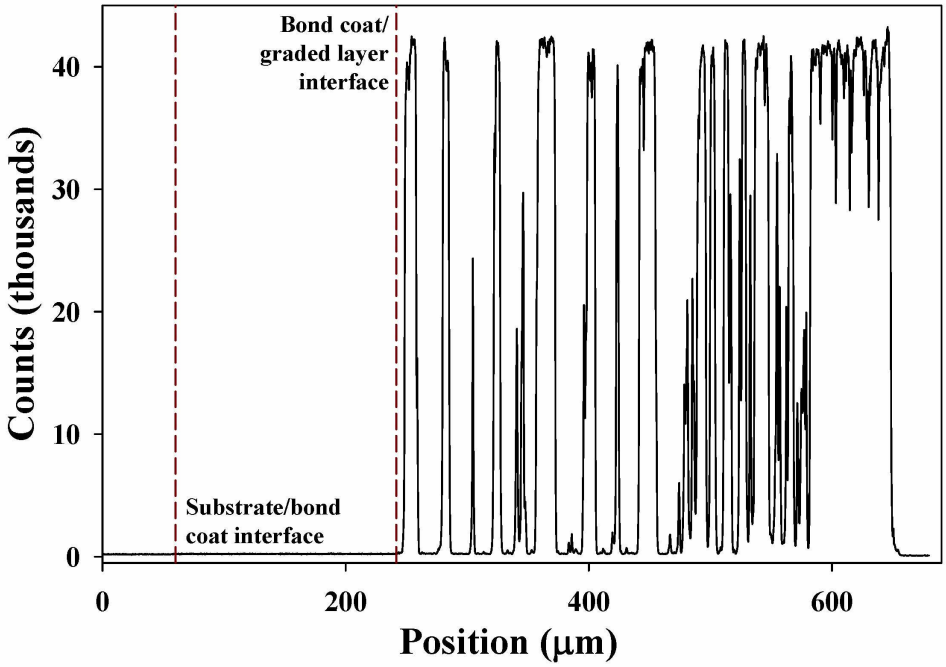

(a): Variation in W counts with position across graded coating 65b

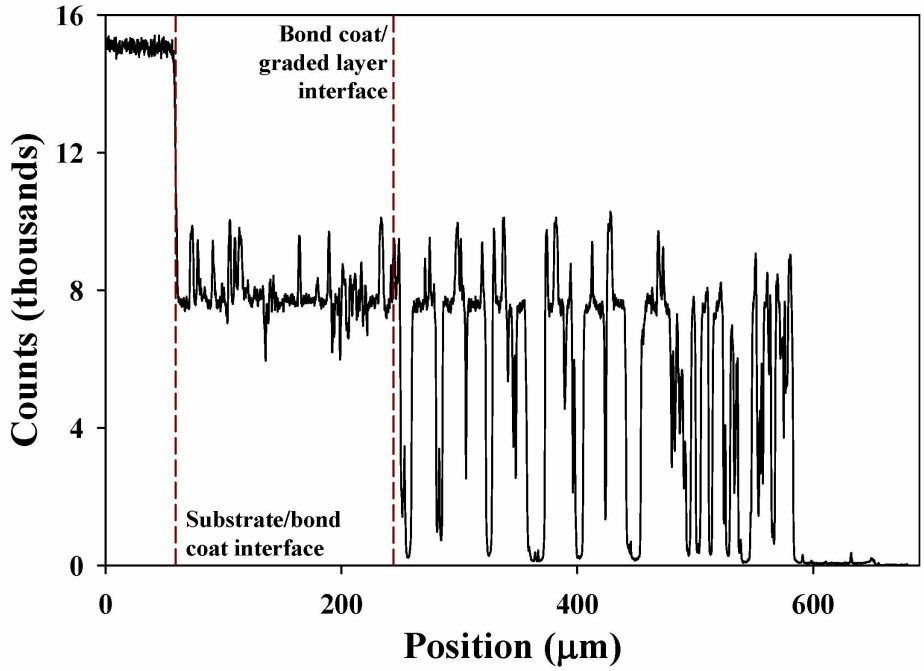

(b): Variation in Fe counts with position across graded coating 65b

Figure 4.9: EPMA line-scans across graded coating 65b.

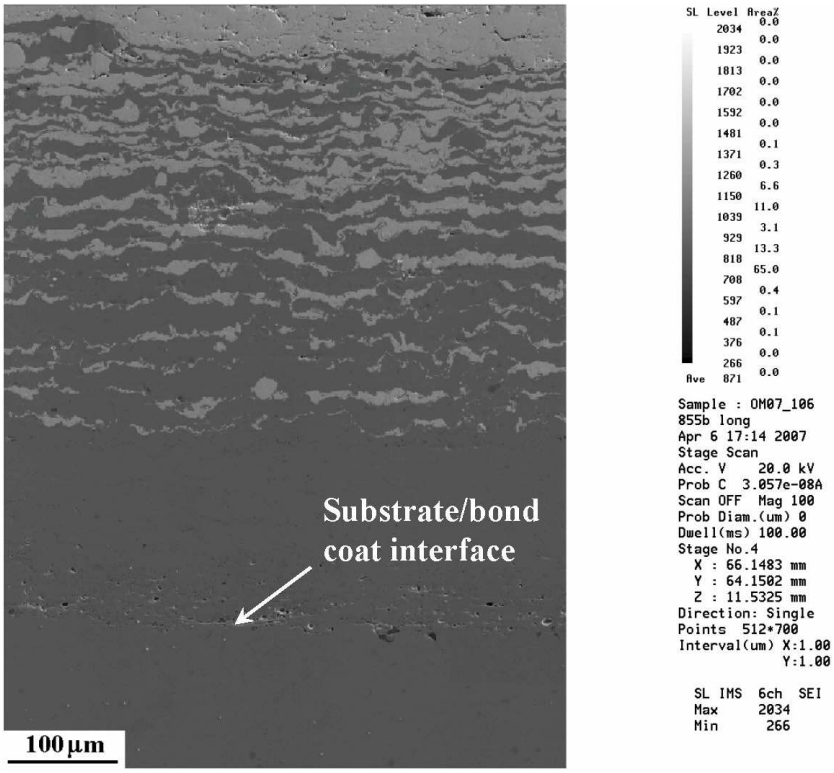

(a): The area of graded coating 65b using for EPMA analysis

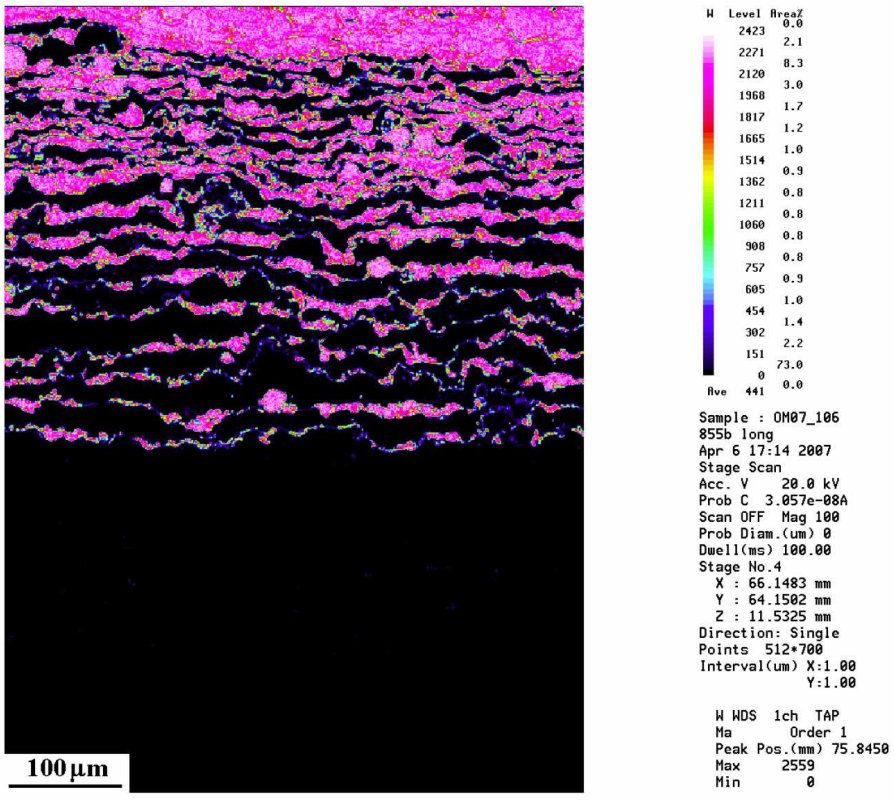

(b): Variation in W concentration

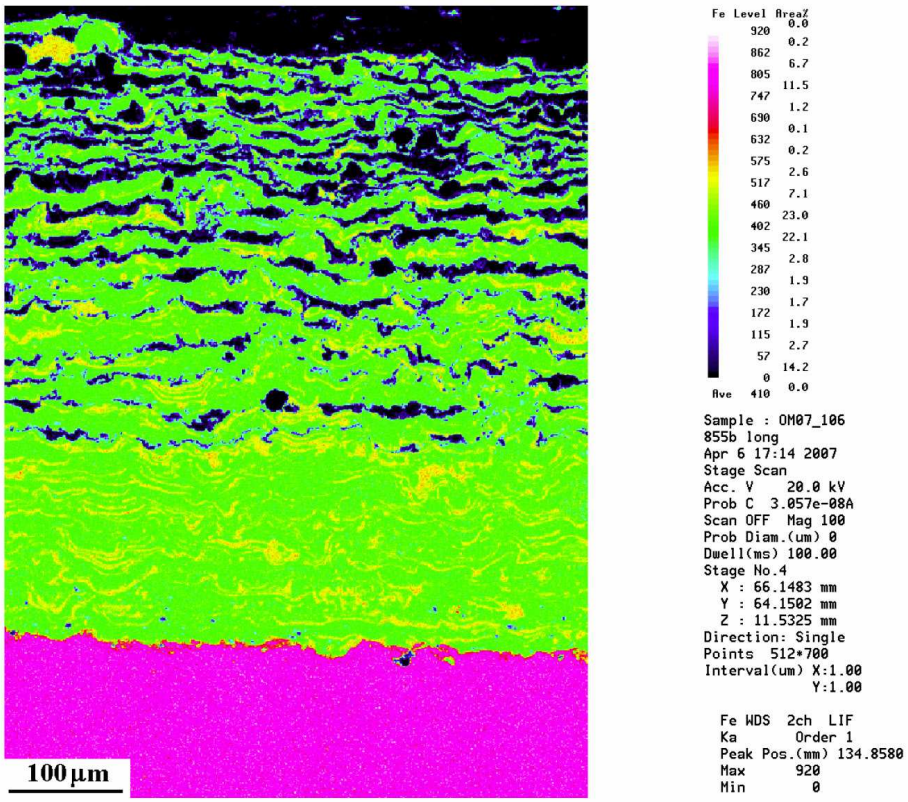

(c): Variation in Fe concentration

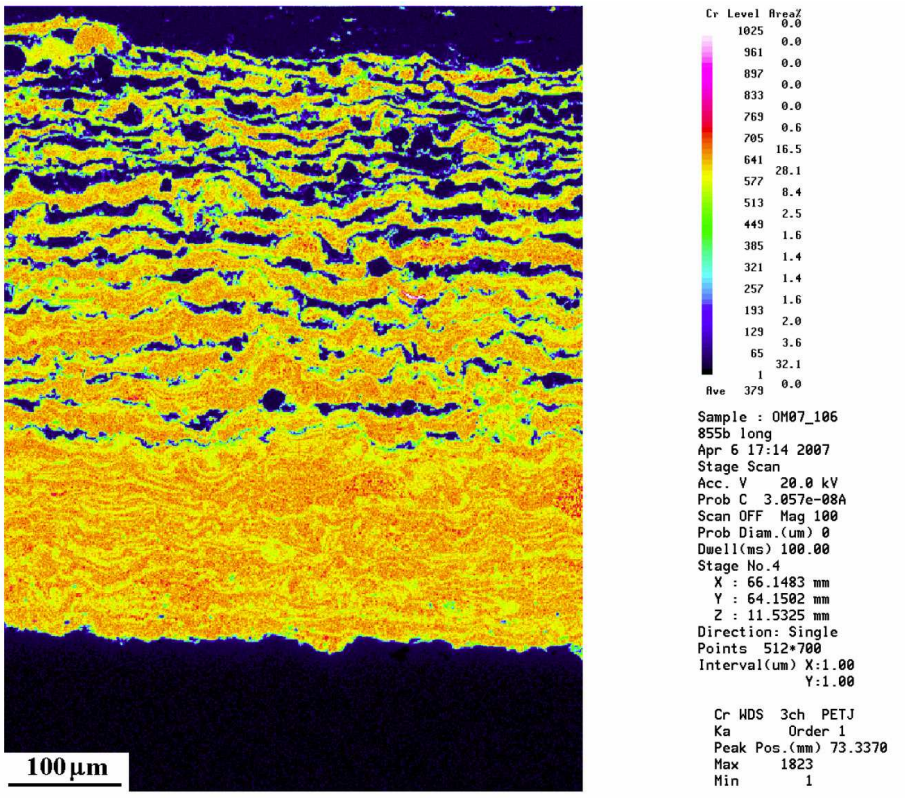

(d): Variation in Cr concentration

Figure 4.10: Elemental concentration maps obtained by EPMA for graded coating 65b.

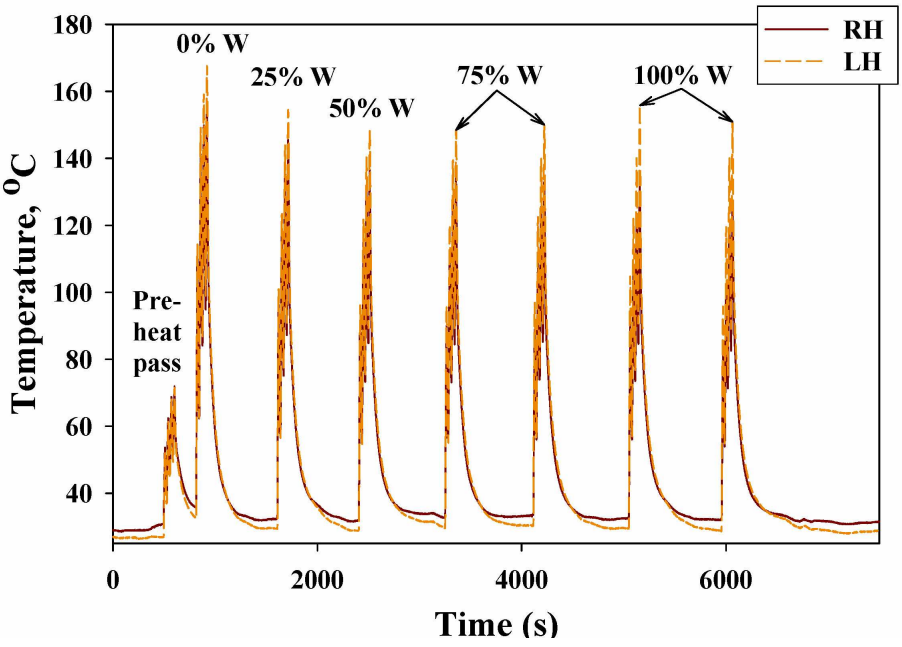

Figure 4.11: The thermal histories for the two coatings manufactured in strike 119b.

spraying. Regardless of W fraction, peak temperatures were limited to the range 150^{o}C to 170^{o}C compared with ∼300^{o}C in earlier experiments, implying excellent and reproducible thermal contact between the substrates and the water cooled holder because of the thermal paste.

The number of spraying passes was limited to four because although substrate cooling was efficient, plasma gun cooling water temperatures approached their pre-set limit of 56^{o}C on account of the very high plasma powers of 52.5kW required to melt significant W fractions, as previously described. In the periods between spraying, the plasma current was reduced from 760 to 500A and the hydrogen flow rate from 7 to 0lmin^{-1} so that power reduced to <20kW and recirculating water temperatures to ∼10^{o}C after ∼480s. In the same period, substrate temperatures reduced to ∼30^{o}C. Note that the series of deposition peaks effectively thermally cycled the coating during manufacture. The thermal history from left and right coatings were also very similar because the thermal paste standardized the critical substrate back face to water cooled holder heat transfer. Similar reproducibility was also achieved from experiment to experiment.

Figure 4.12(a) shows the as-sprayed layered graded microstructure, here capped by a relatively thin upper W coating showing that within the range studied, thermal conditions made no noticeable change to the microstructure. Following the same procedure for coating 63b in Figures 4.3(a) and (b), Figure

Coating feature	Details
Strike no.	109b
Architecture	5-layers, linear (0%, 25%, 50%, 75% and 100%)
Thermal paste	Yes
Heat treated bond-coat	No
Additional notes	W and Diamalloy 1008 mixed after exiting powder hoppers, equal mixed proportions injected above/below plasma flame

Table 4.4: Coating features, coating 109b.

4.12(b) shows the variation in W fraction through the graded coating thickness. Once again, despite the W fraction varying in discrete steps according to preset mass fraction flow rates, on average, a progressive change from 0% W within the bond-coat to a >97% dense W coating at a distance of ∼550μm from the substrate/coating interface was achieved. Again, individual points occasionally lay outside the general linear trend and were due to local agglomerations of partially or un-melted particles.

4.2.3 5-layer graded coating with post-hopper mixing

The aim of these experiments was to investigate if the layering of Diamalloy and W within the regions of nominally constant W fraction due to Diamalloy/W non-mixing in the plasma flame could be reduced. Rather than injecting W and Diamalloy separately into the plasma from opposing sides of plasma flow, the powders were mixed dynamically post-hopper in a short length of PTFE tube, whose diameter was chosen to maintain feed gas velocity, and this single feed then was split into two again to feed the opposing powder injectors at the plasma torch. The key coating parameters are shown in Table 4.4.

Figure 4.13 is a backscattered electron image of typical coating 109b. There was much improved W and Diamalloy intermixing, with intermixing now occurring at the individual droplet/splat length scale. However, the W fraction in the graded regions was lower than without post-hopper mixing because a proportion of W powder was now being injected from above, rather than all from below, the plasma flame. Because of the high density of W, when injected into the plasma from above, it tended to traverse the hot plasma core and drop out the lower region of the plasma, leading to restricted melting. While this might be compensated for by a reduction in injection flow rate - and therefore

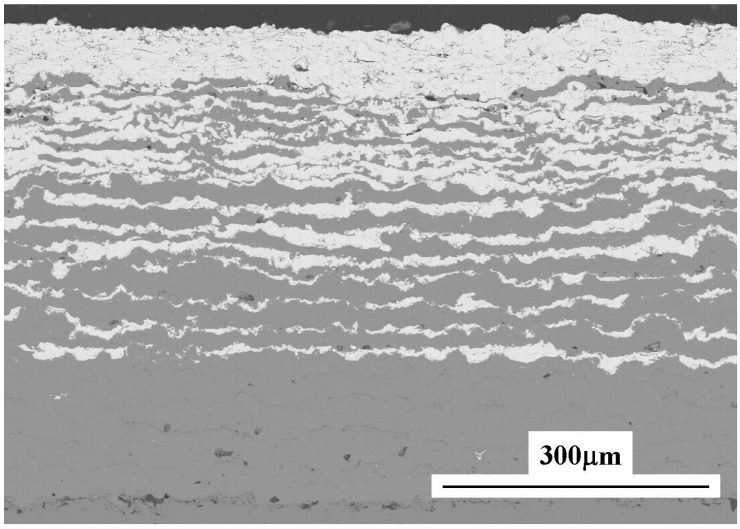

(a): Backscattered electron image of a cross-section of coating 119b

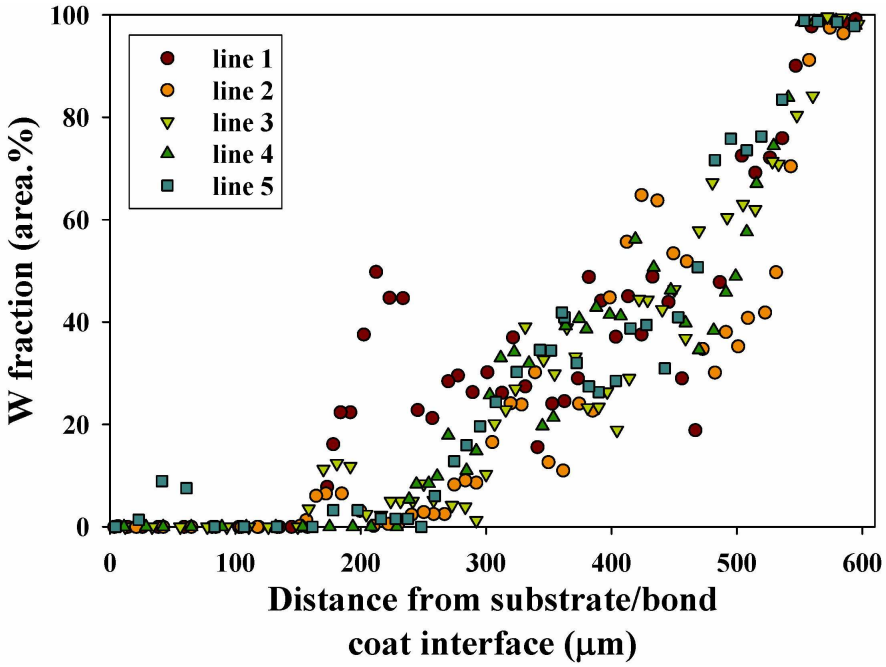

(b): W fraction through-thickness variation for coating 119b

Figure 4.12: Backscatter electron micrographs and W through-thickness variation for cross-sections of coating 119b.

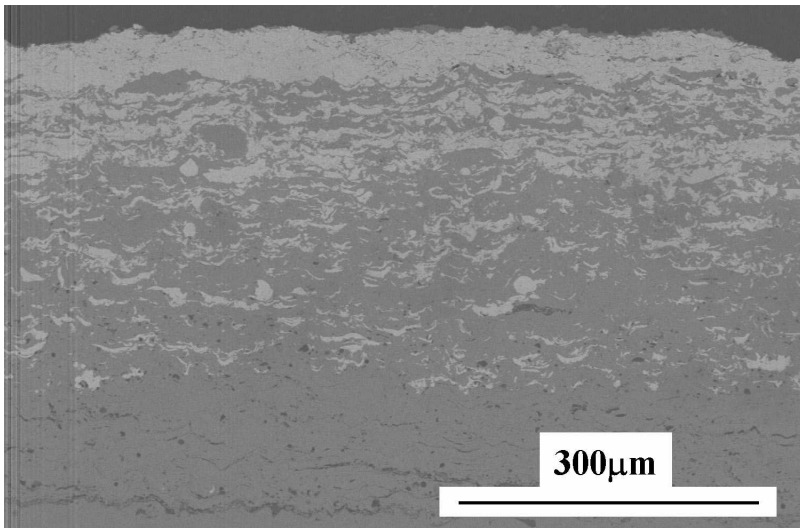

Figure 4.13: Backscattered electron image of a cross-section of coating 109b.

W powder downwards momentum - this would lead to insufficient penetration of the Diamalloy into the plasma core. Alternatively, relative mass flow rates could be re-optimised, possibly changing the number of passes required to achieve a given thickness.

The thermal histories of these type of coatings is shown Figure 4.14, for left and right coatings, and was essentially unaffected by the post-hopper mixing, with the peak temperatures again restricted to 180-200^{o}C.

Similar to previous examples, Figure 4.15 shows the variation of W fraction with distance through the coating. There was now more scatter in the measurements and the reduced deposition efficiency of the W in the graded region was evident, with the best-fit variation of W fraction with distance now being parabolic rather than linear and the proportion of W increasing from 0% at ∼100μm from the substrate/coating interface to ∼60% at ∼400μm, rather than the desired 75% W. Once again, EPMA investigations showed no significant Diamalloy/W interaction.

4.3 Graded coatings with heat-treated bond coats

Although various approaches such as consistent substrate cooling and control over the grading fraction helped to reduce W coating delamination during/after manufacture, there were still occasional delaminations at the steel/Diamalloy bond coat interface, even under nominally identical conditions.

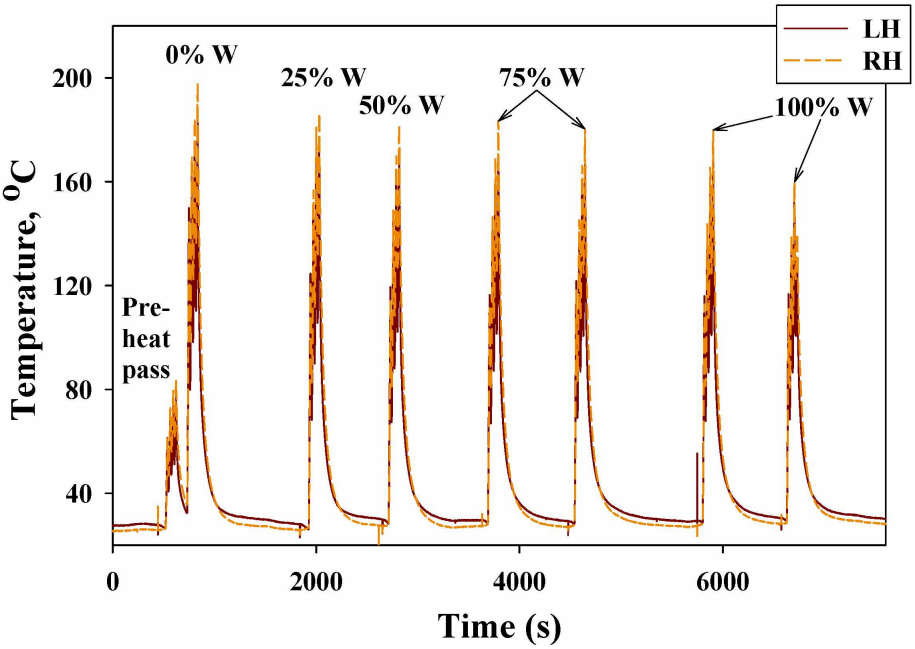

Figure 4.14: The thermal histories for the two coatings manufactured in strike 109b.

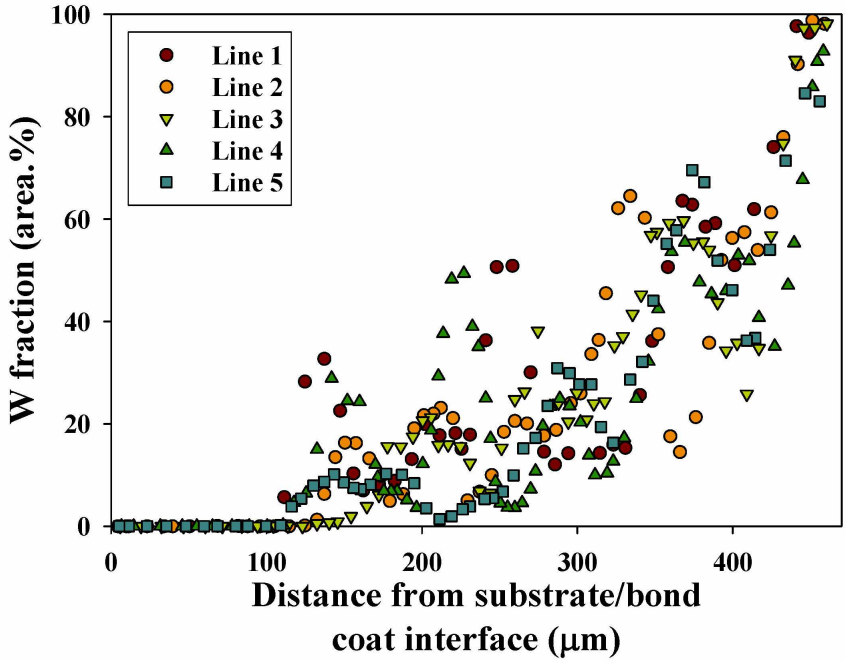

Figure 4.15: W fraction through-thickness variation for coating 109b.

Coating feature	Details
Strike No.'s	128b, 129b and 141b
Architecture	5-layers, linear (0%, 25%, 50%, 75% and 100%)
Thermal paste	Yes
Heat treated bond-coat	Yes

Table 4.5: Coating details for 5-layer graded coatings with heat-treated bond coats (128b, 129b and 141b).

Therefore to increase the strength of this interface, and particularly to improve the consistency of interfacial strength, as-sprayed Diamalloy bond coats were heat-treated at 1,000^{o}C for 24 hours (+ 1 hour for the ramp-up/down time at each end of the heat-treatment) in a reducing atmosphere comprising a positive pressure of 4%H_2/96%Ar.

Very many 5-layer graded coatings were made using heat-treated Diamalloy 1008 bond coats and microstructures and thermal histories were essentially identical to their non heat-treated equivalents - with typical coating parameters for coatings 128b, 129b and 141b presented in Table 4.5. Delamination during manufacture was effectively eliminated by the use of heat-treated bond coats. In the case of coating 141b, the improved adhesion of the substrate/bond coat interface was leveraged to produce a thicker 150-200μm upper W layer as opposed to a layer of $\sim$100μm in previous cases. Figure 4.16(a) shows a backscattered electron image of coating 141b, with (b) the corresponding thermal history and (c) the W fraction as a function of through-thickness position. The upper layer was $\sim$170μm thick and again there occurred unmelted particles, micro-scale layering within constant W/Diamalloy fraction regions due to non-mixing of W/Diamalloy in the plasma flame, and micro-cracking and porosity inherent in VPS W. Figure 4.16(b) shows that peak temperatures were well-controlled at $\sim$140^{o}C, reducing to $\sim$30^{o}C in between passes.

Typical W porosities of <5% from W fraction versus distance curves such as 4.16(c) were felt to be an under-estimation due to the low definition in the W layer of the backscatter electron images covering the entire graded coating. Consequently similar analysis of a higher magnification image, shown in Figure 4.17(a) and in binary form in Figure 4.17(b), of the W coating of sample 129b was undertaken, using sampling boxes with a minimum dimension > the observed maximum pore size. This gave a mean porosity of 9% $\pm$ 1.6, considered more typical of the as-sprayed W.

The variation in hardness through the coating thickness was investigated by Vickers micro-indentation using coating 141b and loads of 500N and 1000N. In each case, at least four indents were made at the same through thickness then averaged. At both 500N and 1000N, the hardness was relatively low in the heat-treated bond coat (at 3.4-4.4GPa versus 5GPa in the non heat-treated case), increased as the non heat-treated graded interlayers were entered and then progressively decreased again as the W fraction increased. The heat-treated bond coat had been annealed but not aged and so had low

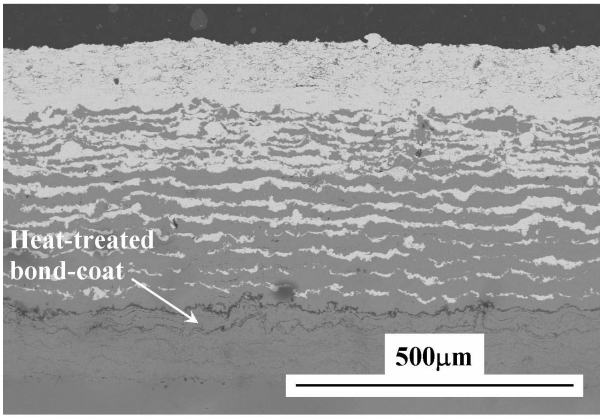

(a): Backscattered electron image of a cross-section of coating 141b

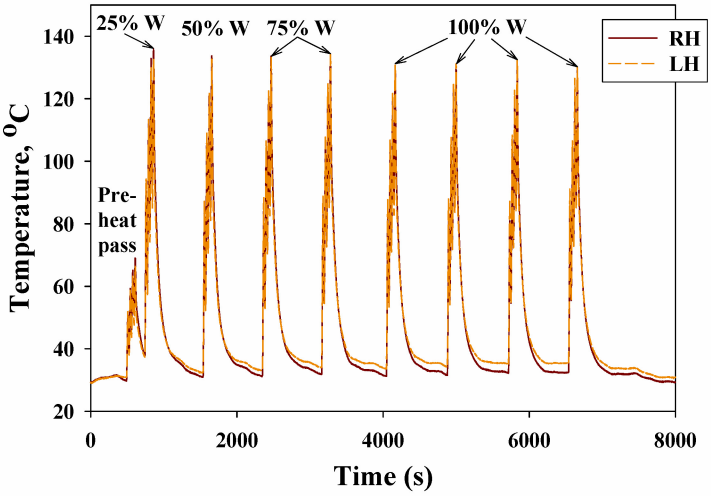

(b): The thermal histories for the two coatings manufactured in strike 141b

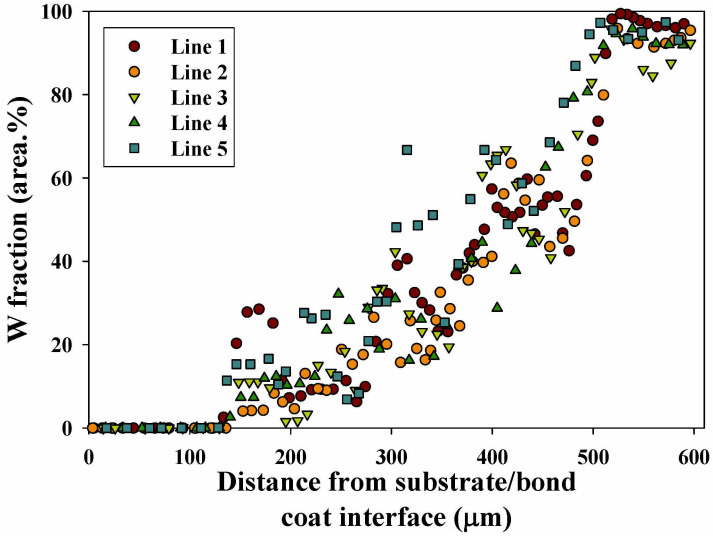

(c): W fraction through-thickness variation for coating 141b

Figure 4.16: Backscattered electron image, thermal history and W fraction through-thickness variation for coating 141b.

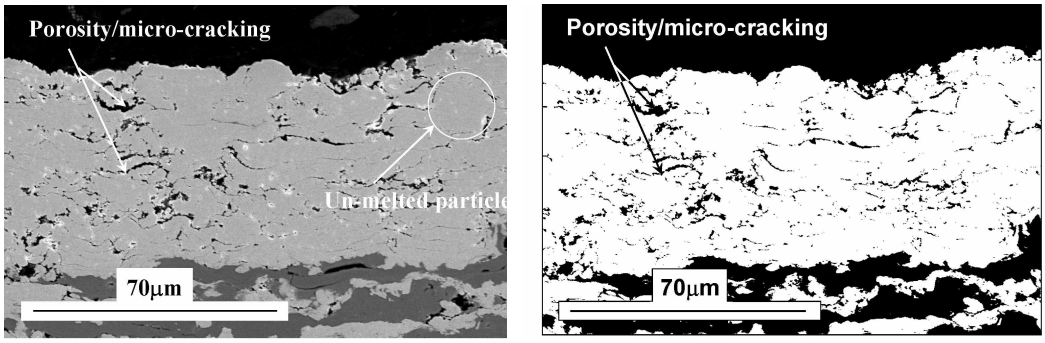

(a): Secondary electron image

(b): Binary version of secondary electron image

Figure 4.17: Cross-sectional micrographs of coating 129b used to determine porosity of as-sprayed VPS W.

Coating feature	Details
Strike no.	142b
Architecture	11-layers, parabolic → n^2 (0%, 1%, 4%, 9%, 16%, 25%, 36%, 49%, 64%, 81% and 100%)
Thermal paste	No
Heat treated bond-coat	Yes
Additional notes	Delamination on cool-down

Table 4.6: Coating features, coating 142b.

hardness, whereas the as-sprayed Diamalloy was rapidly solidified, presumably with extended solid solution strengthening of some elements. As with coating 63b in Figure 4.8, the compositional grading on average and at the micro-indentation length scale, gave a gradient in hardness and therefore Young's modulus.

Both EPMA scans and maps were conducted across coating 129b to investigate the effects of the heat-treatment on the Diamalloy 1008 bond-coat. As expected, there was significant evidence of inter-diffusion and typical EPMA elemental concentration line-scans for W, Fe and Cr are shown in Figures 4.18(a) to (c). For example, Figure 4.18(c) clearly shows the diffusion of Cr from the bond coat to the mild steel. Heat-treatment also improved the homogeneity of the bond coat itself as diffusion occurred between individual splats.

A series of EPMA maps were also produced across both the cross-section and the interfacial regions of sample 129b, confirming the homogenization of the bond-coat and diffusion of elements across the mild steel/Diamalloy interface. For example, EPMA maps for W and Cr across cross-sections of coating 129b are shown in Figures 4.19(a) and (b) respectively, indicating once again no significant interaction/diffusion of W and extensive diffusion of Cr, indicative of diffusion bonding to increase interfacial strength and integrity.

4.3.1 11-layer graded coating

Coating 142b comprised two simultaneously sprayed 11-layer graded coatings each with a parabolically graded fraction of W as given in Table 4.6. These coatings were manufactured using heat-treated bond coats previously deposited on mild steel substrates. The objective was to investigate the capability of producing different gradient architectures.

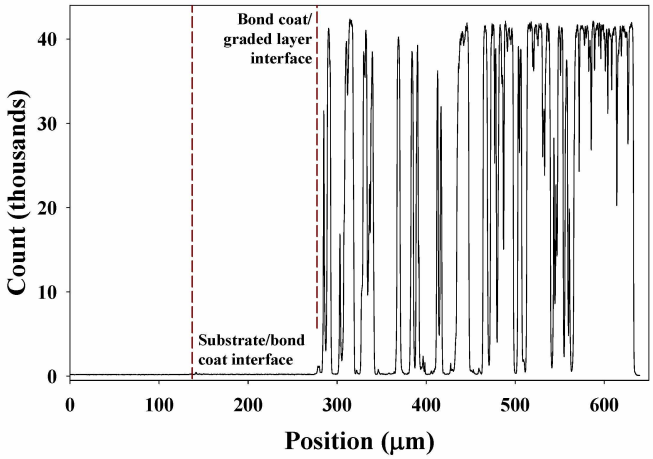

(a): Variation in W counts with position across graded coating 129b

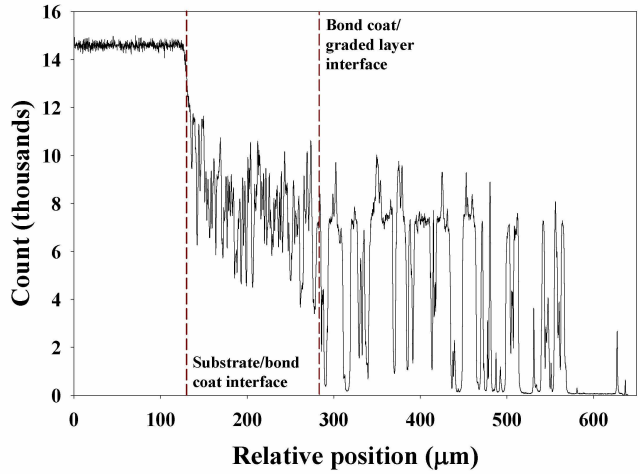

(b): Variation in Fe counts with position across graded coating 129b

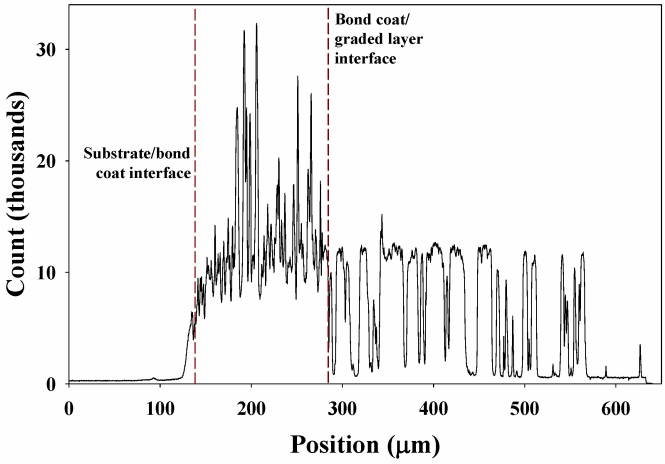

(c): Variation in Cr counts with position across graded coating 129b

Figure 4.18: EPMA line-scans across coating 129b.

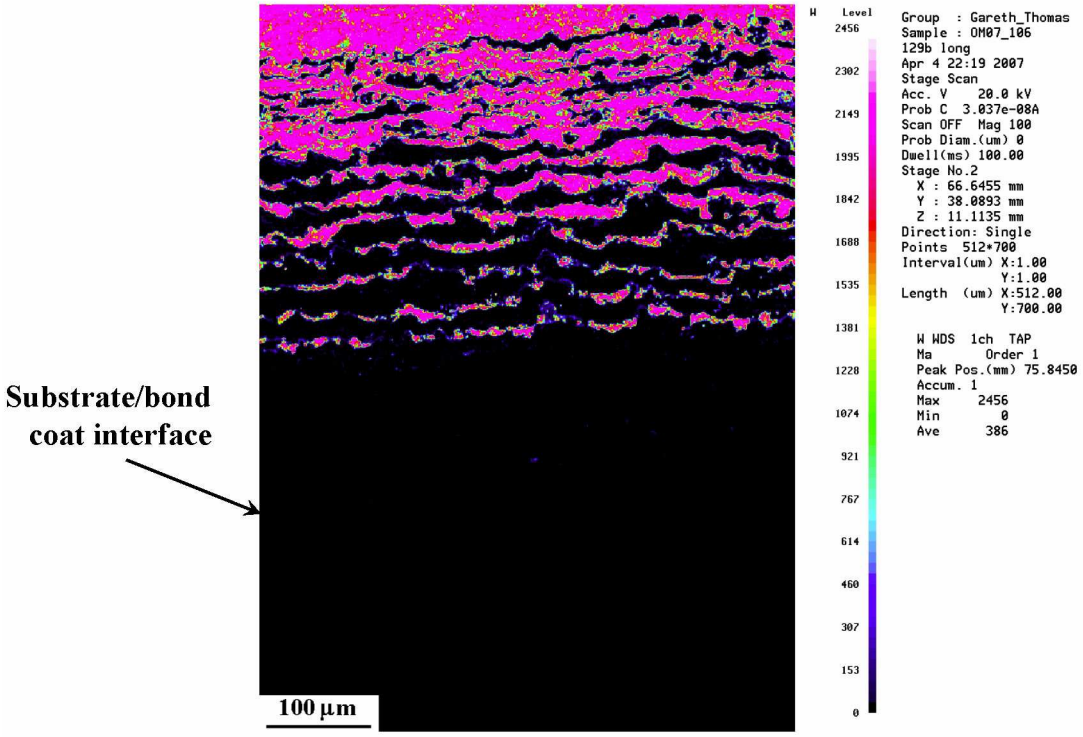

(a): Variation in W concentration

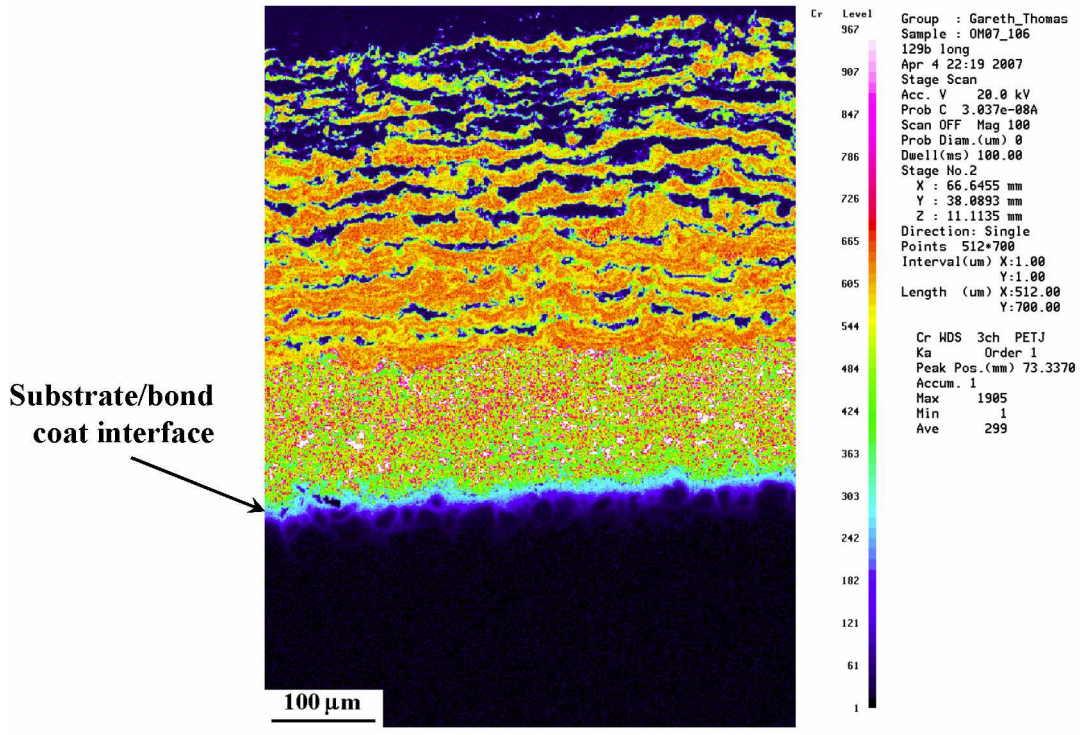

(b): Variation in Cr concentration

Figure 4.19: Elemental concentration maps obtained by EPMA for graded coating 129b.

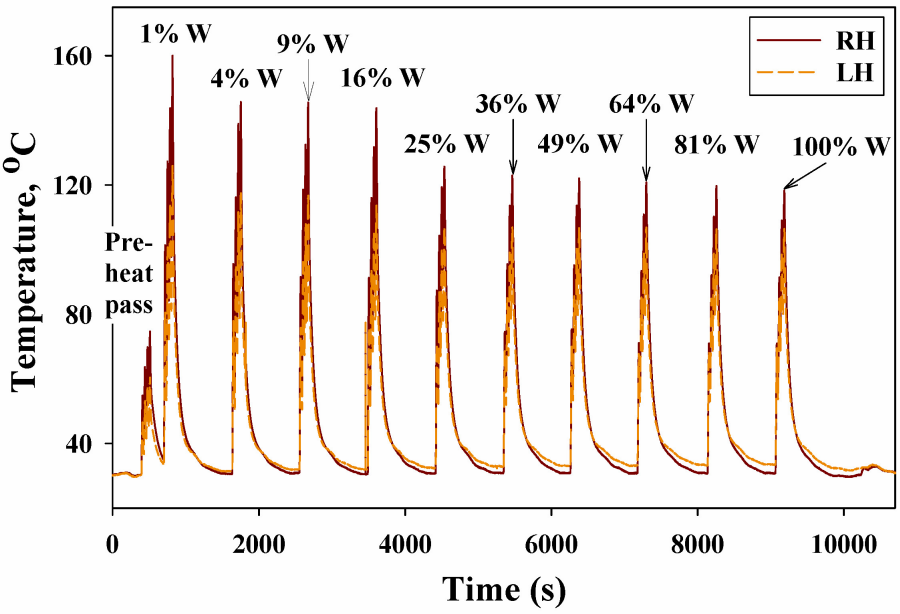

Figure 4.20: The thermal histories for the two coatings manufactured in strike 142b.

The thermal histories of coating 142b are shown in Figures 4.20. Once again a pre-heating set of passes was used before layers with increasing fraction of W were deposited. The peak temperatures during deposition varied between $\sim 120^{o}$C and $\sim 160^{o}$C, with a continuously but reducing tendency towards lower peak temperatures with time. As in previous cases, the thermal histories of the two coatings were essentially identical.

Figure 4.21 shows a backscattered electron image of a cross-section of coating 142b. In comparison with the 5-layer graded coatings for instance in Figure 4.16(a), there was a more gradual grading of the W fraction as intended. There was again some splat-scale layering of W and Diamalloy 1008. These coatings delaminated at the substrate/bond coat interface during cooling after the final deposition pass of W. This behaviour - and delamination/failure of coatings in general - is discussed later.

Following the standard method described earlier, Figure 4.22 shows a plot of local W fraction as a function of distance through coating 142b. Best-fit lines of the form $\%\mathrm{W} \propto y^2$ and $\%\mathrm{W} \propto y^n$ where the best-fit value of n=3.6 are also shown. The W variation was non-linear with a greater proportion of W towards the upper surface of the coating as intended. However, rather then the targeted parabolic architecture, the W fraction varied with n=3.6 rather than n=2. The lower W fraction towards the base of the coating was attributed to insufficient W mass at lower feed-rates to penetrate the plasma

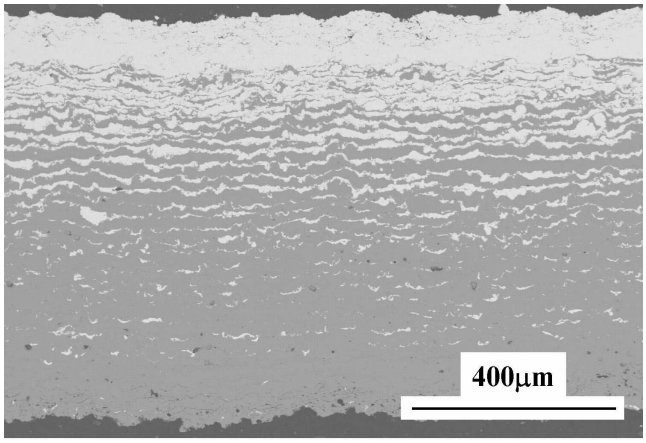

Figure 4.21: Backscattered electron image of a cross-section of coating 142b.

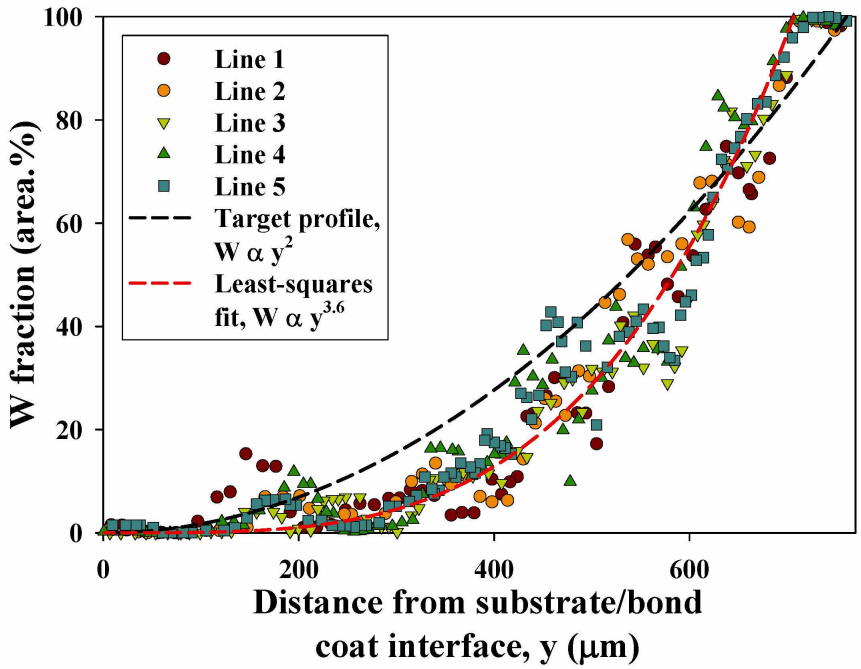

Figure 4.22: W fraction through-thickness variation for coating 142b.

flame and achieve sufficient melting.

The delaminated coating proved ideal for XRD analysis as described in Chapter 3. Figure 4.23(a) shows an XRD trace from the upper surface of the delaminated coating and may be compared with the XRD trace for α-W in Figure 4.23(b) from [18]. The as-sprayed W comprised BCC α-W only, with a lattice parameter estimated from Figure 4.23(a) of 3.1661$\mathring{A}$. The narrow peaks in Figure 4.23(a) suggested little microstrain localised within the W grains (e.g. dislocations), while the lack of noticeable shifts in α-W peak position compared to Figure 4.23(b) appeared indicative of little longer-range macrostrain [96]. Since the coating had delaminated to relieve any stored strain energy due to CTE substrate/coating mismatch, low strains should be expected.

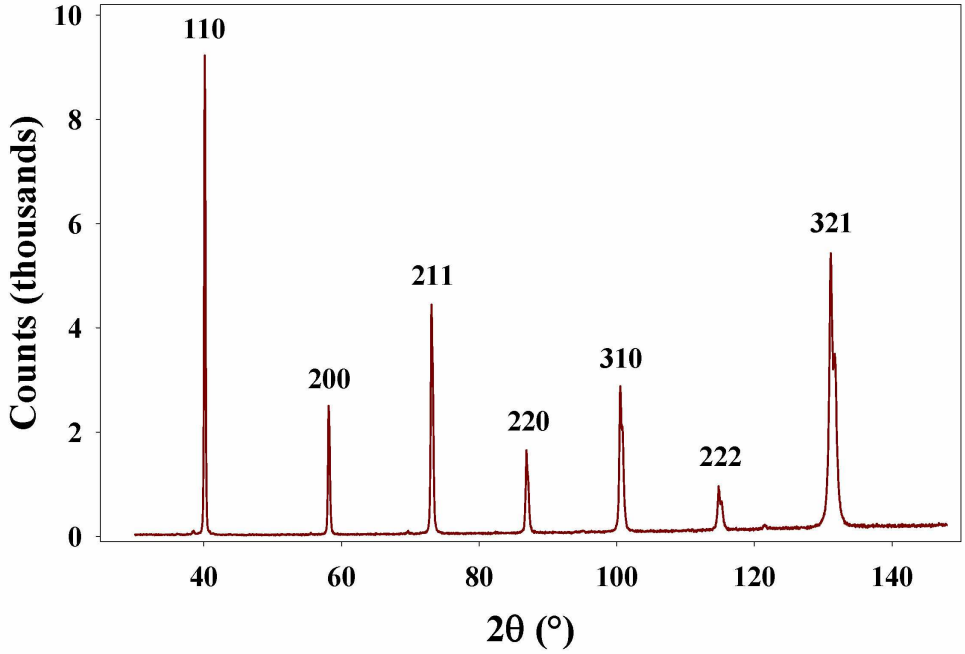

(a): XRD trace, top surface of coating 142b

The figure originally presented here cannot be made available via ORA for copyright reasons.

(b): XRD trace for α-W (from [18])

Figure 4.23: XRD traces for top surface of coating 142b and α-W.

4.4 Surfi-sculpt

Surfi-sculpt surfaces were planar stainless substrates modified using a rastered e-beam to produce regular millimetre-scale surface protrusions and intrusions in a regular pre-planned pattern. These structures increased the effective surface area of the planar substrates several times and lend themselves to numerous possible applications ranging from heat-sinks to keying surfaces for various coatings. The overall objective here was to investigate if surfi-sculpt substrates would allow the deposition of thick VPS W coatings, up to reactor-relevant (millimetre plus) thicknesses, as an alternative to the successful, but more complex, graded interlayers.

Initially nine different types of surfi-sculpt modified 316L stainless steel substrates were provided by TWI. These were viewed in the SEM and then coated under virtually identical conditions with up to ∼1mm of VPS W. It was postulated initially that as well as increased mechanical keying, the surfi-sculpt structures may help W coating retention by re-distributing stresses away from a discrete planar interface.

4.4.1 Surfi-sculpt topography

Nine different surfi-sculpt topographies were investigated. Scanning electron micrographs of these substrates, numbered 1-9, are shown in Figures 4.24(a) to (i). Substrates 1-3 and 8-9 were 'cellular in nature' with a repeating cell topography. Topographies 1-3 were ∼2mm^2 cells with relatively small peaked structures, while topographies 8 and 9 had smaller unit cells of ∼1mm^2. Topographies 4 and 5 had a 'wishbone' topography, with central peaks and twin sub-surface 'troughs' from which the material for these structures was drawn. Finally, topographies 6 and 7 consisted of a sequence of trough/tower structures.

VPS W coatings were deposited onto all the substrates in three groups of three. Although there were slight differences between the experiments due to changes in mounting of the substrates, deposition conditions were similar and based on protocols already developed for the graded coatings. Therefore, variation in any W cracking/delamination behaviour was attributed in the first instance to the large differences in substrate topography. However, note that while the region of 100% W in the graded

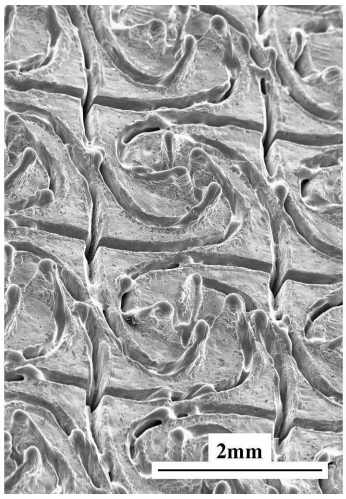

(a): Substrate no.1

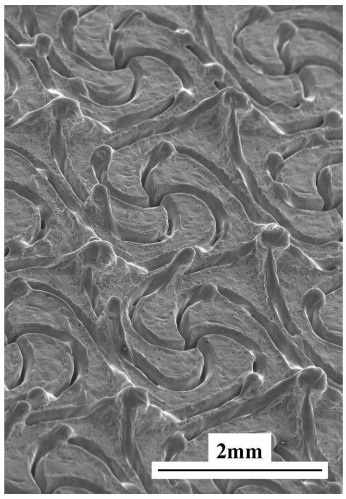

(b): Substrate no.2

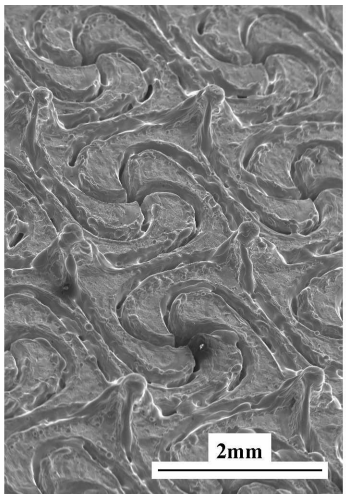

(c): Substrate no.3

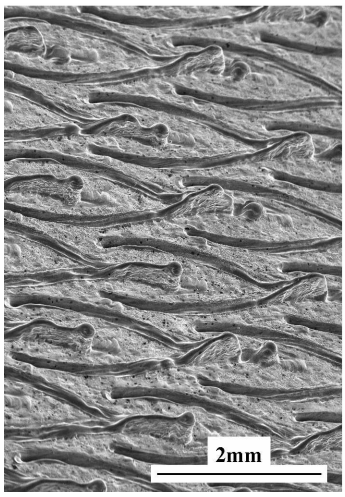

(d): Substrate no.4

(e): Substrate no.5

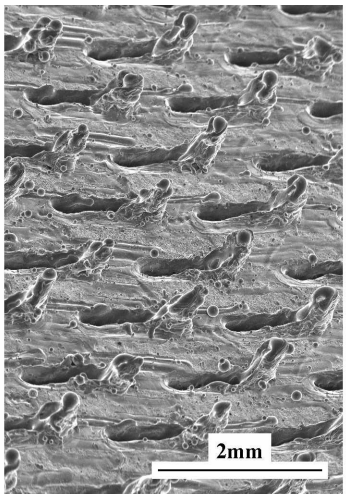

(f): Substrate no.6

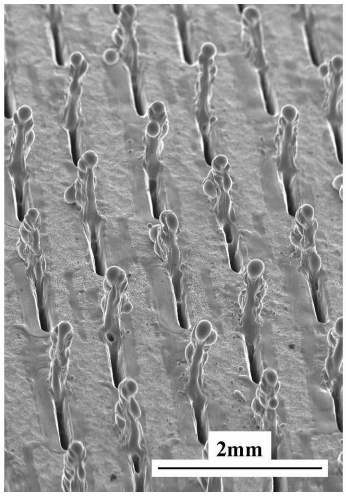

(g): Substrate no.7

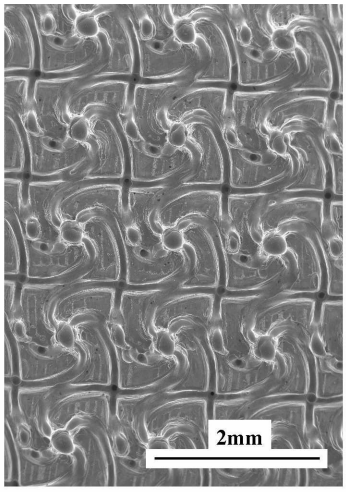

(h): Substrate no.8

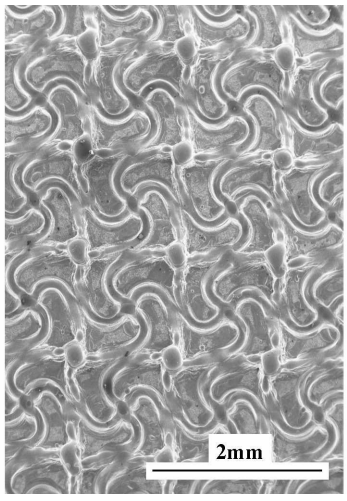

(i): Substrate no.9

Figure 4.24: Scanning electron images of surfi-sculpt substrates 1-9.

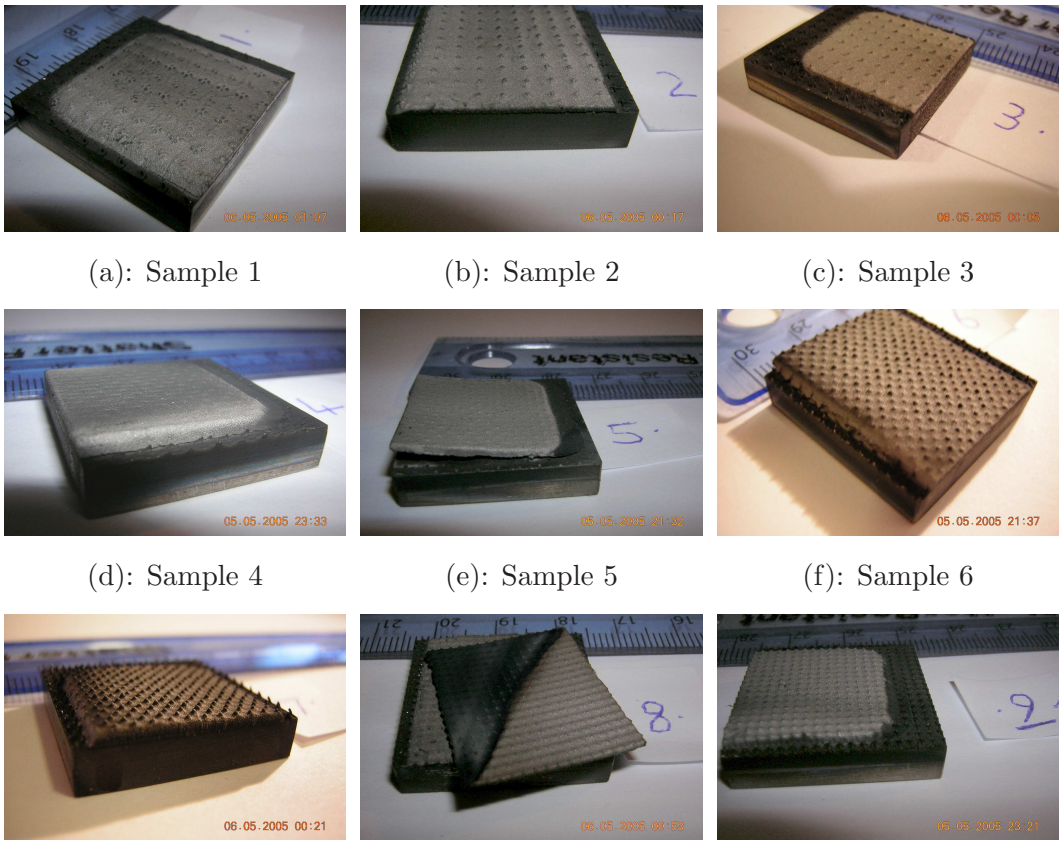

(a): Sample 1 (b): Sample 2 (c): Sample 3

(d): Sample 4 (e): Sample 5 (f): Sample 6

(g): Sample 7 (h): Sample 8 (i): Sample 9

Figure 4.25: Photographs of the as-sprayed VPS W coatings on topographies 1-9.

coating was limited to ~200μm, in these experiments 1mm of W directly onto steel with no bond coat or inter-layer(s) was investigated.

Photographs of all nine coatings taken using a Nikon Coolpix 2200 2 Mega Pixel digital camera are shown in Figures 4.25(a) to (i). In all cases, there was surface topography replication by the VPS W coating. There was some cracking/delamination along the edges of substrates 1, 2, and 4 and significant coating delamination along the edges of substrates 5 and 6. The coating on substrate 8 delaminated entirely. Table 4.7 gives a summary of the visual analysis of the coatings. Seven of the VPS W/surfi-sculpt coatings survived VPS, with coatings 5 and 8 delaminating during/post-manufacture. SEM investigations of cross-sections of coatings 1, 7 and 9 - as they exhibited some of the key microstructural features - are shown in Figures 4.26(a) to (c).

In all cases, there was replication of the underlying topography and there were two principal failure/delamination modes. Firstly, a lack of penetration of the W droplets into sub-surface features, as

Sample no.	**Cracking within W coating**	**Evidence of areas with no W penetration**
1	YES	YES
2	NO	YES
3	YES	YES
4	*Delaminated on preparation*	*Delaminated on preparation*
5	*Delaminated on cool-down*	*Delaminated on cool-down*
6	YES	NO
7	YES	YES
8	*Delaminated on cool-down*	*Delaminated on cool-down*
9	NO	NO

Table 4.7: Cracking or lack of penetration in W coated surfi-sculpt substrates.

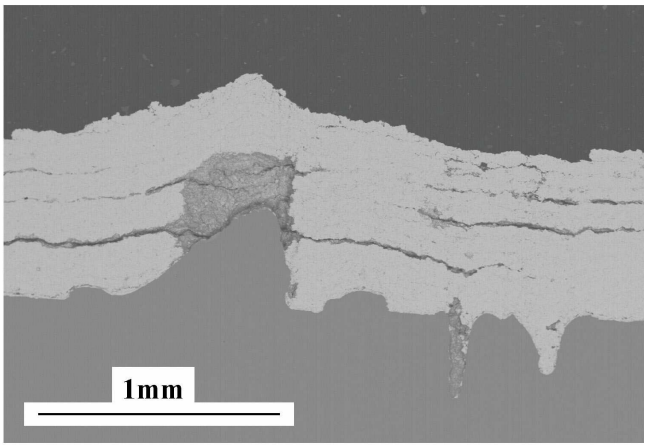

(a): Substrate 1

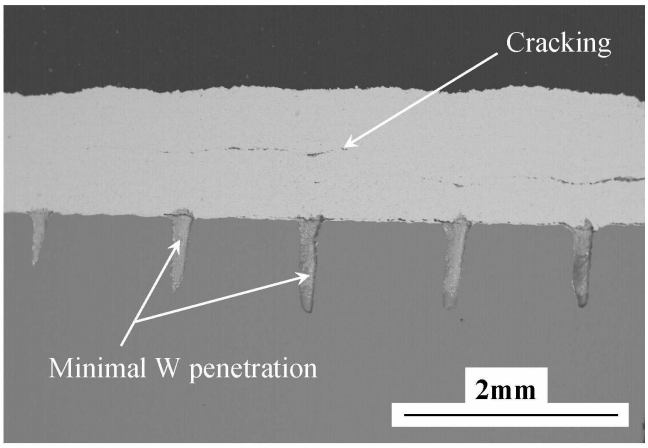

(b): Substrate 7

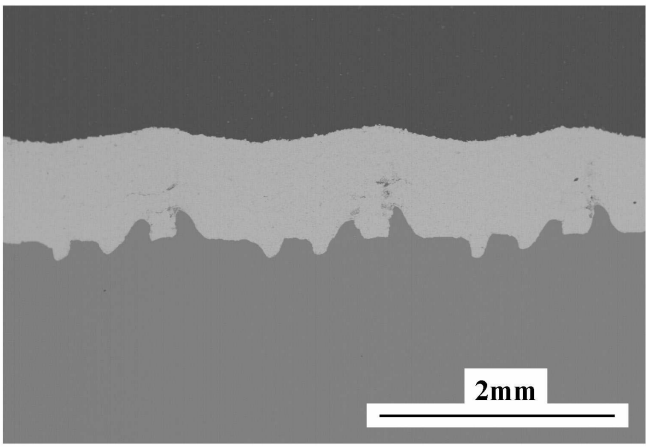

(c): Substrate 9

Figure 4.26: Backscattered electron images of cross-sections of selected VPS W coated surfi-sculpt substrates highlighting typical coating features.

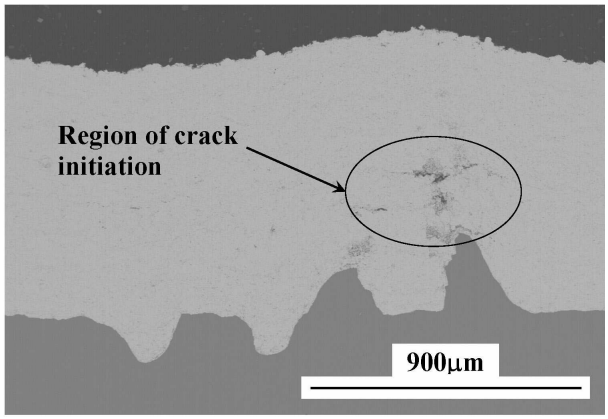

Figure 4.27: Backscattered electron image of coating 9 about a site of possible crack initiation.

in the case of coatings 1 and 7 shown in Figures 4.26(a) and (b) respectively. These small scale/narrow sub-surface features could not not be filled before 'bridging' over the top of the features occurred, and consequently there was little topographic contribution to adhesion. Secondly, there was widespread sub-surface cracking in the W, as should be expected from the stress concentrating effects of the peaked surfi-sculpt features. This effect is shown in Figures 4.26(a) and (b) for substrates 1 and 7 respectively. Substrate/coating 9 did not initially appear to have any significant internal cracking, however, a higher magnification image near one of the substrate peaks in Figure 4.27 shows a region of possible cracking/increased porosity.

Table 4.7 highlights the failure mechanisms within each of six different as-sprayed coatings that survived post-spray sample preparation. However, substrate/coating 9 offered significant encouragement for the successful use of surfi-sculpt substrates, with no delamination or gross sub-surface cracking and was chosen for further experimentation. The topography of substrate 9 was sufficiently torturous to provide enhanced mechanical keying (bonding) to retain the thick W coating, while the comparatively gentle curvature and rounded nature of the peaks in Figure 4.24(i) avoided promotion of gross 'internal' cracking. Further, the wide and shallow nature of the surfi-sculpt features appeared to allow full penetration of as-sprayed W into sub-surface features. While the delaminated coating examined by XRD in Figure 4.23 showed little/no residual strain, the coatings here were much thicker and were retained on the substrate. If W is assumed essentially stress free at the temperature of manufacture, then given the difference in stainless steel substrate and W coating coefficient of thermal expansion of $\Delta\alpha = 8{\times}10^{-6}\mathrm{K}^{-1}$ [18, 84], the W may be expected to be in compression within the plane of the

coating, which may contribute to obscuring some internal coating cracking. Because the arbitrary 2D cross-sections shown in Figures 4.26(c) and 4.27 did not cut the surfi-sculpt peaks at their 'summit', any further evidence of cracking for substrate 9 was investigated by progressive removal of material.

A total of seven progressive cross-sections each spaced by a thickness, or depth, of $\sim 50\mu$m that was removed by metallography using SiC papers of finer grit and polished in diamond paste were investigated. The thickness of the layers of material removed in each grinding/polishing sequence was monitored using a micrometer, with the thickness measured at least five times before and after each stage and averaged across the sample. Since all sprayed coatings are susceptible to 'pull-out' of poorly integrated splats or unmelted particles, care was taken to minimise force and time during grinding/polishing.

Backscattered electron images about one of the peaks are shown in Figures 4.28(a) to (g), spanning $\sim 300\mu$m of material removed. In Figure 4.28(a) there was a region of higher porosity above the largest peak. On material removal in (b), (c) and (d), this was revealed to be associated with a 'taller' peak underneath, and the moving together of the minor 'ridges' up to the main peak (see Figure 4.24(i)). In (c) and (d) close to the peak summit, the VPS W was poorly adhered to the peak and there was in-plane cracking following inter-splat boundaries. As material was further removed, the ridges on the other side of the peak were exposed, again with a local increase in porosity/cracking in (d) and (e) until another large peak was encountered. Overall, cracking was highly localised and occurred about the high radius of curvature associated with ridges and peaks, or the porosity between closely spaced features. However, despite care taken with grinding/polishing, it was considered highly likely that the cracking and porosity (due to pull-out) were amplified in this region and that Figure 4.28, in comparison to the many microstructures of VPS W on surfi-sculpt substrates, gave a slightly false impression of the porosity and cracking for this topography. Time permitting, other techniques such as chemical or electro-discharge machining would have been explored, but these were unlikely to be any less problematic. X-ray tomography might have been considered but would have been unable to resolve fine-scale cracking.

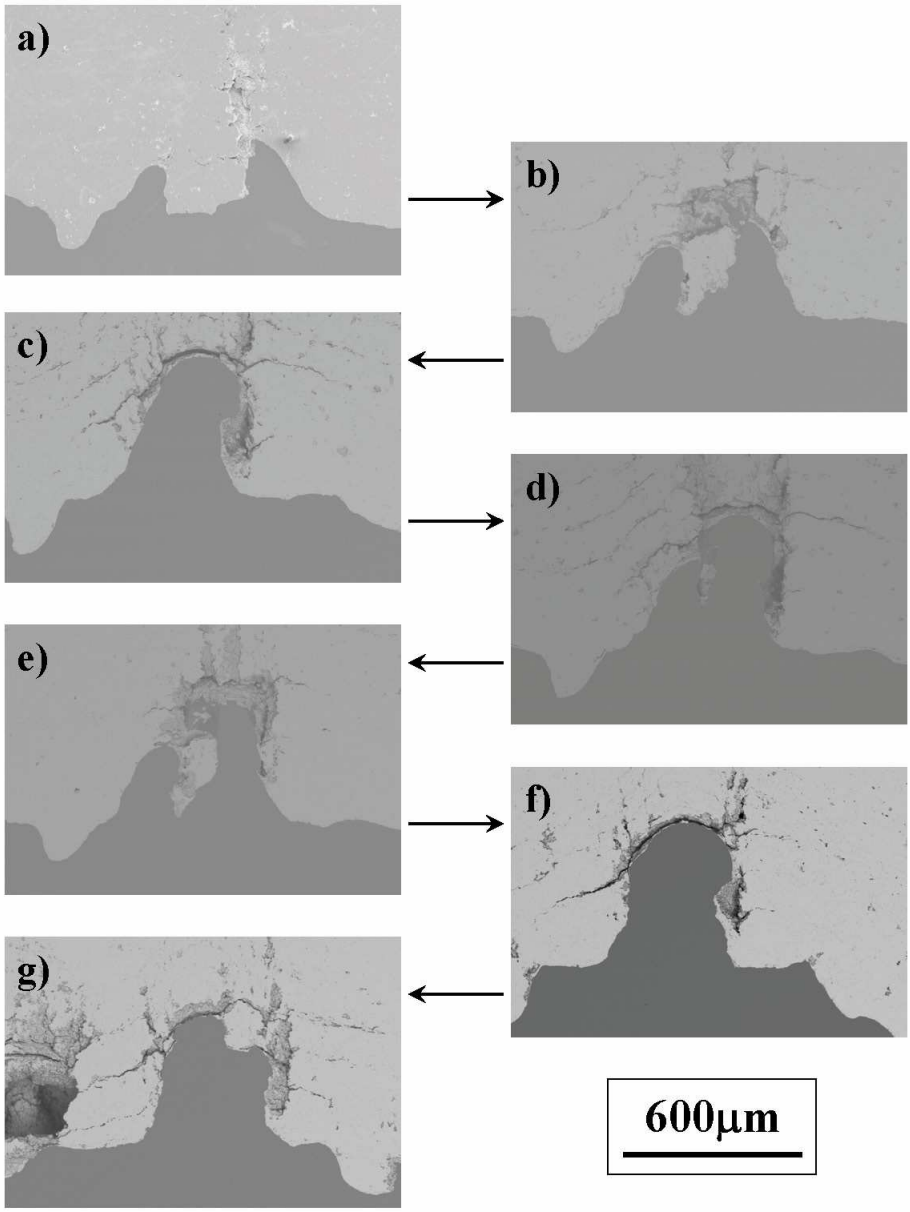

Figure 4.28: Backscattered electron images of the same region of VPS W on surfi-sculpt substrate 9 at a relative depth of (a) 0μm, (b) 52μm, (c) 99μm, (d) 153μm, (e) 201μm, (f) 256μm, and (g) 313μm.

4.4.2 Reactor-relevant VPS W/surfi-sculpt coatings

Many thick (>1mm) VPS W coatings were deposited successfully on surfi-sculpt topography 9, supplied by TWI. Two typical coatings are considered. Strike 158b to produce an ∼1mm thick W coating and strike 164b to produce a reactor-relevant ∼2mm thick W coating. Coating 158b required 24 deposition passes over more than five hours. The thermal history is shown in Figures 4.29(a) to (c). After the first pass, peak temperatures were in the range 130-140^{o}C. According to the regular heating/cooling cycles there was no delamination.

Similar thermal histories were recorded for strike 164b, with peak temperatures of 150-160^{o}C over 33 sets of passes. The peak thermally induced uniaxial stress $\Delta\sigma_t$ in the coatings may be estimated as follows:

Both coating and substrate are stress-free and attached at the manufacturing temperature. Because there is no external force acting when the coating and substrate are attached they are in equilibrium meaning that $\sigma_C \mathrm{A}_C = \sigma_S \mathrm{A}_S$ where σ_C is the stress in the substrate, σ_C is the stress in the coating and A_C and A_C are the cross-sectional areas of the substrate and coating respectively. Both the substrate and coating must be subject to identical strains on cool down to room temperature - which are given by [84]:

$$\varepsilon = \frac{\sigma}{E} + \alpha \Delta T \tag{4.1}$$

where σ is the stress, E the Young's modulus, α the coefficient of thermal expansion, and ΔT the temperature change for the coating or substrate as required.

Equating strains calculated from Equation 4.1 for the substrate and coating it can be shown that [84]:

$$\sigma_C = \frac{A_C E_S E_C \Delta T \Delta\alpha}{A_S E_S + A_C E_C} \tag{4.2}$$

where $\Delta\alpha$ is the difference in CTE between the substrate and coating and by definition $\sigma_S = -\frac{A_C}{A_S}\sigma_C$, $\Delta\alpha$ is the difference in CTE between stainless steel and W of $8\times10^{-6}\mathrm{K}^{-1}$ [18, 84], ΔT is the temperature

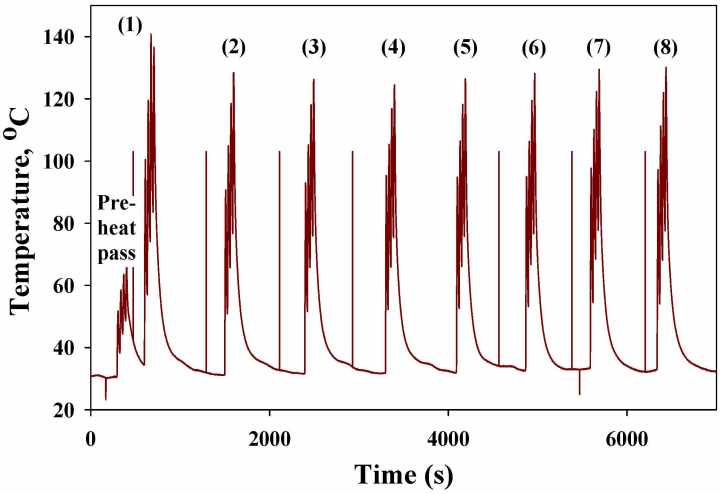

(a): Thermal history, coating 158b, 0s to 7000s

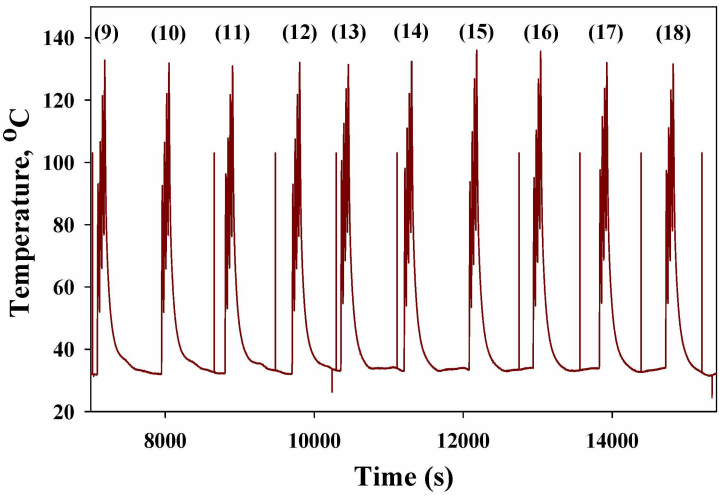

(b): Thermal history, coating 158b, 7000s to 15400s

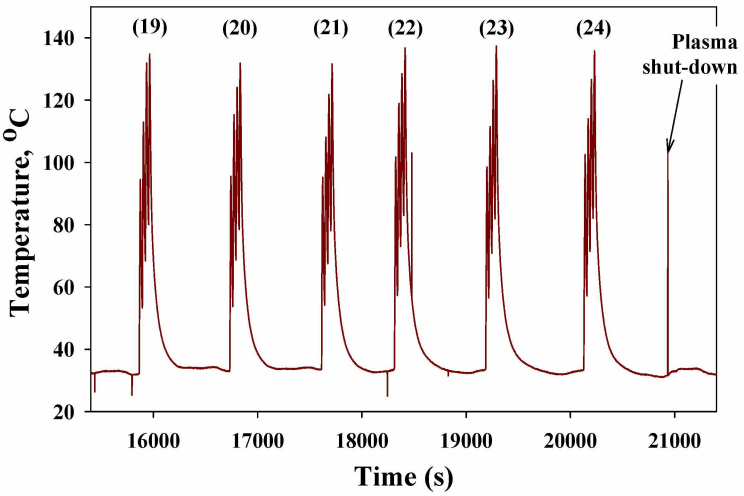

(c): Thermal history, coating 158b, 15400s to 21400s

Figure 4.29: Thermal history, coating 158b.

difference between peak and room temperature of ∼130^{o}C, E_S and E_C are the Young's moduli of steel and W, found via nano-indentation to be 230 and 194GPa respectively and substrate/coating widths are assumed to be nominally 20mm and thicknesses to be 5mm and 1mm respectively. If no stress relaxation mechanisms operated e.g. creep, yielding or micro-cracking, and the coating/substrate were assumed to have been stress-free at the peak temperature, then $\Delta\sigma_t$ ∼-175MPa for W and ∼35MPa for steel. Given a yield stress of ∼400MPa [18, 106] at room temperature and the stress concentrating effects of some elements of the 3D topography, such stresses were unlikely to occur without the initiation of non-plastic phenomena i.e. inter-splat cracking.

Backscattered electron images of cross-sections of coatings 158b and 164b are shown in Figures 4.30(a) and (b) respectively. Coating 158b showed residual porosity of <10%, whereas coating 164b showed remarkably dense W. Because deposition conditions were intended to be identical, this difference was attributed to (1) unintended differences in manual metallographic preparation inducing pull-out in coating 158b; or (2) the variation of local porosity depending upon the precise 2D section through the 3D surface used. The upper surface of both coatings gently followed the underlying topography, although this effect was more damped in the thicker coating 164b. Neither coating nor others like them showed any signs of gross internal cracking/segmentation. In the case of coating 164b, the first material deposited closest to the substrate was subjected to 33 thermal cycles of RT→150^{o}C→RT as other layers were added, without delamination. Plans were well-developed to use the plasma for specific thermal cycling tests of graded and surfi-sculpt coatings, but in the end this approach had to become a suggestion for further work due to time constraints.

Unlike the graded coatings, the thicker coatings achieved on surfi-sculpt substrates allowed nano-indentation of VPS W away from the influence of neighbouring regions. Nano-indentation tests across five different regions of coatings 158b and 164b produced consistent Young's modulus and hardness values for VPS W with average values (with errors of one standard deviation) of 194±25GPa and 4.8±0.6GPa respectively. Typical Young's modulus values for the fully dense 316L substrate were found to be similar to those of VPS W at ∼230GPa.

Preliminary electron backscattered diffraction (EBSD) investigations were carried out on by Dr Simon Hogg on cross-sections of the VPS W coating 164b. W and Fe were studied and EBSD data sets were

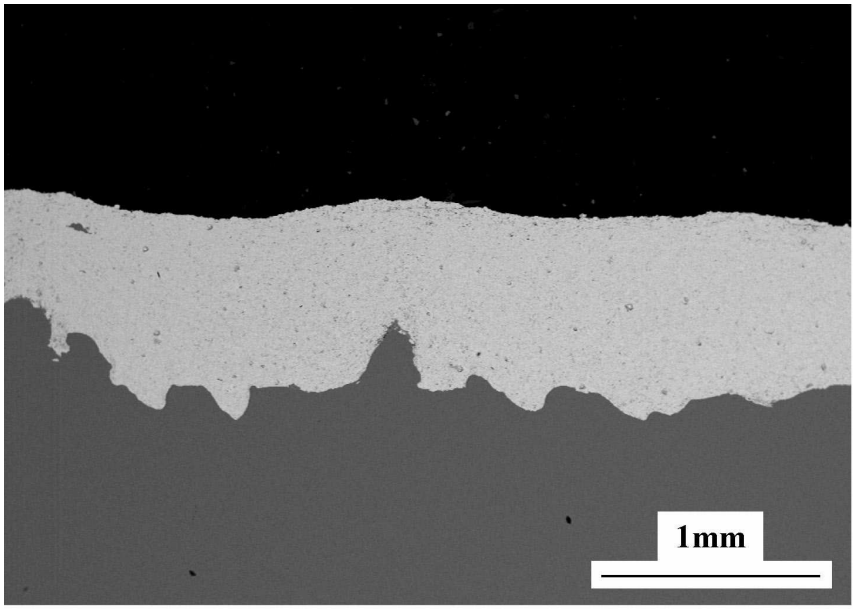

(a): Coating 158b, ∼1mm thick VPS W coating on surfi-sculpt substrate 9

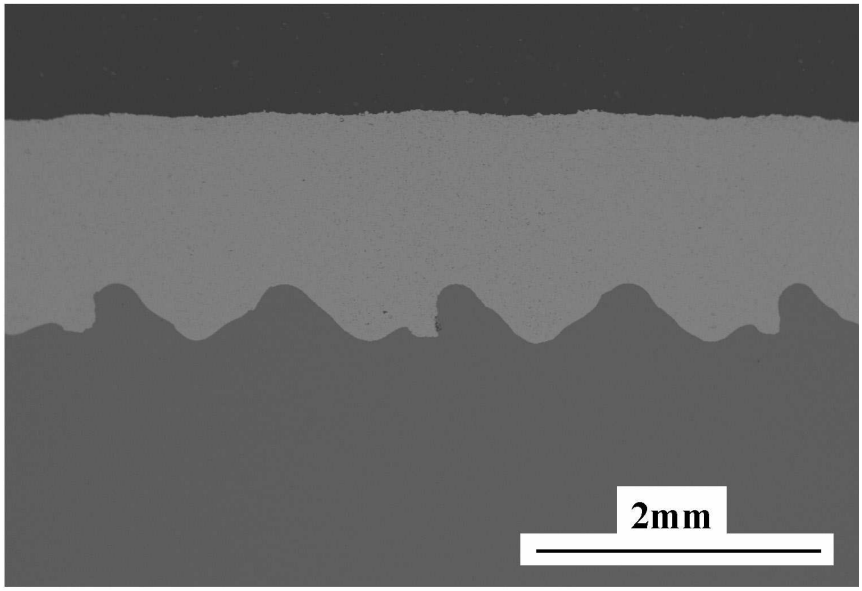

(b): Coating 164b, ∼2mm thick VPS W coating on surfi-sculpt substrate 9

Figure 4.30: Cross-sectional backscattered electron images of reactor-relevant thick VPS W coatings on 316L stainless steel surfi-sculpt substrates.

reduced to leave only data with a net confidence index (a measure of the degree of conformity of the local diffraction pattern to selected phases) of 0.5. This was achieved by: (a) increasing the number of points required before crystallographic orientation was assumed to change i.e. the number of scanning steps that must lie within a region for it to be defined as a grain, and (b) removing data-points that had an image quality or confidence index lower than a certain value. Figure 4.31 shows (a) a secondary electron image of coating 164b, (b) the corresponding orientation map with inset inverse pole figure, and (c) the corresponding image quality map. There was a sub-micron average grain size of 0.9μm suggesting rapid solidification of well-melted W powder particles. There was significant unassigned regions (black) due to either porosity or low confidence/quality of the data in some regions.

Three different regions are highlighted in Figures 4.31: (I) a region exhibiting a large number of columnar grains; (II) a pore in the W coating - interpreted as a agglomeration of partially/un-melted particles in Figure 4.31(b); and (III) several examples of agglomerations of partially/un-melted particles. Figure 4.31(b) and the inverse pole figure in Figure 4.32 suggested some preferential grain orientation in the (001) plane in the [111] direction (perpendicular to the substrate/coating interface).

In order to improve EBSD data electro-polishing was used but it proved difficult to find appropriate conditions that did not result in strongly preferential grain boundary attack. Figures 4.33 shows (a) a secondary electron image of a electro-polished region of coating 164b, (b) the corresponding EBSD orientation map with inset inverse pole figure, and (c) the corresponding image quality map. The orientation map contained large areas of data where image quality was too low to be useful. Other regions clearly showed the splat structure and the columnar grains within the splats, solidifying with [001] normal to the primary heat flow direction towards the substrate.

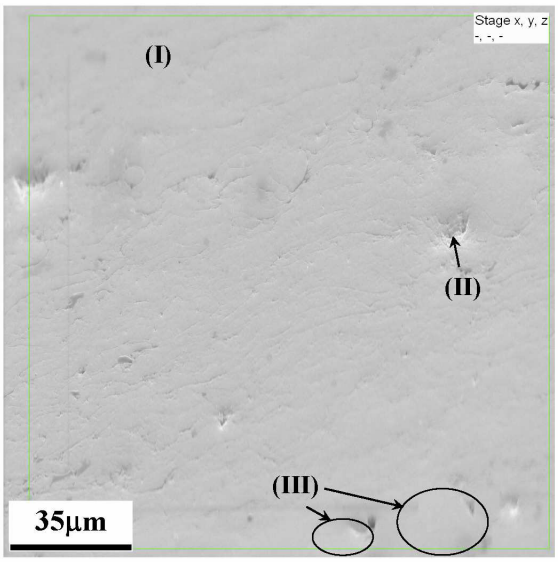

(a): Secondary electron image

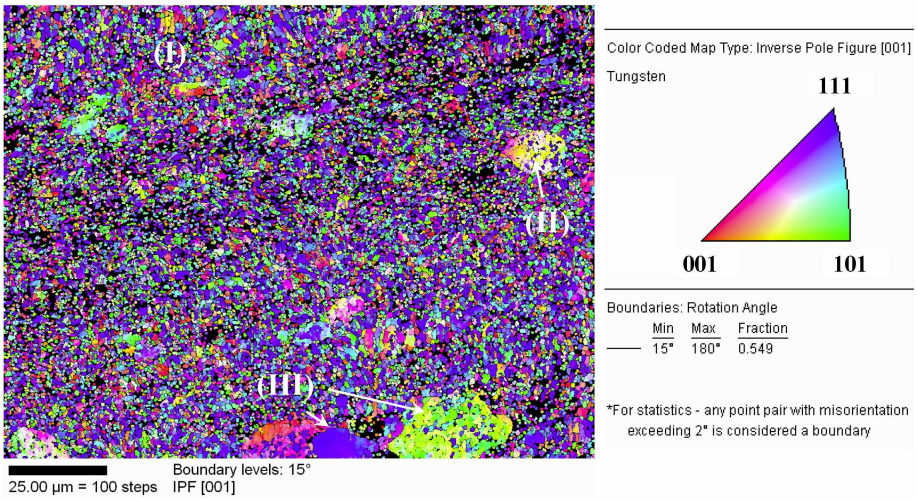

(b): Orientation map with inset inverse pole figure

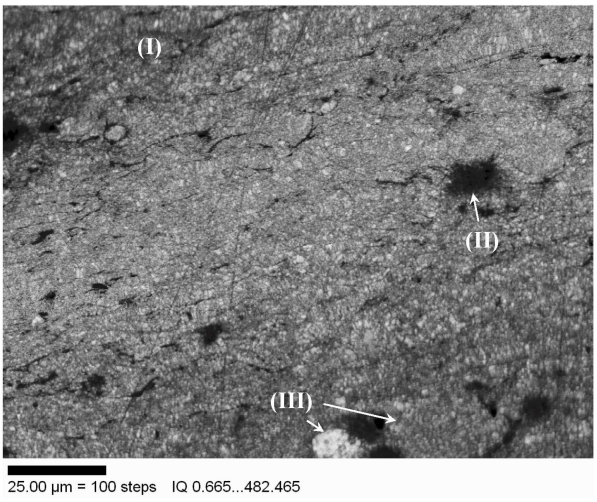

(c): Image quality map

Figure 4.31: EBSD analysis of VPS W in coating 164b.

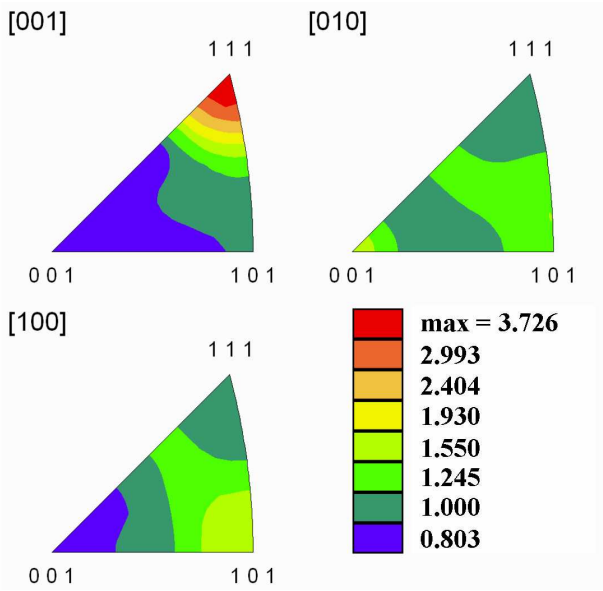

Figure 4.32: Inverse pole figure from EBSD analysis of VPS W in coating 164b - Figure 4.31(b).

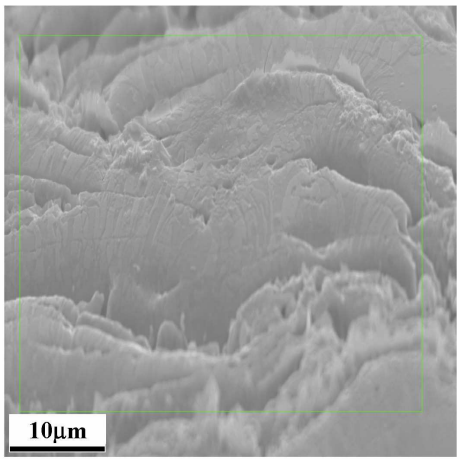

(a): Secondary electron image

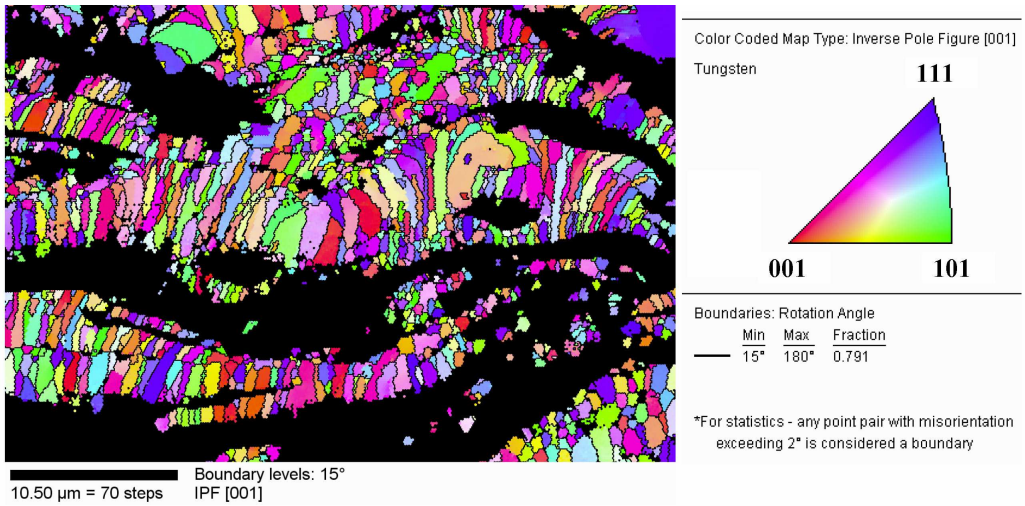

(b): Orientation map with inset inverse pole figure

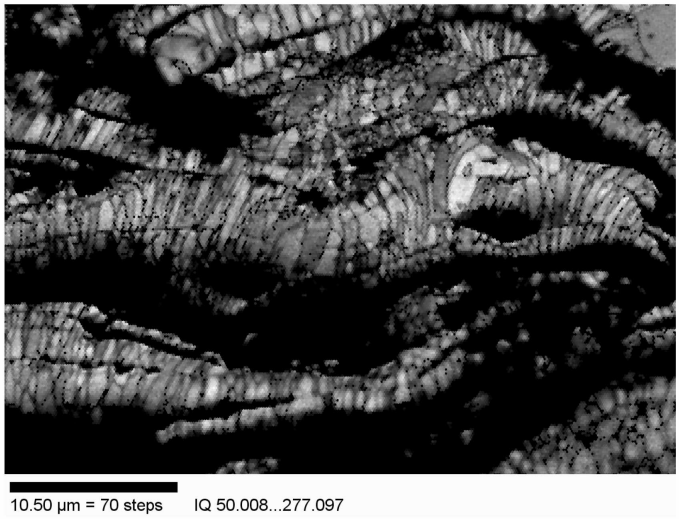

(c): Image quality map

Figure 4.33: EBSD analysis of electro-polished VPS W in coating 164b.

Chapter 5

Results - modelling

5.1 Introduction

The development of residual stresses within the graded and surfi-sculpt coatings during manufacture has been investigated using finite element analysis (FEA) in which different geometries are created, each with assigned material properties, divided up into discrete points via a mesh, given suitable boundary conditions and then subjected to a physical change, in this case a change in temperature equivalent to the recorded manufacturing thermal histories. If each of the points/nodes making up each discrete element of the mesh is assumed to be in equilibrium with its neighbors at the end of the physical change to the system then the deformation - and therefore, based on the material properties, the stress distribution - may be calculated [84]. Because thermally induced residual stresses were of primary interest the main equation governing the evolution of residual strains at particular points within the computational domains is [107]:

$$\varepsilon_{thermal} = \alpha_{vector} \left(T_{strain} - T_{strain-free} \right) \tag{5.1}$$

where

(1) $\varepsilon_{thermal}$ is the thermally induced strain and

$$\alpha_{vector} = \text{the CTE vector} = \begin{bmatrix} \epsilon_x \\ \epsilon_y \\ \epsilon_z \\ \gamma_{xy} \\ \gamma_{yz} \\ \gamma_{xz} \end{bmatrix}$$

and ϵ_a is the in-plane strain in the 'a' direction and γ_{ab} is the shear-strain component acting in the 'bc' plane in the b direction; (2) $T_{strain-free}$ is the strain-free manufacturing temperature; and (3) T_{strain} is the final strained temperature and taken here to be room temperature at 30^oC.

These thermal stresses were combined with the elastic and plastic strains arising from structural loads to give the total strain ε_{total} acting at a particular point within the computational domain [107]:

$$\varepsilon_{total} = \varepsilon_{elastic} + \varepsilon_{plastic} + \varepsilon_{thermal} \tag{5.2}$$

In a linear elastic system, the stress acting at a particular point arises out of the constitutive relation below [107] (the sign convention is slightly different to that in Equation 5.2, which was only designed to highlight the additive nature of residual strains):

$$\sigma = D\varepsilon_{element} + \sigma_0 = D\left(\varepsilon - \varepsilon_{thermal} - \varepsilon_0\right) + \sigma_0 \tag{5.3}$$

where

(1) σ is the stress at a particular point, composed of:

$$\sigma = \begin{bmatrix} \sigma_x \\ \sigma_y \\ \sigma_z \\ \tau_{xy} \\ \tau_{yz} \\ \tau_{xz} \end{bmatrix}$$

and σ_a is the in-plane stress in the 'a' direction and τ_{ab} is the shear-stress component acting in the 'bc' plane in the b direction;

(2) D is the 6×6 elasticity matrix, which for an isotropic material (the only type considered in this project) is:

$$D = \frac{E}{(1+\nu)(1-2\nu)} \begin{bmatrix} 1-\nu & \nu & \nu & 0 & 0 & 0 \\ \nu & 1-\nu & \nu & 0 & 0 & 0 \\ \nu & \nu & 1-\nu & 0 & 0 & 0 \\ 0 & 0 & 0 & \frac{1-2\nu}{2} & 0 & 0 \\ 0 & 0 & 0 & 0 & \frac{1-2\nu}{2} & 0 \\ 0 & 0 & 0 & 0 & 0 & \frac{1-2\nu}{2} \end{bmatrix}$$

and E is the Young's modulus and ν is the Poisson's ratio;

(3) σ_0 is the initial stress at a particular point; and

(4) ε_0 is the initial strain at a particular point.

In the case of plastic deformation, Equation 5.3 was modified to include the plastic strain, $\varepsilon_{plastic}$:

$$\sigma = D\varepsilon_{element} + \sigma_0 = D\left(\varepsilon - \varepsilon_{plastic} - \varepsilon_{thermal} - \varepsilon_0\right) + \sigma_0 \tag{5.4}$$

Additionally, where plastic deformation was required, an isotropic elastic-plastic hardening model e.g.

isotropic plastic overstrain after the yield point was reached, resulting in the new yield point lying at the peak stress achieved, was implemented based around the use of a von Mises yield surface [84].

The equations outlined in Equations 5.1 to 5.4 were implemented in Comsol Multiphysics^{TM}, which is a commercial finite element (FE) software package. Its principal attraction lay in the in-built partial differential equations, interface and FE solver. Where further complexity was required, Comsol Multiphysics was combined with MatLab^{TM} to allow for code-line control of model parameters. Linear solvers were used for all elastic models and a non-linear solver was used for an elastic-plastic model. All models were solved via implementation of the Principal of Virtual Work which states that the sum of virtual work from internal strains is equal to the work done by externally applied loads e.g. the change in total stored energy both internally and externally following a particular operation will be zero i.e. $\delta W=0$.

All models considered conditions of plane stress - a 2D (x and y directions) system with a finite depth in the z-plane. The alternative approach of plane strain deals with 2D situations where the computational domain is assumed to be infinite is the z-plane. Plane strain is equivalent to plane stress, except that the Poisson effect is taken into account and the Young's modulus E replaced by the effective Young's modulus, $E'=E/(1-\nu)$ [71]. While at first the approach of plane strain seems more appropriate, the use of plane stress was chosen because plane strain is more applicable to systems where the z domain length is much larger than the x and y domain size. This is not the case for the modelled coatings, where x, y, z dimensions were comparable. The plane stress assumption gives $\sigma_z = 0$ [107]. As a starting point to understanding how stresses evolve in graded and surfi-sculpt coatings and with regards to generating a good approximation of the x-y plane stresses generated, this is assumed to be a reasonable approximation, and has been applied widely in the literature e.g. [82] and [83].

5.2 Quenching stresses

Section 5.1 described a major contribution to residual stresses in multi-layer systems as the mismatch in coefficient of thermal expansion between a substrate and a coating. However Kuroda and Clyne

[108] highlighted the potential importance of the splat-scale 'quenching stress' in sprayed coatings. As discussed in Section 2.6.1, this arises from contraction of a molten splat itself (rather than the whole coating) on deposition as it rapidly cools to the temperature of the substrate/underlying material. Assuming adherence to the substrate, the splat will be constrained from contracting as it cools to its 'natural' extent and internal tensile stresses will be established. The maximum quenching stress for a splat can be estimated by [108]:

$$\sigma_q = \alpha_d \Delta T E_0 \tag{5.5}$$

where σ_q is the quenching stress, α_d is the coefficient of thermal expansion of the splat - $\sim 4.5 \times 10^{-6} \mathrm{K}^{-1}$ for W [18], ΔT is the melting temperature of the splat minus the substrate temperature e.g. $\sim$3200K for W where T_{melt}=3695K [18], and E_0 is the bulk value of the Young's modulus for the deposit material assumed to be 410GPa for W [18].

From Equation 5.5, assuming a temperature change of 120^oC (150 to 30^oC) on post-deposition cool-down and a Young's modulus and CTE of 205GPa and $12.3 \times 10^{-6} \mathrm{K}^{-1}$ respectively for steel, the likely elastic thermal residual stresses arising out of CTE mismatch caused by depositing W on steel is $\sim$190MPa, whereas σ_q for W would be significantly greater at $\sim$6GPa. However, experimental studies investigating curvature of as-sprayed metal coatings on same-material substrates where there was no CTE mismatch effect have shown quenching stresses were 10-60MPa [56, 71, 77, 81, 108], because: at the edges of coatings the splat profile is likely to be curved (it debonds at the periphery) resulting in a reduction in the local quenching stress; since sprayed coatings typically exhibit a significant proportion of partially/un-melted particles, these particles will not generate a quenching stress; micro-cracking and sliding occurs between splats/un-melted particles and releases strain energy and; there may be internal yielding within the splats.

Kuroda and Clyne [108] used the model of Tsui and Clyne [71, 77, 81] to study sprayed Mo, data exploited by You and Lindig [56] to predict residual stress distributions in a W/steel bi-layer system. Quenching stresses of 35-65MPa were inferred for W [56] based on results for Mo [108] at a substrate temperature >300^oC. Therefore, in the case of the coatings manufactured in this project, quenching

stresses were likely to be <30MPa since substrate temperatures were much lower at ∼150^{o}C. Overall, the magnitude of microscopic quenching stresses was likely to be significantly less than that arising from the macroscopic CTE difference between the substrate and coating, and similarly to others [56, 71, 77, 81, 82, 108, 109], quenching stresses have been assumed negligibly small in the modelling studies here.

5.3 Material properties

Calculation of residual stresses in graded and surfi-sculpt structures required appropriate material properties. Key material properties were the elastic constants and the coefficients of thermal expansion, plus thermophysical properties such as thermal conductivity and specific heat capacity when through-thickness thermal gradients were considered. Both literature values and average measured values obtained by nano-indentation were used. Since temperature changes were reasonably low, room temperature properties were assumed at all temperatures.

Elastic moduli were established using nano-indentation for VPS W, Diamalloy, mild steel and 316L stainless steel, and checked against the literature for the VPS W and mild steel, and were found to be in good agreement. Other properties were assumed from the literature, with the properties of mild steel and Diamalloy taken as those of AISI 4340, built-in to Comsol Multiphysics and which in general lay midway between those of mild steel and 316L [110]. Literature values for the CTE of the sprayed materials was used since thermal expansion is not influenced by pores etc in as-sprayed coatings [108]. The material properties used are summarised in Table 5.1. It is recognised that if accurate predictions are required, greater effort would be needed to obtain all thermophysical data by experiment. However, the motivation for the modelling here was qualitative, rather than prediction. In Chapter 6, some attempt at comparing measured and experimental stresses is undertaken, but is intended only for initial comparison.

Material property	**W [17, 18, 55, 106]**	**Diamalloy**[1]	**Mild steel [110]**	**316L [110]**
Coefficient of thermal expansion (K^{-1})	4.5×10^{-6}	12.3×10^{-6}	12.3×10^{-6}	15.9×10^{-6}
Density, ρ (kg m^{-3})	19350	7850	7850	8000
Isotropic hardening gradient (MPa)	100[2]	12.4	7.8	12.4
Poissons ratio, ν	0.28	0.28	0.28	0.30
Specific heat capacity, C (J kg^{-1} K^{-1})	132	475	475	500
Thermal conductivity, k (W m^{-1} K^{-1})	174	44.5	44.5	16.2 *(annealed)*
Yield stress (MPa)	400	472	205	472
Young's modulus, E E (GPa)	194[3]	144[3]	210[3]	228[3]

[1]all properties except Yield stress and Young's modulus were based on those of mild steel from [110] as little data existed in the literature. Yield stress arbitrarily taken from [110] for 316L in order to provide sufficient contrast to the Yield stresses for W and mild steel in the qualitative elastic-plastic model (see later). Young's modulus from nano-indentation.
[2]a nominal hardening gradient value was assumed as little data existed in the literature and this was chosen to be sufficiently different to the elastic modulus and hardening gradients of other materials to allow the W/steel effects to be distinguished (see later).
[3]measured properties, via nano-indentation.

Table 5.1: Material properties used for FEA analysis.

Substrate/coating system	Description
bi-layer	planar W coating on mild steel
inter-layer	50:50 W/steel inter-layer plus W upper coating on mild steel
5-layer linear graded coating	0%, 25%, 50%, 75% and 100% W layers (rest steel) on a mild steel substrate
11-layer linear graded coating	0% to 100% W layers, in 10% steps (rest steel) on a mild steel substrate
11-layer parabolic graded coating	0% to 100% W layers → fractional W content of nth graded layer = (n-1)^2, rest mild steel

Table 5.2: Graded architectures used in FE models to investigate post-manufacture residual stress distributions.

5.3.1 Graded coating interlayers

The thermophysical properties of the different graded layers, each comprised of different proportions of W and steel, were defined by the simple 'rule-of-mixtures' approach shown in Equation 5.6 used to determine relative graded coating compositional fractions during manufacture both here and elsewhere [82, 83]:

$$Property = \left(\frac{vol.W}{100}\right) \times property(100\%W) + \left(1 - \frac{vol.W}{100}\right) \times property(100\%Steel) \tag{5.6}$$

5.4 Graded coating models

Up to five different graded architectures, representative of both manufactured and potentially beneficial architectures, have been investigated using a variety of different 2D FE models - as summarised in Table 5.2.

5.4.1 No bending moments

The first graded coating models employed boundary conditions that eliminated bending moments, as shown in Figure 5.1. While not representative of experimental as-sprayed systems, during model development, this maintained simplicity. The effects of bending were then introduced.

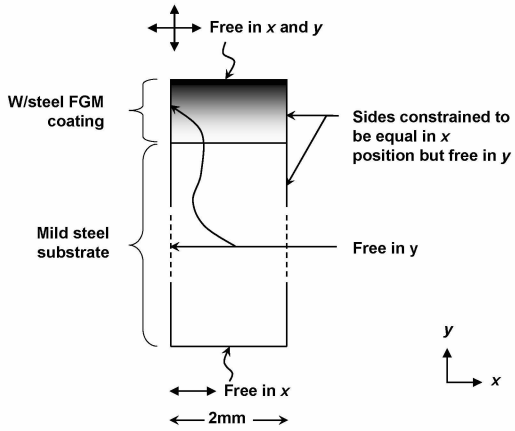

Figure 5.1: Generic FE model setup/boundary conditions for graded systems with no bending-moments.

Graded coating arrange-ment	**No. of graded layers (n_{max})**	**%age W of the n^{th} discrete layer**	**Discrete layer thickness (mm)**	**Total graded inter-layer + W coating thickness (mm)**	**Substrate thickness (mm)**
bi-layer	1	100n	0.25	0.25	5
50:50 interlayer	2	50n	0.167	0.5	4.75
5-layer linear	5	25(n-1)	0.1	0.5	4.75
11-layer linear	11	10(n-1)	0.046	0.5	4.75
11-layer parabolic	11	$(n-1)^2$	0.065	0.714	4.54

Table 5.3: W fraction for graded coatings in the FE models.

The lack of bending moments implied that FE models were effectively 1D simulations, but projected in the x-plane (with no variation of stresses in the y-plane in the graded case). Consequently, a nominal 2mm width was used, sufficient for easy visual analysis. Because the residual stresses were directly proportional to the relative W/steel fractions, the thickness of the individual substrate/graded layers was chosen for each graded architecture so that the total volume (area.%) of the W was normalised to a constant 0.25mm^2, with 5mm^2 of steel (a combination of the mild steel substrate and Diamalloy in the graded layers) as shown in Table 5.3. It was felt that W fraction normalisation, rather than keeping the coating thickness constant as in all previous studies e.g. [71, 77, 81, 82, 83], would allow a clearer insight into the effect of grading architecture.

Typical arrangements for the bi-layer, 5-layer and 11-layer linear systems are illustrated in Figures 5.2(a) to (c) respectively, and a typical calculated x-plane stress distribution for the 11-layer linear system, following an elastic 150 to 30^{o}C temperature change is shown in Figure 5.3. For this temperature condition, the model type is referred to hereafter as 'isothermal', which means there were no temperature gradients and no heat flow in the coating/substrate arrangement. Therefore these calculations were time independent. Non-isothermal cases are considered later. Figure 5.3 shows that a lack of bending moments led to a uniform stress distribution within each layer (subdomain). Effectively this is a 1D model, however, 2D structures were used because subsequent introduction of a non-planar substrate/coating interface e.g. surfi-sculpt, or alternatively bending-moments, was required that would result in stress distributions which were non-uniform in the x and y-planes. The coating stresses in the upper graded layers were compressive while the stress in the substrate was tensile, because the CTE of the steel substrate was higher than that of W, meaning that during the modeled temperature

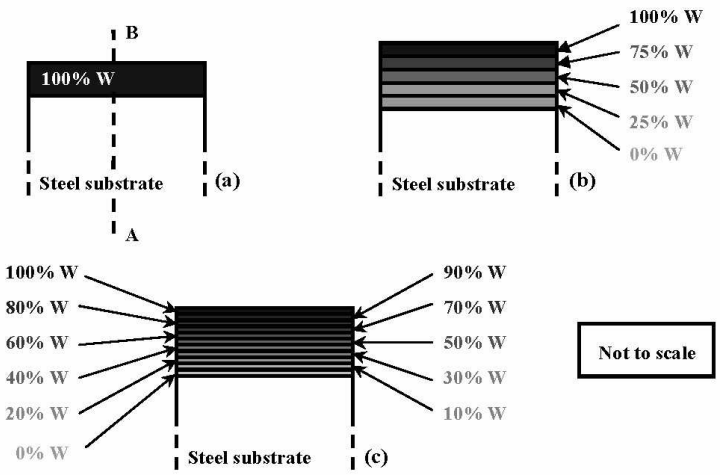

Figure 5.2: Schematics illustrating the structures of various graded coating FEA arrangements; (a) bi-layer, (b) 5-layer, and (c) 11-layer linear.

reduction the steel coating tried to contract more than the W but was restrained, resulting in tension. Conversely, the lower CTE of the W-rich graded layers resulted in them becoming compressed. Peak stresses in the W coating were -174MPa, ∼225MPa below the likely yield stress for bulk W in Table 5.1 implying the system remained entirely elastic under these conditions.

The σ_x, $\sigma_{vonMises}$ and stored elastic strain energy distributions across the five different W/steel architectures considered along the line A-B in Figure 5.2(a) are shown in Figures 5.4(a) to (c) respectively (σ_y is not included as there were no bending-moments). In order to facilitate comparison with later models incorporating larger computational domains, the stored strain energy magnitudes were scaled to represent a computational domain of 20mm rather than 2mm width. Figures 5.4(a) and (b) show similar patterns, although with opposite stress signs because the von Mises stress is related to the principal stresses by:

$$\sigma_{vonMises} = \sqrt{\sigma_1^2 + \sigma_2^2 + \sigma_1\sigma_2} \tag{5.7}$$

where σ_1 and σ_2 are the principal stresses in the x and y-planes respectively [84].

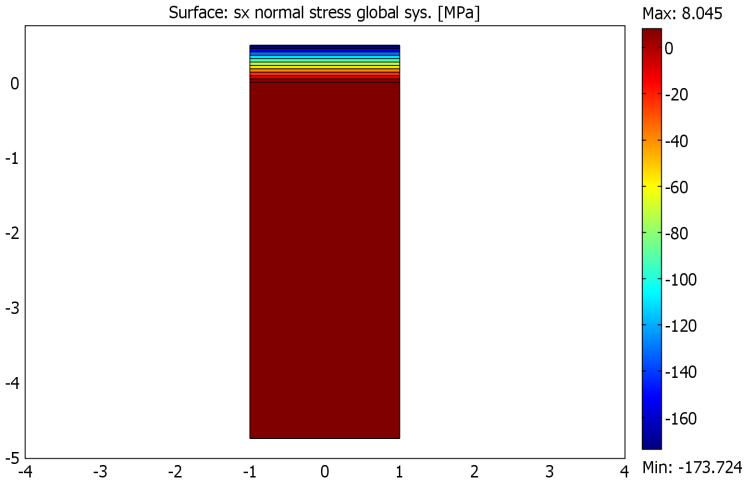

Figure 5.3: σ_x distribution, 11-layer linear graded coating FE system with no bending-moments and ΔT = 150 to 30^{o}C.

From Equation 5.7 and Figure 5.1(b), as σ_y is essentially zero, $\sigma_{von-Mises} \sim \sqrt{\sigma_x^2} = \mid \sigma_x \mid$.

The peak stresses experienced in the substrate and upper W layer for all five architectures shown in Figures 5.4(a) and (b) was identical due to normalisation of the W/steel volume fraction and the elastic only model. There was a reduction in the magnitude of the stress discontinuity across all interfaces and particularly the substrate/coating (bi-layer) and bond coat/1^{st} W rich layer (graded coatings) interfaces as the degree of W grading increased. The concept of increasing the degree of grading may be generalised to imply movement of the point of highest W fraction further from the substrate/coating interface (by which definition the 11-layer parabolic coating had the greatest effect).

Figure 5.4(c) shows the effect of increasing the degree of grading on the magnitude of stored elastic strain energy in the 1^{st} W rich layer, calculated by integrating the stored strain energy density (Jm^{-2}) across each subdomain. Stored strain energy density W is defined as:

$$W = \frac{1}{2}t\left[\varepsilon_x\sigma_x + \varepsilon_y\sigma_y + \varepsilon_{xy}\sigma_{xy}\right] = \frac{1}{2}t\left[\frac{\sigma_x^2}{E} + \frac{\sigma_y^2}{E} + \frac{\sigma_{xy}^2}{G}\right] \tag{5.8}$$

where t is the thickness (=1 for plane-stress), E is the Young's modulus and G is the shear modulus of the subdomain in question.

The magnitude of the stored elastic strain energy in Figure 5.4(c) was a function of the size of the computational (integrating) domain. Therefore reduced energies resulted from reduced layer thicknesses with increased grading (Table 5.3). However, this reduction was greater than that of layer thickness itself due to W/steel fraction normalisation. As cracks will initiate once the magnitude of the stored strain energy is greater than the interfacial bond strength [47], any reduction in stored strain energy between different layers will decrease the probability of crack formation/coating failure. Figure 5.4(c) shows that the introduction of a bond coat and any form of grading reduced the magnitude of the stored elastic strain energy between any adjacent layers. As the degree of grading was increased the magnitude of stored strain energy in any particular layer decreased. Overall, introducing finer degrees of grading led to a re-distribution of stored elastic strain energy across a larger volume fraction of material. The total (substrate + coating) stored elastic strain energy for all five architectures is shown in Figure 5.5 - as with Figure 5.4(c) and in order to allow comparison with later models, the energy

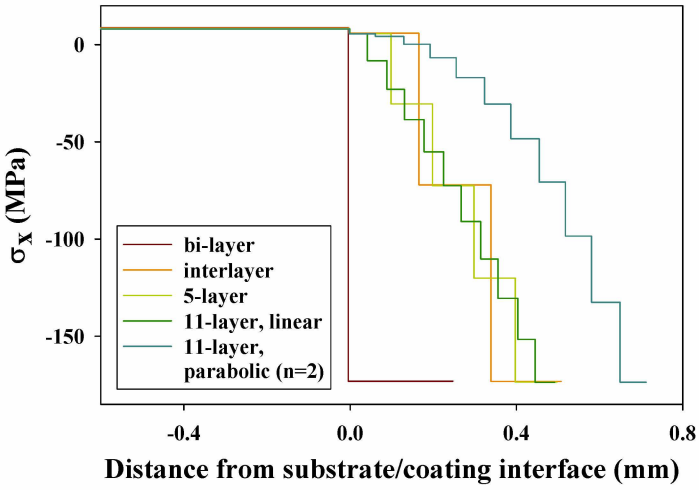

(a): Variation of σ_x with position

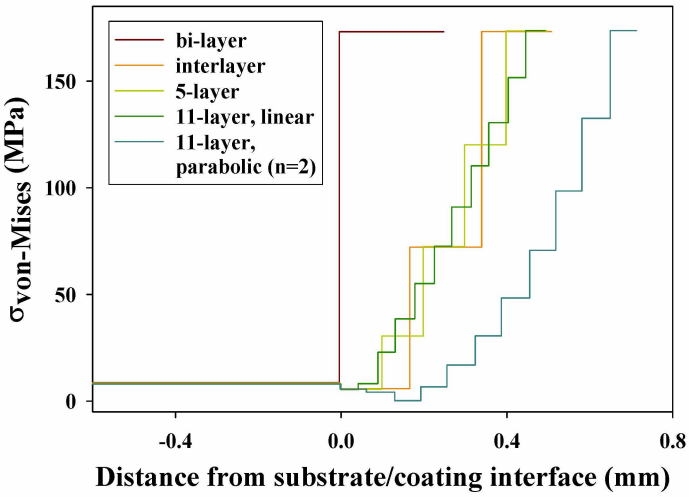

(b): Variation of $\sigma_{vonMises}$ with position

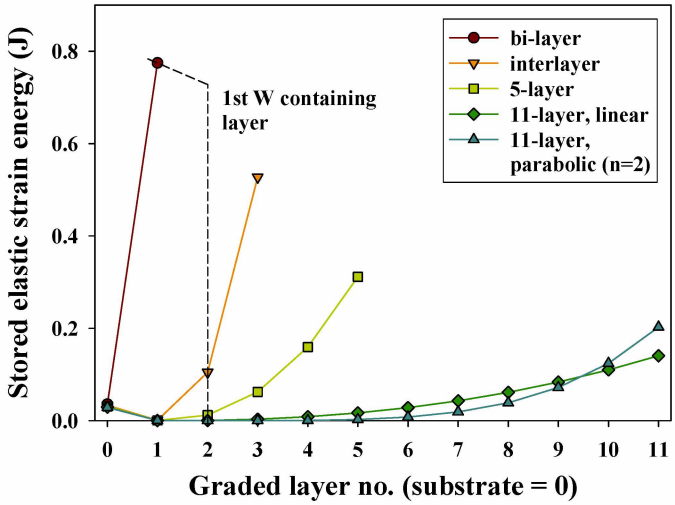

(c): Variation of stored elastic strain energy with graded layer number (scaled to represent a 20mm wide computational domain)

Figure 5.4: Stress/stored elastic strain energy distributions along the line A-B in Figure 5.2 for various graded coatings with no bending moments following an elastic 150 to 30°C temperature transition.

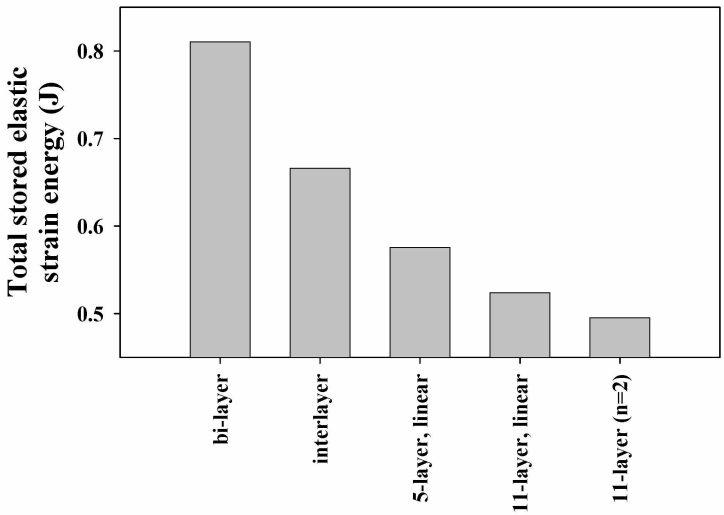

Figure 5.5: Total (substrate + coating) stored elastic strain energy for different graded coating architectures following an isothermal 150 to 30^{o}C temperature change (scaled to represent a 20mm wide computational domain).

was again scaled to represent a computational domain of 20mm width. Total stored strain energy in the coating decreased with increasing compositional gradient, implying a reduction in the probability of subsequent coating delamination as W concentration was 'moved' further from the dissimilar steel towards the upper surface of the coating. The reduced step-change in stress between successive interlayers visible in Figures 5.4(a) and (b) for σ_x and $\sigma_{vonMises}$ respectively as the degree of gradation increased was linked to this effect. Because the magnitude of stress that developed in a particular layer directly affected the resulting residual stress in adjacent layers, this reduction in stress resulted in a decrease in residual stress in the adjacent layers. The cumulative effect was a combination of the redistribution of residual stresses already highlighted and the reduction in the total stored strain energy in the coating illustrated in Figure 5.5.

Layer addition and plasticity

While initial elastic only calculations suggested that stresses that developed during manufacture were unlikely to reach the W or steel yield stress - because the porous W had a low as measured modulus - it was still of interest to investigate the effects of any material plasticity (or stress-relieving mechanisms). Therefore an elastic-plastic model for a 5-layer graded system using plastic properties (yield stress and isotropic hardening gradient) one quarter of those in Table 5.1 was considered. This reduction in the

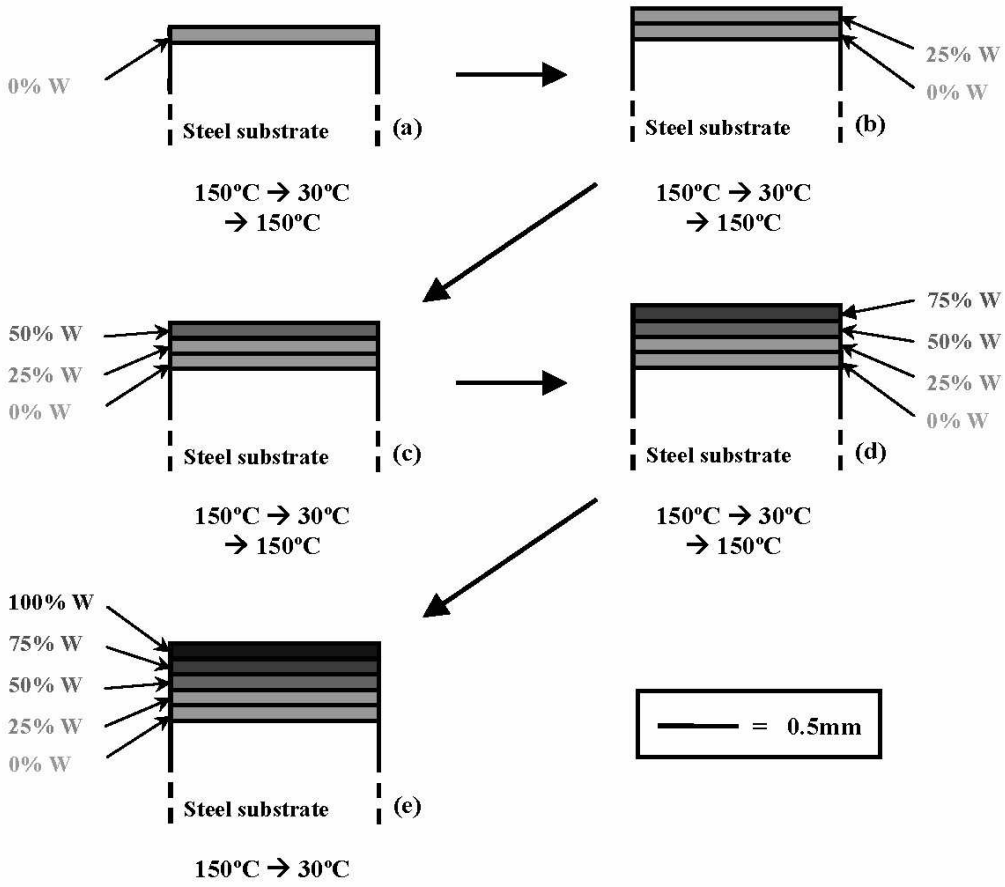

Figure 5.6: Schematic illustration of the basis behind the layer-addition elastic-plastic FEA model.

yield stress was chosen entirely arbitrarily to ensure that at least within the upper W-rich layers, the yield stress would be exceeded since the effect of plasticity in a generic way was of interest.

A multi-layered model (again, for simplicity, with boundary conditions based on those in Figure 5.1 e.g. excluding bending moments) was constructed in which the five graded layers were activated sequentially following a 150 to 30 to 150^{o}C isothermal temperature change, as shown in Figure 5.6. This arrangement was intended to mimic simply the real spraying process where layers were added in groups of passes as shown in Chapter 4. This model allowed for the plastic behaviour of material following the deposition of individual layers - any residual stresses from one cycle were introduced into that layer as an initial condition for the next.

The resultant σ_x stress distribution is shown in Figure 5.7(a), while the variation of σ_x over all five cycles at these sampling points are plotted as a function of dimensionless time used to step the model

forward in Figure 5.7(b).

Over cycles 1-3, all layers behaved elastically. However, in cycles 4 and 5 the 75%W (0,0.35) and upper 100%W (0,0.45) layers underwent yield at the artificially reduced yield stress of 104MPa and then strain hardening, with the reduced strain gradients of 8.6MPa and 25MPa respectively. A net tensile residual stress of ∼20MPa resulted in the 75% W layer at the end of the 4^{th}/beginning of the 5^{th} cycles of deposition. The effects of this strain hardening are shown in Figure 5.8 that shows the residual stress distribution along the line C-D in Figure 5.7(a). Essentially the net tensile plastic residual stresses in the upper two layers led to a reduction in residual compressive stress in the upper two layers from the 5-layer elastic case (included for comparison).

5.4.2 Bending moments

Bending moments meant that y-plane stresses were no longer zero and the computational domain could distort non-orthogonally. The computational domain was expanded to a width of 20mm, representative of the width of the standard samples used during graded coating manufacture and the relative proportions of W and steel were re-normalised to 2.5mm^2 and 100mm^2 respectively, again for the five different graded architectures in Table 5.2. The boundary conditions employed, together with information on data sampling positions and calculated σ_x (half the computational domain only) and σ_{xy} stress distributions for the 5-layer case are shown in Figure 5.9.

Figure 5.9 shows that the introduction of bending moments resulted in a non-zero shear stress σ_{xy}. However, it remained relatively small compared with the peak σ_x stress and was therefore neglected (although contributing to the $\sigma_{vonMises}$ stress distribution via the principal stresses). Stress distributions were investigated along the lines x=1 and x=10 in Figure 5.9, reflecting edge effects and the central position within the computational domain respectively. As indicated in the upper image, the only boundary condition was constraint of the lower surface of the computational domain in the y-plane, which was judged the best (but still not ideal) representation of the real manufacturing boundary conditions shown in Figure 5.10 in which the base of the substrate was held against the substrate holder by retention bolts.

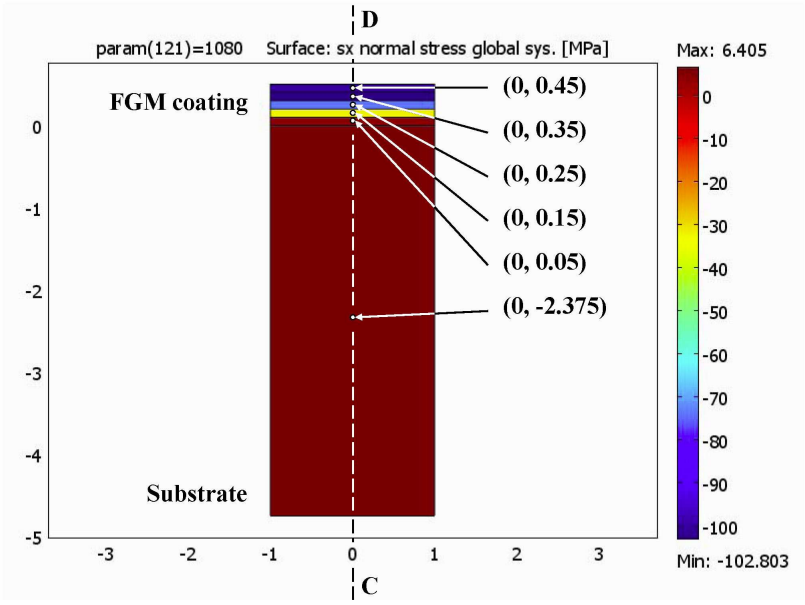

(a): Final σ_x distribution plus sampling positions

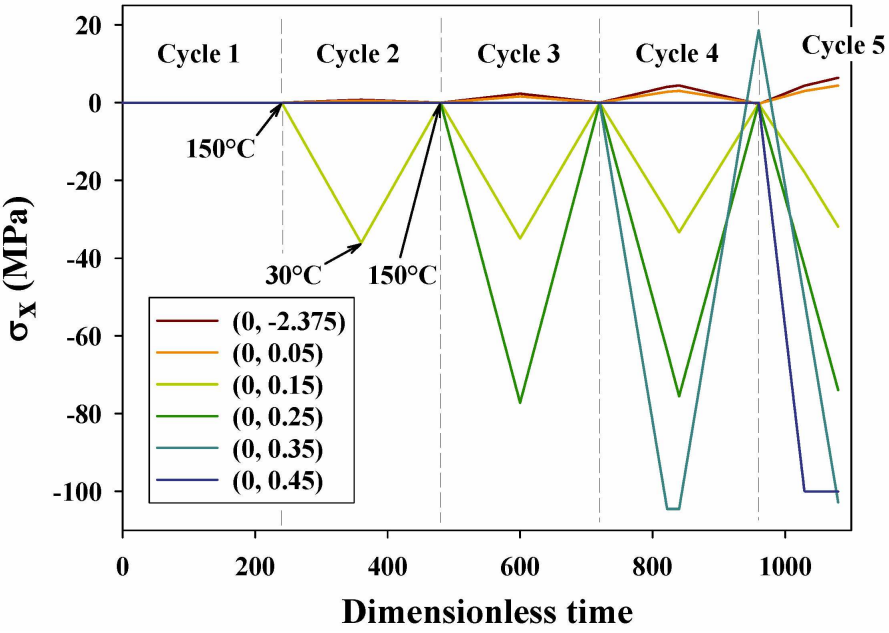

(b): Variation of σ_x over all 5 cycles at the sampling points in Figure 5.7(a)

Figure 5.7: σ_x distribution and sampling positions, 5-layer elastic-plastic multi-layer graded coating FE model.

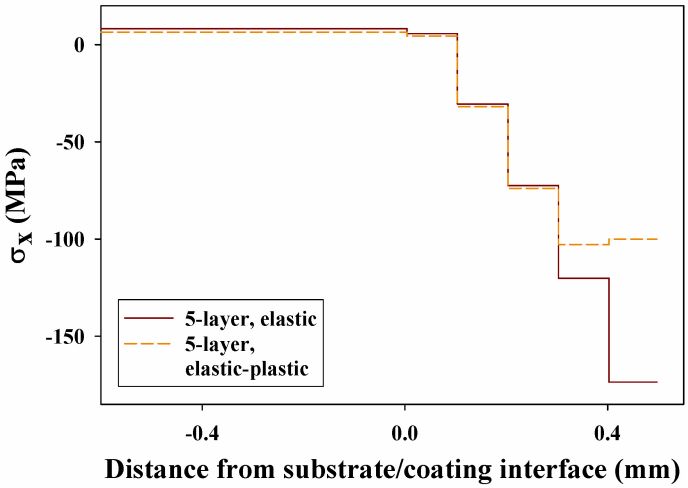

Figure 5.8: Comparison of variation of σ_x with position across 5-layer linearly graded coatings using elastic and elastic-plastic material models.

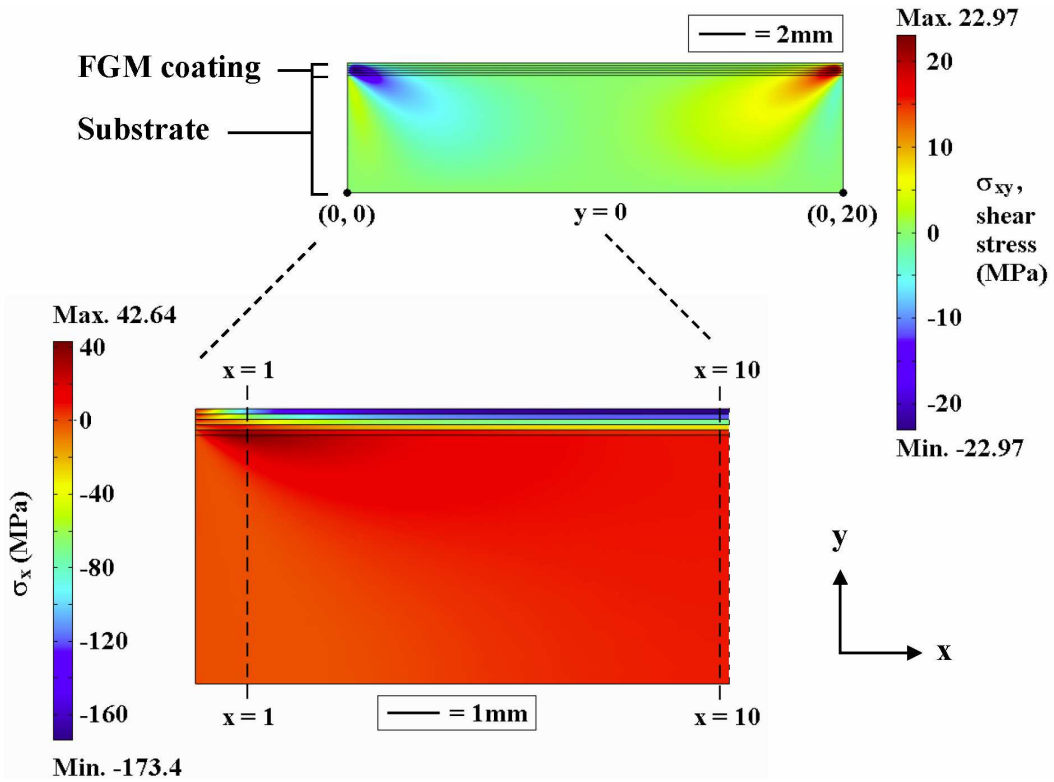

Figure 5.9: Boundary conditions and data sampling points for the bending moment 2D 5-layer graded coating FE model.

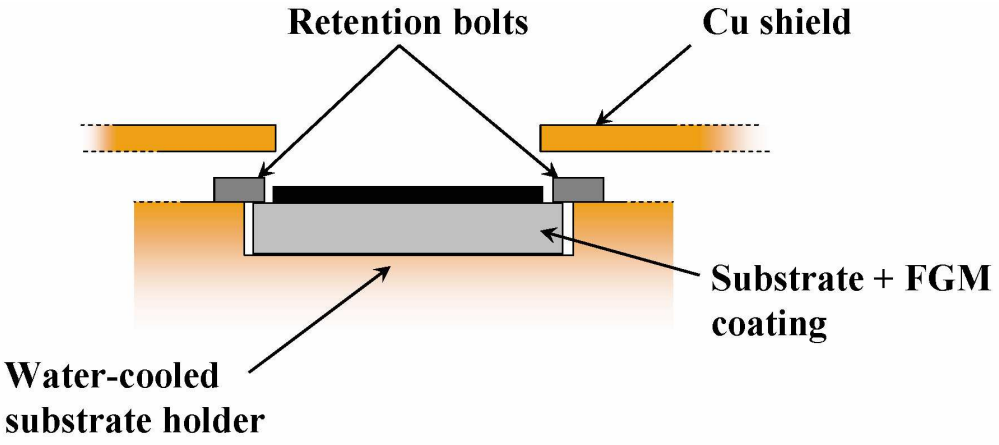

Figure 5.10: Schematic illustrating the methodology of graded coating substrate retention during manufacture.

The variations in different types of stress along the lines x=1 and x=10 in Figure 5.9, along with the change in stored elastic strain energy in the different graded layers and the variation in total stored elastic strain energy with graded architecture, are shown in Figures 5.11 to 5.13.

Along the computational domain edge (x=1) bending moments led to an increase in peak stress intensity as the substrate/bond coat interface was approached, as opposed to the uniform distribution without bending moments (Figures 5.4(a) to (c)). Again, there was a reduction in the step-change in residual stress between successive graded interlayers with increasing compositional grading. As compared with the no bending moment case, peak stresses within the W-rich coatings were no longer equal in each of Figures 5.11(a) to (c), with the peak stresses both at the substrate/coating interface (tensile) and the base of the upper layer (compressive) much larger for the bi-layer system than the graded coatings. This re-distribution of residual stresses was attributed to lower induced bending as the compositional grading increased, due to a closer CTE match between adjacent graded layers. This effect was illustrated further by a reduction in total stored elastic strain energy as the degree of grading increased. Total stored elastic strain energy calculated by integrating stored strain energy density across all subdomains is shown in Figure 5.13(b). As noted when no bending moments were present in Figure 5.5, increased compositional grading led to a decrease in net coating stored elastic strain energy within the graded systems and therefore a corresponding decrease in the likelihood of coating failure. Overall, the magnitude of the stored elastic strain energy was reduced for all architectures considered compared to the isothermal case (which was scaled to represent a similar 20mm wide computational domain). For example, comparing Figures 5.5 and 5.13(b) in the bi-layer case, the introduction of bending moments reduces the total (coating plus substrate) stored elastic strain energy from 0.81J to 0.72J. Similar reductions occurred for the other coatings and were attributed to the lower residual stresses that develop away from the centre of the computational domain due to allowed bending - thereby reducing total stored elastic strain energy. Further evidence of the beneficial effects of introducing a graded architecture is seen in Figure 5.13(a), with the reduction in stored (elastic) strain energy within the first W containing layer which would also decrease the likelihood of subsequent coating delamination/failure. Overall, Figures 5.12(a) to (c) show equivalence to the no bending moment cases in Figures 5.4(a) to (c), and the same general conclusions apply regarding the effects of grading.

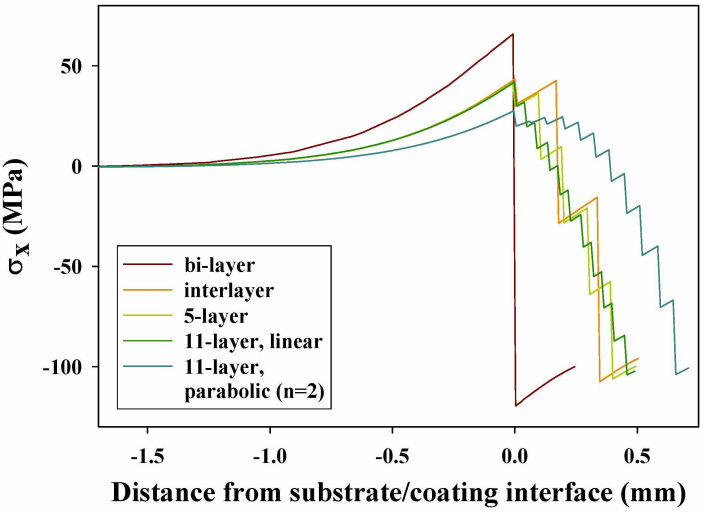

(a): Variation of σ_x with position

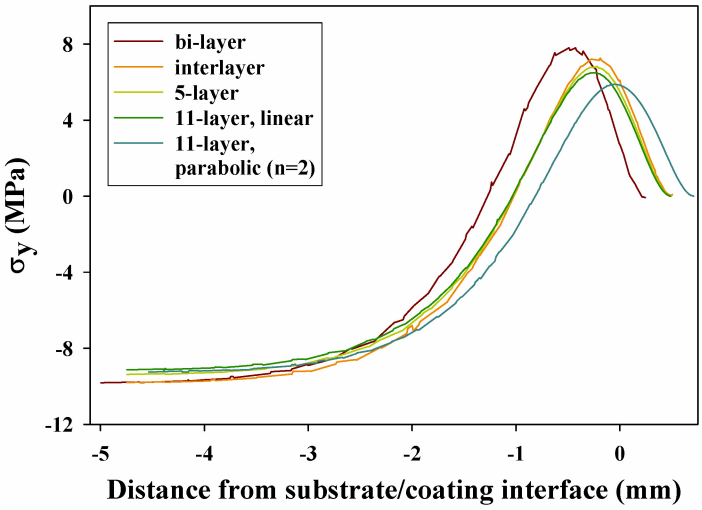

(b): Variation of σ_y with position

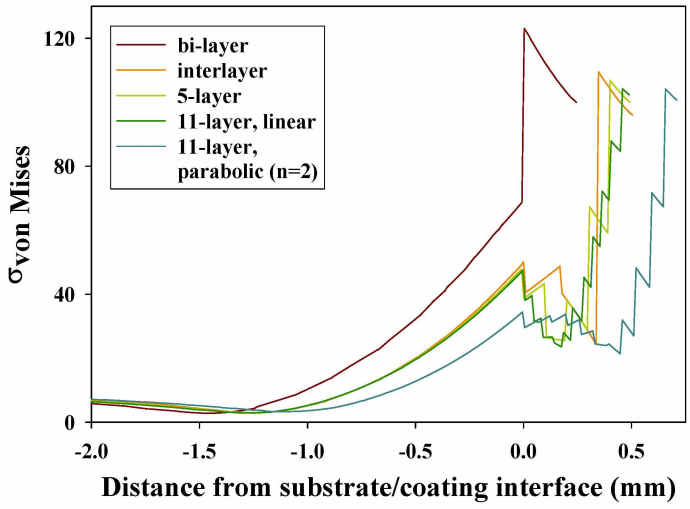

(c): Variation of $\sigma_{vonMises}$ with position

Figure 5.11: Stress distributions along the line x=1 in Figure 5.9 for various FE models of graded coating pinned along the bottom edge following an isothermal elastic 150 to 30^{o}C temperature transition.

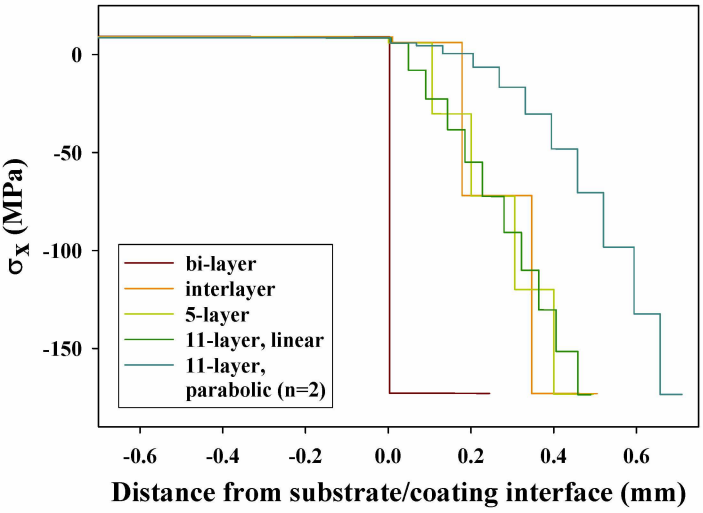

(a): Variation of σ_x with position

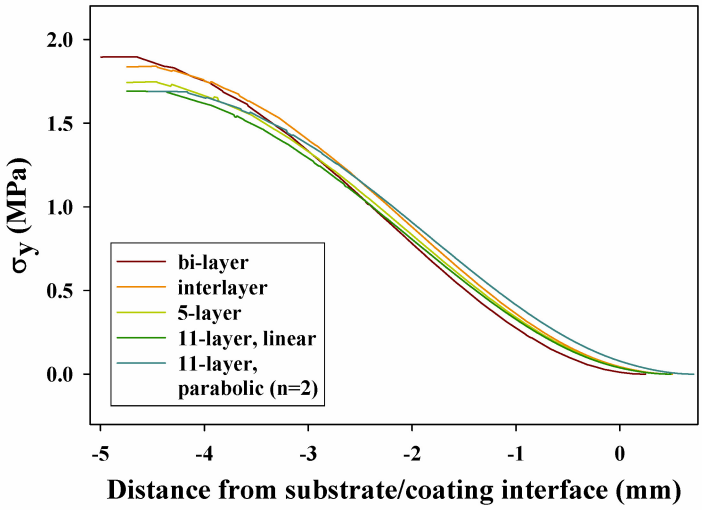

(b): Variation of σ_y with position

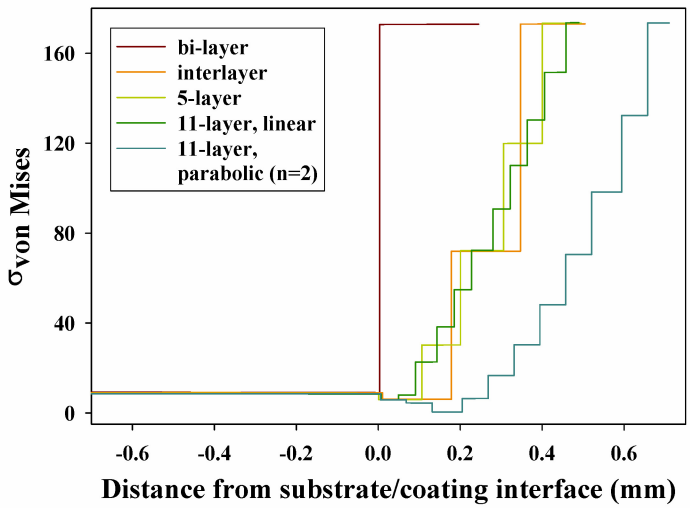

(c): Variation of $\sigma_{vonMises}$ with position

Figure 5.12: Stress distributions along the line x=10 in Figure 5.9 for various FE models of graded coating pinned along the bottom edge following an isothermal elastic 150 to 30^{o}C temperature transition.

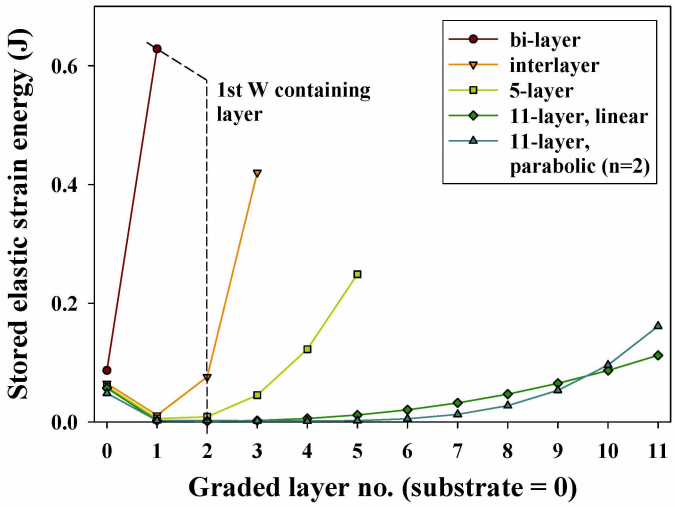

(a): Variation of stored elastic strain energy with graded layer number

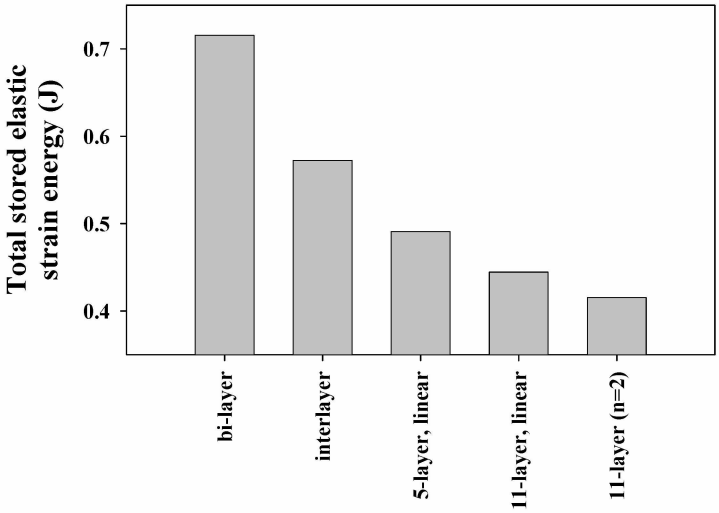

(b): Variation of total coating stored elastic strain energy with graded architecture

Figure 5.13: Variation of stored elastic strain energy and total coating stored elastic strain energy for various graded architectures pinned along the bottom edge following an isothermal elastic 150 to 30^{o}C temperature transition.

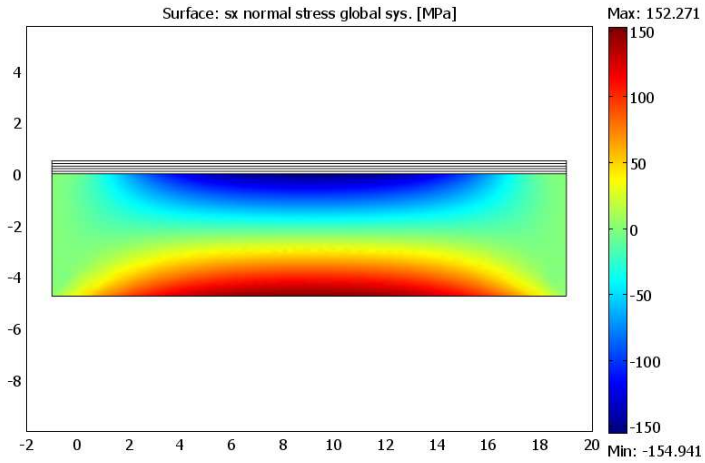

Figure 5.14: Initial σ_x stress distribution (σ_i) following the increase in temperature of the 5-layer FEA graded coating substrate from an isothermal temperature of 30^{o}C to the non-isothermal state shown in Figure 5.15(a).

5.4.3 Non-isothermal systems

The initial assumption of an isothermal system was an oversimplification since the active extraction of heat via the use of a water cooled sample holder will have induced thermal gradients through the substrate thickness during manufacture. To assess this effect a series of models with an assumed internal near-linear temperature gradient in the substrate (at coating deposition) were developed. The substrate was assumed stress-free when un-restrained at 30^{o}C. Based on thermocouples situated at the water cooled back face and close to the substrate surface during manufacture, the assumed internal near-linear temperature gradient ran from 150^{o}C at the substrate surface to 30^{o}C at its base. This initial temperature gradient in the substrate was calculated on the basis of the solution to the 1D steady-state heat flow equation representing heat flow from the front to the back face. Bending moments were allowed and a 20mm wide computational domain was again used. Figure 5.14 shows a typical σ_x substrate distribution generated by heating a initially stress-free substrate at 30^{o}C to the calculated through-thickness 150^{o}C to 30^{o}C temperature profile. There was a tensile (at the base) to compressive stress gradient that provided the initial stress distribution (σ_i) for when the coatings were subsequently attached.

When the various coatings were added to the pre-stressed/pre-heated substrate, they were assumed isothermal and stress free at 150^{o}C. The combined pre-stressed substrate plus isothermal coating

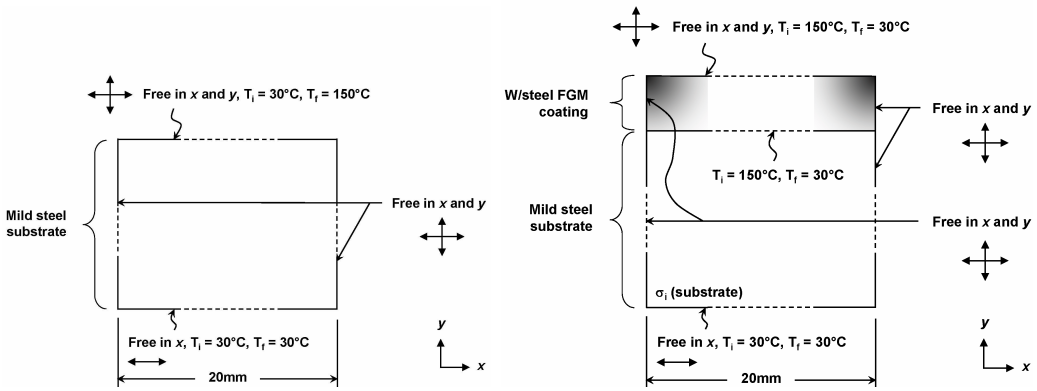

(a): Substrate

(b): Substrate, initial stress σ_i from (a), plus coating

Figure 5.15: Schematic diagrams illustrating the non-isothermal elastic FE model boundary conditions.

arrangement was then reduced in temperature back to a uniform 30^{o}C, and the resultant stress distribution calculated.

The boundary conditions for the development of the 'pre-stressed' substrate are shown in Figure 5.15(a). Stress/stored elastic strain energy distributions following the decrease in temperature to an isothermal temperature of 30^{o}C were then calculated according to the boundary conditions setout in Figure 5.15(b). Through-thickness σ_x distributions were considered along the lines x=1mm and x=10mm (as shown previously for the bending moment case in Figure 5.9) for each of the five graded coatings. Additionally, the variation of both the stored elastic strain energy in each computational domain and total (coating plus substrate) stored elastic strain energy with compositional grading was considered. The resultant distributions are shown in Figures 5.16(a) to (f).

The assumption that the substrate was non-isothermal and had an initial through thickness stress distribution modified strongly the post-manufacture room temperature stress distributions. At the edge of the computational domain, the x-plane stress distribution shown in Figures 5.16(a) and (b) was broadly similar to that for bending only at x=1mm, shown previously in Figure 5.11(a). However, the non-isothermal model resulted in a higher peak stress at the W surface in the bi-layer system of -162MPa compared to -96MPa in the bending moment only case. At the centre of the computational domain the non-isothermal stress distribution shown in Figures 5.16(c) and (d) was more strongly modified compared with the bending moment only case shown in Figure 5.12(a). Substrate stresses

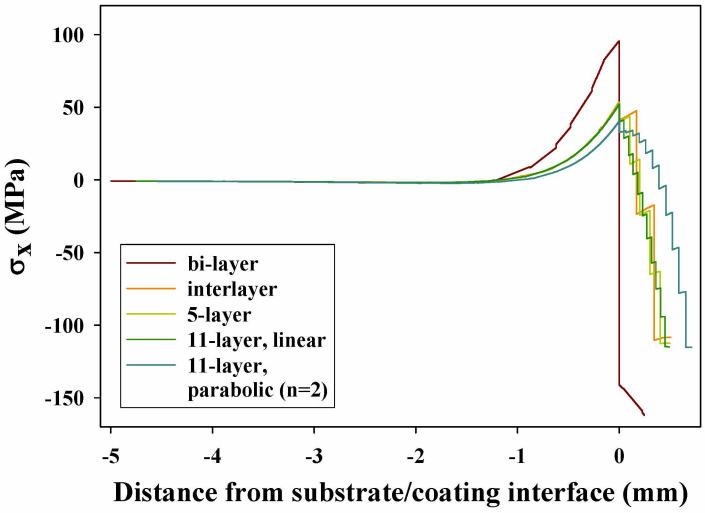

(a): Variation of σ_x with position, x=1mm

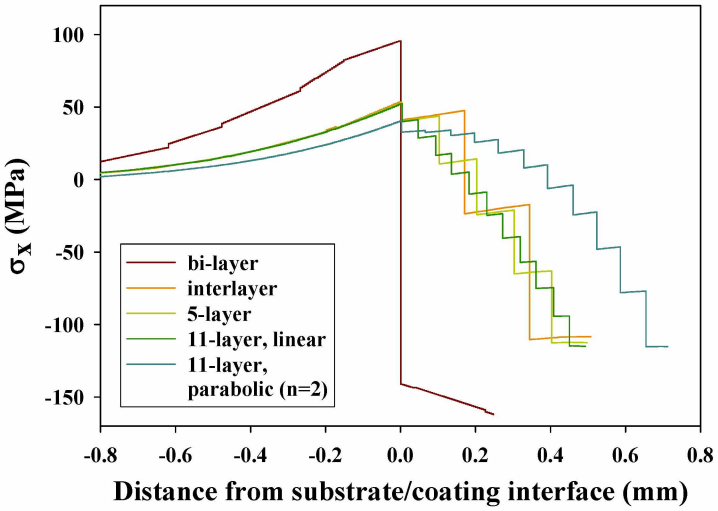

(b): Variation of σ_x with position, x=1mm

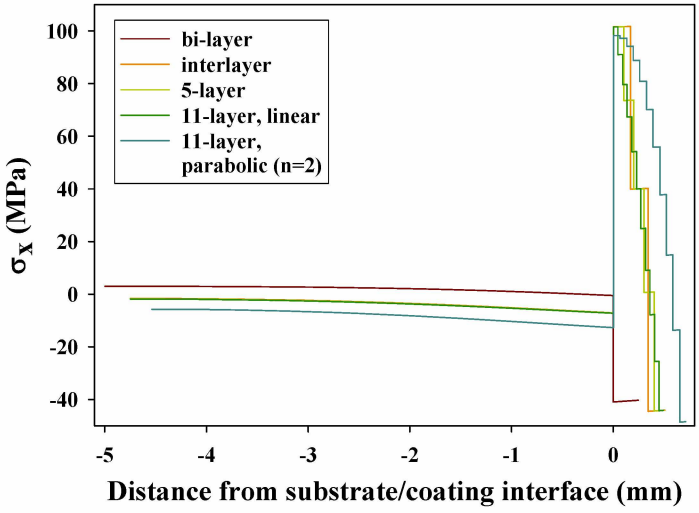

(c): Variation of σ_x with position, x=10mm

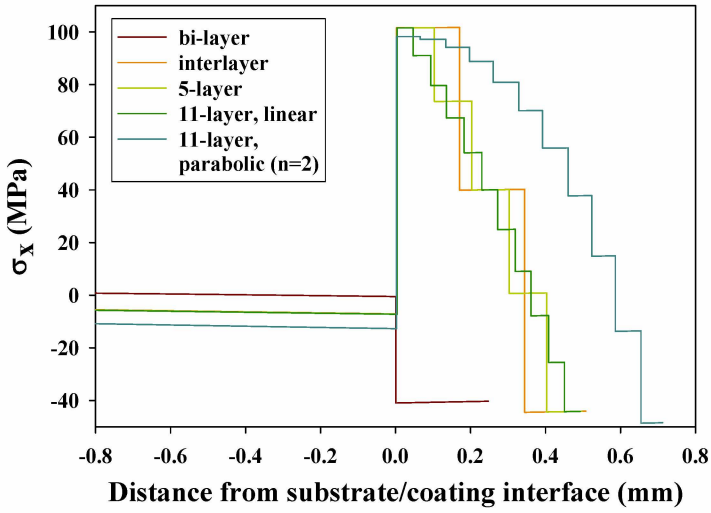

(d): Variation of σ_x with position, x=10mm

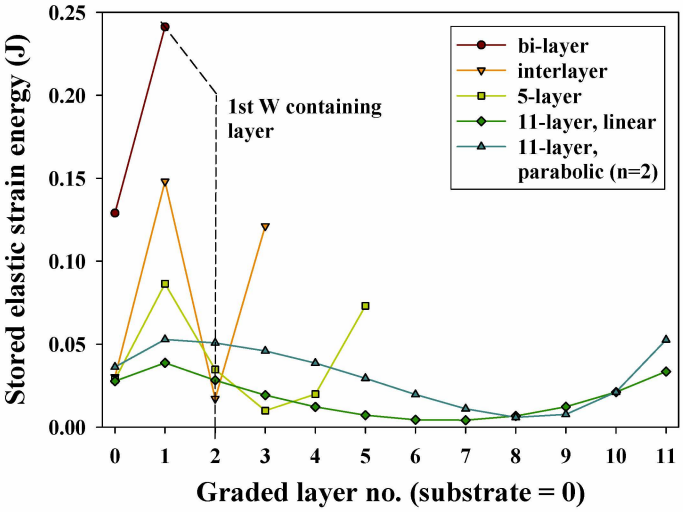

(e): Variation of stored elastic strain energy with graded layer number

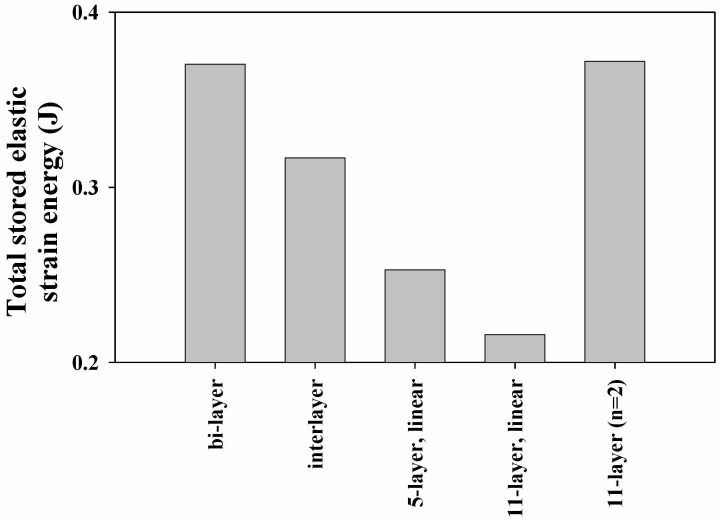

(f): Variation of total stored elastic strain energy with graded architecture

Figure 5.16: Stress, stored strain energy and total stored elastic strain energy distributions from non-isothermal FE models subject to a manufacturing to room temperature thermal excursion.

were comparable for all architectures considered, however within the coating, peak compressive stresses in the non-isothermal case had a much lower magnitude of -40MPa compared to -173MPa in the bending moment only case. In the bi-layer case, the coating had a uniform compressive stress, whereas for the graded coatings, the non-isothermal model led to a significant tensile stress in the graded layers closest to the substrate/coating interface followed by a steady reduction in stress with compositional graduation/layer number until the peak compressive stress at the coating surface was reached.

The modified stress distributions were a result of the lower initial temperature at the substrate rear face, and therefore reduced thermal contraction after deposition. This led to a reduction in compressive/increase in tensile stress at the substrate/bond coat interface and the upper half of the computational domain.

Figures 5.16(b) and (d) show that peak substrate/graded layer σ_x stresses again decreased with increased grading, although this effect was less marked at the substrate/bond coat interface, with the three linear graded coatings (50:50 inter-layer, 5 and 11 layers) having comparable interfacial stresses. The net increase in tensile stress meant that now, only the upper W-rich layers were in compression. Stored elastic strain energy decreased with increased grading at the bond coat/1^{st} W containing layer interface in Figure 5.16(e), an effect apparent to a larger extent at the substrate/bond coat interface. For the linearly graded arrangements, Figure 5.16(f) shows that total stored elastic strain energy behaved similarly to the equivalent isothermal bending moment only case in Figure 5.13(b). The stored elastic strain energy again decreased with compositional grading. However, in the case of the 11-layer parabolically graded arrangement, the stored elastic strain energy was much higher than in the equivalent linearly graded system. This was attributed to the higher proportion of W near the coating surface in the parabolic case - with the addition of a non-isothermal substrate the residual stress arrangement became more similar to the bi-layer system. In addition, due to the modified stress distributions, the total stored elastic strain energy in any particular graded system was reduced when compared with the isothermal bending moment case. For example, for the bi-layer arrangement the total elastic stored strain energies were 0.37J (non-isothermal) and 0.72J (isothermal) respectively. However, as with the isothermal no bending moment case shown in Figure 5.5, the stored elastic energy in the 11-layer parabolic arrangement was (in this case very much) higher than in the 11-layer

linear case.

Overall, the main effect of assuming that the substrate was pre-stressed with a through thickness temperature gradient at coating deposition was a radical change in internal stress distributions compared with the isothermal case, and a reduction in stored elastic strain energy at the substrate/bond coat interface. The associated reduction in compressive residual stress in the upper W layer was a further striking feature.

5.5 Surfi-sculpt FE models

Unlike the mild steel substrates in graded systems, surfi-sculpt substrates had a non-planar upper surface/interface. Therefore, stresses in both the x and y-planes were of importance. In all cases the properties for W and 316L stainless steel from Table 5.1 were used in calculations.

5.5.1 Peaked unit cells

To learn about the effect of a non-planar interface on thermally induced residual stresses, a model of a unit cell comprising a single peak, but with differing curvature of radii were studied, as shown in Figure 5.17. The W and steel volume fractions were normalised to 6 and 15mm^2 respectively and equivalent to a 3mm wide bi-layer system with a 5mm thick substrate and 2mm thick W layer. As only the effect of introducing a perturbation on the planar interface was of interest in this preliminary model, no bending moments were considered, as shown Figure 5.17. This arrangement was subject to a 150 to 30^{o}C isothermal temperature change and the peak radii of curvature varied from 0.10mm to 1.00mm. A planar bi-layer steel/W system was considered for comparison. In each case, the 'shoulders' of the peaks were rounded with constant curvature to reduce stress concentrations in this region.

Typical 2D stress distributions for the case of a 0.25mm rounded peaked structure are presented in Figures 5.18(a) to (d) for σ_x, σ_y, σ_{xy} and $\sigma_{vonMises}$ respectively. The maximum residual stresses developed about the top of the peak. Shear stresses developed because of the more complex 2D geometry, although unlike σ_x, σ_y and $\sigma_{vonMises}$, they were localised along the sides of the structural

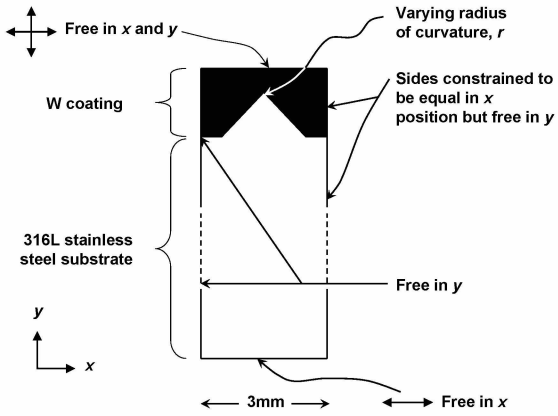

Figure 5.17: Schematic illustrating the boundary conditions used for the elastic peaked unit cell model.

feature rather than at its peak. Figure 5.18(d) shows that von Mises stresses about the structural peak, even with this smoothly curved topography, exceeded the assumed W yield stress of 400MPa. Non-elastic behaviour - microcracking, yield, etc - might therefore be expected in this region.

The variation of all stresses along the line E-F in Figure 5.18(a) for the different peak radii of curvature are shown in Figure 5.19 (apart from σ_{xy} which was $\sim$0 along this line due to symmetry). There was a steady increase in σ_x, σ_y and $\sigma_{vonMises}$ as the peaks became progressively sharper. The σ_x discontinuity across the interface at the peak decreased slightly, according to Figure 5.19(a), from 277MPa for the bi-layer coating to 236MPa for the r=0.10mm coating. However, the maximum σ_x stress within the W coating at the substrate/coating interface due to the stress concentrating effect of the surface protrusion increased from -198MPa for the planar bi-layer case to -342MPa for r=0.10mm. This stress concentrating effect was assumed to contribute significantly to the localised cracking observed experimentally about surfi-sculpt peaks, such as that shown in Figure 4.28.

5.5.2 VPS W coated surfi-sculpt structures

In Chapter 4, topographies 1-3 exhibited $\sim$2mm^2 cellular structures with internal peaks of different forms. Topographies 4 and 5 showed a regular 'diving-rod/wishbone' type structure with small $\sim$200-300μm peaks (larger on substrate 4), while 6 and 7 exhibited a regular linear array of troughs and towers. Finally, topographies 8 and 9 were again cellular in nature, but with smaller unit cells than substrates 1-3 and, in the case of substrate 9, more benign, e.g. less sharply defined, surface features. Only one typical topography from each of the above broad topography categories was considered for analysis - topographies 1, 4, 7 and 9. Only 2D models, due to advantages in terms of ease of grid generation and computational time required for solution were considered. Profiles of 'unit cells' - the repeating pattern of features in 2D - were extracted via image analysis from cross-sectional micrographs of actual sprayed substrates (those for samples 1, 7 and 9 are shown in Figures 4.26(a) to (c) respectively) and then reproduced as FE grids, with the unit cells repeated to the maximum integer number of repeats possible within an 11mm width. Any extra width up to the 11mm width at the edges was filled in by a planar segment. The 2D experimental cross-section geometries were taken at $\sim 45^o$ to any repeating pattern in an attempt to capture the majority of significant interfacial features.

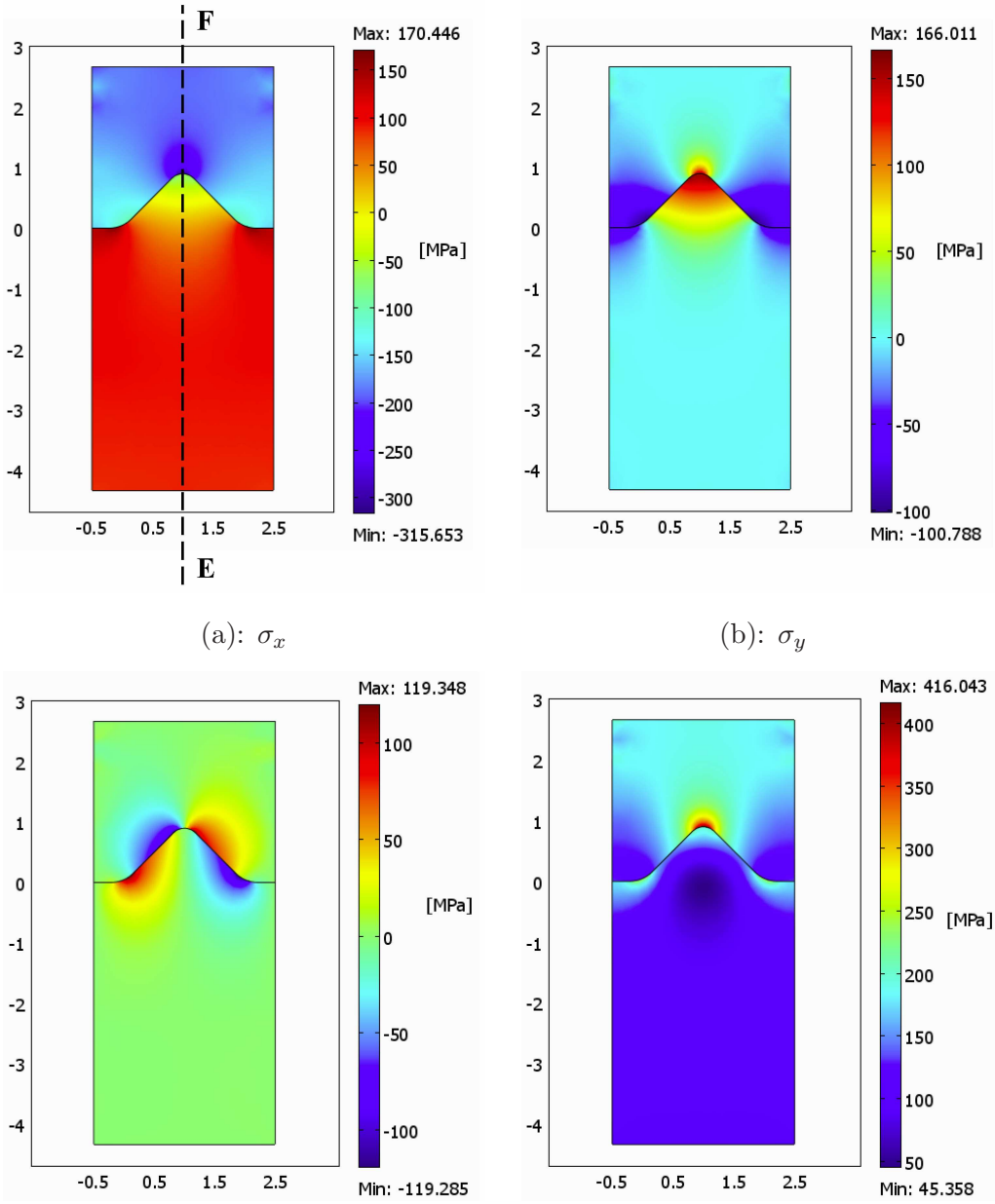

(a): σ_x (b): σ_y

(c): σ_{xy} (d): $\sigma_{vonMises}$

Figure 5.18: 2D stress distributions for an elastic peaked-surface unit cell model, r=0.25mm, following a 150 to 30^{o}C isothermal thermal transition (all dimensions in mm).

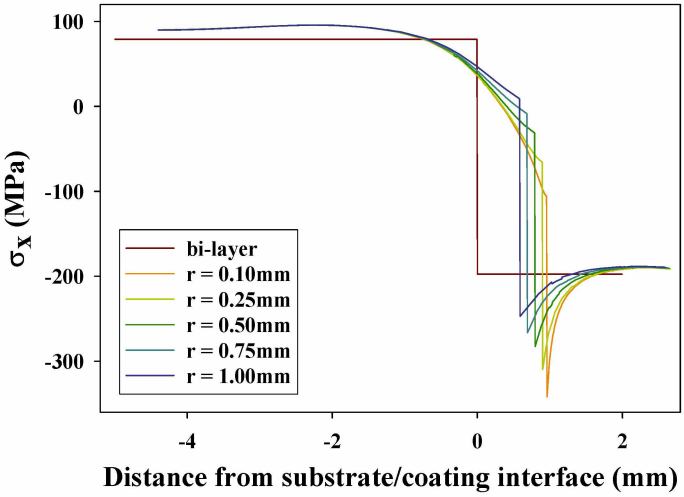

(a): Variation of σ_x with position

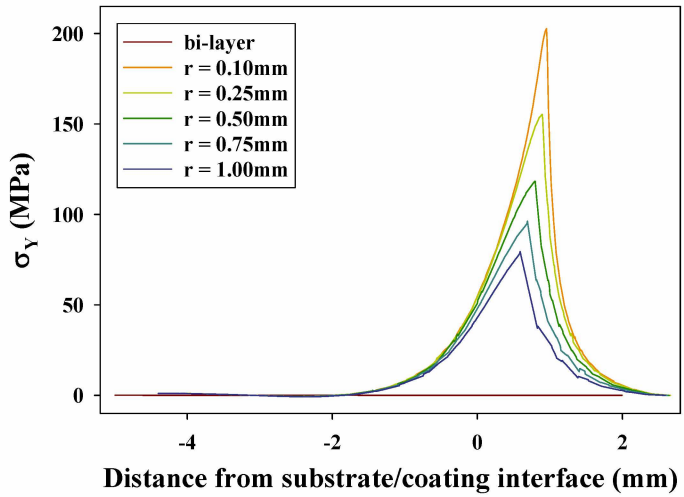

(b): Variation of σ_y with position

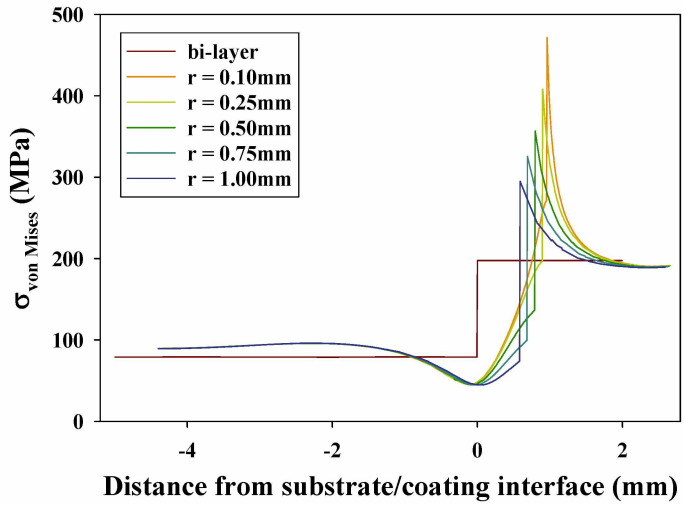

(c): Variation of $\sigma_{vonMises}$ with position

Figure 5.19: Stress distributions along the line E-F in Figure 5.18(a) for unit cells with various radii of curvature following an isothermal elastic 150 to 30^{o}C temperature transition.

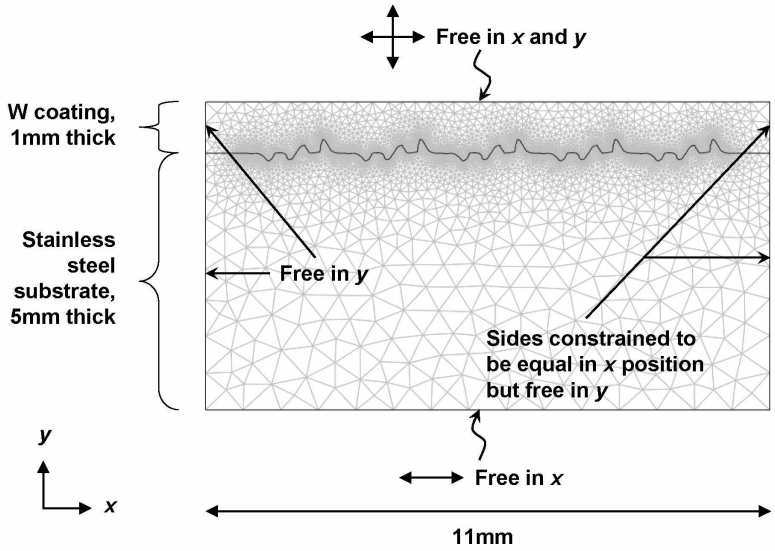

Figure 5.20: Schematic illustrating the boundary conditions used for the isotropic elastic surfi-sculpt models with no bending moments (mesh plus interface for sample 9 shown).

A 1mm coating of W was assumed, along with a 5mm thick substrate, with W fraction normalisation required due to the presence of differing both peak and trough structures in the surfi-sculpt substrates. Meshing was automated, with manual refinement about possible points of rapid stress variation as required.

No bending moments

Similar boundary conditions to those in Figure 5.17 were employed - namely a lack of bending moments, as shown in Figure 5.20.

Due to the complex topography of the surfi-sculpt substrates, it was considered likely that even with no bending moments present, σ_y and σ_{xy} would be significant. Calculated stress distributions were broadly similar and consequently only the σ_x, σ_y and σ_{xy} distributions for the most successful topography 9 are shown in Figures 5.21(a) to (c) respectively.

The sculptured interfaces concentrated stress strongly, close to the non-planar features. The σ_x stresses in the bulk of the substrates were relatively low, $\leq$50MPa in all cases, due to the comparatively large volume over which stresses were distributed, and were tensile because of the higher CTE of the steel.

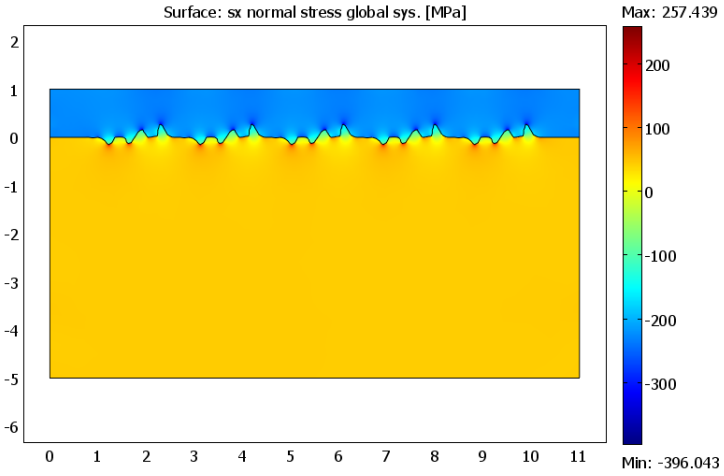

(a): σ_x distribution

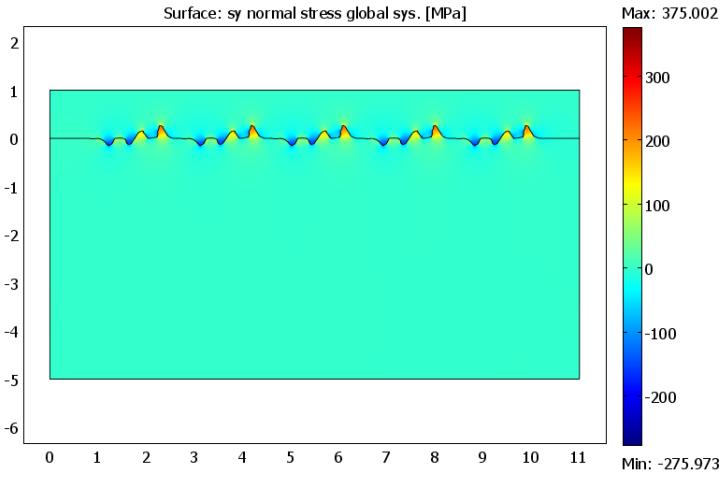

(b): σ_y distribution

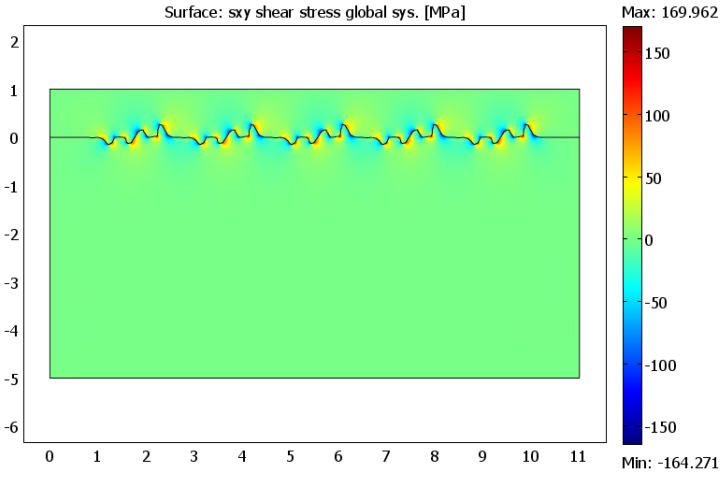

(c): σ_{xy} distribution

Figure 5.21: Stress distributions for surfi-sculpt substrate 9 following an isothermal elastic 150 to 30^{o}C temperature change with no bending moments (all dimensions in mm, stresses in MPa).

Within the bulk of the W coating, σ_x stresses were compressive and comparatively large at up to 150-200MPa. About the peaks, σ_x rose to -372MPa for topography 1 and -396MPa for topography 9 i.e. similar regardless of detailed topography. There were also compressive σ_x stresses in the steel regions of peaks and therefore similar effects occurred about the sub-surface features, with tension in the steel and in the W regions close to sub-surface features.

Because the boundary conditions prevented bending, σ_y stresses were localised about the interface features only. In these regions, σ_y stresses had similar distributions to σ_x, except with maximum tensile stresses about the top of/within surface protrusions and maximum compressive values about/within sub-surface features. Overall, maximum σ_y stresses were comparable with σ_x stresses. Despite the lack of bending, the complex interfacial topographies led to local shear stresses of typically 200MPa.

Based on these results which showed the importance of the interfacial surface features, the distribution of $\sigma_{vonMises}$ (which combines σ_x, σ_y and σ_{xy} contributions) was considered in detail about various typical surfi-sculpt features in Figures 5.22(a) to (d) for topographies 1, 4, 7 and 9 respectively. Maximum von Mises stresses were comparable across all topographies at ∼500MPa at the tips of the surfi-sculpt structures, exceeding the assumed bulk W yield stress of 400MPa [17, 18, 55, 106] and consequently implying that, even though under compression, non-elastic behaviour will occur in these regions. Away from the structural peaks, von Mises stresses were significantly lower. The high local stresses for all types at the surfi-sculpt features in all cases was consistent with the observed cracking e.g. Figure 4.28 in these regions.

Bending moments

As with the graded models in Section 5.4.2, the four surfi-sculpt models considered were studied following an isothermal elastic 150 to 30^{o}C temperature transition with the base of the models pinned in the y-plane, as shown in Figure 5.23.

As with the no bending moment case, key features of the stress distributions for the different topographies were comparable and consequently only the distributions for the most successful topography 9 are presented in Figures 5.24(a) to (d).

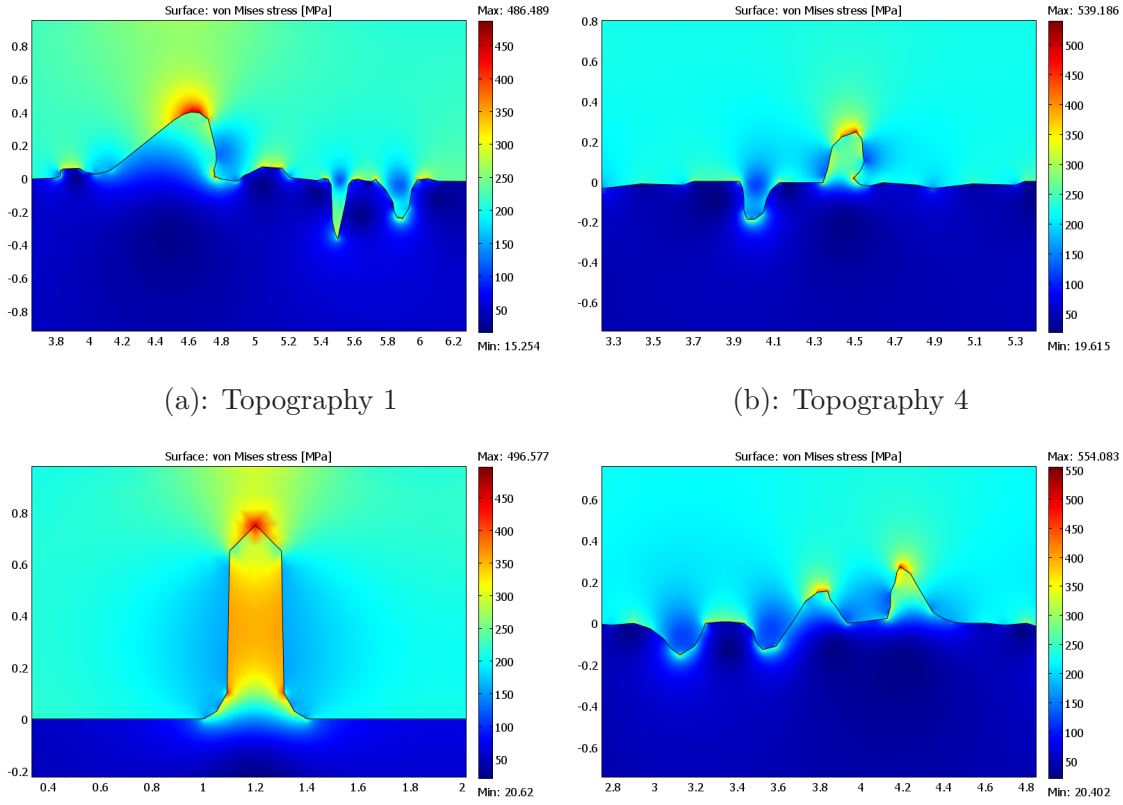

(a): Topography 1

(b): Topography 4

(c): Topography 7

(d): Topography 9

Figure 5.22: Von Mises stress distributions about the peaked structures for architectures 1, 4, 7 and 9, following an isothermal elastic 150 to 30^{o}C temperature transition with no bending moments.

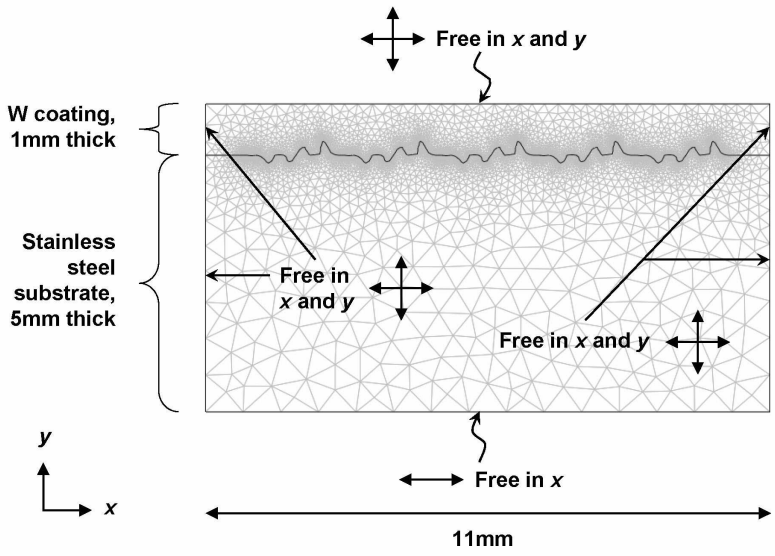

Figure 5.23: Schematic illustrating the boundary conditions used for the isotropic elastic surfi-sculpt models with allowed bending-moments (mesh plus interface for substrate 9 shown).

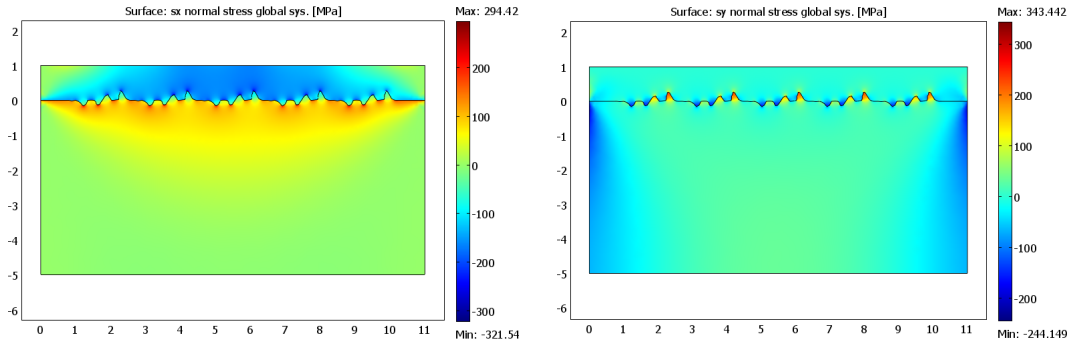

(a): σ_x (b): σ_y

(c): σ_{xy} (d): $\sigma_{vonMises}$

Figure 5.24: Stress distributions for surfi-sculpt sample 9 following an isothermal elastic 150 to 30^{o}C temperature transition, including bending moment affects.

Compared with the equivalent no bending moment case in Figures 5.21(a) to (c) and 5.22(d) for σ_x, σ_y, σ_{xy} and $\sigma_{vonMises}$ respectively, the bending most affected stresses at the domain edges. Stress concentrations again arose around interfacial features, although maximum stresses were reduced e.g. the presence of bending moments reduced the maximum σ_x in the W about the surfi-sculpt peaks from -396MPa to -322MPa. This stress re-distribution also reduced peak stresses in the substrate, particularly at the domain edges.

Non-isothermal temperature profile

Identical assumptions to those employed for the graded coatings in Section 5.4.3 were considered for surfi-sculpt topography 9. Similar reductions in stresses in the upper region of the W coating were expected, although complicated by the non-planar interface. Boundary conditions are shown in Figures 5.25(a) and (b), with the resulting σ_x and σ_y stress distributions shown in Figures 5.26(a) and (b) respectively.

Comparing Figures 5.26(a) and 5.24(a) for σ_x, the non-isothermal case was comparable to the equivalent isothermal bending moment only case. Peak compressive σ_x stresses at the structural peaks increased to -561MPa (non-isothermal) from -322MPa (isothermal), although local peak tensile stresses around sub-surface features in the substrate were broadly comparable at 313MPa (non-isothermal) and 294MPa respectively. The average stress distributions in 0.05mm vertical steps through the sampling region shown in Figure 5.26(a) and an identical region (not marked) in Figure 5.24(a) are shown in Figure 5.27. The good agreement between these two distributions suggests that the increased compressive stress about structural peaks in the non-isothermal case was predominately a local phenomenon. Similarly to the graded coatings, there was a reduction in W coating stresses, accompanied by a rapid increase in tensile stress at the interface. These effects led to a reduction in average peak stresses in Figure 5.27 from -171MPa to -134MPa for the non-isothermal case and a shift in its position from a thickness of 0.33mm to 0.98mm at the upper W surface.

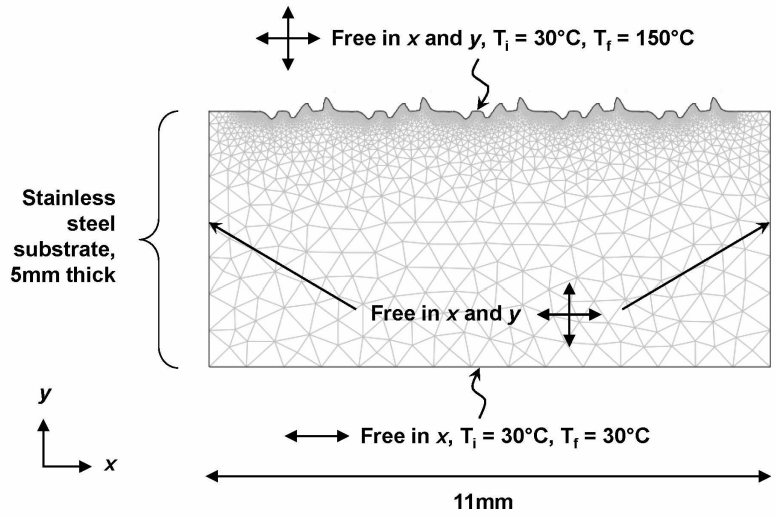

(a): Substrate (σ_i) elastic FE model boundary conditions

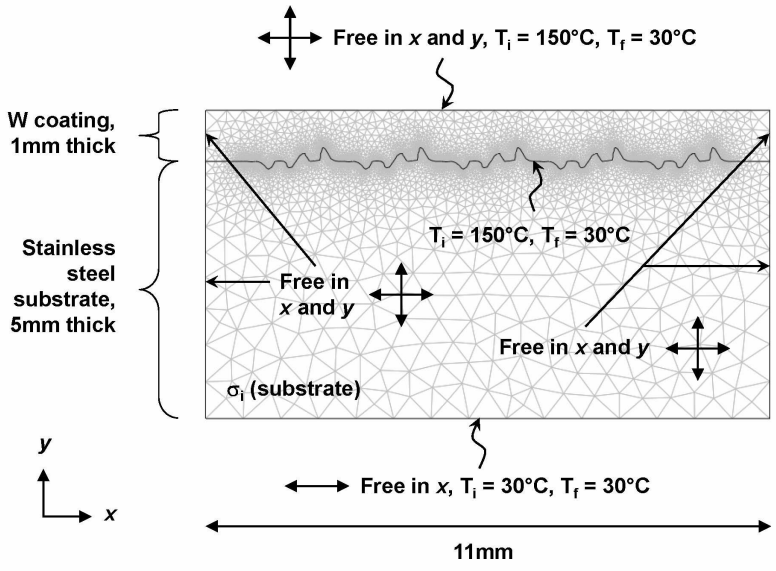

(b): Substrate/coating elastic FE model boundary conditions

Figure 5.25: Elastic model boundary conditions for surfi-sculpt sample 9 with bending moments allowed and a non-isothermal substrate temperature profile. T_i = initial temperature; T_f = final temperature in both cases.

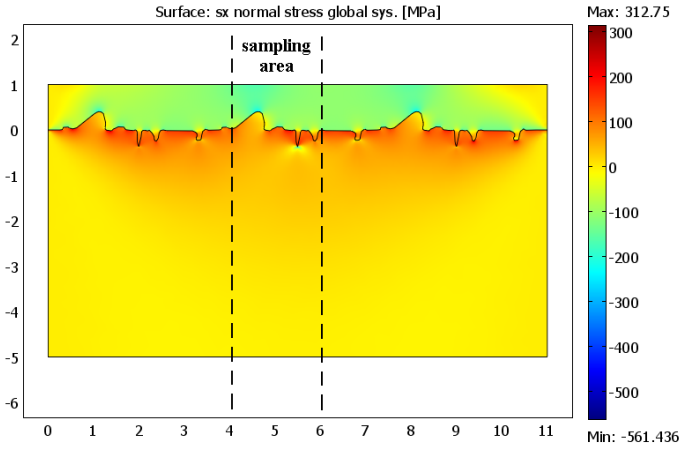

(a): σ_x distribution (sampling region running between x=4.05mm and x=6.05mm)

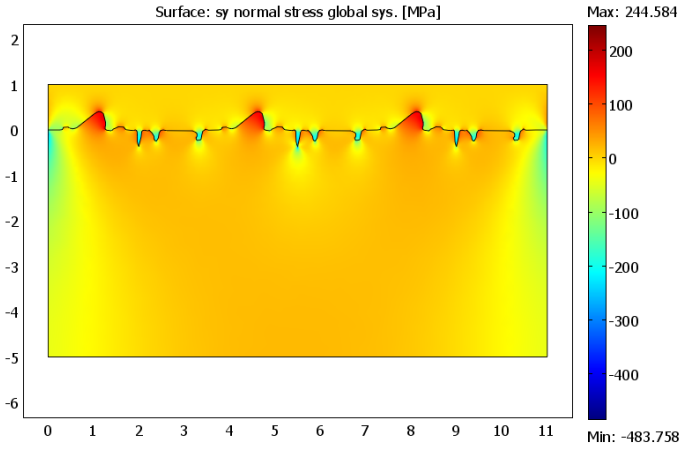

(b): σ_y distribution

Figure 5.26: Resultant stress distributions for surfi-sculpt sample 9 subject to the non-isothermal boundary conditions outlined in Figures 5.25(a) and (b).

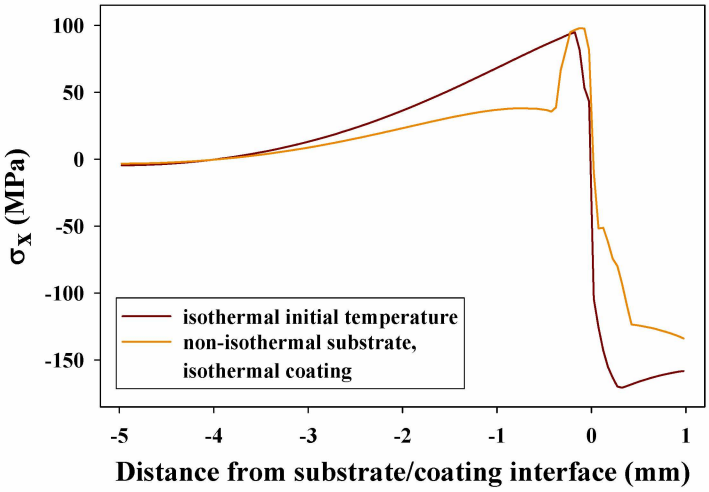

Figure 5.27: Comparison of average σ_x residual stress distributions within the sampling region defined in Figure 5.26(a), for sample 9 for both an isothermal case of 150^{o}C cooled to 30^{o}C and a non-isothermal case with an initial substrate temperature gradient of 150^{o}C at the upper surface to 30^{o}C at the base, followed by coating deposition at 150^{o}C and post deposition cooling to an isothermal 30^{o}C, with bending allowed in both cases.

Chapter 6

Discussion

6.1 VPS W

The high melting point and density of W made the successful manufacture of W coatings by VPS challenging and the parameters developed here for VPS W required the apparatus to operate close to its power and temperature limits to ensure sufficient W melting, and involved successive stop-start cycles to avoid plasma gun/torch overheating. Finally, very many W coatings were produced with densities as good as those reported elsewhere, and in thicknesses far exceeding those reported elsewhere without an interlayer.

6.1.1 VPS W properties

Porosity of the as-sprayed W coatings was ∼9%, comparable with that produced elsewhere by VPS [14, 24, 86, 111]. This porosity has been shown here and elsewhere to lead to a reduction in the W Young's modulus from 410GPa for bulk W [18] to approximately 194GPa obtained here by nano-indentation. The link between porosity and Young's modulus for W is illustrated, using various sources from the literature, in Figure 6.1. Nano-indentation results from this study are shown with an error bar of 1 standard deviation. There is an approximate linear relationship between Young's modulus and porosity. Although nano-indentation values and those obtained by dynamic resonant frequency might not be safely compared, overall, Figure 6.1 shows reasonable agreement. From Figure 6.1, the

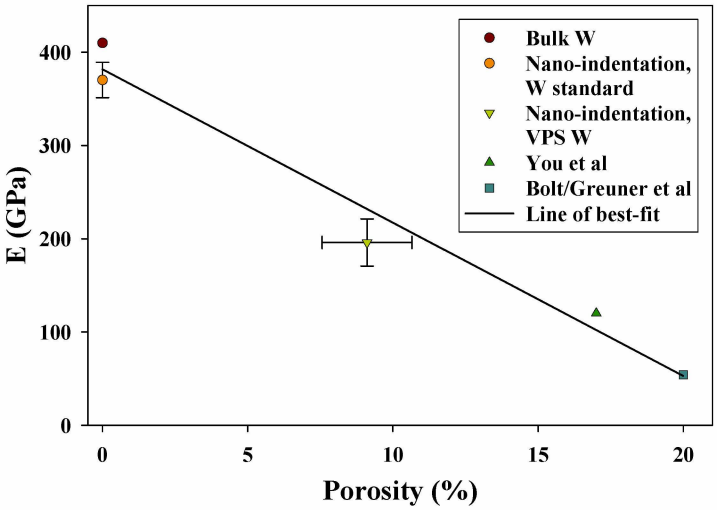

Figure 6.1: Variation of Young's modulus with porosity for W [18, 56, 86].

VPS W coatings in this study have porosities and moduli lying between those of bulk W and the other reported VPS W coatings with higher porosity. It should be noted that attributing the reduction in modulus to porosity only does not recognise the lack of integrity of the coating and that inter-splat cracking may also contribute to modulus reduction.

6.2 Graded coatings

The previous 'state-of-the-art' in W/steel functionally graded coatings was a 0.5mm thick 50:50 W/Eurofer pre-mixed inter-layer on a Eurofer substrate plus 2mm VPS W coating developed by Bolt *et al.* at Plansee AG [14, 24]. The ability to use VPS deposition to control W fraction in graded coatings has been demonstrated here with architectures including 50:50 inter-layers, 5-layer and 11-layer parabolically graded coatings. The graded coatings were shown to vary hardness and Young's modulus through the coating thickness via nano-indentation and Vickers micro-indentation. The effect of load in determining either local or average properties was also shown.

EPMA analysis showed inter-diffusion across the substrate/bond coat interface that enhanced coating adhesion occurred during heat treatment of the bond coat. Heat treatment then allowed a $\sim$200μm thick W top layer to be manufactured. In all cases, there was a lack of inter-mixing between the W and Fe-rich regions on the microscale and EPMA analysis showed no evidence of reaction phases such

as WC or W oxides because of active cooling of the substrates during manufacture. The layered nature of the graded coatings was attributed to the different paths taken by the W and Diamalloy 1008 steel powders in the plasma flow, as previously observed by Pintsuk *et al.* [55] for W/Cu FGMs. A potential solution in the form of post-hopper, dynamic mixing of the feedstock powders was investigated and gave promising results as shown in Figure 4.13.

All graded coating thermal histories were similar comprising several steps: (i) a step-wise increase to a peak deposition temperature comprising several rasters/passes, (ii) a decrease back to $\sim 30^{o}$C, (iii) a plasma torch cool-down pause, and (iv) repetition of the cycle to deposit the next layer. In all cases a slight decrease in peak temperature with successive layer deposition occurred. The total reduction in temperature reached up to $\sim 40^{o}$C by the deposition of the final W layer. While initially attributed to heat dissipation with increased coating thickness, for pure W deposition this effect was small e.g. coating 158b in Figure 4.29, implying it was related to the presence of Diamalloy 1008 during co-spraying. It is postulated that as the grading/W fraction increased so did the emissivity of the upper surface, reducing peak temperatures by radiating slightly more energy over successive passes.

In all graded coatings, W fraction when co-sprayed with Diamalloy was consistently slightly lower than expected e.g. the W fraction variations in Figures 4.3(b) and 4.22 for coatings 63b and 142b respectively, despite efforts to optimise and balance approximately W/Diamalloy mass flow rates into the plasma based on analysis of W and Diamalloy deposition efficiencies in single material bilayer coatings. This effect was attributed to the influence of the Diamalloy on the W melting and possible explanations include quenching of the plasma when Diamalloy was introduced and the effect of the Diamalloy on the path of the W through the plasma flame - as previously discussed, this path was critical for W melting.

6.3 Surfi-sculpt coatings

Preliminary surfi-sculpt/VPS W experiments qualitatively identified both key failure mechanisms and beneficial topographic features required to deposit thick VPS coatings as outlined below.

1. Coating delamination, typified by substrate 4 in Figure 4.26(b) because of insufficient mechanical adhesion with peak heights $<200\mu$m.

2. Narrow and/or deep sub-surface features prevented VPS W penetration and enhanced adhesion, as typified by substrate 7 in Figure 4.26(c). Conversely, coating 9 with wide and shallow sub-surface features allowed ready penetration of W droplets.

3. Sub-surface VPS W coating cracking was minimised by gently sloping and smoothly peaked surface protrusions, again as typified by substrate 9.

Reactor-relevant, up to 2mm thick, VPS W coatings exhibiting high densities were successfully deposited on surfi-sculpt substrates without delamination e.g. coatings 158b and 164b, Figures 4.30(a) and (b) respectively. EPMA analysis across the substrate/coating interface of sample 164b found no evidence of inter-diffusion. Therefore the ability to retain thick W is proposed to arise from a combination of mechanical adhesion due to the torturous nature of the surfi-sculpt topography and residual stress relief due to now regulated coating cracking and segmentation, as discussed further later. These coatings were sufficiently thick that their 'bulk' could be investigated by very many nano-indents and elastic modulus measurements were then integrated into FE models.

With the thicker W coatings, as discussed in Section 6.2, thermal histories were very reproducible with cycles comprising peak temperatures of $\sim 170^{o}$C followed by rapid cooling to $\sim 30^{o}$C. The consistent peak temperature at the back of the coating as it thickened e.g. Figure 4.29 for coating 158b, implied good through thickness thermal conductivity. The survival without delamination of coatings 158b/164b manufactured using 24/33 passes respectively implied a good resistance to thermal cycling (certainly better then the bilayer equivalents) - or that a mechanism for stress-relief i.e. microcracking to reduce stored strain energy and leading to a reduction in modulus was occurring.

EBSD analysis of coating 164b showed an average W grain size of $\sim 1\mu$m and some preferred grain directions. Given the initial average W particle size of 11.4μm in Figure 3.4, this implies rapid solidification of the W droplets with heat rapidly extracted through previously deposited layers to the water cooled substrate. The small grain size might facilitate relief of residual stress by creep at higher temperatures, but temperatures here were too low to expect any significant contribution of creep to

stress relaxation.

6.4 Modelling and experiments

To help understand experimental behaviour a number of FE models employing different boundary conditions and assumptions were formulated, for both graded and surfi-sculpt coatings. There were several similarities between the calculation of residual stresses from the graded and surfi-sculpt FE models. In both cases, initial assumptions of no bending moments gave the highest residual stresses and there was no variation across the width of the computational domain, except in the case of surfi-sculpt substrates close to the W/substrate interface. When bending moments were introduced the stress distributions became more complex as the substrate/coating arrangement relaxed and σ_x stresses reduced and σ_y stresses increased, particularly at the edge of the computational domain. Unlike previous studies care was taken to keep the overall W fraction constant regardless of graded/surfi-sculpt geometry. Consequently, comparisons of stored elastic strain energy in the W/graded layers and substrate were meaningful. Overall, the total stored elastic strain energy for the whole computational domain tended to decrease with compositional grading.

6.4.1 Graded coating FE models

Numerical approaches to estimate residual stresses in graded coatings based on final post-manufacture curvature of the substrate/coating system are available from the literature, see Section 2.6.2 [71, 77, 81, 82, 83]. In order to compare the FE approach taken in this study against one of these independent models from the literature, Hsueh *et al.*'s [83] 1D analytical approach described in Section 2.6.2 was implemented in Microsoft Excel for a 150 to 30^{o}C isothermal temperature change, elastic, 5-layer, linearly graded W/Diamalloy 1008 coating using the material properties from Table 5.1 and the W/steel graded layer thicknesses set out in Table 5.3. This analytical model assumed boundary conditions in which the corners of the computational domain corners were pinned, and the FE model developed in this thesis was adapted to calculate residual stress under the same conditions. Figure 6.2 compares the through thickness coating stress distribution from the analytical model and the

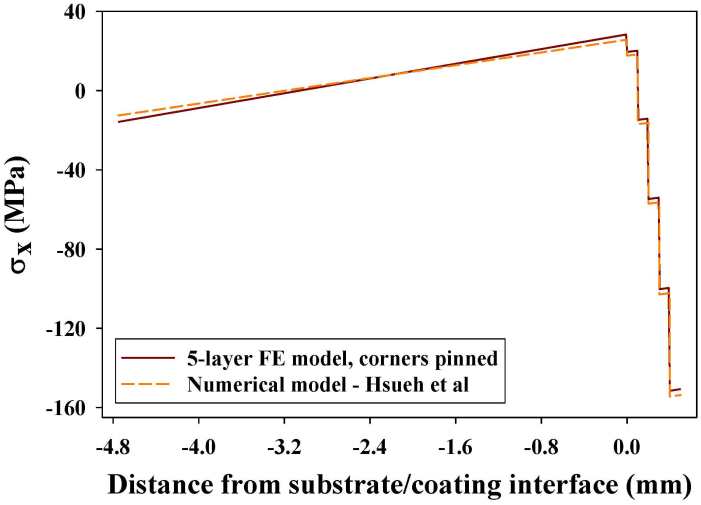

Figure 6.2: Comparison of residual stress σ_x in a five layer graded W/Diamalloy coating on mild steel, using the FE approach developed in this thesis for the case of a geometry pinned at the corners and using the analytical model of Hsueh *et al.* [83].

equivalent FE model. The distributions are in good agreement, with small differences attributed to approximations due to meshing of the FE method.

Investigation of residual stress evolution within the graded coatings using the FE models provided various insights into the mechanisms by which graded coatings 'manage' thermal residual stresses. Increased compositional grading reduced stress discontinuities at the interface between different graded layers, particularly across the substrate/coating interface, and as reported in [82, 109]. This effect is typified by the σ_x distribution for the no bending moment case in Figure 5.4(a), based on which the absolute change in stress from one discrete layer to another for the five different graded coating architectures is shown in Figure 6.3. The notation '0/1' refers to the difference in σ_x between layers '0' (substrate) and '1'; '1/2' between layers 1 and 2; etc.

Figure 6.3 shows reduced inter-layer stresses with the introduction of graded layers. The discontinuity in stress between the substrate and the W coating for the bi-layer system is 182MPa and just 3MPa across the substrate/bond coat for all graded coatings; and between the bond coat and the 1^{st} W containing layer, the stress discontinuity reduced to 78MPa, 36MPa, 14MPa and 1MPa for the interlayer, 5-layer, 11-layer linear and 11-layer parabolic systems respectively. Because these elastic residual stresses are directly proportional to the difference in W/Diamalloy volume fraction, after the

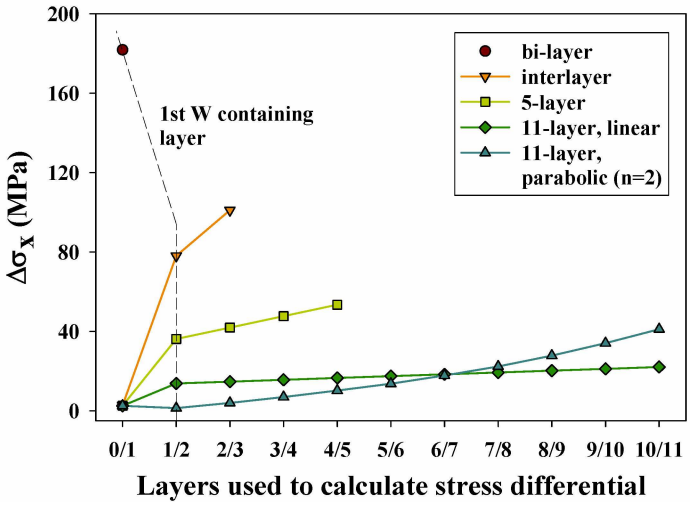

Figure 6.3: Variation in stress discontinuity with graded coating architecture using measured material properties with no bending moments, Figure 5.4(a).

1^{st} W containing layer, stress discontinuities increased consistent with the increasing W fraction, with the 11-layer parabolic case surpassing the 11-layer linear system around boundary 6/7.

The stress discontinuities in Figure 6.3 are directly proportional to the stored strain energy density distribution in Figure 5.4(d) because stored elastic strain energy is a function of stress - see Equation 5.8. When no bending moments are allowed, σ_y and $\sigma_{xy} \rightarrow 0$, giving stored elastic strain energy $\approx \frac{1}{2}t\left[\frac{\sigma_x^2}{E}\right]$ where t is the nominal thickness (unity in the case of plane-stress) and E is the Young's modulus of the layer in question.

Increased compositional grading significantly reduced stored elastic strain energy in the graded layers, particularly in the bond coat and the 1^{st} W containing layer e.g. see Figure 5.4(d). A fracture mechanics consideration of what causes delamination in coated bi-layer systems suggested that crack growth occurs when the stored strain energy is greater than the interfacial fracture energy [47], related to bond strength. In graded coatings, the failure criterion may be more complex since there are various discontinuities/interfaces and stored strain energy in each layer varies, as shown in Figure 5.13(a). In [65] and [66], it was shown that graded coating delamination can occur away from the substrate interface, as in Figures 2.25 and 2.26 respectively, while [112] showed that for a positive CTE mismatch i.e. where $\alpha_{substrate} > \alpha_{coating}$ - as with the W/steel graded coatings considered here - cracking within the graded layers dominated. Without knowing the interfacial fracture energy (related to interfacial toughness) for each layer, comparison of experiment and model is difficult. Time permitting, nano-indentation could have been considered as a way to measure interfacial properties. Nonetheless, if it is assumed that each of the interfacial fracture energies between regions of nominally constant W fraction in the graded layers are constant, then the effect of grading can be understood to reduce the stored elastic strain energy in any particular layer to below the interfacial fracture energy of the bounding interfaces.

When bending is allowed, σ_x stress reduces and σ_y increases, but overall stored elastic strain energy in each W containing layer is reduced in all cases because compared with the bi-layer case, grading of the W content fraction reduced the curvature caused by CTE mismatch between each discrete layer. The W fraction is re-distributed away from the interface with the dissimilar substrate, overall leading to reduction in total curvature and stored elastic strain energy e.g. Figure 5.13(b), while Figure 5.13(a)

shows the corresponding reduction in stored elastic strain energy over all layers.

The above cases were for no internal, through thickness temperature gradients within the substrate and represent one extreme assumption of the thermal condition during real experiments. Additionally both the substrate and coating were assumed to be stress-free at the elevated manufacturing temperature. These assumptions were considered unrealistic and an alternative assumption was also explored: a pre-stressed substrate according to a temperature gradient from 150^oC at the substrate surface to 30^oC at the substrate back face, followed by isothermal coating deposition at 150^oC, before cooling to a uniform temperature of 30^oC. When these assumptions were applied, the magnitude of σ_x stresses in the uppermost W layer reduced, and through thickness stress profiles became more complex e.g. there was now essentially zero stress within the substrate and a significant discontinuity across the substrate/coating interface - see Figure 5.16(a).

In order to rationalise this behaviour, consider Figure 6.4 that shows (a) a W at 150^oC on steel at 30^oC bi-layer arrangement and (b) a bi-layer system where the substrate is assumed to already have a through-thickness temperature gradient at the coating deposition temperature. For simplicity, Figure 6.4(b) shows this steel substrate divided into two layers, the lower kept at a constant 30^oC and the upper raised to 150^oC, and then on the right, deposition of a W layer at 150^oC onto this arrangement, before the entire system reduced in temperature to an isothermal 30^oC. In Figure 6.4(a), the W coating undergoes a contraction when the temperature is reduced from 150 to 30^oC and there is no net change in the unconstrained substrate length. However, since the W coating and steel substrate are attached at the interface, a force balance argument leads to the W having residual tensile stress and the substrate a residual compressive stress i.e. the opposite to the bi-layer case when both start at 150^oC.

For the tri-layer system in Figure 6.4(b), that seeks to explain the effect of substrate temperature gradient on the same basis, before coating deposition, the restrained expansion of the hotter upper half of the substrate leads to a compressive residual stress, while the cooler bottom half is placed into tension. This is shown on the left of Figure 6.4(b). Following W coating deposition at 150^oC and due to its lower CTE, the W coating contracts on cooling to a lesser extent than the upper-most steel substrate layer: this puts the W coating into compression. The contraction of the upper half of the

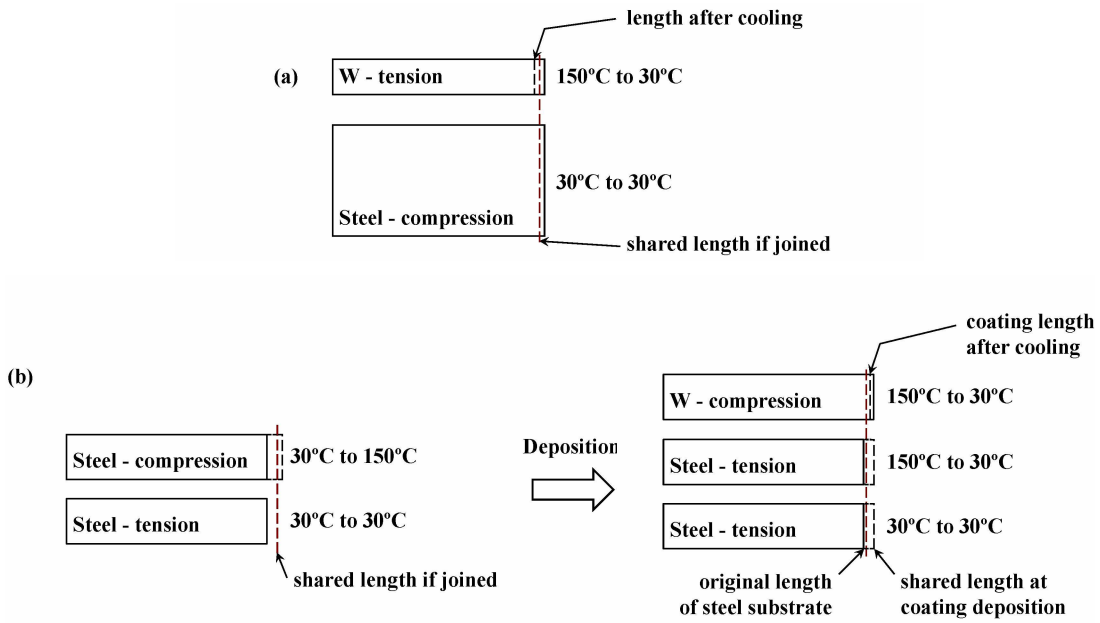

Figure 6.4: Schematic illustration of the effects of assuming that: (1) the substrate is stress-free at room temperature, and; (2) the substrate possesses a thermal and stress gradient at coating deposition.

substrate is restrained on its upper interface by the lower CTE W and on its lower interface by the cooler and non-contracting/expanding lower half, and is consequently in tension. The lowest steel layer undergoes no temperature change related contraction/expansion, but instead is pulled slightly into tension by the upper half as the arrangement reaches a uniform temperature. By comparing (a) and (b), the effect of the through thickness temperature and stress arrangement has reversed qualitatively the final residual stress state at 30^{o}C.

6.4.2 Graded coating residual stress measurement

In Section 4.3.1, a delaminated graded W coating was investigated by XRD and showed low or zero residual stress, as expected. However, there of course remained a need to measure W residual stresses in non-delaminated coatings, and this proved far from trivial. Coated substrates did not fit in the powder diffractometer and could not be machined as this would relieve stress and/or damage the W. Therefore X-ray diffraction measurements of near-surface residual stresses in central regions of adhered non-machined as-sprayed graded coating 128b were carried out with a PROTO iXRD combo diffractometer machine at the University of Manchester Materials Science Centre using incident 2mm diameter Mn Kα X-ray radiation. The high density of W reduced the estimated penetration depth to

E_W (GPa)	Stress x-direction (MPa)	Stress y-direction (MPa)
402	-20 ± 27.3	-29 ± 37.8
200	-9.9 ± 13.6	-14.4 ± 18.8

Table 6.1: Average W near-surface σ_x in-plane stresses for graded coating 128b for various W Young's moduli determined using a Proto iXRD combo diffractometer.

$\sim$10μm. Residual stresses were calculated via the $\sin^2\Psi$ approach at Manchester [47, 95, 98].

The surface stress from XRD is shown in Table 6.1 and suggested very low, nominally compressive, residual stresses. The measurement error in the estimated stress was large and depended upon the assumed modulus of W. Table 6.1 shows estimated stresses based on bulk values from the literature and nano-indentation VPS W values obtained here. The strongest conclusion that might be drawn from Table 6.1 was that residual stresses were small.

Even using the reduced Young's modulus from experiment because of the inherent porosity of the VPS W/Diamalloy, initial FE calculations still gave the magnitude of the W surface stresses >150MPa. When bending and then non-isothermal boundary conditions were introduced, the magnitude of the calculated stresses were much lower and closer to the experimental estimate.

Figure 6.5 shows three different σ_x stress distributions along the lines x=1 and x=10 from Figure 5.9 where bending moments are considered and using the material properties from Table 5.1. Figure 6.5 also shows the average measured W surface stress from Table 6.1 assuming E_W=200GPa. The models were 5-layer linearly graded coatings with: (1) the base pinned in the y-plane e.g. Figure 5.11(a), (2) and (3) a 30 to 150^{o}C non-isothermal initial temperature profile followed by isothermal coating deposition at 150^{o}C (with bending allowed) and then cooling to 30^{o}C along the lines x=1 and x=10 respectively, as shown in Figures 5.15(a) and (b).

As expected, Figure 6.5 shows that the combination of both bending moments and a non-isothermal temperature distribution within the substrate at coating deposition reduced the magnitude of the graded coating compressive stresses in the upper W layers. Reduced bending due to lower temperatures towards the substrate base resulted in higher tensile stresses towards the base of the coating and correspondingly lower compressive stresses at the coating surface. The best approximation to the measured surface stress was the non-isothermal with bending case. This is also, arguably, the most

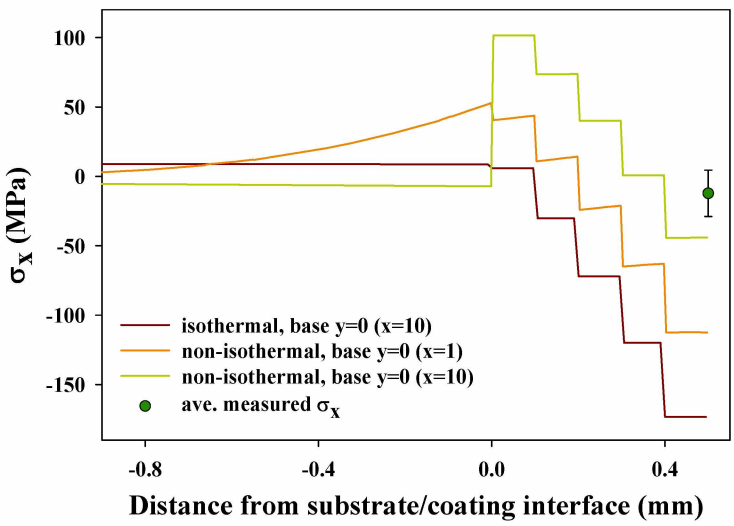

Figure 6.5: Comparison of FEA FGM models about the substrate/coating interface subject to various boundary/initial conditions to measured W surface residual stress for graded coating 128b.

physically sensible case. Particularly good agreement occurred at the centre of the computational domain (x=10) where the peak surface stress was ∼-44MPa.

The isothermal and non-isothermal thermal profiles in the FE calculation represent two extremes, and isothermal conditions have typically been used in other studies e.g. [71, 77, 81, 82, 83]. From the very limited experimental data, it might be concluded that non-isothermal conditions existed within the substrate during manufacture and this model arrangement provides the best agreement with experiment that can be reasonably expected. However, without more experimental data and given the broad assumptions in the model, this cannot be stated with confidence. Nonetheless, some tentative conclusions may be drawn:

1. An assumption of isothermal conditions during manufacture may be unsafe and it is judged likely that some temperature gradients existed, particularly in the substrate, helping to minimise residual stresses in the W. One further insight is that substrate cooling not only reduces the temperature at manufacture to minimise thermal residual stresses after coating, but where a temperature gradient may be generated, this provides an *additional* reduction in residual stress in the upper W coating. Further, it is clearly important to consider both boundary conditions and the initial stress state of each computational domain when attempting to understand the evolution of thermal residual stresses.

2. Measured residual stresses in the W are very low and when compared with calculations strongly suggest that some non-elastic behaviour was occurring at stresses below the bulk W yield stress from the literature.

Elastic-plastic material models were shown here to reduce W surface stresses in Figure 5.7. However, under the considered experimental conditions this required a reduction in the assumed yield stress by a factor of four from literature values given in Table 5.1. Clearly independent measurement of the yield stress of as-sprayed VPS W would be extremely helpful in assessing the presence of any non-elastic behaviour. Sadly, although nano-indentation was explored for this application, there was insufficient confidence in results to be used here.

Quenching stresses were not included in the FE calculations. As discussed in Section 5.2, estimates of

likely refractory metal quenching stresses were ∼30MPa for VPS W under these conditions [56, 108]. Because quenching stresses are independent of CTE mismatch stresses [71, 77, 81], this contribution would act to reduce compressive stresses at the W coating surface.

6.4.3 Surfi-sculpt FE models

Three different sets of boundary conditions for FE models of 2D cross-sections of surfi-sculpt substrates 1, 4, 7 and 9 were considered: no bending and bending moments both with and without an initial non-isothermal substrate temperature profile followed by isothermal coating deposition and then cooling. Much of the resulting residual stress behaviour has already been discussed for the graded coatings. However, unlike graded systems, both in-plane σ_x and now vertical σ_y stresses were significant, with σ_y stresses comparable to σ_x stresses, e.g. for substrate 9 with no bending where the maximum σ_x was -396MPa and maximum σ_y was 375MPa at the surface peaks in Figures 5.21(a) and(b) respectively. Maximum σ_y stresses were primarily associated with interfacial topography and were localised around the surfi-sculpt structures independent of boundary conditions - with very low σ_y stresses away from the interface in the 'bulk'. While maximum σ_x stresses were also localised about interfacial topographic features, significant local CTE mismatch compressive stresses occurred just above the substrate/coating interface and significant tensile stresses just below. There were high compressive σ_x stresses at the top of the surfi-sculpt peaks in the W coating, with corresponding compressive stresses induced below the sub-surface surfi-sculpt features in the steel substrate.

Von Mises stresses can be used to indicate the onset of plastic behaviour and in all cases the largest values were above structural peaks and were consistently >400MPa - above both the W/316L bulk yield stresses of 205/400MPa respectively in Table 5.1. This implied that any cracking was likely to initiate about structural peaks, a concept discussed in more detail later.

6.4.4 Surfi-sculpt coating residual stress measurement

Using the same $\sin^2\Psi$ approach [47, 95, 98] and PROTO iXRD combo diffractometer at the University of Manchester Materials Science Centre as with sample 128b in Section 6.4.2 but using progressive

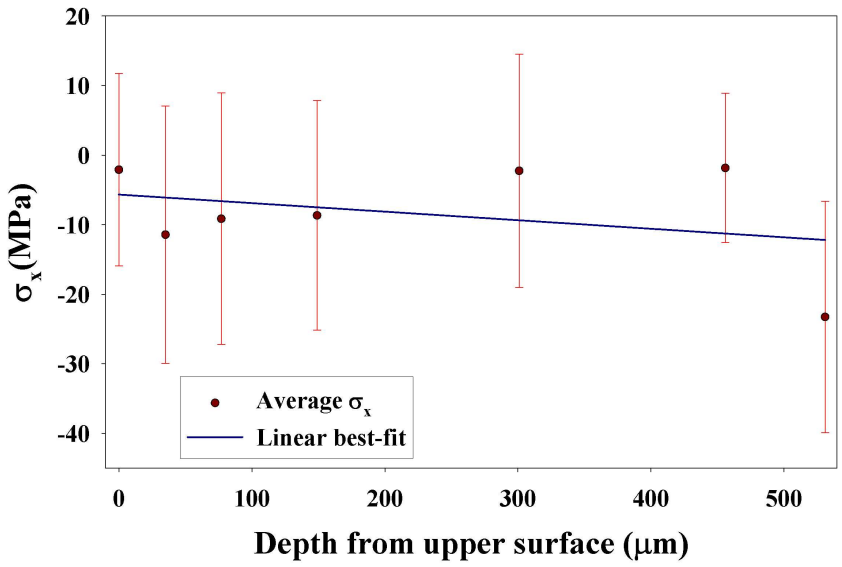

Figure 6.6: Average measured through thickness in-plane σ_x stresses for sample 158b.

W removal, a through thickness residual stress distribution for sample 158b was acquired. Layer removal involved electro-polishing, considered the most benign process to minimise additional damage during layer removal. The resultant through thickness residual stress distribution is shown in Figure 6.6. There was again low or zero stress at the top of the W coating, and as W was removed, a low compressive stress of magnitude 15-50MPa developed. Again, measurement uncertainty was large. Calculated stresses in this region were larger at -60 to -80MPa in the isothermal bending moment case e.g. Figure 5.24(a). Taken at face value and as with the graded coating surface stress measurements and calculations, these results may indicate the presence of stress redistribution/relief in the W containing layers.

The presence of low VPS W residual stresses was then further investigated by XRD using a 1mm thick section of surfi-sculpt substrate and coating 164b and a highly collimated 0.2mm^2 white hard (high energy) X-ray beam on station 16.3 (Engineering Strain Scanning and High Resolution Single Crystal Diffraction) of the Daresbury (UK) Synchrotron Radiation Source (SRS). These measurements were performed by Prof. Alexander Korsunsky and colleagues of the Department of Engineering, University of Oxford, and the results discussed with the author. This high energy X-ray source was able to fully penetrate the 1mm thick slice allowing internal strains/stresses to be calculated via the $\sin^2\Psi$ approach integrated over the sampling volume. The experimental arrangement is illustrated schematically in Figure 6.7.

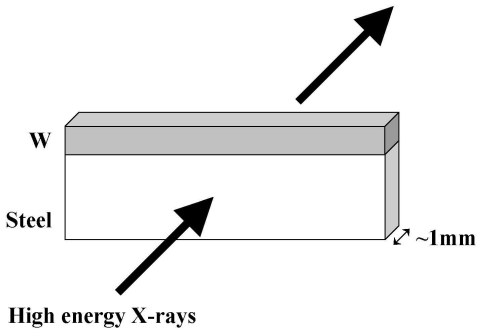

Figure 6.7: Schematic illustration of XRD measurement approach at Daresbury, UK.

Maps of σ_x and σ_y from these measurements and estimated using the measured W and 316L Young's modulus values of 194 and 228GPa respectively are presented in Figures 6.8(a) and 6.9(a) respectively. The black line demarks the boundary where the different Young's modulus values (W above) had to be assumed and were a best-guess of where the interface between the surfi-sculpt 316L and VPS W lay. However, since the moduli were close, the difference in calculated stresses in this area was relatively small. For comparison, σ_x and σ_y maps calculated by a FE model for a matching 2mm thick W coating with bending and a non-isothermal substrate temperature profile at isothermal coating deposition, are included in Figures 6.8(b) and 6.9(b) respectively.

The average σ_x tensile stress in the substrate of ∼40MPa in Figure 6.8(a) (as expected from its higher CTE) was predicted as ∼70MPa by the FE model in Figure 6.8(b). However, the measured σ_y tensile stress in Figure 6.9(a) was not predicted by the corresponding FE model. The high degree of local residual stress variation within the substrate was attributed to the processing history - e.g. repeated rastering with an e-beam to form the surface architecture may have induced complex sub-surface residual stresses in the stainless steel.

The bulk VPS W σ_x stresses were -20 to -30MPa compared to FE calculations of ∼-70MPa. However, the magnitude of the measured 'bulk' W σ_y stresses of -40 to -100MPa were higher than the magnitude of the FE stress of ∼0MPa. Maximum compressive σ_x stresses were found at surfi-sculpt peaks, with values of ∼-40MPa (measured) and ∼-250MPa (FE). The maximum compressive σ_y measured/FE values were comparable at ∼-240MPa. However, the maximum σ_y stresses occurred at different points, around the peaks in the measured distribution and about the troughs in the FE model. Further, a very high tensile σ_y stress of 355MPa was predicted by the model about the surfi-sculpt peaks but was not seen in the measured stress distribution.

These differences may be attributed to a combination of: (1) stress relief/redistribution due to the horizontal cracking observed to occur in all surfi-sculpt systems (discussed later), (2) the use of 2D FE models of arbitrary cross-sections to approximate the complex 3D nature of the surfi-sculpt substrates, and (3) stresses measured at any particular point are an average through the 1mm thick sampled volume/underlying 3D sections of the surfi-sculpt substrate.

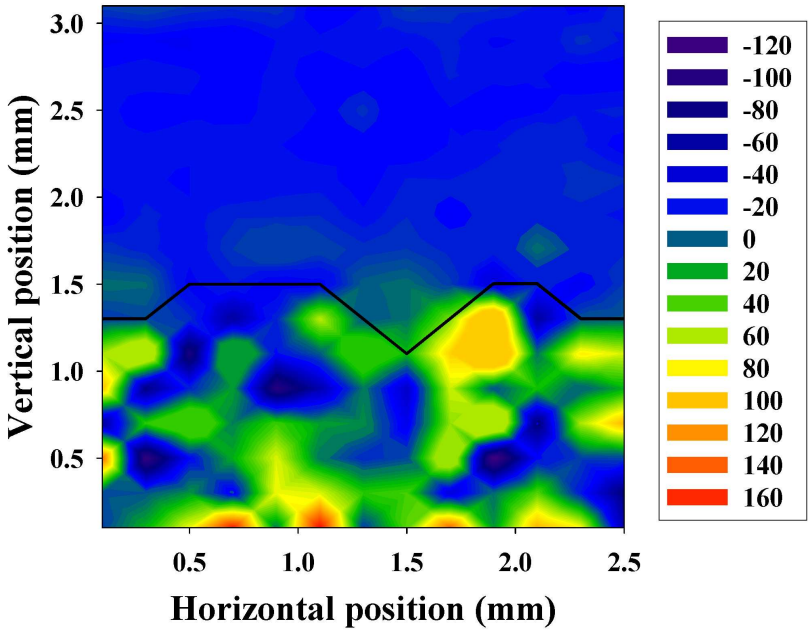

(a): Measured σ_x distribution, sample 164b (MPa)

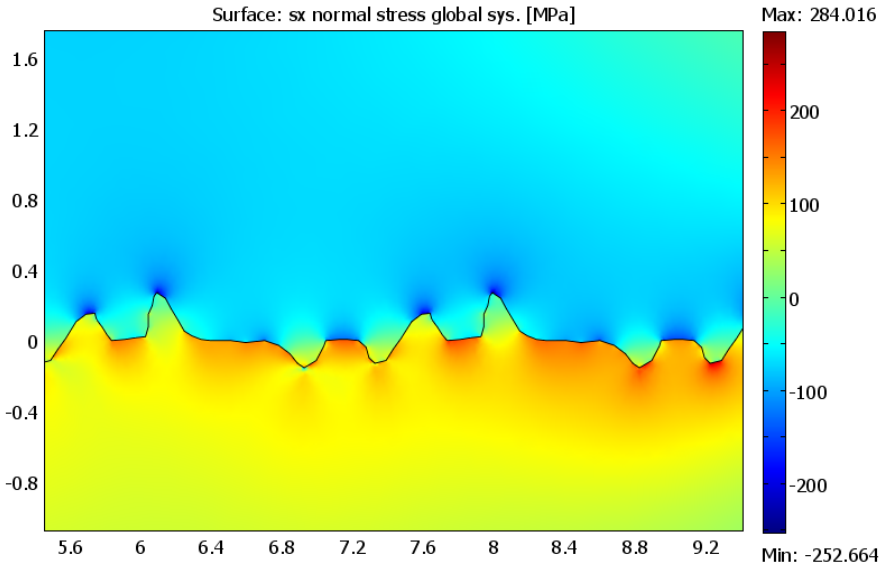

(b): FE model of σ_x distribution, sample 164b

Figure 6.8: Comparison of measured and calculated σ_x distributions for sample 164b - Figure 4.30(b) (all dimensions in mm).

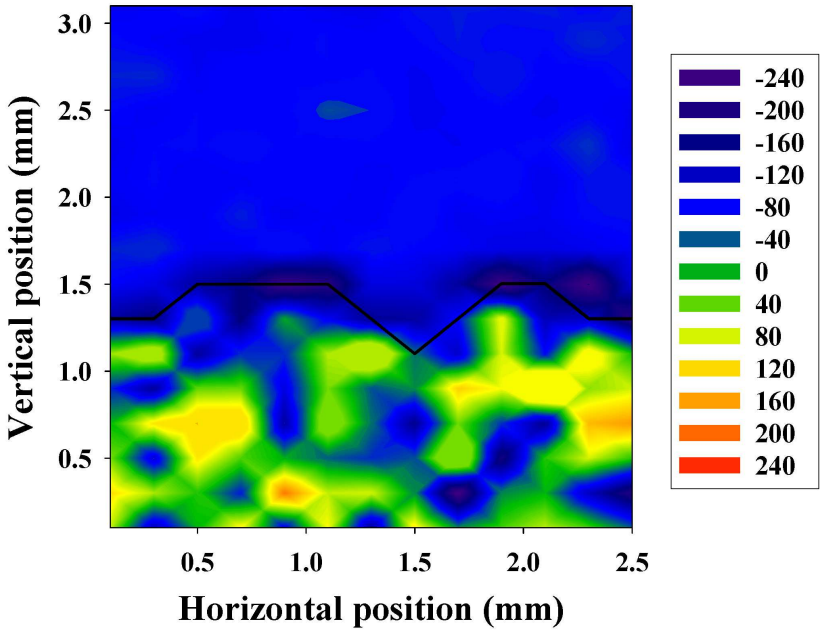

(a): Measured σ_y distribution, sample 164b (MPa)

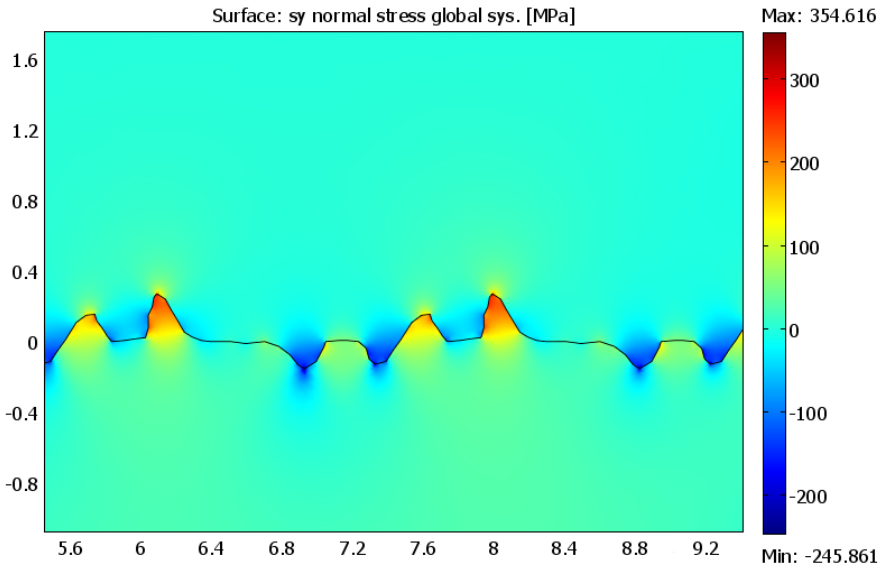

(b): FE model of σ_y distribution, sample 164b

Figure 6.9: Comparison of measured and calculated σ_y distributions for sample 164b - Figure 4.30(b) (all dimensions in mm).

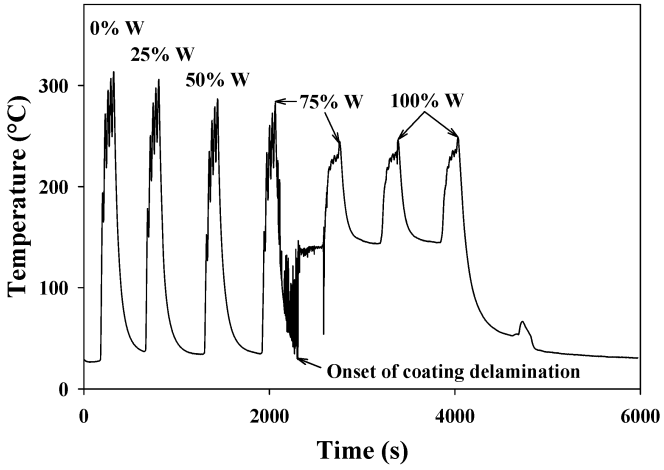

Figure 6.10: Thermal history, sample 63b.

6.5 Stress management

6.5.1 Graded coating delamination

The FE model was used to try to understand coating delamination under certain conditions and two examples for coatings 63b and 142b (5-layer linearly graded and 11-layer parabolically graded respectively) are now presented. The thermal history for coating 63b is shown in Figure 6.10 and on cool-down after deposition of the 2^{nd} 75% W pass, there were erratic spikes in the substrate temperature and a change in peak temperature behaviour thereafter. This was linked to the partial delamination of the coating at the non-heat treated substrate/bond coat interface. Both 142b coatings delaminated during cool down after the final pass at the substrate/bond coat interface.

The σ_x and elastic stored strain energy distributions for these two cases are presented in Figures 6.11(a) and (b) respectively, with both bending moments and a non-isothermal substrate temperature distribution at isothermal coating deposition assumed. Additionally, a 5-layer linearly graded coating considered previously and which in general did not delaminate in experiment is included for comparison.

For coating 63b, due to the higher peak temperatures of $\sim$280^{o}C, delamination is attributed to the correspondingly large stored strain energy that developed in the bond coat in Figure 6.11(b) and weak interfacial fracture energy because no heat treatment was used. For coating 142b, the majority

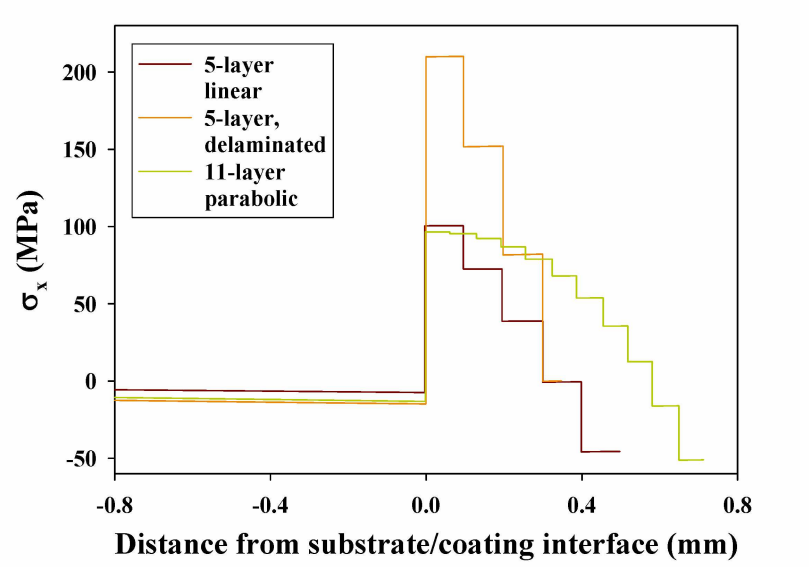

(a): σ_x variation, various graded coating arrangements

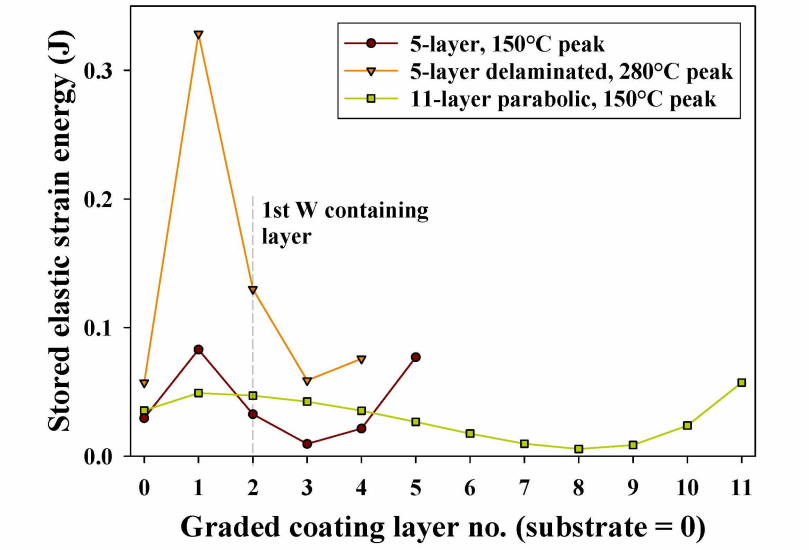

(b): Variation of stored elastic strain energy, various graded coating arrangements

Figure 6.11: Comparison of calculated FE distributions for as-sprayed and delaminated coatings of various arrangements.

of the W volume fraction is located comparatively far from the interface. As shown previously in Figure 5.16(f), the re-distribution of W towards the upper surface of the coating associated with the introduction of a parabolic arrangement leads to a total stored strain energy closer to that of a bi-layer system. Despite the similar coating thickness compared with the much thicker substrate in all cases, this re-distribution of W effectively provides a 'lever' effect, with the resultant force acting at the non heat treated and comparatively weak substrate/bond coat interface.

6.5.2 Surfi-sculpt coatings

Surfi-sculpt VPS W coatings have been shown to survive up to 33 thermal cycles during manufacture and, as suggested by the FE models, must 'manage' thermal residual stresses greater than the yield stress of W in the region of interfacial topography because of the strong stress concentrating effects near the interface. The lower value of measured residual stresses compared with FE calculations implies that a stress relieving mechanism is in operation within the as-sprayed W coatings. FE models have consistently shown stress concentration about surfi-sculpt peaks and through thickness analysis of a cross-section of sample 9 found evidence of in-plane inter-splat cracking about these points of stress concentration e.g. Figure 4.28. Yet the W is retained. The retention of these thick VPS W coatings combined with the low measured surface and internal residual stresses implies that this cracking is non-catastrophic and instead acts to relieve residual stresses via a process of 'coating segmentation'.

It is postulated that internal cracking at the regular points of stress concentration prevents transmission of residual stress from close to the interface to the 'bulk' of the coating, minimising the magnitude of stresses away from the interface, and consistent with the observed and modelled bulk σ_x and σ_y stresses. To explain the measured compressive rather than tensile σ_y stresses in the W about structural peaks, it is postulated that local coating segmentation acts to relieve the tensile stresses which the FE model in Figure 6.9(b) predicts and instead only the average compressive stress from the underlying sub-surface features is contributing to the measured stress in the local region. Internal coating segmentation has been both observed, and implied by the low residual stresses, and the ability of the surfi-sculpt coatings to retain reactor-relevant thicknesses of W has been demonstrated. FE models represent a useful tool for identifying the location of this segmentation, but full confidence in their

application will require development of a suitable segmentation model and further consideration of the effects of underlying structural features on the resultant residual stress distribution, especially in 3D.

Chapter 7

Conclusions

Different VPS W/steel PFC options have been investigated and trial coatings with reactor-relevant thicknesses manufactured. Qualitative insight into the development and management of CTE mismatch residual stress in these coatings has been gained by FE analysis. Key conclusions are:

7.1 VPS W

- A successful VPS W recipe has been developed and refined, capable of manufacturing <10% porosity thick W coatings. VPS powers of 53kW accompanied by a high secondary H_2 gas flow rate of 7lmin^{-1} were required to ensure adequate W powder melting.
- To overcome VPS machine power limitations a strategy of intermittent deposition was developed and successfully used.
- W coating porosity and the interwoven splat nature of as-sprayed coatings led to a reduction in Young's modulus of the as-sprayed VPS W to ∼194GPa by nano-indentation, compared to a bulk W Young's modulus of 410GPa.
- EBSD analysis of VPS W showed evidence of ∼1μm W grains and splat-scale directionality/columnar grain growth in the direction of heat removal.
- Active water cooling within the inert low pressure spraying chamber ensured minimal VPS W

oxidisation.

7.2 Graded coatings

- The difficulty of co-spraying W and steel (a Eurofer analogue, Diamalloy 1008) due to the importance of centering the W powder flow into the hottest region of the plasma core was highlighted and a strategy for solving this problem by balancing W/steel flows and optimising W injection strategies into the plasma was considered.

- 50:50 W/Diamalloy interlayers similar to the previous 'state-of-the-art' in W/steel graded coatings have been successfully manufactured on a Diamalloy bond coat on mild steel allowing deposition of a $\sim$150μm thick W coating.

- The potential to manufacture W/Diamalloy graded coatings with non-linear variations of W fraction with thickness up to 1mm by VPS has been demonstrated, although linear variations were found to be most effective in managing thermal residual stresses.

- Very many W/Diamalloy linearly graded coatings with thicknesses of $\sim$500μm were manufactured under repeatable thermal conditions and retained up to 200μm thick VPS W coatings.

- Active cooling, combined with a thermal heat transfer paste, was found essential for consistent W coating retention because it minimised peak substrate manufacturing temperatures and consequently peak thermally induced stresses.

- Heat treatment of graded coating bond coats was shown to enhance subsequent coating adhesion due to substrate/bond coat inter-diffusion and was considered essential for successful graded coating manufacture.

- The microstructure of as-sprayed W/Diamalloy graded coatings was investigated and regular splat-scale W/Diamalloy layering was observed due to different feedstock behaviours in the plasma flame. The use of post-hopper mixing of feedstock powders to overcome this issue was successfully demonstrated.

- Through thickness variation in W fraction was shown via nano-indentation to produce a corresponding approximate variation in hardness and Young's modulus.

- Finite element analysis allowed qualitative prediction of thermally induced residual stress distributions in as-sprayed graded coatings and calculations were found to be broadly consistent with preliminary residual stress measurements on as-sprayed coatings when an initially stress-free substrate with a non-linear temperature distribution at coating deposition was assumed.

- Key features of graded coatings that allowed the retention of thick W coatings were identified via FE analysis and included: (a) reduction in the step-change in stress across the interface with increasing compositional graduation; (b) most importantly, a reduction in stored strain energy, the driving force for coating delamination, within the coating and particularly at the substrate/bond and bond coat/graded layer interface, especially when a linear compositional gradient was employed; and (c) a reduction in peak interfacial stresses and total stored elastic strain energy with increased (linear) compositional graduation due to lower total coating bending.

7.3 Surfi-sculpt coatings

- Different surfi-sculpt topographies were investigated and optimum surface features required to enhance coating retention and prevent catastrophic sub-surface coating cracking were identified: wide and shallowly sloping peaked structures, and wide, shallow sub-surface features.

- Surfi-sculpt substrates with a suitable topography were shown to be efficient at retaining reactor-relevant up to 2mm thick VPS W coatings without subsequent delamination.

- The intermittent nature of coating deposition meant that as-sprayed coatings were required to survive up to 33 manufacturing to room temperature thermal cycles.

- Elastic 2D FE modelling demonstrated similarities between all topographies considered, with the key feature being stress concentration about peaked surfi-sculpt structures.

- Successive layer removal/microstructural analysis established that surfi-sculpt substrates promote regular cracking/segmentation about structural peaks.

- Preliminary X-ray diffraction residual stress measurements showed low surface and bulk W stresses, implying the presence of a stress relieving mechanism within the as-sprayed VPS W coatings.

- The combination of retention of reactor-relevant thicknesses of VPS W through up to 33 manufacturing cycles, stress concentration in FE models, observed cracking and lower than calculated residual stresses was attributed primarily to regulated sub-surface cracking caused by the regular array of peaked features in the surfi-scuplt substrate.

Overall, the main aims of this project have been achieved. A successful manufacturing strategy for VPS W/steel graded coatings has been developed and shown consistent and repeatable. Approaches to minimise the development of residual stress during manufacture have been implemented. FE modelling, combined with preliminary surface residual measurements, has proved useful: (a) to aid understanding of the thermal conditions during manufacture, and (b) to provide insight of how graded coatings manage thermal residual stresses. The emerging technology of surfi-sculpt modification of substrate surfaces has been shown useful for plasma spraying applications. Surfi-sculpt substrates with no interlayers were able to retain thicknesses of up to 2mm of VPS W without delamination and microstructural characterisation and FE analysis, combined with initial residual stress measurements from two separate sources, provided strong evidence of regulated, non-catastrophic internal coating segmentation which acts to relieve CTE mismatch stresses.

Chapter 8

Future work

While the manufacture of thick VPS coatings, particularly on surfi-sculpt substrates, has been demonstrated and initial investigations into the management of thermal residual stresses initiated there is scope to extend this work further. In particular:

1. Manufacture of thick 1mm+ VPS W coatings on graded interlayers (not attempted due to time constraints) to provide a more adequate point of comparison with surfi-sculpt VPS W coatings.

2. Thermal cycling of as-sprayed coatings using the VPS torch to determine thermal cycling and thermal shock response, an approach considered but not implemented due to time constraints.

3. Use of the 'hot cell' feature of the Nano Test machine to characterise the elastic modulus of VPS W at elevated temperatures.

4. To explore W/steel interfacial fracture energies by nano-indentation.

5. The development of 3D FE models to account for the complexity of the 3D topographies would allow for the design, manufacture by TWI, subsequent coating with VPS W and characterisation of an optimum surfi-sculpt substrate topography.

6. Further X-ray residual stress measurements through thin sections of as-sprayed coatings, combined with 3D surfi-sculpt models, would allow for a greater understanding of the extent of the stress-relieving mechanisms in operation.

7. To investigate surfi-sculpt regulated coating segmentation for other material combinations, e.g. ceramics on metal substrates.

Bibliography

[1] P.A. Tipler. *Physics for Scientists and Engineers.* W.H. Freeman and Company, New York, 1999.

[2] K.S. Krane. *Introductory Nuclear Physics.* John Wiley & Sons, Inc., USA, 1998.

[3] R. Dendy (ed). *Plasma Physics: An Introductory Course.* Cambridge University Press, Cambridge, 1996.

[4] Jet and fusion energy for the next millenia (presentation published online). http://fusfis.frascati.enea.it/Documents/Presentations/PDFfiles/JET-Slides.pdf.

[5] J. Wesson. *The Science of JET.* JET Joint Undertaking [Publications - JET-R(99)13], Oxford, 1st edition, 2000.

[6] G. Ferderici, C.H. Skinner, J.N. Brooks, J.P. Coad, C. Grisolia, A.A. Haasz, A. Hassanein, V. Philipps, C.S. Pitcher, J. Roth, W.R. Wampler, and D.G. Whyte. Plasma-material interactions in current tokamaks and their implications for next step fusion reactors. *Nuc. Fus.*, **41**:1967–2137, December 2001.

[7] P.C. Stangeby. *The Plasma Boundary of Magnetic Fusion Devices.* Institute of Physics Publishing, Bristol, 2001.

[8] ITER Physics Basis Editors, ITER Physics Expert Group Chairs and Co-Chairs, and ITER Joint Central Team and Physics Integration Unit. Chapter 1: Overview and summary. *Nuc. Fus.*, **39**:2137, December 1999.

[9] J. Linke, R. Duwe, A. Gervash, R.H. Qian, M. Rödig, and A. Schuster. Material damage to beryllium, carbon, and tungsten under severe thermal shocks. *J. Nuc. Mater.*, **258-263**, Part 1:634–639, October 1998.

[10] J. Hugill. Plasma transport. Course notes, 41^{st} Culham Plasma Phys. Sum. Sch., 2004.

[11] B. Alper. Paths to magnetic confinement. Course notes, 41^{st} Culham Plasma Phys. Sum. Sch., 2004.

[12] S.L. Dudarev. Material science for plasma physicists. Course notes, 41^{st} Culham Plasma Phys. Sum. Sch., 2004.

[13] A. Hassanein, I. Konkashbaev, and V.A. Glukhikh (ed.). Dynamic behavior of plasma-facing materials during plasma instabilities in tokamak reactors. *Plasma Devices and Operations*, **5**, 4:297–313, 1998.

[14] H. Bolt, V. Barabash, W. Krauss, J. Linke, R. Neu, S. Suzuki, N. Yoshida, and the ASDEX Upgrade Team. Materials for plasma-facing components of fusion reactors. *J. of Nuc. Mater.*, **329-333**:66–73, 2004.

[15] The judith facility (background information, published online). www.fz-juelich.de/bd/hz/b_z_service_judith_e.html.

[16] R. Duwe, W. Khnlein, and H. Mnstermann. In K. Herschbach, W. Maurer, and J.E. Vetter, editors, *Proc. 18^{th} Symp. on Fus. Tech*, pages 355–358, Karlsruhe, Germany, 22-26 Aug 1994.

[17] S.W.H. Yih and C.T. Wang. *Tungsten, Sources, Metallurgy, Properties and Applications*. Plenum Press, New York, 1979.

[18] E. Lassner and W.D. Schubert. *Tungsten: Properties, Chemistry, Technology of the Element, Alloys, and Chemical Compounds*. Kluwer Academic/Plenum Publishers, New York, 1999.

[19] J.W. Davis, V.R. Barabash, A. Makhankov, L. Plöchl, and K.T. Slattery. Assessment of tungsten for use in the iter plasma facing components. *J. Nuc. Mater.*, **258-263**:308–312, 1998.

[20] A.G. Ioltukhovsky, V.P. Kondrat'ev, M.V. Leont'eva-Smirnova, S.N. Votinov, V.K. Shamardin, A.V. Povstyanko, and T. M. Bulanova. Metallurgical aspects of possibility of 9-12% chromium

steel application as a structural material for first wall and blanket of fusion reactors. *J. Nuc. Mater.*, **233-237**:299–304, Oct 1996.

[21] K. Tokunaga, Y. Kubota, N. Noda, Y. Imamura, A. Kurumada, N. Yoshida, T. Sogabe, T. Kato, and B. Schedler. Behaviour of actively cooled mock-ups with plasma sprayed tungsten coating under high heat flux conditions. *J. Fus. Eng. & Des.*, **81**:133–138, 2006.

[22] R. Neu, K. Asmussen, S. Deschka, A. Thoma, M. Bessenrodt-Weberpals, R. Dux, W. Engelhardt, J.C. Fuchs, J. Gaffert, C. García-Rosales, A. Herrmann, K. Krieger, F. Mast, J. Roth, V. Rohde, M. Weinlich, U. Wenzel, ASDSX Upgrade Team, and ASDEX NI-Team. The tungsten experiment in asdex upgrade. *J. Nuc. Mater.*, **241-243**:678–683, 1997.

[23] S. Lehto, J. Likonen, J.P. Coad, T. Ahlgren, D.E. Hole, M. Mayer, and J. Kolehmainen. Tungsten coating on jet divertor tiles for erosion/deposition studies. *Fus. Eng. & Des.*, **66-68**:241–245, Sept 2003.

[24] H. Bolt, H. Greuner, B. Böswirth, S. Lindig, W. Kühnlein, T. Huber, K. Sato, and S. Suzuki. Plasma spray coating: Development and characterisation of 2 mm thick plasma sprayed tungsten coatings on steel, esp. eurofer. Max-Planck-Institut für Plasmaphysik, Final Report EFDA task TW3-TTMA-002, awaiting publication, 2004.

[25] I. Mazul, M. Akiba, I. Arkhipov, V. Barabash, S. Chiocchio, K. Ezato, G. Federici, G. Janeschitz, C. Ibbott, A. Makhankov, A. Markin, M. Merola, S. Suzuki, R. Tivey, M. Ulrickson, G. Vieider, and C.H. Wu. Status of r&d of the plasma facing components for the iter diverter (published online). *http://web.gat.com/iter/iter-ga/images/pdfs/iter_6.pdf.*

[26] K. Sato, K. Ezato, M. Taniguchi, S. Suzuki, and M. Akiba. Development of iter divertor plate with annular swirl tube and tungsten rods. *J. Plasma Fusion Res. Ser.*, **5**:556–560, 2003.

[27] H. Tsuji, K. Hamamatsu, H. Matsumoto, and H. Yoshida (ed). *JAERI-Review 2003-035: Annual Report of Naka Fusion Research Establishment From April 1 2002 to March 31 2003, Japan Atomic Energy Research Institute.* 2003.

[28] R. Neu, R. Dux, A. Geier, O. Gruber, A. Kallenbach, K. Krieger, H. Maier, R. Pugno, V. Rohde, and S. Schweizer. Tungsten as plasma-facing material in asdex upgrade. *Fus. Eng. & Des.*, **65**:367–374, April 2003.

[29] Y. Ueda, T. Tanabe, V. Philipps, L. Könen, A. Pospieszczyk, U. Samm, B. Schweer, B. Unterberg, M. Wada, N. Hawkes, and N. Noda. Effects of impurities released from high z test limiter on plasma performance in textor. *J. Nuc. Mater.*, **220-222**:240–243, April 1995.

[30] I. Smid, M.Akiba, G. Vieider, and L. Plochl. Development of tungsten armor and bonding to copper for plasma-interactive components. *J. Nuc. Mater.*, **258-268**:160–172, Oct 1998.

[31] K. Ehrlich. Materials research towards a fusion reactor. *Fus. Eng. & Des.*, **56-57**:71–82, Oct 2001.

[32] L. Schäfer, M. Schirra, and K. Ehrlich. Mechanical properties of low activating martensitic 8-10% crwvta steels of type optifer. *J. Nuc. Mater.*, **233-237**:264–269, Oct 1996.

[33] C. Petersen and D. Rodrian. Thermo-mechanical fatigue behavior of reduced activation ferrite/martensite stainless steels. *J. Nuc. Mater.*, **307-311**:500–504, Dec 2002.

[34] C. Petersen, R. Schmitt, and D. Garnier. Thermal and isothermal low cycle fatigue of manet i and ii. *J. Nuc. Mater.*, **233-237**:285–288, Oct 1996.

[35] P. Fernández, A.M. Lancha, J. Lapeña, and M. Hernández-Mayoral. Metallurgical characterization of the reduced activation ferritic/martensitic steel eurofer 97 on as-received condition. *Fus. Eng. & Des.*, **58-59**:787–792, Nov 2001.

[36] A. Alamo. Irradiated behaviour of reduced activation (ra) martensitic steels after neutron irradiation at 325^{o}c, ut-sm&c-lam2. *Fusion Technology: Annual Report of the Association EURATOM/CEA*, pages 277–280, 1998.

[37] P. Fernández, A.M. Lancha, J. Lapeña, M. Serrano, and M. Hernández-Mayoral. Metallurgical properties of reduced activation martensitic steel eurofer′97 in the as-received condition and after thermal ageing. *J. Nuc. Mater.*, **307-311**:495–499, Dec 2002.

[38] P. Spätig, G.R. Odette, G.E. Lucas, and M. Victoria. On the mechanical properties of the advanced martensitic steel eurofer 97. *J. Nuc. Mater.*, **307-311**:536–539, Dec 2002.

[39] R. Schaeublin, D. Gelles, and M. Victoria. Microstructure of irradiated ferritic/martensitic steels in relation to mechanical properties. *J. Nuc. Mater.*, **307-311**:197–202, Dec 2002.

[40] B. van der Schaaf, F. Tavassoli, C. Fazio, E. Rigal, E. Diegele, R. Lindau, and G. LeMarois. The development of eurofer reduced activation steel. *Fus. Eng. & Des.*, **69**:197–203, Sept 2003.

[41] H. Sakasegawa, T. Hirose, A. Kohyama, Y. Katoh, T. Harada, K. Asakura, and T. Kumagai. Effects of precipitation morphology on toughness of reduced activation ferritic/martensitic steels. *J. Nuc. Mater.*, **307-311**:490–494, Dec 2002.

[42] D.S. Gelles. Microstructural examination of commercial ferritic alloys at 200 dpa. *J. Nuc. Mater.*, **233-237**:293–298, Oct 1996.

[43] N. Baluc, R. Schäublin, P. Spätig, and M. Victoria. On the potentiality of using ferritic/martensitic steels as structural materials for fusion reactors. *J. Nuc. Fus.*, **44, No.1**:56–61, Jan 2004.

[44] T. Shibayama, A. Kimura, and H. Kayanoet. The effect of small additional elements on the precipitation of reduced activation fe-9cr-2w steels. *J. Nuc. Mater.*, **233-237**:270–275, Oct 1996.

[45] http://www.plasmacoat.co.uk/print-plasma_spray.htm.

[46] C. Moon. *Part II Thesis: Vacuum Plasma Spraying of CoNiCrAlY coatings.* Pembroke College, Oxford Univerity, 1994.

[47] Vernon John. *Introduction to Engineering Materials.* Palgrave Macmillan, Hampshire, 4th edition, 2003.

[48] J.H. Perepezko. Nucleation in undercooled liquids. *Mater. Sci. & Eng.*, **65**:125–135, July 1984.

[49] K. Baik and P. Grant. *Proc. 5^{th} European Conference on Advanced Materials, Processes and Applications*, pages 341–346, 1997.

[50] K.H. Baik. *Spray/wind processing of hoop reinforced high temperature composites.* Oxford Univerity, 1999.

[51] R.G. Castro and P.W. Stanek. *Microlaminate Composite Structures by Low Pressure Plasma Spray Deposition.* Materials Science and Technology Division, Los Alamos National Laboratory, Los Alamos, NM 87545, 1985.

[52] http://www.plansee.com/index_ENG_HTML.htm.

[53] http://www.plasmapros.com/nozzles.htm.

[54] F. Zimmerman. Advanced technology development'96: Manufacturing of refractory containment cartridges. http://spaceresearch.hamptonu.edu/ATD/zimmerman.html, 1996.

[55] G. Pintsuk, I. Smid, J.E. Döring, W. Hohenauer, and J. Linke. Fabrication and characterization of vacuum plasma sprayed w/cu-composites for extreme thermal conditions. *J. Mater. Sci.*, **42**:30–39, 2007.

[56] J.H. You, T. Höschen, and S. Lindig. Determination of elastic modulus and residual stress of plasma-sprayed tungsten coating on steel substrate. *J. of Nuc. Mater.*, **348**:94–101, 2006.

[57] M. Koizumi and M. Niino. Overview of fgm research in japan. *MRS Bul.*, **Vol. XX No. 1**:19–21, 1995.

[58] A. Mortensen and S. Suresh. Functionally graded metals and metal-ceramic composites part i. processing. *Int. Mater. Reviews*, **Vol. 40 (6) No. 1**:239–265, 1996.

[59] B.H. Rabin and I. Shiota. Functionally gradient materials. *MRS Bul.*, **Vol. XX No. 1**:14–18, 1995.

[60] G. Bao and H. Cai. Delamination cracking in functionally graded coating/metal substrate systems. *Acta Mater.*, **Vol. 45 No. 3**:1055–1066, 1997.

[61] S. Sampath, H. Herman, N. Shimoda, and T. Saito. Thermal spray processing of fgms. *MRS Bul.*, **Vol. XX No. 1**:27–31, 1995.

[62] N. Hill. *Part II Thesis: Processing of Functionally Gradient Ni-PSZ Coatings by Low Pressure Plasma Spraying.* St. Catherine's College, Oxford Univerity, 1996.

[63] K.A. Khor and Y.W. Gu. Effects of residual stress on the performance of plasma sprayed functionally graded zro_2/nicocraly coatings. *Mater. Sci. & Eng. A*, **277**:64–76, 2000.

[64] R. Watanabe. Powder processing of functionally gradient materials. *MRS Bul.*, **Vol. XX No. 1**:32–34, 1995.

[65] H. Ahn and S.H. Hong. *Proc.* 15^{th} *Int. Ther. Spray Conf., 25-29 May, Nice, France*, pages 1635–1640.

[66] Hua-Ping Xiong, Akira Kawasaki, Yan-Sheng Kang, and Ryuzo Watanabe. Experimental study on heat insulation performance of functionally graded metal/ceramic coatings and their fracture behavior at high surface temperatures. *Surface & Coatings Tech.*, **194**:203–214, 2005.

[67] N. Sakamoto and H. Kawamura. Preliminary characterization of interlayer for be-cu functionally gradient materials. *J. Nuc. Mater.*, **233-237**:609–611, 1996.

[68] J.W. Davis, K.T. Slattery, D.E. Driemeyer, and M.A. Ulrickson. Use of tungsten coating on iter plasma facing components. *J. Nuc. Mater.*, **233-237**:604–608, 1996.

[69] Chang-Chun Ge, Jiang-Tao Li, Zhang-Jian Zhou, Wen-Bin Cao, Wei-Peng Shen, Ming-Xu Wang, Nian-Man Zhang, Xiang Liu, and Zheng-Yu Xu. Development of functionally graded plasma-facing materials. *J. Nuc. Mater.*, **283-287**:1116–1120, 2000.

[70] Yun-Han Ling, Jiang-Tao Li, Chang-Chun Ge, and Xin-De Bai. Fabrication and evaluation of sic/cu functionally graded material used for plasma facing components in a fusion reactor. *J. Nuc. Mater.*, **303**:188–195, 2000.

[71] Y.C. Tsui and T.W. Clyne. An analytical model for predicting residual stresses in progressively deposited coatings. part 3: Further development and applications. *Thin Solid Films*, **306**:52–61, 1997.

[72] Y. Guo, T. Nakamura, L. Prchlik, S. Sampath, and J. Wallace. Micro-indentation and inverse analysis to characterize elastic-plastic graded materials. *Mater. Sci. & Eng. A*, **345**:223–233, 2003.

[73] T. Nakamura, T. Wang, and S. Sampath. Determination of properties of graded materials by inverse analysis and instrumented indentation. *Acta Mater.*, **48**:4293–4306, 2000.

[74] J. Ilavsky, C.C. Berndt, H. Herman, and M.B. Beardsleya. Thermal expansion of metallic and cermet coatings. *Proc. Nat. Ther. Spray Conf., 7-11 June Anaheim, CA*, pages 601–606, 1993.

[75] S.C. Gill and T.W. Clyne. Investigation of residual stress generation during thermal spraying by continuous curvature measurement. *Thin Solid Films*, **250**:172–180, 1994.

[76] R. Knight and R.W. Smith. Residual stress in thermally sprayed coatings. *Proc. Nat. Ther. Spray Conf., 7-11 June, Anaheim, CA*, pages 607–612, 1993.

[77] Y.C. Tsui and T.W. Clyne. An analytical model for predicting residual stresses in progressively deposited coatings. part 1: Planar geometry. *Thin Solid Films*, **306**:23–33, 1997.

[78] R. Roy and J.R. Craig. *Mechanics of Materials*. John Whiley & Sons Inc., USA, 1996.

[79] S.P. Timoshenko and J.M. Gere. *Mechanics of Materials*. Van Nostrand Reinhold Company, New York, USA, 1972.

[80] K. Pete and A.E. Palmer. *Mechanics of Materials*. McGraw-Hill Book Company, Inc., USA, 1963.

[81] Y.C. Tsui and T.W. Clyne. An analytical model for predicting residual stresses in progressively deposited coatings. part 2: Cylindrical geometry. *Thin Solid Films*, **306**:34–51, 1997.

[82] C.H. Hsueh and S. Lee. Modelling of elastic thermal stresses in two materials joined by a graded layer. *Compsities: Part B*, **34**:747–752, 2003.

[83] C.H. Hsueh. Modelling of elastic deformation of multilayers due to residual stresses and external bending. *J. Appl. Phys.*, **Vol.91** No. 12:9652–9656, June 2002.

[84] P.P. Benham, R.J. Crawford, and C.G. Armstrong. *Mechanics of Engineering Materials*. Pearson Education Ltd., Harlow, U.K., 2nd edition, 1996.

[85] Y.M. Shabanaa and N. Noda. Thermo-elasto-plastic stresses in functionally graded materials subjected to thermal loading taking residual stresses of the fabrication process into consideration. *Compsities: Part B*, **32**:111–121, 2001.

[86] H. Greuner, H. Bolt, B. Böswirth, S. Lindig, W. Kühnlein, T. Huber, K. Sato, and S. Suzuki. Vacuum plasma-sprayed tungsten on eurofer and 316l: Results of characterisation and thermal loading tests. *Fus. Eng. & Des.*, **75-79**:333–338, 2005.

[87] http://www.sulzermetco.com/en/desktopdefault.aspx.

[88] E. Mainsah *ed*, K.J. Stout, T.R. Thomas, J.A. Greenwood *ed*, and D.G. Chetwynd *ed*. *Metrology and Properties of Engineering Surfaces.* Boston, 2001.

[89] K.A. Roberts and T.W. Clyne. A simple procedure for the characterization of spray deposition processes - the linescan test. *Surf. & Coatings Tech.*, **Vol. 41 No. 1**:103–115, 1990.

[90] A.P. Newbery and P.S. Grant. A particle image velocimetry investigation of in-flight and deposition behaviour of steel droplets during electric arc sprayforming. *Mater. Sci. & Eng. A*, **Vol. 383**:137–145, 1990.

[91] Air liquide gas data. http://www.airliquide.com/en/business/products/gases/gasdata/.

[92] M. Hamer. Micro-sculptures give metal the velcro touch. *New Sci.*, **Vol. 2447**:21, 2004.

[93] B.G.I. Dance and E.J.C. Kellar. Workpiece structure modification. International Patent Publication No. WO 2004/028731A1.

[94] http://www.ebsd.com.

[95] M. Eckhardt and H. Ruppersberg. *Residual Stresses in Science and Technology, Volume 1 (Eds. E. Macherauch and V. Hauk),* Non-linear ($\sin^2\Psi$) curves observed for a cold rolled nickel sheet. FB Ingenieurwissenschaften der Universität des Saarlandes, 6600 Saarbrücken, Germany, 1987.

[96] B.D. Cullity. *Element of X-Ray Diffraction.* Addison-Wesley Publishing Company, Inc., USA, 2nd edition, 1978.

[97] H.U. Baron, V. Hauk, R.W.M. Oudelhoven, and B. Weber. *Residual Stresses in Science and Technology, Volume 1 (Eds. E. Macherauch and V. Hauk),* Evaluation of Residual Stresses in FCC-Textured Metals Using Strain and Intensity Polefigures. Rein.-Westf.Techn.Hochschule, Institut für Werkstoffkunde, Aachen, FRG, 1987.

[98] M. Miyano, T. Sasaki, S. Takago, S. Ejiri, and Y. Hirose. X-ray elastic constants of sintered high chromium steel containing titanium nitride: Comparison of models. *Proc. Denver X-ray Conf.: Advances in X-ray Analysis*, **Vol. 41**, 1997.

[99] W.C. Oliver and G.M. Pharr. An improved technique for determining hardness and elastic modulus using load and displacement sensing indentation experiments. *J. Matter. Res.*, **Vol.7, No.6**:1564–1583, 1992.

[100] H.J. Albrecht, T. Hannach, A. Häse, A. Juritza, and K. Müller. Nanoindentation: a suitable tool to determine local mechanical properties in microelectronic packages and materials? *Arch. Appl. Mech.*, **74**:728–738, 2005.

[101] A.C. Fischer-Cripps. Critical review of analysis and interpretation of nanoindentation test data. *Surface & Coatings Tech.*, **200**:4153–4165, 2006.

[102] F. Gao and T. Takemoto. Mechanical properties evolution of sn-3.5ag based lead-free solders by nanoindentation. *Mater. Letters*, **Vol. 60, Issue. 19**:2315–2318, 2006.

[103] S.O. Chwa and A. Ohmori. Microstructures of zro_2-8wt.%y_2o_3 coatings prepared by a plasma laser hybrid spraying technique. *Surface and Coatings Tech.*, **Vol. 153**:304–312, 2002.

[104] Mingyuan Liu, Bi Shi, Junxia Guo, Xun Cai, and Hongwei Song. Lattice constant dependence of elastic modulus for ultrafine grained mild steel. *Scripta Materialia*, **49**:167–171, 2003.

[105] R. Saha and W.D. Nix. Soft films on hard substrates - nanoindentation of tungsten films on saphire substrates. *Mater. Sci. & Eng. A*, **319-321**:898–901, 2001.

[106] M.M. Gasik. Micromechanical modelling of functionally graded materials. *Computational Mater. Sci.*, **13**:42–55, 1998.

[107] *Structural Mechanics Module User's Guide, Comsol 3.2.* Comsol AB, 2005.

[108] S. Kuroda and T.W. Clyne. The quenching stress in thermally sprayed coatings. *Thin Solid Films*, **200**:49–66, 1991.

[109] S. Joshi, A. Mukherjee, and S. Schmauder. Exact solutions for characterization of electro-elastically graded materials. *Computational Mater. Sci.*, **28**:548–555, 2003.

[110] William D. Callister Jr. *Materials Science and Engineering: An Introduction*. John Wiley & Sons Inc., USA, international edition edition, 2003.

[111] J.E. Döring, R. Vaßen, G. Pintsuk, and D. Stöver. The processing of vacuum plasma-sprayed tungsten-copper composite coatings for high heat flux components. *Fus. Eng. & Des.*, **66-68**:259–263, Sept 2003.

[112] A. Bartlett, A.G. Evans, and M. Rühle. Residual stress cracking of metal/ceramic bonds. *Acta Metall. Mater.*, **Vol. 39 No. 7**:1579–1585, 1991.